frontiers | Research Topics

The mechanism of trace elements on regulating immunity in prevention and control of human and animal diseases

Edited by
Mengyao Guo, Changwei Qiu, Haidong Yao, Yunhe Fu and Ziwei Zhang

Published in
Frontiers in Immunology

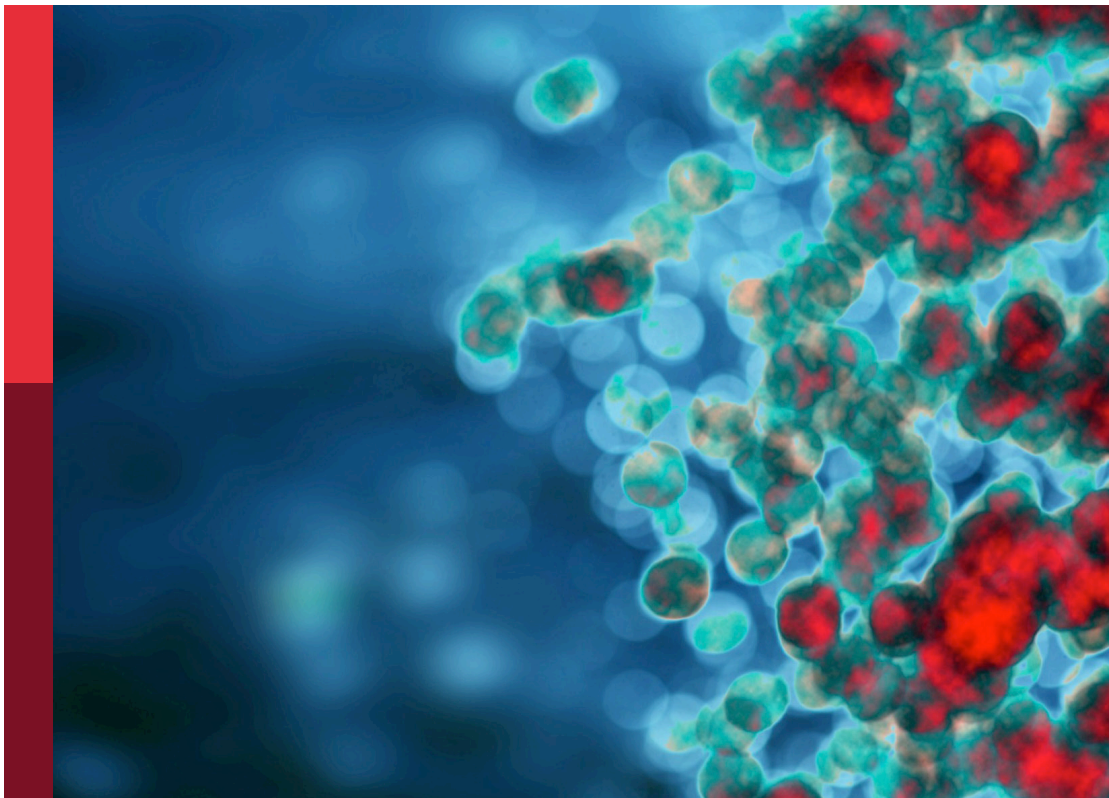

ISSN 1664-8714
ISBN 978-2-83251-861-8
DOI 10.3389/978-2-83251-861-8

About Frontiers

Frontiers is more than just an open access publisher of scholarly articles: it is a pioneering approach to the world of academia, radically improving the way scholarly research is managed. The grand vision of Frontiers is a world where all people have an equal opportunity to seek, share and generate knowledge. Frontiers provides immediate and permanent online open access to all its publications, but this alone is not enough to realize our grand goals.

Frontiers journal series

The Frontiers journal series is a multi-tier and interdisciplinary set of open-access, online journals, promising a paradigm shift from the current review, selection and dissemination processes in academic publishing. All Frontiers journals are driven by researchers for researchers; therefore, they constitute a service to the scholarly community. At the same time, the *Frontiers journal series* operates on a revolutionary invention, the tiered publishing system, initially addressing specific communities of scholars, and gradually climbing up to broader public understanding, thus serving the interests of the lay society, too.

Dedication to quality

Each Frontiers article is a landmark of the highest quality, thanks to genuinely collaborative interactions between authors and review editors, who include some of the world's best academicians. Research must be certified by peers before entering a stream of knowledge that may eventually reach the public - and shape society; therefore, Frontiers only applies the most rigorous and unbiased reviews. Frontiers revolutionizes research publishing by freely delivering the most outstanding research, evaluated with no bias from both the academic and social point of view. By applying the most advanced information technologies, Frontiers is catapulting scholarly publishing into a new generation.

What are Frontiers Research Topics?

Frontiers Research Topics are very popular trademarks of the *Frontiers journals series*: they are collections of at least ten articles, all centered on a particular subject. With their unique mix of varied contributions from Original Research to Review Articles, Frontiers Research Topics unify the most influential researchers, the latest key findings and historical advances in a hot research area.

Find out more on how to host your own Frontiers Research Topic or contribute to one as an author by contacting the Frontiers editorial office: frontiersin.org/about/contact

The mechanism of trace elements on regulating immunity in prevention and control of human and animal diseases

Topic editors

Mengyao Guo — Northeast Agricultural University, China
Changwei Qiu — Huazhong Agricultural University, China
Haidong Yao — Karolinska Institutet (KI), Sweden
Yunhe Fu — Jilin University, China
Ziwei Zhang — Northeast Agricultural University, China

Citation

Guo, M., Qiu, C., Yao, H., Fu, Y., Zhang, Z., eds. (2023). *The mechanism of trace elements on regulating immunity in prevention and control of human and animal diseases*. Lausanne: Frontiers Media SA. doi: 10.3389/978-2-83251-861-8

The authors declare that the research was conducted in the absence of any commercial or financial relationships that could be construed as a potential conflict of interest

Table of contents

frontiers | Frontiers in Immunology

TYPE Editorial
PUBLISHED 23 February 2023
DOI 10.3389/fimmu.2023.1159289

OPEN ACCESS

EDITED AND REVIEWED BY
Willem Van Eden,
Utrecht University, Netherlands

*CORRESPONDENCE
Ziwei Zhang
zhangziwei@neau.edu.cn
Jingzeng Cai
caijingzeng@neau.edu.cn

SPECIALTY SECTION
This article was submitted to Nutritional Immunology, a section of the journal Frontiers in Immunology

RECEIVED 05 February 2023
ACCEPTED 10 February 2023
PUBLISHED 23 February 2023

CITATION
Zhang X, Xu L, Liu P, Ma W, Liu Y, Qiao S, Liu Q, Cai J and Zhang Z (2023) Editorial: The mechanism of trace elements on regulating immunity in prevention and control of human and animal diseases. *Front. Immunol.* 14:1159289. doi: 10.3389/fimmu.2023.1159289

Editorial: The mechanism of trace elements on regulating immunity in prevention and control of human and animal diseases

Xintong Zhang[1], Lihua Xu[1], Pinnan Liu[1], Wenxue Ma[1], Yue Liu[1], Senqiu Qiao[1], Qiaohan Liu[1], Jingzeng Cai[1]* and Ziwei Zhang[1,2]*

[1]College of Veterinary Medicine, Northeast Agricultural University, Harbin, China, [2]Key Laboratory of the Provincial Education, Department of Heilongjiang for Common Animal Disease Prevention and Treatment, Harbin, China

KEYWORDS

selenoprotein M(SelM), TXNRD3, NiCl2, melatonin, mice

Editorial on the Research Topic

The mechanism of trace elements on regulating immunity in prevention and control of human and animal diseases

Nickel is a hard, malleable, silver-white transition metal that is widely used in metallurgical processes such as alloy manufacturing, nickel cadmium battery manufacturing, and food industries (1). Nickel can be enriched in humans and animals through the food chain and direct contact, and when it accumulates to a certain level in the body without proper treatment, it can be harmful to living organisms as a toxic metal ion (2–4). Human exposure to excessive nickel can cause toxic side effects such as allergies, cardiovascular disease, kidney disease, pulmonary fibrosis, and cancers (5). It has been shown that nickel nanoparticles can cause reproductive toxicity in mice (6). Melatonin (MT) is an indole hormone secreted primarily by the pineal gland in mammals and humans (7). It is used for the treatment of hypertension, hyperlipidemia, myocardial injury, and myocardial ischemia reperfusion injury (8). Previous experiments by Cai et al. showed that MT ameliorates trimethyltin chloride-induced cardiotoxicity through the nuclear xenobiotic metabolism and Keap1-Nrf2/ARE axis-mediated pyroptosis.

Selenium is an essential trace element for the human body, which exists in selenoproteins in the form of selenocysteine and selenomethionine, and exerts its biological functions through 25 selenoproteins. Selenoprotein M (SelM) is one of the executive factors of selenium *in vivo* and may be involved in antioxidant, neuroprotection and the regulation of intracellular calcium (9). Existing studies have shown that the overexpression of human SelM in rats increases the activity of antioxidant enzymes such as glutathione peroxidase (GPX) and superoxide dismutase (SOD) (10). In addition, SelM has

a neuroprotective function in the regulation of cytosolic calcium, which plays an important role in the pathogenesis of neurodegenerative diseases (11). Of note, previous studies have shown that SelM$^{-/-}$ mice are observed to be obese and leptin-resistant (12, 13). Our previous research showed that in a high-fat diet (HFD) induced non-alcoholic fatty liver disease (NAFLD) model, there is a significant downregulation of SelM expression. Notably, SelM contains a redox-active CXXU motif that has been shown to bind Zn^{2+} and Cu^{+}, thereby acting as a metal regulator (14, 15). Thioredoxin/glutathione reductase (TXNRD3) is a selenoprotein composed of thioredoxin reductase and glutaredoxin domains. It has been shown that TXNRD3 plays an important role in male reproduction by supporting redox homeostasis during spermatogenesis (16). To investigate the role of SelM and Txnrd3 in nickel poisoning, we established a nickel exposure model by 21 days of $NiCl_2$ gavage in wild-type C57BL/6N (WT) mice, SelM$^{-/-}$ C57BL/6N (SelM$^{-/-}$) mice, and Txnrd3$^{-/-}$ C57BL/6N (Txnrd3$^{-/-}$) mice.

$NiCl_2$ damages the immune system, including the spleen and primary splenic lymphocytes. The splenic white and red pulp of SelM $^{-/-}$ mice has shown greater destruction than WT mice after nickel exposure. Ma et al. also demonstrated that oxidative stress, inflammation, and apoptosis occurred in the spleen of mice during this period. In our ongoing study of the toxicity of $NiCl_2$ on primary splenic lymphocytes, we found that cells undergo oxidative stress-induced inflammation and necroptosis with increasing concentrations of $NiCl_2$. When N-Acetyl-L-cysteine (NAC) alleviated oxidative stress, the inflammation and necroptosis were also reduced in the primary splenic lymphocytes (nonpublic data).

We then investigated the circulatory system by examining the heart. In Txnrd3$^{-/-}$ mice, we found that compared with wild-type mice, reduced Txnrd3 expression promoted nickel-induced mitochondrial apoptosis and an oxidative stress-induced inflammatory response, which exacerbated cardiac injury. Specific manifestations include increased messenger mRNA levels of mitochondrial apoptosis (caspase-3, caspase-9, cytochrome c, p53, and BAX), autophagy (LC3, ATG 1, ATG 7, and Beclin-1), and inflammation (TNF-α, COX 2, IL-1, IL-2, IL-6, and IL-7), but decreased levels of bcl-2, p62, and mTOR (Liu Yue et al.). We also discovered that $NiCl_2$ caused changes in the microstructure and ultrastructure of the hearts of WT and SelM$^{-/-}$ mice, which were caused by oxidative stress, endoplasmic reticulum (ER) stress, and apoptosis, as evidenced by a decrease in the MDA content and T-AOC activity. At the same time, ER stress-related genes (ATF4, IRE-1, JNK, and CHOP) and apoptosis-related genes (Bax, Caspase-3, Caspase-9, Caspase-12, and bcl-2) changed their mRNA and protein expression. It is worth noting that SelM$^{-/-}$ mice were more severely injured (nonpublic data).

Regarding the metabolic system, we observed changes in the liver and kidneys. In the liver, liver fibrosis was more severe, and organelle damage was more pronounced in Txnrd3$^{-/-}$ mice compared to wild-type mice after nickel exposure. In this process, activation of the IRE1/Nuclear factor kappa B/NLRP3 16 axis leads to liver pyroptosis, while upregulation of PERK/TGF-β17 promotes the liver fibrosis process. Moreover, Txnrd3 knockdown has been found to exacerbate liver injury during nickel exposure (Liu Qi et al.). Our current findings suggest that SelM$^{-/-}$ mice experience more severe ferroptosis caused by lipid peroxidation in the liver (nonpublic). We also confirmed that Txnrd3 knockdown can aggravate the oxidative stress and mitochondrial apoptosis caused by the increase of reactive oxygen species in the kidney caused by $NiCl_2$ (nonpublic).

We also investigated the $NiCl_2$ toxicology in nervous system. Neuronal brain atrophy and other neurotoxic features in brain tissue were observed in WT mice, and Qiao's study also proposed that nickel induces oxidative stress damage and autophagy in the mouse brain through the inhibition of the PI3K/AKT/mTOR pathway.

In addition, for the respiratory system, we focused on the changes in the lung tissue after $NiCl_2$ exposure. In the lung tissue of SelM$^{-/-}$mice and WT mice, light microscopy revealed inflammatory cell infiltration, alveolar collapse, and alveolar wall thickening, while electron microscopy of the lung tissue showed a large accumulation of fibroblasts, the proliferation of collagen fibers, and dense collagen deposition. Lung fibrosis was more severe in SelM$^{-/-}$ mice than that in WT mice. We suggest that SelM knockdown leads to epithelial mesenchymal transition through the activation of the oxidative stress-mediated TGF-β1/Smad signaling pathway and promotes lung fibrosis development (nonpublic data). In the lung tissue of Txnrd3$^{-/-}$, pathological results showed that after exposure to nickel, the lung tissue was significantly damaged and infiltrated with inflammatory cells. Inflammatory cells and protein fragments were found in the bronchioles of Txnrd3$^{-/-}$ mice. Ultrastructural examination showed that mitochondria in the Txnrd3$^{-/-}$ mice were abnormal, and pulmonary capillary endothelial cells were dense and short. qPCR and WB results suggested that $NiCl_2$ activated the TNF-α/NF-κB pathway by increasing the expression of HO-1, IL-1β, iNOS, and COX2 and inducing the inflammatory response (nonpublic data).

We added melatonin to the above model for intervention and found that it could significantly alleviate the damage caused by Ni poisoning in WT and knockout mice. However, in the tissues and organs of the gene knockout mice, the antagonism of melatonin on Ni was not as obvious as that of the wild-type mice, and a certain degree of damage still existed, indicating that SelM and Txnrd3 play an important role in the process of multiple tissues and organs damage caused by exposure to Ni.

All our data suggest that SelM and Txnrd3 play an important role in nickel toxicity. MT showed a protective effect in WT mice after $NiCl_2$ exposure, but this effect was markedly attenuated in knockout mice. During this process, biological processes such as oxidative stress, inflammation, apoptosis, and ER stress occur. Next, we will examine the specific biological effects of SelM and Txnrd3.

Author contributions

XZ and LX: Writing – original draft. PL and WM: Writing – review and editing. YL and SQ: Investigation, Visualization. QL and JC: References collection. ZZ: Supervision, Writing – review & editing, Funding acquisition. All authors contributed to the article and approved the submitted version.

Funding

This study was supported by Heilongjiang Provincial Natural Science Foundation for Outstanding Youth (YQ2021C021).

Conflict of interest

The authors declare that the research was conducted in the absence of any commercial or financial relationships that could be construed as a potential conflict of interest.

Publisher's note

References

1. Song X, Fiati Kenston SS, Kong L, Zhao J. Molecular mechanisms of nickel induced neurotoxicity and chemoprevention. *Toxicology* (2017) 392:47–54. doi: 10.1016/j.tox.2017.10.006

2. Muñoz A, Costa M. Elucidating the mechanisms of nickel compound uptake: a review of particulate and nano-nickel endocytosis and toxicity. *Toxicol Appl Pharmacol* (2012) 260(1):1–16. doi: 10.1016/j.taap.2011.12.014

3. Jing H, Zhang Q, Li S, Gao X-J. Pb exposure triggers MAPK-dependent inflammation by activating oxidative stress and miRNA-155 expression in carp head kidney. *Fish Shellfish Immunol* (2020) 106:219–27. doi: 10.1016/j.fsi.2020.08.015

4. Wang Y, Liu X, Jing H, Ren H, Su S, Guo M. Trimethyltin induces apoptosis and necroptosis of mouse liver by oxidative stress through YAP phosphorylation. *Ecotoxicol Environ Saf* (2022) 248:114327. doi: 10.1016/j.ecoenv.2022.114327

5. Genchi G, Carocci A, Lauria G, Sinicropi MS, Catalano A. Nickel: Human health and environmental toxicology. *Int J Environ Res Public Health* (2020) 17(3):679–87. doi: 10.3390/ijerph17030679

6. Kong L, Gao X, Zhu J, Cheng K, Tang M. Mechanisms involved in reproductive toxicity caused by nickel nanoparticle in female rats. *Environ Toxicol* (2016) 31 (11):1674–83. doi: 10.1002/tox.22288

7. Xi L, Zhang H, Qiao S, Ma W, Cai J, Zhang X, et al. Melatonin administration alleviates 2,2,4,4-tetra-brominated diphenyl ether (PBDE-47)-induced necroptosis and secretion of inflammatory factors via miR-140-5p/TLR4/NF-κB axis in fish kidney cells. *Fish & Shellfish Immunology* (2022) 128:228–37. doi: 10.1016/j.fsi.2022.08.004

8. Zhai M, Li B, Duan W, Jing L, Zhang B, Zhang M, et al. Melatonin ameliorates myocardial ischemia reperfusion injury through SIRT3-dependent regulation of oxidative stress and apoptosis. *J pineal Res* (2017) 63(2). doi: 10.1111/jpi.12419

9. Chen P, Wang R, Ma X, Liu Q, Ni J. Different forms of selenoprotein m differentially affect aβ aggregation and ROS generation. *Int J Mol Sci* (2013) 14 (3):4385–99. doi: 10.3390/ijms14034385

10. Hwang D, Sin J, Kim M, Yim S, Kim Y, Kim C, et al. Overexpression of human selenoprotein m differentially regulates the concentrations of antioxidants and H2O2, the activity of antioxidant enzymes, and the composition of white blood cells in a transgenic rat. *Int J Mol Med* (2008) 21(2):169–79. doi: 10.3892/ijmm.21.2.169

11. Reeves MA, Bellinger FP, Berry MJ. The neuroprotective functions of selenoprotein m and its role in cytosolic calcium regulation. *Antioxidants Redox Signaling* (2010) 12(7):809–18. doi: 10.1089/ars.2009.2883

12. Pitts MW, Reeves MA, Hashimoto AC, Ogawa A, Kremer P, Seale LA, et al. Deletion of selenoprotein m leads to obesity without cognitive deficits. *J Biol Chem* (2013) 288(36):26121–34. doi: 10.1074/jbc.m113.471235

13. Gong T, Hashimoto AC, Sasuclark AR, Khadka VS, Gurary A, Pitts MW. Selenoprotein m promotes hypothalamic leptin signaling and thioredoxin antioxidant activity. *Antioxid Redox Signal* (2021) 35(10):775–87. doi: 10.1089/ars.2018.7594

14. Chen P, Wang RR, Ma XJ, Liu Q, Ni JZ. Different forms of selenoprotein m differentially affect a beta aggregation and ROS generation. *Int J Mol Sci* (2013) 14 (3):4385–99. doi: 10.3390/ijms14034385

15. Du XB, Li HP, Wang Z, Qiu S, Liu Q, Ni JZ. Selenoprotein p and selenoprotein m block Zn2+-mediated a beta(42) aggregation and toxicity. *Metallomics* (2013) 5 (7):861–70. doi: 10.1039/c3mt20282h

16. Dou Q, Turanov A, Mariotti M, Hwang J, Wang H, Lee S, et al. Selenoprotein TXNRD3 supports male fertility *via* the redox regulation of spermatogenesis. *J Biol Chem* (2022) 298(8):102183. doi: 10.1016/j.jbc.2022.102183

frontiers in Immunology

ORIGINAL RESEARCH
published: 28 March 2022
doi: 10.3389/fimmu.2022.857069

Schisandrin B Induced ROS-Mediated Autophagy and Th1/Th2 Imbalance *via* Selenoproteins in Hepa1-6 Cells

Siran Tan[1], *Zhi Zheng*[2], *Tianqi Liu*[3], *Xiaoyun Yao*[4], *Miao Yu*[1]* *and Yubin Ji*[1]*

[1] Engineering Research Center for Medicine, Ministry of Education, Harbin University of Commerce, Harbin, China, [2] Jiangxi Province People's Hospital, First Affiliated Hospital of Nanchang Medical College, Nanchang, China, [3] Heilongjiang River Fisheries Research Institute, Chinese Academy of Fishery Sciences, Harbin, China, [4] Jiangxi Cancer Hospital, Jiangxi TCM Cancer Center, Nanchang, China

OPEN ACCESS

Edited by:
Ziwei Zhang,
Northeast Agricultural University, China

Reviewed by:
Yunan Gao,
Harbin Medical University, China
Jian Huang,
Harbin Medical University Cancer Hospital, China
Haidong Yao,
Karolinska Institutet (KI), Sweden

***Correspondence:**
Miao Yu
yumiao913@163.com
Yubin Ji
jyb@hrbcu.edu.cn

Specialty section:
This article was submitted to Nutritional Immunology, a section of the journal Frontiers in Immunology

Received: *18 January 2022*
Accepted: *14 February 2022*
Published: *28 March 2022*

Citation:
Tan S, Zheng Z, Liu T, Yao X, Yu M and Ji Y (2022) Schisandrin B Induced ROS-Mediated Autophagy and Th1/Th2 Imbalance via Selenoproteins in Hepa1-6 Cells. Front. Immunol. 13:857069. doi: 10.3389/fimmu.2022.857069

Schisandrin B (Sch B) is well-known for its antitumor effect; however, its underlying mechanism remains confusing. Our study aimed to investigate the role of selenoproteins in Sch B-induced autophagy and Th1/Th2 imbalance in Hepa1-6 cells. Hepa1-6 cells were chosen to explore the antitumor mechanism and were treated with 0, 25, 50, and 100 μM of Sch B for 24 h, respectively. We detected the inhibition rate of proliferation, transmission electron microscopy (TEM), monodansylcadaverine (MDC) staining, reactive oxygen species (ROS) level and oxidative stress-related indicators, autophagy-related genes, related Th1/Th2 cytokines, and selenoprotein mRNA expression. Moreover, the heat map, principal component analysis (PCA), and correlation analysis were used for further bioinformatics analysis. The results revealed that Sch B exhibited well-inhibited effects on Hepa1-6 cells. Subsequently, under Sch B treatment, typical autophagy characteristics were increasingly apparent, and the level of punctate MDC staining enhanced and regulated the autophagy-related genes. Overall, Sch B induced autophagy in Hepa1-6 cells. In addition, Sch B-promoted ROS accumulation eventually triggered autophagy initiation. Results of Th1 and Th2 cytokine mRNA expression indicated that Th1/Th2 immune imbalance was observed by Sch B treatment in Hepa1-6 cells. Intriguingly, Sch B downregulated the majority of selenoprotein expression. Also, the heat map results observed significant variation of autophagy-related genes, related Th1/Th2 cytokines, and selenoprotein expression in response to Sch B treatment. PCA outcome suggested the key role of Txnrd1, Txnrd3, Selp, GPX2, Dio3, and Selr with its potential interactions in ROS-mediated autophagy and Th1/Th2 imbalance of Hepa1-6 cells. In conclusion, Sch B induced ROS-mediated autophagy and Th1/Th2 imbalance in Hepa1-6 cells. More importantly, the majority of selenoproteins were intimately involved in the process of autophagy and Th1/Th2 imbalance, Txnrd3, Selp, GPX2, Dio3, and Selr had considerable impacts on the process.

Keywords: schisandrin B (Sch B), Hepa1-6, autophagy, oxidative stress, Th1/Th2 imbalance, selenoprotein

INTRODUCTION

Tumor treatment and uncovering antineoplastic drug mechanisms have attracted intense research efforts. Extensive research has established that natural products extracted and isolated from plants combined with anticancer active substances can help reduce the dosage of anticancer agents and the occurrence of side effects, so these natural active ingredients can be used as cofactors for anticancer treatment (1). Schisandrin B (Sch B), extracted from the traditional Chinese medicinal herb *Schisandra chinensis* Baill., is one of the most active monomers of lignans (2). Existing research recognized the critical role of Sch B in anti-tumor, antioxidant and hepatoprotective effects (3, 4). The antitumor activity of Sch B included promoting apoptosis, inhibiting proliferation, and impairing tumor angiogenesis in various cancer cells (5). There has been little analysis, and systematic understanding of how Sch B exerts its anticancer action is still lacking.

Autophagy is an evolutionarily conserved mechanism for cellular self-digestion that can be involved in maintaining the stability of the internal environment and cellular viability (6). Autophagy is closely linked to tumor suppression and tumor survival. Under normal physiological conditions, autophagy facilitates cells to maintain a self-stable state (7). In case of stress, it can prevent the accumulation of toxic or oncogenic damaged proteins and organelles and inhibits cellular carcinogenesis. Whereas, once tumors are formed, autophagy provides richer nutrients for cancer cells and promotes tumor growth (8). Therefore, autophagy suppresses tumor initiation yet enhances tumor progression (9). Autophagy can be activated under multiple states of stress such as oxidative stress, growth factor deficiency, microbial infection, organelle damage, protein misfolding or aggregation, and DNA damage (10). High levels of reactive oxygen species (ROS) have been detected in the promotion and progression of multiple tumors (11); meanwhile, ROS accumulation is indispensable for the initiation of autophagy (12). Therefore, the mechanisms by which drugs exert anticancer effects by activating oxidative stress and thus inducing autophagy are of notable attention. The ginsenoside Rb1 metabolite K induced both autophagy and apoptosis in HCT-116 cells by producing ROS and activating the c-Jun N-terminal kinase (JNK) pathway (13). Saxifragifolin D increased the expression of *LC3-II, Beclin-1* proteins in MCF-7 and MDA-MB-231 cells, and induced apoptosis and autophagy in breast cancer cells through the ROS-mediated endoplasmic reticulum (ER) stress pathway, therefore inhibiting cancer cell proliferation (14). The induction of ROS and activation of nuclear factor (NF)-κB by gemcitabine (GEM) are required for the effect of antiproliferative synergism in pancreatic cancer cells (15). There is mounting evidence that Th1/Th2 imbalance leads to cancer progression due to their essential role in immunomodulatory function (16, 17). Th1 and Th2 are two subgroups of CD4+ T cells with diverse cytokine production and regulating multiple mechanisms of action in tumor immunity (18, 19). Studies have shown that most tumor tissues are in a state of Th2 cytokine dominance, which is one of the mechanisms of tumor immune escape (20). Compared to healthy subjects, most melanoma patients revealed visibly lower expressions of *interleukin (IL)-2* and *interferon (IFN)-γ* and elevated pathological levels of *IL-4, IL-6,* and *IL-10* demonstrated that the disease was related to Th1/Th2 imbalance (21). Therefore, transferring the Th1/Th2 balance to Th1 to provide a novel protocol for tumor immunotherapy has become a current research hot spot. Saikosaponin A enhanced antitumor immunity by shifting the Th1/Th2 balance toward Th1 and significantly inhibited breast cancer tumor growth and tumor cell proliferation (22). The study aimed to investigate the impact of fire needle stimulation at Sihua acupoints combined with chemotherapy on Th1/Th2 imbalance in non-small cell lung cancer (NSCLC). The results indicated that the expressions of *IL-2* and *IFN-γ* were elevated and of IL-4 and IL-10 were reduced in the treatment group, which illustrated that it can enhance the function of Th1 cells and decrease the function of Th2 cells, altering the imbalance of Th1 and Th2 (23).

Selenoproteins, the catalytic activity center is selenocysteine (Sec), are the main carriers of selenium for physiological functions (24). Sec is mainly located in the redox catalytic site and has a higher redox potential (25). Selenoproteins exist primarily in the form of redox enzymes and carry out very diverse functions such as regulation of cellular oxidative stress, immune function, ER stress, and autophagy, which are integrally related to the development of diverse tumors (26, 27). As mentioned, autophagy is activated under oxidative stress situations. Hence, extensive research suggested selenoproteins as potential molecular targets for anticancer agents that induce oxidative stress, autophagy, and immunity (28–30). Overexpression of Selh in HT22 cells reversed glutamate-induced increase in ROS production and autophagy imbalance (31). The inhibition effect of cyanidin on renal cell carcinoma was correlated with downregulation of early growth response gene 1 (*EGR1*) and *Selw* expression, while modulating the expression of autophagy-related proteins *P62* and *ATG4* (32). Txndr suppression increased the expression of *IL-1β, IL-6, IL-8,* and *IL-10*, which indicated autophagy occurred with a strong immune response in Txn-deficient cardiomyocytes (33).

This study set out to assess the effect of selenoproteins on Sch B inhibiting Hepa1-6 cell proliferation through increasing ROS production and subsequent activation of autophagy and shifting

Abbreviations: Sch B, schisandrin B; ROS, reactive oxygen species; SOD, superoxide dismutase; MDA, malondialdehyde; GSH, glutathione; GSH-px, glutathione peroxidase; Txnrd1, thioredoxin reductase 1; Txnrd2, thioredoxin reductase 2; Txnrd3, thioredoxin reductase 3; Gpx1, glutathione peroxidase 1; Gpx2, glutathione peroxidase 2; Gpx3, glutathione peroxidase 3; Gpx4, glutathione peroxidase 4; Gpx6, glutathione peroxidase 6; Dio1, deiodinase 1; Dio2, deiodinase 2; Dio3, deiodinase 3; Selt, selenoprotein t; Selw, selenoprotein w; Selk, selenoprotein k; Selm, selenoprotein m; Selh, selenoprotein h; Selu, selenoprotein u; Seli, selenoprotein i; Seln, selenoprotein n; Selo, selenoprotein o; Sels, selenoprotein s; Selp, selenoprotein p; Selp15, 15-kDa selenoprotein; Sps2, selenoprotein synthetase 2; Se, selenium; Sec, selenocysteine; LC3, microtubule-associated protein light chain 3; mTOR, mammalian target of rapamycin; ATG1, autophagy-related gene-1; ATG4, autophagy-related gene-4; ATG5, autophagy-related gene-5; ATG7, autophagy-related gene-7; ATG10, autophagy-related gene-10; TNF-α, tumor necrosis factor α; IL-2, interleukin-2; IL-4, interleukin-4; IL-5, interleukin-5; IL-6, interleukin-6; IL-10, interleukin-10; IL-12, interleukin-12; DMEM, Dulbecco's modified Eagle's medium; GAPDH, Glyceraldehyde-3-phosphate Dehydrogenase; qPCR, Quantitative real-time PCR.

Th1/Th2 balance then regulating immunity. We cultured Hepa1-6 cells with 0-, 25-, 50-, and 100-μM Sch B treatment and then detected the proliferation, autophagy, Th1/Th2 imbalance, and oxidative stress levels in Hepa1-6 cells. Accordingly, to reveal the specific role of selenoproteins in regulating autophagy, oxidative stress, and Th1/Th2 imbalance, we examined the mRNA levels of 25 selenoproteins and performed bioinformatic analysis.

MATERIALS AND METHODS

Cell Culture

Murine hepatocarcinoma cell line Hepa1-6 was gifted by Jiangxi TCM Cancer Center Laboratory. Cells were cultivated in Dulbecco's modified Eagle's medium (DMEM) with 10% Fetal Bovine Serum (FBS) and 1% penicillin/streptomycin and maintained at 37°C in a 5% CO_2 incubator. Hepa1-6 cells incubated with culture medium were added with 25-, 50-, and 100-μM concentrations of Sch B dissolved in dimethyl sulfoxide (DMSO) for 24 h. The same volume of DMSO was substituted as a control.

Cell Proliferation Assay

The Cell Counting Kit-8 assay (Sant Biotechnology, Shanghai, China) was used to monitor cell proliferation. Here, 5×10^3 cells/well were seeded into 96-well plates and cultivated with Sch B treatment at 0-, 25-, 50-, and 100-μM concentrations for 24 h. Then, 10-μl CCK8 solution was transferred into each well for 2 h, and the absorbance was measured at 450 nm.

Sections for Electron Microscopy

Hepa1-6 cells were treated with 0-, 25-, 50-, 100-μM concentrations of Sch B dissolved in DMSO for 24 h. The cells were collected into a tube and centrifuged at 250×g for 10 min, then the supernatant was discarded. Cell samples were fixed overnight in 2.5% glutaraldehyde at 4°C, rinsed 3 times with 0.1 M phosphate buffer, and then fixed with osmic acid for 1 h at 4°C. Immediately afterward, they were dehydrated with 50%, 70%, 90%, and 100% ethanol and 100% acetone, respectively, rinsed 3 times with 0.1 M phosphate-buffered saline (pH 7.2), and then fixed with 1% osmic acid for 1 h at 4°C. Afterward, samples were dehydrated with 50%, 70%, 90%, and 100% ethanol and 100% acetone, respectively. Next, the samples were macerated, embedded, aggregated, and then sectioned approximately 50–60 nm with an ultramicrotome. The microphotographs were taken with a transmission electron microscope (GEM-1200ES, Japan).

Monodansylcadaverine Staining

Monodansylcadaverine (MDC) is a fluorescent chrome that is commonly used to detect specific marker stains for autophagosome formation. The analysis of autophagy was undergone by MDC (Solarbio, Beijing, China). Hepa1-6 cells were treated with 0-, 25-, 50-, 100-μM concentrations of Sch B dissolved in DMSO for 24 h in 12-well plates. Cells were incubated with 0.05 mM MDC in PBS at room temperature away from light for 30 min. The fluorescent images were obtained with a fluorescence microscope with 355-nm excitation filter and 512-nm barrier filter (Leica, Wetzlar, Germany), and cell number was counted to normalize the measurement.

Detection of Intracellular Reactive Oxygen Species and Oxidative Stress-Related Indicators

Measurement of intracellular ROS used the ROS detection kit (Beyotime, Shanghai, China). After 24-h incubation with 0-, 25-, 50-, 100-μM concentrations of Sch B, cells were incubated with 10 μM 2,7-Dichlorodihydrofluorescein diacetate (DCFH-DA) for 30 min at 37°C. Then, cells were washed with serum-free medium 3 times and measured by fluorescence microscopy (Leica, Wetzlar, Germany). Oxidative stress-related factors superoxide dismutase (SOD), malondialdehyde (MDA), glutathione (GSH), and glutathione peroxidase (GSH-px) were explored according to the protocols of the corresponding kit (Nanjing Jiancheng Bioengineering Institute, China). The absorbance was estimated at 550, 532, 405, and 412 nm, respectively.

Determination of the mRNA Expression of Autophagy-Related Genes, Related Th1/Th2 Cytokines, and Selenoproteins

Total RNA was extracted from cultured cells by using TRIzol reagent (Invitrogen, Shanghai, China). cDNA was synthesized from 5 mg of the total RNA using oligo dT primers and Superscript II reverse transcriptase according to the manufacturer's instructions (Promega, Beijing, China). Autophagy-related genes (*LC3, P62, Beclin1, mTOR, ATG1, ATG4, ATG5, ATG7, ATG10, ATG12*), related Th1/Th2 cytokines (*IL-2, TNF-α, IFN-γ, IL-12, IL-4, IL-5, IL-6, IL-10*), and selenoprotein primers (*GPX1, GPX2, GPX3, GPX4, GPX6, Txnrd1, Txnrd2, Txnrd3, Dio1, Dio2, Dio3, Sep15, Selh, Selt, Selw, SPS2, Selm, Selp, Selv, Selo, Selr, Sels, Seli, Selk*) were designed by Primer Premier Software (PREMIER Biosoft International, USA) and are listed in **Table 1**. qRT-PCR was performed to detect the target genes by using Fast Universal SYBR Green Master Mix (Roche, Basel, Switzerland) on the Light Cycler® 480 System (Roche, Basel, Switzerland). Reactions were performed in a 10-μl reaction mixture containing 5 μl of 2× SYBR Green I PCR Master Mix (Roche, Basel, Switzerland), 1 μl of cDNA, 0.2 μl of each primer (10 μM), 0.2 μl of 50× ROX reference Dye II, and 3.4 μl of PCR-grade water. The reaction mixture was then subjected to a thermal profile of denaturation as follows: 1 cycle at 95°C for 30 s and 40 cycles at 95°C for 15 s and 60°C for 30 s. mRNA expression was normalized to β-actin and calculated using the $2^{-\Delta\Delta CT}$ method.

Statistical Analyses

The heat map was generated by https://hiplot.com.cn/basic/heatmap and ranked genes by the degree of expression levels of autophagy-related genes, related Th1/Th2 cytokines, and selenoproteins. SPSS 13.0 program (SPSS, Chicago, IL, USA) was used to execute principal component analysis (PCA), and

TABLE 1 | The primers used in the present study.

Gene	Forward primer (5′–3′)	Reverse primer (5′–3′)
GPX6	GCCCAGAAGTTGTGGGGTTC	TCCATACTCATAGACGGTGCC
GPX1	AGTCCACCGTGTATCCTTCT	GAGACGCGATTCTCAATGA
GPX2	GCCTCAAGTATGTCCGACCTG	GGAGAACGGGTCATCATAAGGG
GPX3	CCTTTTAAGCAGTATGCAGGCA	CAAGCCAAATGGCCCAAGTT
GPX4	GATGGAGCCCATTCCTGAACC	CCCTGTACTTATCCAGGCAGA
Txnrd 1	CCCACTTGCCCCAACTGTT	GGGAGTGTCTTGGAGGGAC
Txnrd 2	GATCCGGTGGCCTAGCTTG	TCGGGGAGAAGGTTCCACAT
Txnrd 3	GGCAACAGGGTGATGATCTTC	CTGGAAAGTTCGGTCACATCC
Dio1	GCTGAAGCGGCTTGTGATATT	GTTGTCAGGGGCGAATCGG
Dio2	AATTATGCCTCGGAGAAGACCG	GGCAGTTGCCTAGTGAAAGGT
Dio3	CACGGCCTTCATGCTCTGG	CGGTTGTCGTCTGATACGCA
Sep15	CTGGCGACTGCGTTTCAAG	CTGTCCAAGAAGATCGCAAGAG
Selh	TGGACAAGCGCGAGAAACTG	CAGCTCGTACAATGCTCAATGA
Selt	GAGGAGTACATGCGGGTTATCA	CTGACAGGAAAGATGCTATGTGT
Selw	GCCGTTCGAGTCGTGTATTGT	CACTTCAAAGAACCCGGTGAC
SPS2	GCCGGAGTTTCTCCAACTACC	TTCCTGCACCGTCTCTTCCT
Selm	GTTGAATCGCCTAAAGGAGGTG	AGGTCGTCGTGTTCTGAAGC
Selp	CATCTGGTTCAGTGCTTTGATCT	ACCCGTGAGTTATTCCATGAGT
Selv	CTCGTCCTCCAAGACACAAGG	AACTCTAGTGTAGGGTTGGGG
Selo	GCACTGCTACTGTGGACACC	ACTTTGCGACCATCGGCTT
Selr	CTTCGGAGGCGAGGTTTTCC	TCTCAGGGCACTTGGTCACA
Sels	GACCGAGAGCCTGCGATTC	AGCCCTCAGTCGAAGGGAG
Seli	TTGGCTGGCTCCCAATCTTAT	GGTCGAAGTATGTCAGGAGTAGG
Selk	GTTTACATCTCGAATGGTCAGGT	CCCTCTTCCATCGTCGTATCTG
β-actin	CCGCTCTATGAAGGCTACGC	CTCTCGGCTGTGGTGGTGAA
LC3	AGTGAAGTGTAGCAGGATGA	AAGCCTTGTGAACGAGAT
P62	TCCTTCACTCACGCCATGC	CTGCTTGACAGGTATCAGCAC
mTOR	GGACTCTTCCCTGCTGGCTAA	TACGGGTGCCCTGGTTCTG
Beclin1	CGACTGGAGCAGGAAGAAG	TCTGAGCATAACGCATCTGG
ATG1	AAGTTCGAGTTCTCTCGCAAG	CGATGTTTTCGTGCTTTAGTTCC
ATG4	GATGTCAGTGCTCGTCTC	GGAGGATTCTGTGATATTCTTC
ATG5	GGCACCGACCGATTTAGT	GCTGATGGGTTTGCTTTT
ATG7	TCAGATTCAAGCACTTCAGA	GAGGAGATACAACCACAGAG
ATG12	GGTGACGCCAAGAAGAAA	TTGATGAAGTCGCACAGG
IFN-γ	ATGAACGCTACACACTGCATC	CCATCCTTTTGCCAGTTCCTC
TNF-α	CCCTCACACTCAGATCATCTTCT	GCTACGACGTGGGCTACAG
IL-2	TGAGCAGGATGGAGAATTACAGG	GTCCAAGTTCATCTTCTAGGCAC
IL-6	TAGTCCTTCCTACCCCAATTTCC	TTGGTCCTTAGCCACTCCTTC
IL-12	TGGTTTGCCATCGTTTTGCTG	ACAGGTGAGGTTCACTGTTTCT
IL-4	GGTCTCAACCCCCAGCTAGT	GCCGATGATCTCTCTCAAGTGAT
IL-5	CTCTGTTGACAAGCAATGAGACG	TCTTCAGTATGTCTAGCCCCTG
IL-10	GCTCTTACTGACTGGCATGAG	CGCAGCTCTAGGAGCATGTG

correlation analysis was performed by Pearson's correlation coefficient analysis. All data were statistically analyzed by one-way ANOVA, showed a normal distribution, and passed equal variance testing using GraphPad Prism version 8.0 software and SPSS 13.0. The experimental data are expressed as the mean ± SD, and the differences were considered to be significant if $P < 0.05$; * means significantly different ($P < 0.05$) from the control group.

RESULTS

Effect of Schisandrin B on the Proliferation of Hepa1-6 Cells

CCK8 proliferation assay aimed to examine the impact on proliferation rates with increased Sch B concentration in Hepa1-6 cells. As can be seen from **Figure 1**, the marked increase in cell inhibition rate was accompanied by increased Sch B treatment.

Effect of Schisandrin B on Autophagy of Hepa1-6 Cells

Hepa1-6 cells were subjected to transmission electron microscopy (TEM) to reveal Sch B-induced ultracellular structure. The control group exhibited normal cell morphology (**Figure 2A**). Here, 25-μM Sch B treatment caused cell shrinkage, nuclear condensation, and mitochondrial swelling, and a few autophagosomes were observed (**Figure 2B**). With growing Sch B treatment, typical autophagy characteristics were increasingly apparent, with an elevated number of the autolysosomes and autophagic vacuolization observed in the Hepa1-6 cells (**Figures 2C, D**).

The fluorescent dye MDC was used to monitor autophagic vacuoles in Hepa1-6 cells. Normal cells show yellow-green

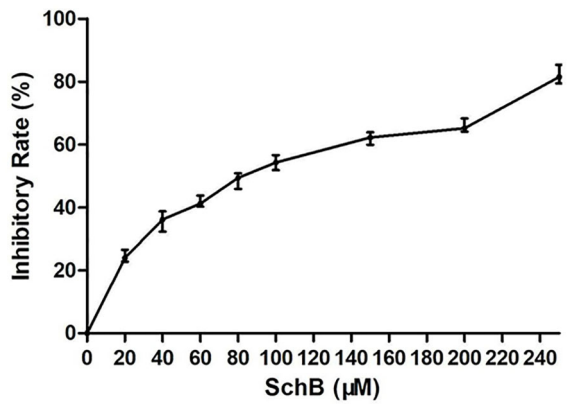

FIGURE 1 | Sch B inhibits proliferation in Hepa1-6 cells. Proliferation curve of Hepa1-6 cells treated with Sch B.

fluorescence; moreover, one hallmark of autophagy is the formation of vacuoles that stain with MDC, resulting in a punctate green fluorescence. As noticed in **Figures 3A, B**, the fluorescence intensity of MDC staining in Hepa1-6 cells was relatively exiguous and weak in the control group. In addition, the level of punctate MDC staining enhanced and outnumbered in a dose-dependent manner with increasing Sch B treatment.

In order to further prove that Sch B induces autophagy of Hepa1-6 cells, we investigated the mRNA expression of autophagy-related genes. qRT-PCR analysis indicated, accompanying increased Sch B concentration, increased levels of LC3, Beclin1, ATG1, ATG4, ATG5, ATG7, ATG10, and ATG12, also, low-level expressions of P62 and mammalian target of rapamycin (mTOR) (**Figure 3C**).

Effect of Schisandrin B on Oxidative Stress of Hepa1-6 Cells

The production of ROS, the content of MDA, GSH and the activity of GSH-Px, SOD set out to determine whether Sch B induced oxidative stress in Hepa1-6 cells. **Figure 4A** illustrated that the increase in Sch B concentration was related to the ROS activities significantly increased. It can be seen from the data in **Figure 4B** that as the concentration of Sch B rises, there was an observed increase in the levels of MDA and a decline in the content of GSH and the activity of SOD and GSH-Px compared to those of the control group in Hepa1-6 cells.

Effect of Schisandrin B on Th1/Th2 Imbalance of Hepa1-6 Cells

In order to explore the effect of Sch B in regulating Th1/Th2 imbalance in Hepa1-6 cells, the mRNA expressions of related Th1/Th2 cytokines were detected. Th1 cytokine contains *IL-2, TNF-α, IFN-γ,* and *IL-12*. Th2 cytokine includes *IL-4, IL-5, IL-6,* and *IL-10*. As revealed in **Figure 5**, Sch B supplement enhanced the expression of *IL-2, TNF-α, IFN-γ,* and *IL-12* and strikingly decreased the expression of *IL-4, IL-5, IL-6,* and *IL-10* ($P < 0.05$). The results indicated the activation of Th1 and the inhibition of Th2 response with Sch B treatment in Hepa1-6 cells. After Sch B treatment, the abnormal expression of cytokines indicated the imbalance of Th1/Th2 occurring in Hepa1-6 cells.

Effect of Schisandrin B on the Expression of Selenoprotein mRNA Levels of Hepa1-6 Cells

We measured the mRNA expression of 25 selenoproteins in Hepa1-6 cells to explore the particular involvement of selenoproteins in Sch B producing oxidative stress hence

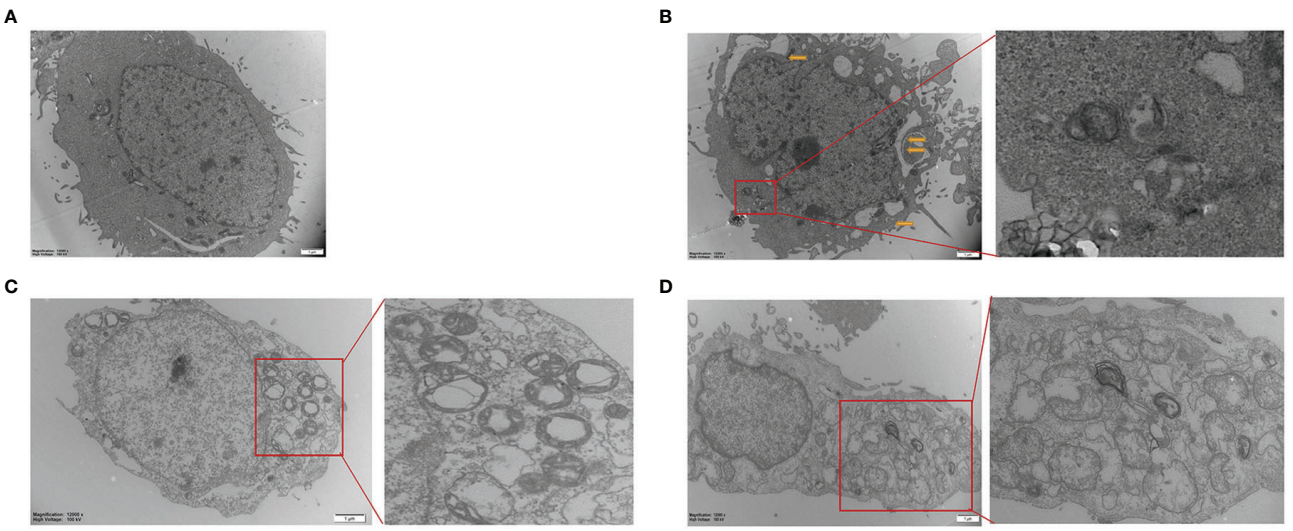

FIGURE 2 | Transmission electron microscope images of Hepa1-6 cells treated with 0 **(A)**, 25-μM **(B)**, 50-μM **(C)**, and 100-μM **(D)** Sch **(B)** The yellow arrows are pointing to the mitochondrial swelling, mitochondrial ridge breakage. An enlarged portion of the spectrogram (red box) is shown on the right showing vacuolar and cytoplasmic localized membrane-bound autophagosome.

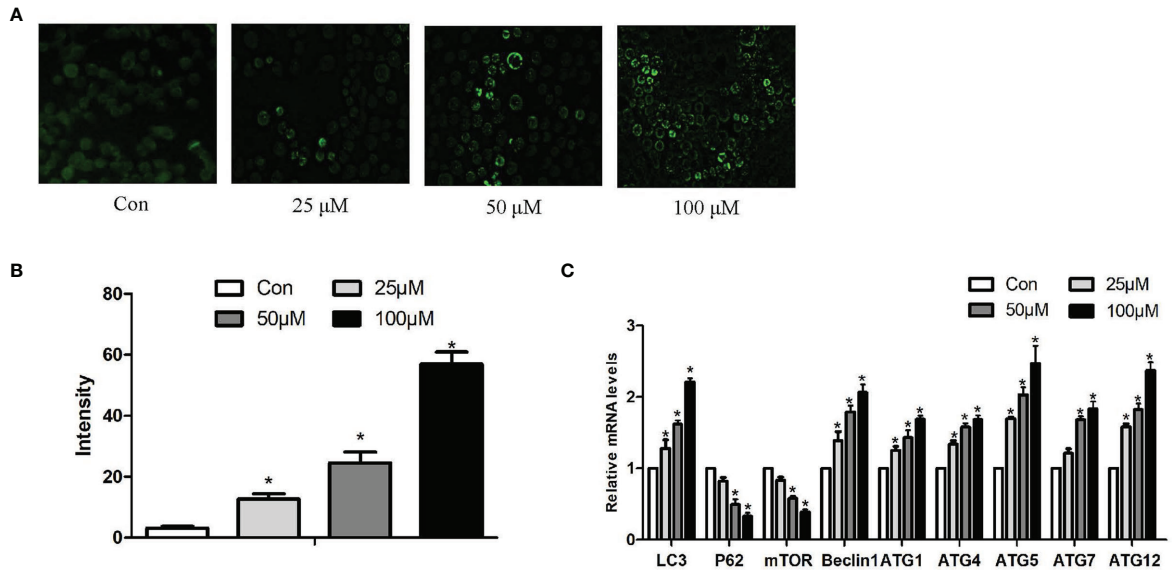

FIGURE 3 | Effects of Sch B on autophagy in Hepa1-6 cells. **(A)** MDC staining was performed in Hepa1-6 cells with Sch B treatment at 0-, 25-, 50-, and 100-μM concentrations. Hepa1-6 cells were visualized using fluorescence microscopy. **(B)** The quantitative analysis of MDC staining. **(C)** Autophagy-related gene mRNA levels in Hepa1-6 cells with 0-, 25-, 50-, and 100-μM Sch B treatment. ∗ shows a significant difference from the corresponding control ($P < 0.05$). n = 3.

initiating autophagy and Th1/Th2 imbalance. **Figure 6** presented the results obtained from the expression of 25 selenoproteins on treatment of Sch B at 0, 25, 50, and 100 μM, respectively. *Txnrd1, Txnrd2, Txnrd3, GPX1, GPX2, Dio1, Dio2, Dio3, GPX6, Selt, Selm, Selp, Selv, Selo, Sels, Selk* expression statistically increased with growing Sch B concentration. There is no distinct trend variation of the expression of *GPX3, GPX4, Selh, Seli, Seln, Selw, SPS2,* and *Sep15*.

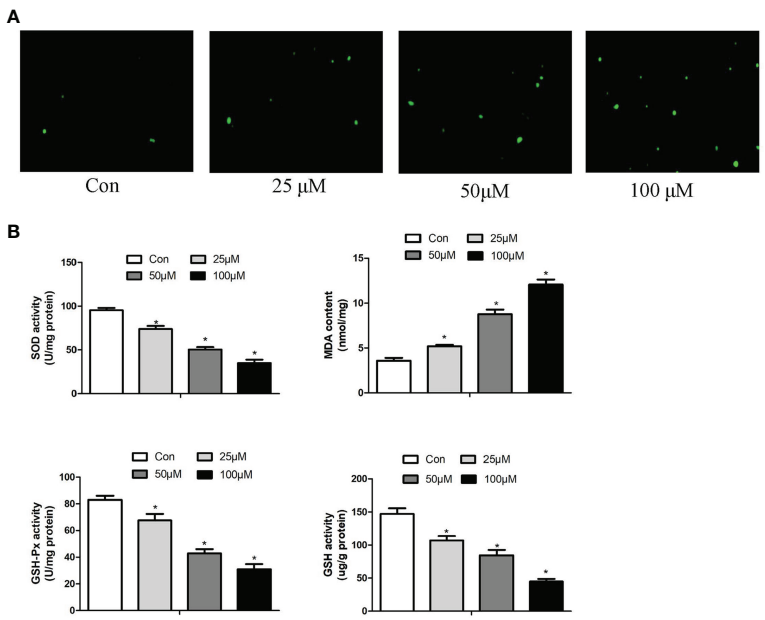

FIGURE 4 | Effects of Sch B on oxidative stress in Hepa1-6 cells. **(A)** ROS generation was performed by immunofluorescence with 0-, 25-, 50-, and 100-μM Sch B treatment in Hepa1-6 cells. Hepa1-6 cells were visualized using fluorescence microscopy. **(B)** Oxidative stress markers of the SOD, MDA, GSH, and GSH-Px contents were measured in Hepa1-6 cells with 0-, 25-, 50-, and 100-μM Sch B treatment. ∗ shows a significant difference from the corresponding control ($P < 0.05$). n = 3.

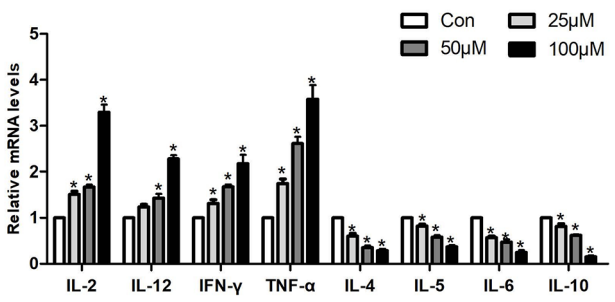

FIGURE 5 | Effects of Sch B on Th1/Th2 imbalance in Hepa1-6 cells. Related Th1/Th2 cytokine mRNA levels with 0-, 25-, 50-, and 100-μM Sch B treatment in Hepa1-6 cells. ∗ shows a significant difference from the corresponding control ($P < 0.05$). n = 3.

Heat Map Analysis

The results of the heat map analysis were set out in **Figure 7**; selenoproteins, autophagy-related genes, and related Th1/Th2 cytokine expression were shown by blue to red (low to high) coloration within the heat map with the concentration of Sch B (below the heat map) correlating with mRNA expressions. The heat map colored in blue designates the 18 genes, encompassing *Txnrd1, Txnrd2, Txnrd3, GPX1, GPX2, Dio1, Dio2, Dio3, GPX6, Selt, Selm, Selp, Selv, Selo, Sels, Selk, P62, mTOR, IL-4, IL-5, IL-6, IL-10,* had negative levels of correlation between increasing Sch B treatment in Hepa1-6 cells. *LC3, Beclin1, ATG1, ATG4, ATG5, ATG7, ATG10, ATG12, TNF-α, IFN-γ, IL-2, IL-12,* colored in red, had positive level of Sch B growing treatment.

Principal Component Analysis and Correlation Analysis

For further factor analysis to explore the particular role of selenoproteins in Sch B inducing autophagy and inflammation in Hepa1-6 cells, the mRNA expression of 25 selenoproteins and autophagy-related genes and related Th1/Th2 cytokines was subjected to PCA (**Figure 8A**) and correlation analysis (**Figure 8B** and **Supplementary Table 2**). PCA revealed 2 major principal components, explaining 85.929% and 10.450% of the variation, respectively. *Txnrd1, Txnrd3, Selp, IL-5, GPX2, Dio3, mTOR,* and *Selr* were highly positively correlated with PC1. *ATG1, Beclin1, TNF-α, ATG5, ATG12,* and *IFN-γ* were highly negatively correlated with PC1. In addition, the correlation analysis exhibited high correlation among selenoproteins with autophagy-related genes and related Th1/Th2 cytokines. Most selenoproteins have a highly positive correlation with *P62, mTOR, IL-4, IL-5, IL-6,* and *IL-10* and a negative correlation with *LC3, Beclin1, ATG1, ATG4, ATG5, ATG7, ATG12, TNF-α, IFN-γ, IL-2,* and *IL-12*.

DISCUSSION

Prior studies have noted that numerous traditional Chinese medicine and related active compounds have been reported to have potent anticancer properties (34). Sch B is the major anticancer monomer of lignans from the traditional Chinese medicinal herb *S. chinensis* Baill (35). Sch B has been confirmed to inhibit the proliferation of glioma, gastric cancer, and prostate cancer cells *via* induction of apoptosis and autophagy, promotion of antioxidant enzyme release, and inhibition of metastasis and invasion (36). While, some research has been carried out on Sch B, the mechanism by which the antineoplastic effect of Sch B on liver cancer has not been established explicitly. Hence, our data verified that Sch B exerted excellent inhibitory effects against Hepa1-6 cells; also, the suppression was dose-dependent (**Figure 1**). Consequently, to further investigate the mechanism by which Sch B inhibits the proliferation of Hepa1-6 cells, we explored whether Sch B induced oxidative stress that

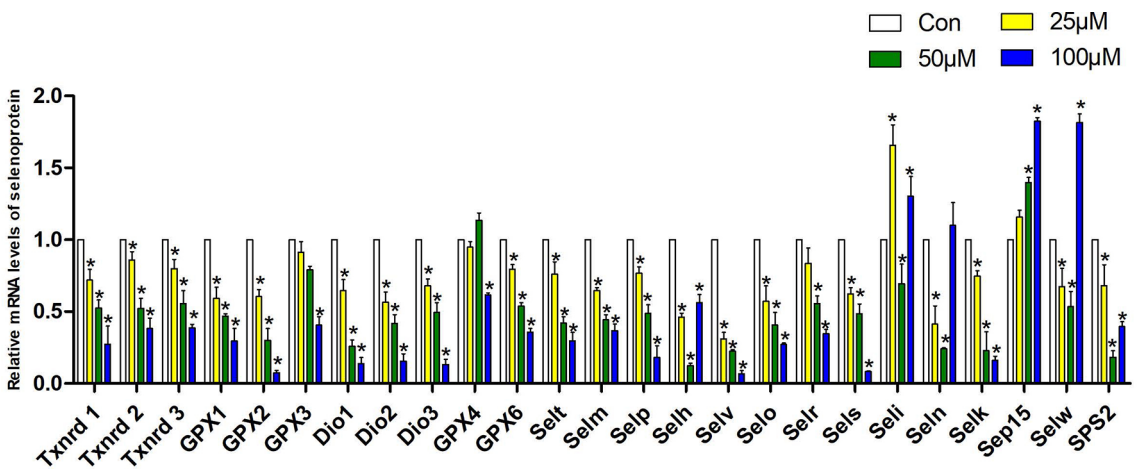

FIGURE 6 | Effects of Sch B on the expression of selenoprotein mRNA levels in Hepa1-6 cells. The 25 selenoprotein mRNA levels with 0-, 25-, 50-, and 100-μM Sch B treatment in Hepa1-6 cells. ∗ shows a significant difference from the corresponding control ($P < 0.05$). n = 3.

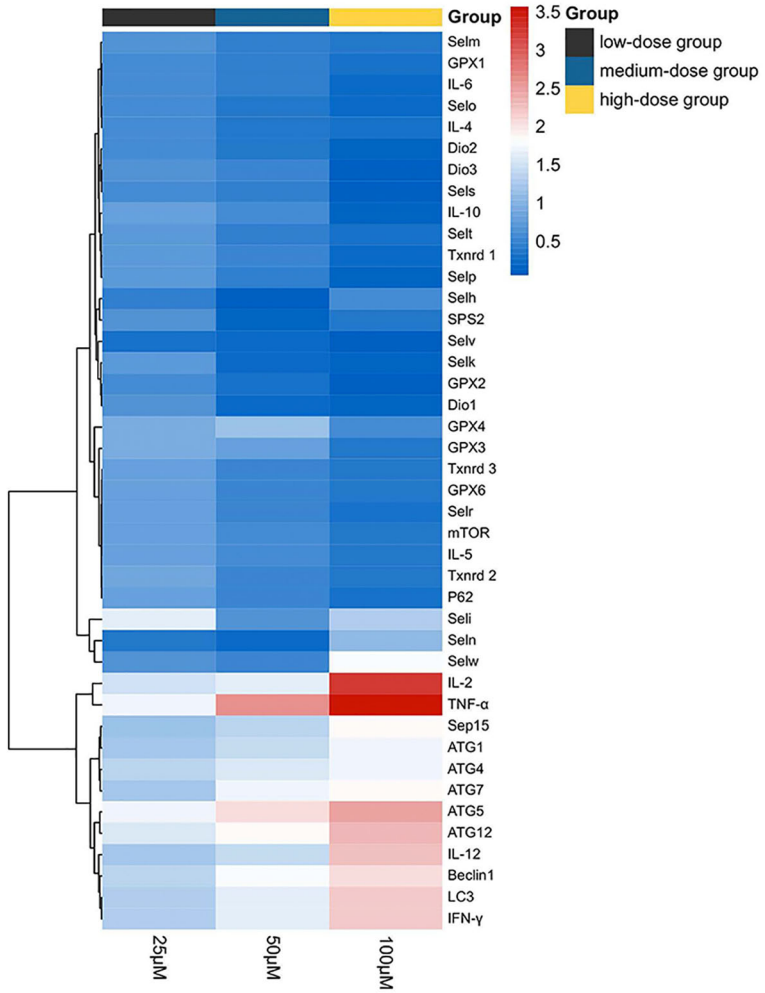

FIGURE 7 | Heat map of autophagy-related genes, related Th1/Th2 cytokines, and selenoprotein mRNA expressions with 25-, 50-, and 100-μM Sch B treatment in Hepa1-6 cells. Rows represent the probe sets. Related genes expressions are shown using the indicated pseudo color scale from blue (0) to red (3.5) relative to values. Red squares represent increased significantly ($P < 0.05$); blue squares represent decreased significantly ($P < 0.05$). Data are presented as mean ± SD.

triggered autophagy and the specific role of selenoprotein and its possible biological mechanism.

The induction of autophagy in tumor cells leads to autophagic cell death, suggesting the possibility of utilizing autophagy activation for cancer therapy and providing a fundamentally new direction for the prevention and treatment of tumors (10). In the present study, to investigate whether Sch B induced autophagy in Hepa1-6 cells, three different methods were applied to explore autophagic flux. Firstly, TEM was used to intuitively diagnose morphological hallmarks of autophagy. Autophagosomes are double-membrane-bound vesicles characteristic of autophagy (37). As the concentration of Sch B increases, the typical autophagic ultrastructures were increasingly obvious, the number of autophagosomes was markedly increased in the TEM images (**Figure 2**). Secondly, MDC, an elective marker for autophagosome formation, was used to quantify the induction of autophagy. Normal cells were uniformly stained yellow-green, and autophagosomes were stained with densely packed green granules of varying sizes (38). As illustrated in **Figures 3A, B**, the control group showed weak fluorescence. The increased MDC positive staining strongly suggested that Sch B treatment induced vesicle acidification and rapidly increased the number of autophagosomes, thus enhancing the punctuate MDC staining. The analysis by ImageJ of fluorescence intensity revealed that the autophagy ratio was increased in a dose-dependent manner. Thirdly, we assessed the expression of autophagy-related mRNA expression (**Figure 3C**). *LC3* is the most widely used marker of autophagy, which is involved in the formation of autophagosomes (39). *Beclin-1* plays an essential function in early autophagosome formation by recruiting other autophagy-related proteins through a complex of *Beclin-1* and Vps34 (10). *P62*, a hallmark protein of the autophagic flux downstream, attaches *LC3* and ubiquitinated substrates and is degraded when autophagosome

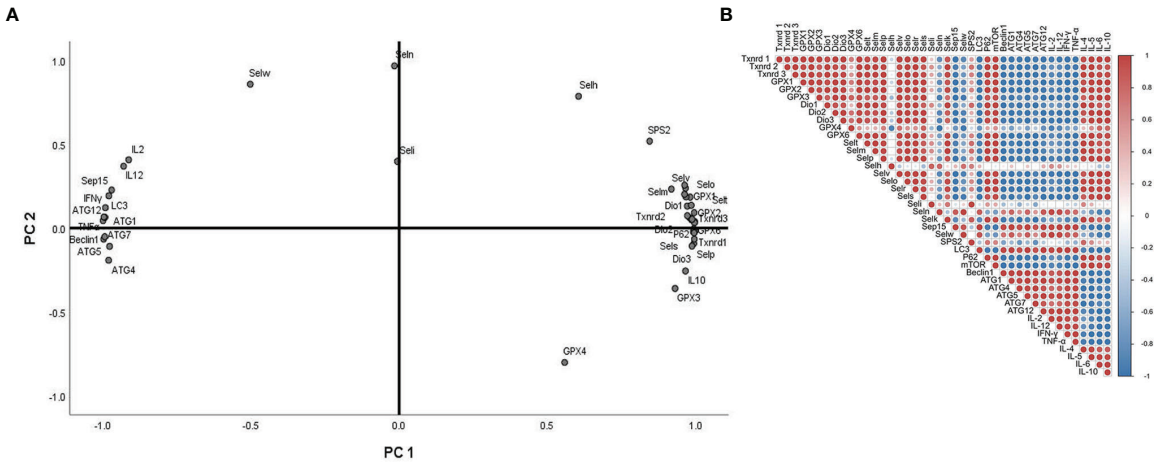

FIGURE 8 | Principal component analysis (PCA) and correlation analysis of autophagy-related genes, related Th1/Th2 cytokines, and selenoprotein mRNA expressions with 0-, 25-, 50-, and 100-μM Sch B treatment in Hepa1-6 cells.

and autolysosome fuse (10). *mTOR* can block autophagy by inhibiting the *ATG1* complex that is involved in the initiation of the autophagy activity (40). Afterward, the ATG-related protein further constructs autophagosomes. The *ATG5-ATG12* covalent protein complex and the *ATG8* coupling are crucial components of the autophagosome membrane (41). *ATG4* mediates the initial lipidation of *LC3* and the cleavage of *LC3* from the autophagosome membrane during the later stages of autophagy (42). In this study, Sch B induced remarkable upregulation of *LC3, Beclin1, ATG1, ATG4, ATG5, ATG7,* and *ATG12* and degradation of *P62* and *mTOR*. These results corroborate the findings of previous work that growing concentration of Sch B induced autophagy; meanwhile, autophagy is one of the causes for the decrease in cell viability induced by Sch B in Hepa1-6 cells.

Evidence of former studies instructed that ROS participated in the regulation of autophagy, which are the switches of cell survival and death (43, 44). Oxidative stress-inducing drugs have preferential anticancer effects, involving the regulation of autophagy. Trichosanthin (TCS) significantly inhibited the growth of human gastric cancer MKN-45 cells by mediating ROS production and NF-κB/p53 pathway (45). Curcumin induced ROS accumulation in cervical cancer cells, thereby inducing apoptosis, autophagy, and cellular senescence, accompanied by upregulation of *p53* and *p21* proteins (46). These previous results confirmed the association between oxidative stress and autophagy. Therefore, here we further investigated whether Sch B overproduced ROS that could be responsible for the initiation of autophagy in Hepa1-6 cells. The production of ROS, the content of MDA and GSH, and the activity of GSH-Px and SOD were examined after treatment with Sch B in Hepa1-6 cells. SOD and GSH-px are both major antioxidant enzymes with efficient ROS-scavenging ability (47). Quantification of MDA is an indicator of lipid peroxidation and ROS-induced damage. GSH is the primary ROS scavenger, and its depletion is considered to contribute to ROS accumulation. In this essay, we investigated that increasing of Sch B concentration promoted ROS accumulation (**Figure 4A**), suppressed SOD activities, elevated the content of MDA, and reduced the activities of GSH and GSH-px (**Figure 4B**). Results demonstrated that increased ROS accumulation induced autophagy and may inhibit Hepa1-6 cell proliferation with increasing of Sch B concentration.

The development and spread of cancer were often accompanied by Th1/Th2 imbalance occurring (48). Th2 drift occurs in a variety of tumors, including non-small cell lung cancer, rectal cancer, ovarian cancer, choriocarcinoma, and melanoma, and it becomes more pronounced as the malignancy of the tumor increases (49). Th1 cells produce *IL-2, TNF-α,* and *IFN-γ* and mediate and participate in cellular immunity and local inflammatory responses. Th2 cells produce *IL-4, IL-5, IL-6,* and *IL-10*, mediate humoral immunity, and are closely associated with the development of hypersensitivity reactions (50). *IL-4* and *IFN-γ* mediate macrophage activation and inhibit *IL-1* and *TNF-α* production. *IL-10* suppresses Th1 cell proliferation and cytokine production such as *IFN* and *IL-2* and blocks the induction activity of *IL-12. IL-10* has growth factor-like effects on tumor cells, and IFN has obvious cytotoxic effects. *IL-5* synergizes with *IL-2* and *IL-4* to stimulate B-cell growth and differentiation (51). This study revealed that Sch B upregulated the expression of *IL-2, TNF-α, IFN-γ,* and *IL-12* and reduced the expression of *IL-4, IL-5, IL-6,* and *IL-10,* which evidenced that Sch B triggered Th1/Th2 imbalance and shifted Th1/Th2 balance toward Th1 (**Figure 5**).

Selenoproteins were known for their antioxidant roles as ROS scavengers (52). Selenoprotein deficiencies led to excess cellular ROS and reduced antioxidant defense ability, thereby triggering autophagy. Selenoprotein U (Selu) deletion induced autophagy by inhibiting the phosphatidylinositol 3-kinase (PI3K)-Akt-mTOR signaling pathway in rooster Sertoli cells (29).

Gpx3 suppression markedly increased ROS levels and promoted autophagy by downregulation of mTOR and increasing the expression of *ATG7, ATG10,* and *ATG12* (53). The supplement of Se could alleviate the imbalance of Th1/Th2 caused by Pb. Meanwhile, the cytokines including *IL-1β, IL-2, IL-8, IL-10,* and *IFN-γ* had a positive correlation with selenoproteins containing *Sepx1, Selo, Selu, Sepp, Sep15, Selw,* and *Selk*. The results indicated that the altered expressions of selenoproteins influenced cytokines related to Th1/Th2 imbalance (54). In chicken dendritic cells, alterations of some selenoprotein expression were correlated with variations of Th1- and Th2-type cytokines such as *IL-12, IFN-γ,* and *IL-10*, thus inducing Th1/Th2 imbalance (55). Accordingly, to explore the specialized role of selenoproteins in ROS-mediated autophagy and Th1/Th2 imbalance in Hepa1-6 cells with growing Sch B treatment, we investigated the mRNA expression of 25 selenoproteins. Based on the results of **Figure 6**, downregulation of the majority of selenoprotein expressions encompassed *Txnrd1, Txnrd2, Txnrd3, GPX1, GPX2, Dio1, Dio2, Dio3, GPX6, Selt, Selm, Selp, Selv, Selo, Sels,* and *Selk*. For in-depth analysis, heat map with clustering analysis of the differentially expressed genes was adopted to assess the expression of 25 selenoproteins with 0-, 25-, 50-, 100-μM Sch B in Hepa1-6 cells. **Figure 7** displayed the heat map results; significant suppression of a spectrum of selenoprotein expression in response to Sch B treatment was observed. Gpx family has prominent antioxidant effects, and its reduced activity resulted in a weakened ROS-scavenging capacity of cells, thus affecting the entire growth phase of cells (56). Txnrd family exerted an irreplaceable antioxidant role, in addition, bound to many proteins and involved in regulating cell growth such as inhibiting apoptosis and autophagy (57, 58). *Sels,* a widely expressed transmembrane protein located in the ER, is critical for ER stress by eliminating misfolding proteins and regulating oxidative stress, apoptosis, and autophagy (59). Together, the former researchers were in agreement with our findings that the majority of selenoprotein expression downregulation arguably is one of the factors most responsible for ROS-mediated autophagy and Th1/Th2 imbalance with Sch B treatment in Hepa1-6 cells. In addition, to identify the principal selenoproteins of Sch B that induced ROS-mediated autophagy and Th1/Th2 imbalance in Hepa1-6 cells, we performed PCA. *Txnrd1, Txnrd3, Selp, IL-5, GPX2, Dio3,* and *Selr* were highly positively correlated with PC1 (**Figure 8A**). Meanwhile, correlation analysis (**Figure 8B**) indicated that autophagy-related genes and related Th1/Th2 cytokines exhibited remarkable correlation with the expression of the majority of selenoproteins including *Txnrd1, Txnrd2, Txnrd3, GPX1, GPX2, GPX3, GPX4, GPX6, Dio1, Dio2, Dio3, Selt, Selm, Selp, Selh, Selv, Selo, Selr,* and *Sels*. The results demonstrated that selenoproteins had essential effects in the regulation of autophagy as well as Th1/Th2 imbalance by Sch B treatment in Hepa1-6 cells. The outcome suggested the key role of these selenoproteins with their potential interactors in ROS-mediated autophagy and Th1/Th2 imbalance of Hepa1-6 cells. Subsequently, we will undertake further in-depth study to investigate the specific mechanism of these selenoproteins in the inhibitory effect of Sch B in Hepa1-6 cells.

CONCLUSION

In summary, we found that Sch B treatment triggered the accumulation of ROS and induced the occurrence of cell autophagy, as well as causing Th1/Th2 imbalance and resulting in inhibiting proliferation of Hepa1-6 cells. Meanwhile, selenoproteins exerted irreplaceable roles in regulating autophagy and Th1/Th2 imbalance in Hepa1-6 cells, and *Txnrd1, Txnrd3, Selp, GPX2, Dio3,* and *Selr* had considerable impacts on the process. More importantly, these findings may help us discover selenoproteins with the specific role involved in Sch B's remarkable antitumor activity and cell death mechanisms, which would be further exploited as a novel small-molecule candidate drug to improve the Sch B antitumor effect.

DATA AVAILABILITY STATEMENT

The original contributions presented in the study are included in the article/**Supplementary Material**, further inquiries can be directed to the corresponding authors.

AUTHOR CONTRIBUTIONS

All authors contributed to the study conception and design. Material preparation and data collection and analysis were performed by ST. The first draft of the article was written by ST. TL, ZZ, and XY carefully examined and revised the article and performed part of the data analysis. All authors read and approved the final article. Article revision was guided by MY and YJ.

FUNDING

This project was funded by the Outstanding Young Talents Project of the Central Government's Reform and Development Fund for Local Universities (Grant No. 2020YQ12), Heilongjiang Provincial Natural Science Foundation of China (Grant No. YQ2020H024), and Supporting Certificate of Heilongjiang Postdoctoral Scientific Research Developmental Fund (Grant No. LBH-Q20027).

ACKNOWLEDGMENTS

This project was funded by the Outstanding Young Talents Project of the Central Government's Reform and Development Fund for Local Universities (Grant No. 2020YQ12), Heilongjiang Provincial Natural Science Foundation of China (Grant No. YQ2020H024), and Supporting Certificate of Heilongjiang Postdoctoral Scientific Research Developmental Fund (Grant No. LBH-Q20027).

SUPPLEMENTARY MATERIAL

The Supplementary Material for this article can be found online at: https://www.frontiersin.org/articles/10.3389/fimmu.2022.857069/full#supplementary-material

REFERENCES

1. Wang K, Chen Q, Shao Y, Yin S, Yu H. Anticancer Activities of TCM and Their Active Components Against Tumor Metastasis. *Biomed Pharmacother* (2021) 133:111044. doi: 10.1016/j.biopha.2020.111044
2. Hong M, Zhang Y, Li S, Tan H, Wang N, Mu S, et al. A Network Pharmacology-Based Study on the Hepatoprotective Effect of Fructus Schisandrae. *Molecules* (2017) 22(10):1617. doi: 10.3390/molecules22101617
3. Yan J, Zhang Q, Bao J, Du C, Chang L. Schisandrin B Inhibits the Proliferation and Invasion of Glioma Cells by Regulating the HOTAIR-micoRNA-125a-mTOR Pathway. *Neuroreport* (2016) 28(2):93–100. doi: 10.1097/wnr.0000000000000717
4. Zhen L, Zhang B, Liu K, Ding Z, Xun H. Schisandrin B Attenuates Cancer Invasion and Metastasis Via Inhibiting Epithelial-Mesenchymal Transition. *PloS One* (2012) 7(7):e40480. doi: 10.1371/journal.pone.0040480
5. Xiang S, Wang X, Li H, Shu Y, Bao R, Zhang F, et al. Schisandrin B Induces Apoptosis and Cell Cycle Arrest of Gallbladder Cancer Cells. *Molecules* (2014) 19:13235–50. doi: 10.3390/molecules190913235
6. Yang J, Shi G, Gong Y, Cai J, Zheng Y, Zhang Z. LncRNA 0003250 Accelerates Heart Autophagy and Binds to miR as a Competitive Endogenous RNA in Chicken Induced by Selenium Deficiency. *J Cell Physiol* (2021) 236(1):157–77. doi: 10.1002/jcp.29831
7. Zheng YY, Guan HY, Yang J, Cai JZ, Liu Q, ZW. Z, et al. Calcium Overload and Reactive Oxygen Species Accumulation Induced by Selenium Deficiency Promote Autophagy in Swine Small Intestine. *Anim Nutr* (2021) 7(4):997–1008. doi: 10.1016/j.aninu.2021.05.005
8. Guo JM, Xing HJ, Cai JZ, Zhang HF, Xu SW. H2S Exposure-Induced Oxidative Stress Promotes LPS-Mediated Hepatocyte Autophagy Through the PI3K/AKT/TOR Pathway. *Ecotoxicol Environ Saf* (2021) 209(1):111801. doi: 10.1016/j.ecoenv.2020.111801
9. Tan ML, Parkinson EK, Yap LF, Paterson IC. Autophagy is Deregulated in Cancer-Associated Fibroblasts From Oral Cancer and is Stimulated During the Induction of Fibroblast Senescence by TGF-β1. *Sci Rep* (2021) 11(1):179. doi: 10.1038/s41598-020-79789-8
10. Yun CW, Jeon J, Go G, Lee JH, Sang HL. The Dual Role of Autophagy in Cancer Development and a Therapeutic Strategy for Cancer by Targeting Autophagy. *Int J Mol Sci* (2020) 22(1):179. doi: 10.3390/ijms22010179
11. Wang SA, Liu JA, Yao YA, Wang YA, Xu S. Polystyrene Microplastics-Induced ROS Overproduction Disrupts the Skeletal Muscle Regeneration by Converting Myoblasts Into Adipocytes. *J Hazard Mater* (202) .417:125962. doi: 10.1016/j.jhazmat.2021.125962
12. Yan J, Dou X, Zhou J, Xiong Y, Lei Y. Tubeimoside-I Sensitizes Colorectal Cancer Cells to Chemotherapy by Inducing ROS-Mediated Impaired Autophagolysosomes Accumulation. *J Exp Clin Cancer Res* (2019) 38 (1):353. doi: 10.1186/s13046-019-1355-0
13. Zhou P, Lu S, Luo Y, Shan W, Yang K, Zhai Y, et al. Attenuation of TNF-α-Induced Inflammatory Injury in Endothelial Cells by Ginsenoside Rb1 via Inhibiting NF-κb, JNK and P38 Signaling Pathways. *Front Pharmacol* (2017) 8:464. doi: 10.3389/fphar.2017.00464
14. Shi JM, Bai LL, Zhang DM, Yiu A, Yin ZQ, Han WL, et al. Saxifragifolin D Induces the Interplay Between Apoptosis and Autophagy in Breast Cancer Cells Through ROS-Dependent Endoplasmic Reticulum Stress. *Biochem Pharmacol* (2013) 85:913–26. doi: 10.1016/j.bcp.2013.01.009
15. Hering J, Garrean S, Dekoj TR, Razzak A, Saied A, Trevino J, et al. Inhibition of Proliferation by Omega-3 Fatty Acids in Chemoresistant Pancreatic Cancer Cells. *Ann Surg Oncol* (2007) 14(12):3620–8. doi: 10.1245/s10434-007-9556-8
16. Zhong R, Zhang Y, Chen D, Cao S, Zhong H. Single-Cell RNA Sequencing Reveals Cellular and Molecular Immune Profile in a Pembrolizumab-Responsive PD-L1-Negative Lung Cancer Patient. *Cancer Immunol Immunother* (2021) 70(8):2261–74. doi: 10.1007/s00262-021-02848-0
17. Ns A, Wei WA, Yue WA, Yg B, Sx A. Hydrogen Sulfide of Air Induces Macrophage Extracellular Traps to Aggravate Inflammatory Injury via the Regulation of miR-15b-5p on MAPK and Insulin Signals in Trachea of Chickens - ScienceDirect. *Sci Total Environ* (2021) 771:145407. doi: 10.1016/j.scitotenv.2021.145407
18. Chen X, Bi M, Yang J, Cai J, Zhang H, Zhu Y, et al. Cadmium Exposure Triggers Oxidative Stress, Necroptosis, Th1/Th2 Imbalance and Promotes Inflammation Through the TNF-Alpha/NF-kappaB Pathway in Swine Small Intestine. *J Hazard Mater* (2022) 421:126704. doi: 10.1016/j.jhazmat.2021.126704
19. Chen Y, Yang J, Huang Z, Jing H, Yin B, Guo S, et al. Exosomal lnc-AFTR as a Novel Translation Regulator of FAS Ameliorates Staphylococcus Aureus-Induced Mastitis. *BioFactors* (2022) 48:148–63. doi: 10.1002/biof.1806
20. Lorvik KB, Hammarstrm C, Fauskanger M, Audun O, Corthay A. Adoptive Transfer of Tumor-Specific Th2 Cells Eradicates Tumors by Triggering an In Situ Inflammatory Immune Response. *Cancer Res* (2016) 76(23):6864. doi: 10.1158/0008-5472.CAN-16-1219
21. Jiang X, Guan S, Qiao Y, Li X, Xu Y, Yang L, et al. Effects of Poly(I:C) and MF59 Co-Adjuvants on Immunogenicity and Efficacy of Survivin Polypeptide Immunogen Against Melanoma. *J Cell Physiol* (2018) 233(6):4926–34. doi: 10.1002/jcp.26317
22. Zhao X, Liu J, Ge S, Chen C, Cai D. Saikosaponin A Inhibits Breast Cancer by Regulating Th1/Th2 Balance. *Front Pharmacol* (2019) 10:624. doi: 10.3389/fphar.2019.00624
23. Lin GH, Lin LZ, Zhang Y, Pei WY, Zeng JC, Zhao WX. Influence of Fire Needle Stimulation at Sihua Acupoints on Performance Status and Th1/Th2 Balance in the Patients With Advanced Non-Small Cell Lung Cancer After Chemotherapy. *Zhen ci yan jiu = Acupuncture Res / [Zhongguo yi xue ke xue yuan Yi xue qing bao yan jiu suo bian ji]* (2019) 44(2):136–9. doi: 10.13702/j.1000-0607.170933
24. Zhang J, Wang S, Hao X, Sun G, Xu S. The Antagonistic Effect of Selenium on Lead-Induced Necroptosis via MAPK/NF-κb Pathway and HSPs Activation in the Chicken Spleen. *Ecotoxicol Environ Saf* (2020) 204(2):111049. doi: 10.1016/j.ecoenv.2020.111049
25. Zhang Z, Liu Q, Yang J, Yao H, Xu S. Proteomic Profiling of Multiple Tissue Damage in Chickens for Selenium Deficiency Biomarker Discovery. *Food Funct* (2020) 11(2):1312. doi: 10.1039/C9FO02861G
26. Chi Q, Zhang Q, Lu Y, Zhang Y, Xu S, Li S. Roles of Selenoprotein S in Reactive Oxygen Species-Dependent Neutrophil Extracellular Trap Formation Induced by Selenium-Deficient Arteritis. *Redox Biol* (2021) 44:102003. doi: 10.1016/j.redox.2021.102003
27. Zhang Y, Xu Y, Chen B, Zhao B, Gao XJ. Selenium Deficiency Promotes Oxidative Stress-Induced Mastitis via Activating the NF-κb and MAPK Pathways in Dairy Cow. *Biol Trace Element Res* (2021) 21:1–11. doi: 10.1007/s12011-021-02882-0
28. Fichman Y, Koncz Z, Reznik N, Miller G, Szabados L, Kramer K, et al. SELENOPROTEIN O Is a Chloroplast Protein Involved in ROS Scavenging and its Absence Increases Dehydration Tolerance in Arabidopsis Thaliana. *Plant Sci* (2018) 270:278–91. doi: 10.1016/j.plantsci.2018.02.023
29. Hamid S, Yang J, Zhao X, Cai J, Qi L, Muhammad I, et al. Selenoprotein-U (SelU) Knockdown Triggers Autophagy Through PI3K–Akt–mTOR Pathway Inhibition in Rooster Sertoli Cells. *Metallomics* (2018) 10:929–40. doi: 10.1039/C8MT00090E
30. Marciel MP, Hoffmann PR. Molecular Mechanisms by Which Selenoprotein K Regulates Immunity and Cancer. *Biol Trace Element Res* (2019) 193:60–8. doi: 10.1007/s12011-019-01774-8
31. Ma YM, Guo YZ, Gordon I, Wang LY, Dong JD, Wang J, et al. Overexpression of Selenoprotein H Prevents Mitochondrial Dynamic Imbalance Induced by Glutamate Exposure. *Int J Biol Sci* (2017) 13(11):1458–69. doi: 10.7150/ijbs.21300
32. Liu X, Zhang D, Hao Y, Liu Q, Wu Y, Liu X, et al. Cyanidin Curtails Renal Cell Carcinoma Tumorigenesis. *Cell Physiol Biochem* (2018) p:2517–31. doi: 10.1159/000489658
33. Yang J, et al. Dysfunction of Thioredoxin Triggers Inflammation Through Activation of Autophagy in Chicken Cardiomyocytes. *BioFactors* (2020) 46 (4):579–90. doi: 10.1002/biof.1625
34. Liu J, Wang Y, Qiu Z, Lv G, Qu P. Impact of TCM on Tumor-Infiltrating Myeloid Precursors in the Tumor Microenvironment. *Front Cell Dev Biol* (2021) 9:635122. doi: 10.3389/fcell.2021.635122
35. Dai XX, Yin CT, Guo GL. Schisandrin B Exhibits Potent Anticancer Activity in Triple Negative Breast Cancer by Inhibiting Stat3. *Toxicol Appl Pharmacol* (2018) 358:110–9. doi: 10.1016/j.taap.2018.09.005
36. Zhou Y, Men L, Sun Y, Wei M, Fan X. Pharmacodynamic Effects and Molecular Mechanisms of Lignans From Schisandra Chinensis Turcz. (Baill.), a Current Review. *Eur J Pharmacol* (2021) 892:173796. doi: 10.1016/j.ejphar.2020.173796

37. Zhao YG, Zhang H. Autophagosome Maturation: An Epic Journey From the ER to Lysosomes. *J Cell Biol* (2018) 218(3):757–70. doi: 10.1083/jcb.201810099
38. Yuan B, Shen H, Li L, Su T, Zhao Y. Autophagy Promotes Microglia Activation Through Beclin-1-Atg5 Pathway in Intracerebral Hemorrhage. *Mol Neurobiol* (2017) 54(1):115–24. doi: 10.1007/s12035-015-9642-z
39. Real E, Rodrigues L, Cabal GG, Enguita FJ, Mancio-Silva L, Mello-Vieir J, et al. Plasmodium UIS3 Sequesters Host LC3 to Avoid Elimination by Autophagy in Hepatocytes. *Nat Microbiol* (2018) 3:17–25. doi: 10.1038/s41564-017-0054-x
40. Loos F, Xie W, Sica V, Pedro BS, Kroe Me RG. Artificial Tethering of LC3 or P62 to Organelles Is Not Sufficient to Trigger Autophagy. *Cell Death Dis* (2019) 10(10):771. doi: 10.1038/s41419-019-2011-5
41. Mauthe M, Langereis M, Jun J, Zho X, Jones A, Omta W, et al. An siRNA Screen for ATG Protein Depletion Reveals the Extent of the Unconventional Functions of the Autophagy Proteome in Virus Replication. *J Cell Biol* (2016) 214(5):619–35. doi: 10.1083/jcb.201602046
42. Agrotis A, Pengo N, Burden JJ, Ketteler R. Redundancy of Human ATG4 Protease Isoforms in Autophagy and LC3/GABARAP Processing Revealed in Cells. *Autophagy* (2019) 15:976–97. doi: 10.1080/15548627.2019.1569925
43. Chen YF, Liu H, Luo XJ, Zhao Z, Zou ZY, Li J, et al. The Roles of Reactive Oxygen Species (ROS) and Autophagy in the Survival and Death of Leukemia Cells. *Crit Rev Oncol Hematol* (2017) 112(Complete):21–30. doi: 10.1016/j.critrevonc.2017.02.004
44. Liu X-J, Wang YQ, Shang SQ, Xu S, Guo M. TMT Induces Apoptosis and Necroptosis in Mouse Kidneys Through Oxidative Stress-Induced Activation of the NLRP3 Inflammasome. *Ecotoxicol Environ Saf* (2022) 230:113167. doi: 10.1016/j.ecoenv.2022.113167
45. Wei B, Huang Q, Huang S, Mai W, Zhong X. Trichosanthin-Induced Autophagy in Gastric Cancer Cell MKN-45 Is Dependent on Reactive Oxygen Species (ROS) and NF-κb/P53 Pathway. *J Pharmacol Sci* (2016) 131(2):77–83. doi: 10.1016/j.jphs.2016.03.001
46. Yi LT, Dong SQ, Wang SS, Chen M, Cheng J. Curcumin Attenuates Cognitive Impairment by Enhancing Autophagy in Chemotherapy. *Neurobiol Dis* (2019) 136:104715. doi: 10.1016/j.nbd.2019.104715
47. Jing HY, Wang F, Gao X. Lithium Intoxication Induced Pyroptosis via ROS/NF-κb/NLRP3 Inflammasome Regulatory Networks in Kidney of Mice. *Environ Toxicol* (2022) 1:11. doi: 10.1002/tox.23446
48. Zhang W, Pan Y, Gou P, Zhou C, Ma L, Liu Q, et al. Effect of Xanthohumol on Th1/Th2 Balance in a Breast Cancer Mouse Model. *Oncol Rep* (2018) 39:280–8. doi: 10.3892/or.2017.6094
49. Benvenuto M, Focaccetti C, Ciuffa S, Fazi S, Bei R. Polyphenols Affect the Humoral Response in Cancer, Infectious and Allergic Diseases and Autoimmunity by Modulating the Activity of TH1 and TH2 Cells. *Curr Opin Pharmacol* (2021) 60:315–30. doi: 10.1016/j.coph.2021.08.005
50. Cheng YH, Lin YC, Chen IS, Liu SD, Wang CC. Immunomodulatory Effects of Taiwanese Neolitsea Species on Th1 and Th2 Functionality. *J Immunol Res* (2017) 1–13. doi: 10.1155/2017/3529859
51. Moverate R, Elfman L. Study of the Th1/Th2 Balance, Including IL-10 Production,in Cultures of Peripheral Blood Mononuclear Cells Frombirch-Pollen-Allergic Patients. *Allergy* (2000) 55:171–5. doi: 10.1034/j.1398-9995.2000.00244.x.
52. Leonardi A, Evke S, Lee M, Melendez JA, Begley TJ, Leonardi A, et al. Epitranscriptomic Systems Regulate the Translation of Reactive Oxygen Species Detoxifying and Disease Linked Selenoproteins. *Free Radical Biol Med* (2019) 143:573–93. doi: 10.1016/j.freeradbiomed.2019.08.030
53. Gong Y, Yang J, Cai J, Liu Q, Zhang JM, Zhang ZW. Effect of Gpx3 Gene Silencing by siRNA on Apoptosis and Autophagy in Chicken Cardiomyocytes. *J Cell Physiol* (2019) 234(6):7828–38. doi: 10.1002/jcp.27842
54. Fu JX, Yang TS, Xu SW. Effect of Selenium Antagonist Lead-Induced Damage on Th1/Th2 Imbalance in the Peripheral Blood Lymphocytes of Chickens. *Ecotoxicol Environ Saf* (2019) 175:74–82. doi: 10.1016/j.ecoenv.2019.03.036
55. Sun Z, Xu Z, Wang D, Yao H, Li S. Selenium Deficiency Inhibits Differentiation and Immune Function and Imbalances the Th1/Th2 of Dendritic Cells. *Metallomics* (2018) 759–67. doi: 10.1039/C8MT00039E
56. Yi Z, Jiang L, Zhao L, Zhou M, Ni Y, Yang Y, et al. Glutathione Peroxidase 3 (GPX3) Suppresses the Growth of Melanoma Cells Through Reactive Oxygen Species (ROS)-Dependent Stabilization of Hypoxia-Inducible Factor 1 and 2. *J Cell Biochem* (2019) 120(11):19124–36. doi: 10.1002/jcb.29240
57. Liu Q, Du P, Zhu Y, Zhang X, Cai J, Zhang Z. Thioredoxin Reductase 3 Suppression Promotes Colitis and Carcinogenesis via Activating Pyroptosis and Necrosis. *Cell Mol Life Sci* (2022) 79(2):106. doi: 10.1007/s00018-022-04155-y
58. Chen Y, Jing H, Chen M, Liang W, Guo M. Transcriptional Profiling of Exosomes Derived From Staphylococcus Aureus-Infected Bovine Mammary Epithelial Cell Line MAC-T by RNA-Seq Analysis. *Oxid Med Cell Longev* (2021) 8460355. doi: 10.1155/2021/8460355
59. Jang JK, Park KJ, Lee JH, Ko KY, Kang S, Kim IY. Selenoprotein S is Required for Clearance of C99 Through Endoplasmic Reticulum-Associated Degradation. *Biochem Biophys Res Commun* (2017) 486(2):444–50. doi: 10.1016/j.bbrc.2017.03.060

Conflict of Interest: The authors declare that the research was conducted in the absence of any commercial or financial relationships that could be construed as a potential conflict of interest.

frontiers | Frontiers in Immunology

ORIGINAL RESEARCH
published: 02 June 2022
doi: 10.3389/fimmu.2022.921317

Correlation Analysis Between Trace Elements and Colorectal Cancer Metabolism by Integrated Serum Proteome and Metabolome

Zhi Zheng[1†], Qingfeng Wei[2†], Xianghui Wan[2], Xiaoming Zhong[2], Lijuan Liu[2], Jiquan Zeng[2], Lihua Mao[1], Xiaojian Han[1], Fangfang Tou[1] and Jun Rao[2*]*

[1] Jiangxi Provincial People's Hospital, The First Affiliated Hospital of Nanchang Medical College, Nanchang, China, [2] Jiangxi Cancer Hospital, The Second Affiliated Hospital of Nanchang Medical College, Jiangxi Clinical Research Center for Cancer, Nanchang, China

OPEN ACCESS

Edited by:
Mengyao Guo,
Northeast Agricultural University, China

Reviewed by:
Heng Yang,
Augusta University, United States
Ting Xie,
Cedars-Sinai Medical Center, United States
Qinghua Yao,
Zhejiang Cancer Hospital, China

***Correspondence:**
Jun Rao
raojun1986@126.com
Fangfang Tou
toufangfang@163.com

[†]These authors have contributed equally to this work

Specialty section:
This article was submitted to Nutritional Immunology, a section of the journal Frontiers in Immunology

Received: 15 April 2022
Accepted: 06 May 2022
Published: 02 June 2022

Citation:
Zheng Z, Wei Q, Wan X, Zhong X, Liu L, Zeng J, Mao L, Han X, Tou F and Rao J (2022) Correlation Analysis Between Trace Elements and Colorectal Cancer Metabolism by Integrated Serum Proteome and Metabolome. Front. Immunol. 13:921317. doi: 10.3389/fimmu.2022.921317

Colorectal cancer (CRC) is currently the third most common cancer with a high mortality rate. The underlying molecular mechanism of CRC, especially advanced CRC, remains poorly understood, resulting in few available therapeutic plans. To expand our knowledge of the molecular characteristics of advanced CRC and explore possible new therapeutic strategies, we herein conducted integrated proteomics and metabolomics analyses of 40 serum samples collected from 20 advanced CRC patients before and after treatment. The mass spectrometry-based proteomics analysis was performed under data-independent acquisition (DIA), and the metabolomics analysis was performed by ultra-performance liquid chromatography coupled with time-of-flight tandem mass spectrometry (UPLC-TOF-MS/MS). Trace elements including Mg, Zn, and Fe were measured by inductively coupled plasma spectrometry (ICP-MS) analysis. Four of the 20 patients had progressive disease (PD) after treatment, and clinical test results indicated that they all had impaired liver functions. In the proteomics analysis, 64 proteins were discovered to be significantly altered after treatment. These proteins were enriched in cancer-related pathways and pathways participating immune responses, such as MAPK signaling pathway and complement/coagulation cascades. In the metabolomics analysis, 128 metabolites were found to be significantly changed after treatment, and most of them are enriched in pathways associated with lipid metabolism. The cholesterol metabolism pathway was significantly enriched in both the proteomics and metabolomics pathway enrichment analyses. The concentrations of Mg in the serums of CRC patients were significantly lower than those in healthy individuals, which returned to the normal range after treatment. Correlation analysis linked key lipids, proteins, and Mg as immune modulators in the development of advanced CRC. The results of this study not only extended our knowledge on the molecular basis of advanced CRC but also provided potential novel therapeutic targets for CRC treatment.

Keywords: colorectal cancer, Mg, cholesterol metabolism, DIA-MS, UPLC/Q-TOF-MS/MS

INTRODUCTION

Colorectal cancer (CRC) is the third most common malignancy and remains the second most deadly cancer all around the world (1, 2). In 2020, there were estimated 1.93 million CRC cases and 0.93 million CRC deaths globally. It is predicted that the global CRC incidence is to be increased to 3.2 million cases in 2040. Among new CRC diagnoses, 20% developed metastasis already, while another 25% with localized tumor would develop metastasis later. The delayed diagnosis leads to the high mortality rate of CRC patients, posing a growing public health challenge. Although genetic factors including germline MLH1 and APC mutations play etiologic roles in CRC development, over half of all cases and deaths are greatly affected by non-genetic risk factors such as cigarette smoking, low physical activity, low nutrition diet, high alcohol consumption, obesity, inflammatory bowel disease, and dysregulated gut microbiota (3).

Trace elements have been reported to be significantly correlated with the mortalities of various cancers including breast, ovary, bladder, lung, and pancreas cancer (4). For example, Lin et al. reported that mercury exposure was a risk factor for CRC; high levels of Hg and Pb may contribute to the occurrence and development of gastrointestinal cancer (5). The main functions of trace elements in human are as enzyme components or catalysts in biochemical reactions, and imbalanced trace elements may induce cell damages, DNA injuries, and overactivation of certain signaling pathways in tumor growth (6). For instance, zinc (Zn) is an essential nutritional element which functions in antitumor immunity through its involvement in cell immunity of T-lymphocytes (7). Magnesium (Mg) is a necessary element and required as a cofactor in over 600 enzymes, controlling cellular homeostasis and metabolic pathways. Low serum Mg concentrations among women were identified to be associated with higher CRC risk in the Atherosclerosis Risk in Communities (ARIC) Study (8). Iron (Fe) is one of the most important and abundant trace elements. A tight association between excess iron and increased cancer risk has been demonstrated in epidemiological studies (9).

Recent advances in "omics" studies including genomics, proteomics, metabolomics, and proteogenomic have greatly expanded our understanding of cancer biomarkers and drivers of tumorigenesis (10–12). Key genes, proteins, metabolites, and their signaling pathways in cancer cells are usually probed for potential therapeutic targets. Proteomics provides high-throughput and simultaneous determination of thousands of proteins in biological samples, and it has been applied in a lot of large-scale clinical studies on various types of diseases including coronavirus disease (COVID-19), cardiovascular diseases, and cancers (13). Corey et al. recently reported an aptamer-based proteomics study of fibrosis and detected 4,783 proteins, of which 16 proteins differed significantly between the disease and control cohorts (14). Further analysis identified the ADAMTSL2 protein and eight other proteins that are closely related to advanced fibrosis in adults with non-alcoholic fatty liver disease (NAFLD). Apart from proteomics, metabolomics is another powerful large-scale study approach that semiquantitatively measures all small-molecule compounds in biological samples. In cancer studies, metabolomics is often used for assessing disease prognosis, prediction, and responses to specific therapies (15). In 2021, Yu et al. conducted an untargeted UHPLC-Q-TOF/MS metabolomic analysis on 123 human serum samples from patients with chronic gastritis or gastric cancer (16). Three metabolites, linoleamide, N-hydroxy arachidonoyl amine, and hexadecasphinganine, were determined to be potential diagnostic biomarkers, indicating that disturbed lipid metabolism may be connected to the development of chronic gastritis or gastric cancer. When compared to single "-omic" analysis, integrative analyses of proteomics and metabolomics would likely gain deeper understanding of the molecular changes in diseases and discover biomarkers for diagnosis and therapy. We previously conducted a combined DIA-based proteomics and UPLC-TOF-MS/MS metabolomics study of cutaneous squamous cell carcinoma tissue samples. Significant protein and metabolite differences between tumor and non-cancerous tissues were uncovered, which are enriched in pathways related to DNA damage responses, apoptosis, autophagy, platelet activation, and protein digestion and absorption (10). The same integrative proteomics and metabolomics approach was also applied to characterize the serum samples of 20 advanced CRC patients at stage III or IV (11). The results extended our understanding on the physiopathology of CRC and revealed novel potential CRC serum biomarkers.

In the present study, proteomics and proteomics analyses were conducted on 40 serum samples from 20 CRC patients before and after treatment. Trace elements in these serum samples were also determined. Correlation analyses among proteins, metabolites, and trace elements in CRC serum samples before and after treatment were performed in order to identify critical regulators (trace elements, proteins, and metabolites) and related pathways that may function as important pathogenic factors in CRC and may be used as new therapeutic targets.

MATERIALS AND METHODS

Subjects

Twenty CRC patients in Jiangxi Cancer Hospital from January 2019 to December 2019 were included in this retrospective study (Rao et al., 2021). All of these 20 patients (N1–N20) were diagnosed with stage III or IV CRC according to the 7th edition of the American Joint Committee on Cancer (AJCC). Therapeutic plans for the 20 patients included cetuximab plus CAPIRI administration, cetuximab plus FOLFOX6 administration, CAPOX administration, bevacizumab plus CAPOX administration, and CAPIRI administration (**Supplementary Table S1**). Meanwhile, the *Yiqi Sanjie* formula was also administered in the treatment according to the crux of the traditional Chinese Medicine (TCM). About 5 ml of serum from each CRC patient before and after treatment was collected and immediately stored at -80°C until analysis. A group of 20 healthy individuals were also recruited as the controls, whose age and gender were matched to the CRC patient group.

Proteomic Analysis

The high-throughput DIA-based proteomics analysis was performed as in the previous report (11). Two microliters of each serum sample was firstly diluted with lysis buffer containing 8 M urea (Sigma, MO, USA), 100 mM Tris–HCl (pH 8.5, Sigma, MO, USA), 1 mM PMSF, and 1 mM EDTA, and then centrifuged at 15,000g for 15 min at 4°C. The extracted proteins in the supernatant were quantified using a BCA protein assay kit (Bi Yuntian, Shanghai, China). The extracted proteins were reduced and digested with trypsin using the filter-aided sample preparation (FASP) method (Promega, Madison, WI). A NanoDrop 2000 instrument (Thermo Scientific, Waltham, MA, USA) was used for determination of the concentrations of digested peptides by measuring absorbance at 280 nm. Three micrograms of trypsin-digested peptides containing iRT peptides (Biognosys, Schlieren, Switzerland) was analyzed in the DDA analysis mode on a Fusion Lumos Orbitrap mass spectrometer (Thermo Fisher Scientific) connected to an EASY-nLC 1000 system (Thermo Fisher Scientific). The LC gradient elution program and MS data acquisition settings were reported previously (11). Meanwhile, the DIA analysis was done the same with DDA. A resolution of 60,000 over an m/z range of 350 to 1,500 was set in the full scan, followed by a resolution of 30,000 in DIA scans. Collision energy, AGC target, maximal injection time, and 45 variable DIA windows were all the same as in the previous report (11). The identification and quantification of proteins were conducted using Spectronaut Pulsar X 12.0 (Biognosys). All results were strictly filtered with a Q value cutoff of 0.01, and p values were calculated according to the kernel density estimator.

Metabolomics Analysis

Metabolites in serum samples were extracted with 120 μl of 50% methanol buffer. Ten microliters of each extraction was mixed to prepare five pooled quality control (QC) samples. All tested samples were injected in a random order. A Triple TOF 5600 Plus mass spectrometer coupled to a UPLC system (Sciex, Cheshire, UK) was used in the metabolomics study. The column for the reversed-phase separation and the gradient elution program were the same as in our previous study (11). The injection volume was 4 μl while the UPLC flow rate was 0.4 ml/min. The Q-TOF mass spectrometer was operated in alternate positive and negative ion modes. The XCMS software was employed for metabolite identification and quantification. Online databases such as Kyoto Encyclopedia of Genes and Genomes (KEGG) and Human Metabolome Database (HMDB) were used for annotation of the identified metabolites. An in-house MS^2 spectrum library of metabolites was also used in the identification of metabolites (11).

Trace Element Analysis

Mg, Fe, and Zn were measured using an iCAP Qc ICP-MS system (Thermo Scientific, Bremen, Germany). The serum samples were washed thoroughly, soaked in HNO_3 (Merck, Darmstadt, Germany), and rinsed several times with 18 Ω deionized water (Millipore, Bedford, MA, USA). Afterward, serum samples were wet digested and analyzed according to the procedures described before (17). Statistical analysis (Student's t-test) was performed using SPSS 17.0 software, while a p value ≤ 0.05 indicated significant difference.

Data Analysis

The proteomics and metabolomics data normalization and analyses were conducted as in a previous report (11). Briefly, all data were normalized by setting the median of each protein (or metabolite) to 1.00, while the missing values (if any) were filled with the minimum value. Significantly changed proteins were determined by a paired non-parametric Wilcoxon test with p-value ≤ 0.05. OmicsBean (http://www.omicsbean.com), a multi-omics data analysis tool, was employed for Gene Ontology (GO) and KEGG pathway enrichment analyses. Principal component analysis (PCA) and partial least square discriminant analysis (PLS-DA) were performed using the SIMCA-P software (v13.0, Umetrics, Malmö, Sweden). PLS-DA is a suitable approach for compositional data that consist of more metabolites (in hundreds) than biological samples (only tens) and serves as one of the most effective strategies for metabolic data analysis. Besides, independent t-tests were performed for determining significantly changed metabolites. Potential biomarkers from the differentially expressed proteins were evaluated by receiver operating characteristic (ROC) analysis *via* the MetaboAnalyst web server (http://www.metaboanalyst.ca). R statistical software was used for the correlation analysis. The corresponding p-values were determined according to the cor.test function, while p values were adjusted in order to control FDR (false discovery rate).

RESULTS

The Pathologic and Clinical Data

The clinical information of the 20 recruited patients was listed in **Table 1**. All patients were diagnosed with CRC at stage III or IV. CEA and CA 19-9 levels of the patients were measured. As shown in **Supplementary Table S1**, four patients, namely, N4, N9, N10, and N17, had progressive disease (PD) after treatment, while the rest 16 patients remained with stable disease (SD) after treatment. Biochemical examinations were performed on the 20 patients (**Supplementary Table S2**). Increased levels of gamma glutamyl transpeptidase (γ GTP) and alanine aminotransferase (ALT) in patients N4 and N10 after treatment indicated that they had damaged liver functions (**Figures 1A, B**). The concentration of total bile acid in patient N9 was increased to the critical threshold after treatment, and the concentration of total bile acid in patient N17 was also increased nearly four times after treatment (**Figure 1C**). The APOB levels in all patients were significantly decreased after treatment (**Figure 1D** and **Supplementary Table S3**). The concentrations of high-density lipoprotein cholesterol (HDL), low-density lipoprotein cholesterol (LDL), triglyceride (TG), and total cholesterol (T-CHO) were not changed.

TABLE 1 | The details of significant correlations related to proteins or Mg.

Element 1	Element 2	r	*p*
PFN1	KRT81	-0.7125	9.06E-04
SFTPB	TCN1	-0.7067	1.04E-03
IGKV6.21	IGLV2.14	0.7002	1.21E-03
MINPP1	KRT81	0.7026	1.15E-03
GPLD1	MASP1	0.7047	1.09E-03
hCG_2039566	ACTB	0.7068	1.04E-03
IGLC7	ICAM2	0.7158	8.37E-04
GSN	MINPP1	0.7201	7.51E-04
PFN1	KIF21A	0.7214	7.27E-04
FLNA	CDH1	0.7453	3.86E-04
CSF1R	SSC5D	0.7463	3.75E-04
SFTPB	IGHV2.5	0.7704	1.84E-04
PFN1	SFTPB	0.7755	1.56E-04
PFN1	IGHV2.5	0.7794	1.37E-04
IGFBP7	KRT14	0.7822	1.25E-04
TAGLN2	KIF21A	0.8076	5.06E-05
KIF21A	IGHV2.5	0.8398	1.30E-05
PFN1	TAGLN2	0.8515	7.36E-06
SFTPB	TAGLN2	0.8823	1.27E-06
TAGLN2	IGHV2.5	0.9092	1.74E-07
Mg	4DN	0.7760	1.53E-04

Serum Protein Changes in Patients With Advanced CRC After Treatment

In total, 551 proteins were identified in the proteomics analysis, among which 64 proteins were altered after treatment (p value < 0.05) (**Supplementary Table S4**). Of the 64 proteins, the levels of 35 proteins including PFN1, CD99, TAGLN2, and KIF21A were increased, and the levels of the other 29 proteins were decreased (0.23 to 0.96 folds) after treatment.

GO enrichment analysis of these 64 significantly changed proteins found that 1,133 biological process (BP) terms, 69 molecular function (MF) terms, and 116 cellular component (CP) terms were significantly (p values < 0.05) enriched (**Supplementary Tables S5–S7**). The top 10 enriched terms for each GO category are shown in **Supplementary Figure S1**. The majorly enriched BP terms were connected to importing into cells, membrane invagination, phagocytosis, engulfment, and adaptive immune response. Immunoglobulin receptor binding, antigen binding, and protein binding were in the top 10 enriched MF terms. The mostly enriched CP terms contained dendritic tree, extracellular space, extracellular region part, extracellular region, and immunoglobulin complex. A pathway enrichment analysis of the significantly changed proteins generated 18

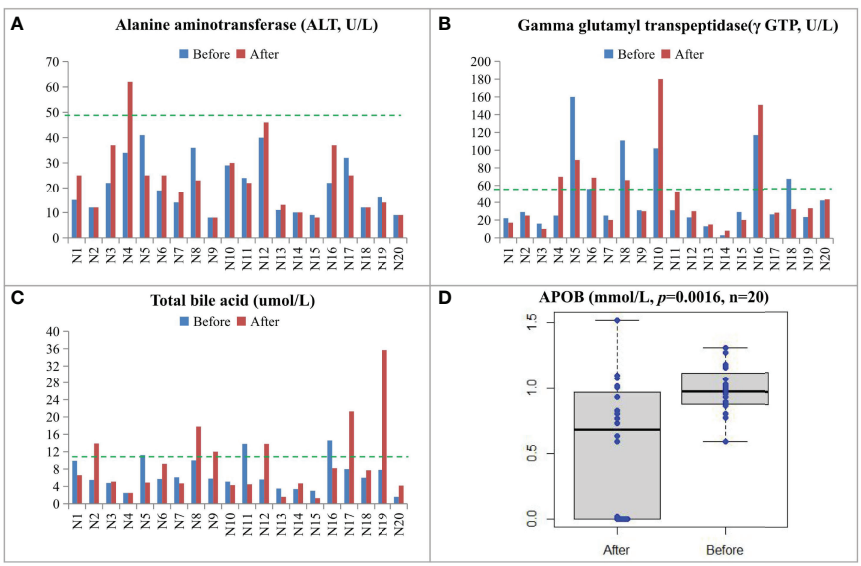

FIGURE 1 | Biochemical examinations and lipid measurements of CRC patients before and after treatment including ALT **(A)**, γ GTP **(B)**, total bile acid **(C)**, and APOB **(D)**. The upper limit of normal level for each item was labeled by a green line.

pathways in five functional groups: environmental information processing, organismal systems, cellular processes, human diseases, and other/unknown (**Figure 2**). The largest group, Human Diseases, included *Staphylococcus aureus* infection, arrhythmogenic right ventricular cardiomyopathy (ARVC), malaria, dilated cardiomyopathy (DCM), viral myocarditis, hypertrophic cardiomyopathy (HCM), and proteoglycans in cancer. The "other/unknown" group contained cholesterol metabolism and fluid shear stress and atherosclerosis pathways. The "cellular processes" group had three enriched pathways, namely, focal adhesion, oocyte meiosis, and phagosome. The enriched pathways in the "environmental information processing" group contained pathways related to cancer development such as hippo signaling pathway, cell adhesion molecules (CAMs), and MAPK signaling pathway. The "organismal systems" group contained three pathways in immune or endocrine system: leukocyte transendothelial migration, complement and coagulation cascades, and oxytocin signaling pathway.

Serum Metabolite Changes in Patients With Advanced CRC After Treatment

A total of 567 metabolites were identified in the positive-ion mode, and 431 metabolites were detected in the negative-ion mode. The supervised statistical method PLS-DA was performed on the metabolomics data, and a clear separation between the before and after treatment groups was revealed (**Figure 3**). One hundred twenty-eight metabolites were determined to be significantly changed (0.33- to 2.34-fold) after treatment (**Supplementary Table S8**). Pathway enrichment analysis of these 128 metabolites revealed 20 significantly enriched pathways ($p < 0.05$, **Supplementary Table S9**). Among the top 10 significantly enriched pathways (**Figure 4**), four were related to lipid metabolism such as glycerophospholipid metabolism, cholesterol metabolism, choline metabolism in cancer, and fat digestion and absorption. The cholesterol metabolism pathway was also found to be enriched in the proteomics data analysis, including two proteins (APOB and LRP1) and two metabolites (glycocholate and triacylglycerol). Notably, the change of triacylglycerol determined by metabolomic analysis was constant with that in five items of serum lipid examined by kits, although the latter of which was not significant ($p > 0.05$). The level of APOB protein was identified to be significantly decreased by both proteomics analysis and serum lipid test.

ICP-MS Trace Element Analysis

To investigate the roles of trace elements in CRC, the levels of Mg, Fe, and Zn were determined by ICP-MS in the healthy group (the controls), the group before treatment, and the group after treatment. As shown in **Figure 5**, the concentrations of Mg and Zn in the CRC patients were both significantly lower ($p < 0.001$) than those in the controls. There was no significant change in the Fe concentrations between CRC patients and the controls. After treatment, the levels of Mg and Zn in the CRC patients were increased ($p < 0.01$ and $p = 0.38$, respectively). Especially, the Mg concentrations returned to normal levels ($p = 0.68$) after treatment, while the contents of Zn were still at a significantly lower levels ($p < 0.001$). These results indicated that Mg and Zn

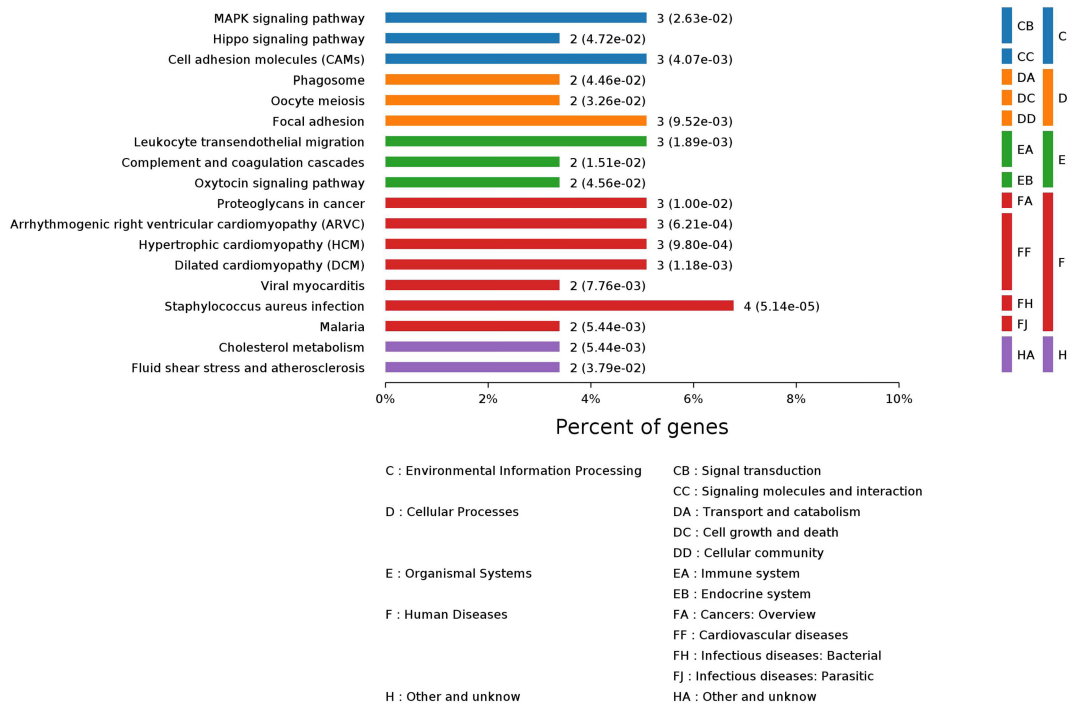

FIGURE 2 | Pathway enrichment analysis of 64 significantly changed proteins in 20 CRC patients after treatment.

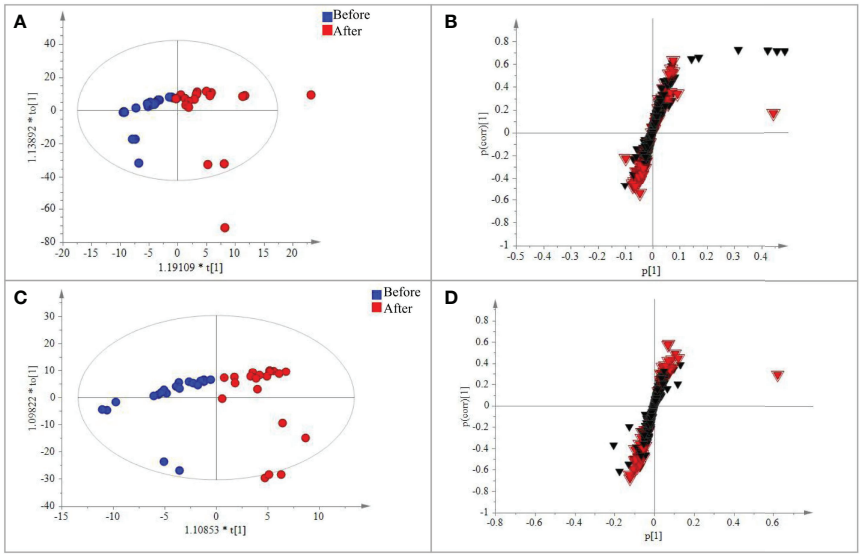

FIGURE 3 | PLS-DA analysis of the metabolic data detected in the positive and negative modes, respectively. **(A)** Plot of the scores from the PLS-DA of metabolic data for CRC patients before and after treatment in the positive negative mode. **(B)** Loading plot from the PLS-DA analysis of metabolic data for CRC patients before and after treatment in the positive–negative mode. **(C)** Plot of the scores from the PLS-DA of metabolic data for CRC patients before and after treatment in the positive–negative mode. **(D)** Loading plot from the PLS-DA analysis of metabolic data for CRC patients before and after treatment in the positive negative mode. The circle dots represent the test serum samples, and metabolites are shown as triangles. Metabolites labeled with the red triangle played important roles for the separation.

may play important roles in the progression and prognosis of CRC.

Correlation Analysis Among Mg, Proteins, and Metabolites

Pearson pairwise correlation analysis was performed among 64 proteins, 128 metabolites, and Mg (**Figure 6**). A total of 18,528 correlations were discovered, ranging from -0.7646 for KRT81 and 1-methyladenosine to 0.9896 for (+)-setoclavine and biliverdin. Among the 18,528 correlations, 412 had FDR ≤ 0.05 and $r^2 \geq 0.49$. Only 7 of the 412 correlations were negative correlations, while the rest 405 were positive correlations. Most of the 412 correlations were between metabolites. There were 106 metabolites that were closely associated with each other (359 correlations) or with certain proteins (32 correlations). There were 20 significant correlations (FDR ≤ 0.05 and $r^2 \geq 0.49$)

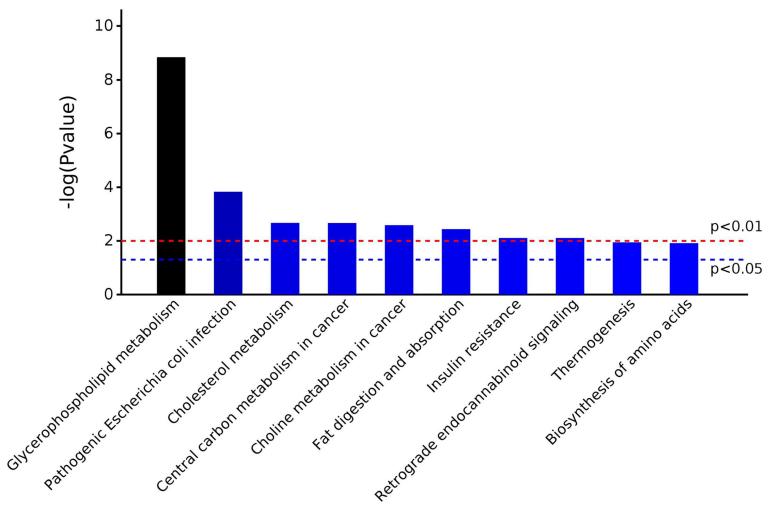

FIGURE 4 | The top 10 significantly enriched pathways in metabolomic analysis.

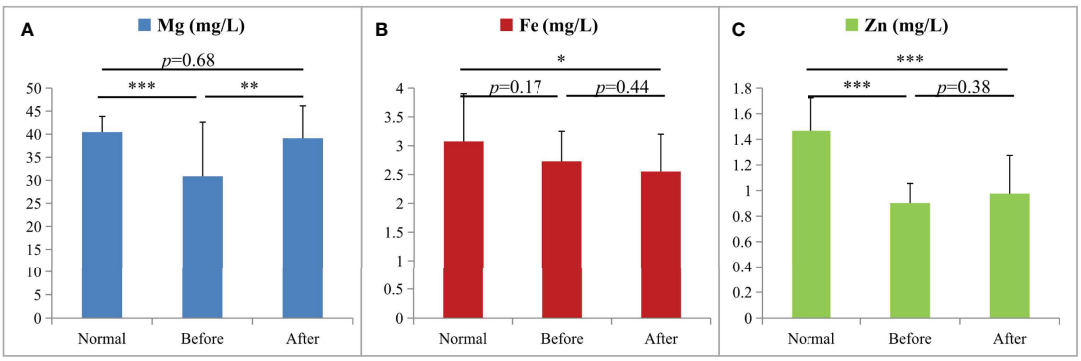

FIGURE 5 | The changes of Mg **(A)**, Fe **(B)**, and Zn **(C)** in ICP-MS analysis among the three groups (*p < 0.05, **p < 0.01, and ***p < 0.001; n = 20 per group): the healthy group (Normal), the group before treatment (Before), and the group after treatment (After).

among 24 proteins, and the correlations between TAGLN2 and PFN1, TAGLN2 and SFTPB, and TAGLN2 and IGHV2-5 were all higher than 0.85 (**Table 1**). Mg was found to be only positively correlated with 4′-hydroxy-3′,5,6,7,8-pentamethoxyflavone (r = 0.7760).

DISCUSSION

The incidence of CRC has dramatically increased in the recent decades, highlighting the significance of understanding its etiology and having effective therapeutic strategies. In the present study, 20 advanced CRC patients at stage III or IV were enrolled to investigate the molecular alterations after treatment. Serum samples were collected and studied by ICP-MS trace element, proteomics, and metabolomics analyses. Most of these advanced CRC patients (80%) had SD after combined traditional Chinese medicine and Western medicine treatment. Hence, the current study aimed to reveal molecular changes of proteins and metabolites after CRC treatment. Serum is one of the most widely used specimens for proteomics and metabolomics investigations, as well as for trace metal research (18). Two high-throughput and non-targeted technologies, DIA-MS and UPLC/Q-TOF-MS/MS, were employed in the proteomics and metabolomics studies. A total of 551 proteins and 719 metabolites were detected, generating large datasets for revealing molecular changes in relation to CRC therapy in a systematic manner.

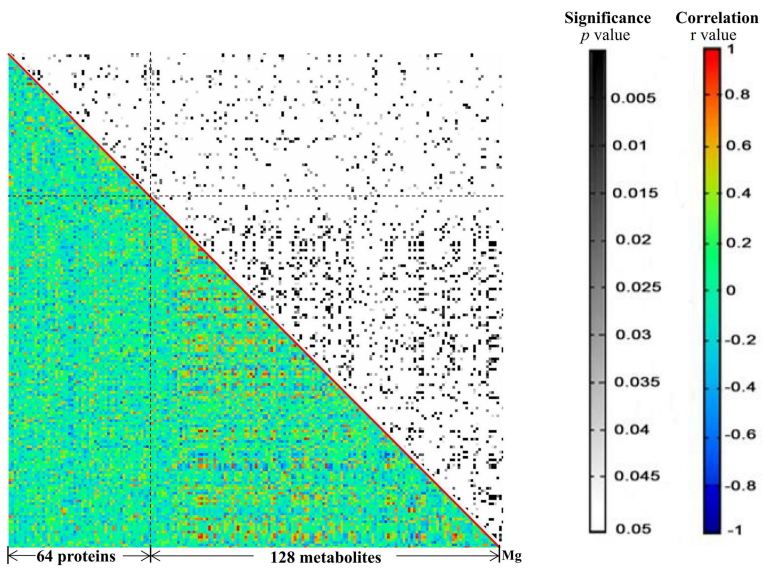

Figure 6

FIGURE 6 | The heat map generated from the results of correlation analysis. The p and r values of the correlations are shown in distinct colors. X- and Y-axes were divided into proteins/metabolites/Mg.

Increasing evidence has associated impaired liver function to CRC (19). In advanced CRC, liver is the primary metastatic site. Moreover, Mikolasevic et al. (2017) showed a positive correlation between NAFLD and CRC and thus suggested that NAFLD may be a predictor for the development of CRC. In the present study, we found that CRC patients with worsening conditions had impaired liver functions including increased levels of transaminase and total bile acid (20). In the 64 proteins that were significantly changed after treatment, some are associated with liver functions. For example, AOPB and IGF-1 are biomarkers reflecting the grade of liver fibrosis in hepatic patients and their levels were both significantly decreased after treatment. Serum IGF-1 has been reported to be an early indicator of CRC (21, 22). ROC analysis using IGF-1 had a very high AUC value (AUC = 1) to distinguish PD and SD patients, so IGF-1 might be a potential new target in CRC therapy. Moreover, a number of immunity-related proteins such as CR2, CD99, CSF1R, and IGHV2-5 were found to be significantly changed after treatment, and these proteins are involved in adaptive immune response, complement activation, immunoglobulin receptor binding, and antigen binding according to their associated GO terms. In addition, other changed proteins including PFN1 and TAGLN2 were reported to be involved in the development of CRC *via* influencing the immune system (23, 24). TAGLN2 is an oncogenic factor in various types of cancers and may be employed as a potential therapeutic target for CRC. Ding et al. reported that TAGLN2 could regulate the Notch1 signaling pathway by interacting with CD44 and facilitating the proliferation and migration of CRC cells (24). Pathway enrichment analysis of these 64 significantly changed proteins returned several cancer-related pathways and pathways in immune responses.

The UPLC-TOF-MS/MS metabolomics results revealed 128 significantly altered ($p \leq 0.05$) serum metabolites after CRC treatment. Nearly half of these 128 metabolites are lipids and lipid-like metabolites, among which the level of one liver function-related metabolite, triacylglycerol, was significantly increased after treatment. Pathway enrichment analysis of the significantly changed metabolites returned 20 significantly enriched pathways such as glycerophospholipid metabolism, autophagy, and protein digestion/absorption. Two pathways, insulin resistance and primary bile acid biosynthesis, were re-confirmed to be influenced by treatment. One of the 20 enriched pathways, cholesterol metabolism, was also discovered in the proteomics analysis. This pathway contains APOB, LRP1, glycocholate, and triacylglycerol. It seemed that abnormal cholesterol metabolism may contribute to the progression of CRC. Cholesterol-derived metabolites and proteins which regulate cholesterol metabolism play critical roles in sustaining cancer development and suppressing immune responses (25). Preclinical and clinical studies have already demonstrated that manipulating cholesterol metabolism could inhibit tumor growth, reinvigorate antitumor activity, and thus reshape the immunological landscape. ICP-MS trace element analysis has indicated that Mg and Zn may play key roles in the regulation of CRC development and prognosis (26). Rayssiguier et al. reported that the quantities of Mg and Zn in diet can influence cholesterol metabolism (27). Particularly, Mg plays a significant role in many cellular metabolic reactions, and decreasing of Mg may function as a novel predictive factor of efficacy and outcome of advanced CRC treatment (26). It should be pointed out that some CRC patients in this study were treated with epidermal-growth-factor receptor (EGFR)-targeting antibody Cetuximab, which inhibits cancer proliferation and decreases Mg level as well (28). Lichun et al. reported the positive correlation between the loss of Mg and liver damage and concluded that the serum magnesium concentrations were correlated with certain TCM patterns of symptoms in the process of hepatitis (29). The TCM *Yiqi Sanjie* formula used for CRC treatment in this study probably plays a significant role in affecting magnesium homeostasis also, since some components of the formula such as *Dangshen*, *Astragalus*, and *Lobelia* contain magnesium.

Correlation analysis has been proved to be useful for the discovery of putative key regulatory elements in network regulation (11). There were 412 significant correlations among the significantly changed 64 proteins, 128 metabolites, and Mg. About 98% of the 412 correlations were positive, and most correlations were found between metabolites. Lipids and lipid-like molecules dominated the correlations, indicating their conserved roles in CRC progression and treatment. Meanwhile, several important proteins including KIF21A, TAGLN2, PFN1, and SFTPB were positively correlated with each other (30, 31). For example, the expression level of KIF21A was significantly related to the clinical prognosis outcome of pancreatic ductal adenocarcinoma (PDAC) patients; patients with increased levels of KIF21A had shorter overall survival (OS) time. The SFTPB gene was reported to be a diagnosis marker of mediastinal lung cancer (32). The correlations between every two of KIF21A, TAGLN2, PFN1, and SFTPB were all higher than 0.8, indicating that they play important roles in therapeutic responses of advance CRC. Additionally, there was only one significant correlation involving Mg, which was the positive correlation between Mg and 4′-hydroxy-3′,5,6,7,8-pentamethoxyflavone. Another name for 4′-hydroxy-3′,5,6,7,8-pentamethoxyflavone is 4′-demethylnobiletin (4DN), which is a major metabolite of nobiletin, an immune modulator displaying potential anticancer effects (33). Wu et al. found that 4DN could induce G0/G1 cell-cycle arrest and apoptosis and thus inhibit human colon cancer cell growth (34).

CONCLUSIONS

Altogether, this study investigated the serum molecular changes after treatment of advanced CRC by proteomics, metabolomics, and trace element ICP-MS analysis. The results from the correlation and pathway enrichment analysis revealed important regulatory elements and pathways involved in responses to the treatment of advanced CRC. This work presents new insights into the underlying mechanisms and potential new therapeutic targets for advanced CRC.

Nevertheless, these findings need to be further validated due to the limited number of samples used in the current study.

DATA AVAILABILITY STATEMENT

All of the raw data have been deposited to the ProteomeXchange Consortium *via* the iProX partner repository with the dataset identifier PXD025041.

ETHICS STATEMENT

The studies involving human participants were reviewed and approved by the local ethics committee of Jiangxi Cancer Hospital. The patients/participants provided their written informed consent to participate in this study. Written informed consent was obtained from the individual(s) for the publication of any potentially identifiable images or data included in this article.

AUTHOR CONTRIBUTIONS

ZZ, JR, and FT designed the study. ZZ, QW, XW, and XZ carried out the experimental work. LL and JZ prepared the dataset and performed data analyses. LM, XH, and JR wrote the manuscript. All authors contributed to the article and approved the submitted version.

FUNDING

This work was supported by grants from the National Natural Science Foundation of China (No. 81960865), Jiangxi Provincial Department of Science (No. 20212BCJL23056 and No. 20212BAG70040), the Excellent Young Scientists Fund of Jiangxi Cancer Hospital (2021EYS01), and National Cancer Center Climbing Fund (No. NCC201814B045). The work was also funded in part by grants from the Science and Technology Plan Project of Jiangxi Provincial Administration of Traditional Chinese Medicine (No. 2019A057).

SUPPLEMENTARY MATERIAL

The Supplementary Material for this article can be found online at: https://www.frontiersin.org/articles/10.3389/fimmu.2022.921317/full#supplementary-material

REFERENCES

1. Xi Y, Xu P. Global Colorectal Cancer Burden in 2020 and Projections to 2040. *Transl Oncol* (2021) 14:101174. doi: 10.1016/j.tranon.2021.101174
2. Siegel RL, Miller KD, Goding Sauer A, Fedewa SA, Butterly LF, Anderson JC, et al. Colorectal Cancer Statistics, 2020. *CA Cancer J Clin* (2020) 70:145–64. doi: 10.3322/caac.21601
3. Keum NN, Giovannucci E. Global Burden of Colorectal Cancer: Emerging Trends, Risk Factors and Prevention Strategies. *Nat Rev Gastroenterol Hepatol* (2019) 16:713–32. doi: 10.1038/s41575-019-0189-8
4. Attar T. A Mini-Review on Importance and Role of Trace Elements in the Human Organism. *Chem Rev Lett* (2020) 3:117–30. doi: 10.22034/crl.2020.229025.1058
5. Lin X, Peng L, Xu X, Chen Y, Zhang Y, Huo X. Connecting Gastrointestinal Cancer Risk to Cadmium and Lead Exposure in the Chaoshan Population of Southeast China. *Environ Sci Pollut Res Int* (2018) 25:17611–9. doi: 10.1007/s11356-018-1914-5
6. Juloski JT, Rakic A, Ćuk VV, Ćuk VM, Stefanović S, Nikolić D, et al. Colorectal Cancer and Trace Elements Alteration. *J Trace Elem Med Biol* (2020) 59:126451. doi: 10.1016/j.jtemb.2020.126451
7. Jouybari L, Kiani F, Akbari A, Sanagoo A, Sayehmiri F, Aaseth J, et al. A Meta-Analysis of Zinc Levels in Breast Cancer. *J Trace Elem Med Biol* (2019) 56:90–9. doi: 10.1016/j.jtemb.2019.06.017
8. Polter EJ, Onyeaghala G, Lutsey PL, Folsom AR, Joshu CE, Platz EA, et al. Prospective Association of Serum and Dietary Magnesium With Colorectal Cancer Incidence. *Cancer Epidemiol Biomarkers Prev* (2019) 28:1292–9. doi: 10.1158/1055-9965.EPI-18-1300
9. Torti SV, Manz DH, Paul BT, Blanchette-Farra N, Torti FM. Iron and Cancer. *Annu Rev Nutr* (2018) 38:97–125. doi: 10.1146/annurev-nutr-082117-051732
10. Chen X, Rao J, Zheng Z, Yu Y, Lou S, Liu L, et al. Integrated Tear Proteome and Metabolome Reveal Panels of Inflammatory-Related Molecules *via* Key Regulatory Pathways in Dry Eye Syndrome. *J Proteome Res* (2019) 18:2321–30. doi: 10.1021/acs.jproteome.9b00149
11. Rao J, Wan X, Tou F, He Q, Xiong A, Chen X, et al. Molecular Characterization of Advanced Colorectal Cancer Using Serum Proteomics and Metabolomics. *Front Mol Biosci* (2021) 8:687229. doi: 10.3389/fmolb.2021.687229
12. Visal TH, den Hollander P, Cristofanilli M, Mani SA. Circulating Tumour Cells in the-Omics Era: How Far are We From Achieving the 'Singularity'? *Br J Cancer* (2022). doi: 10.1038/s41416-022-01768-9
13. da Silva Lima N, Fondevila MF, Nóvoa E, Buqué X, Mercado-Gómez M, Gallet S, et al. Inhibition of ATG3 Ameliorates Liver Steatosis by Increasing Mitochondrial Function. *J Hepatol* (2022) 76:11–24. doi: 10.1016/j.jhep.2021.09.008
14. Corey KE, Pitts R, Lai M, Loureiro J, Masia R, Osganian SA, et al. ADAMTSL2 Protein and a Soluble Biomarker Signature Identify at-Risk non-Alcoholic Steatohepatitis and Fibrosis in Adults With NAFLD. *J Hepatol* (2022) 76(1):25–33. doi: 10.1016/j.jhep.2021.09.026
15. Schmidt DR, Patel R, Kirsch DG, Lewis CA, Vander Heiden MG, Locasale JW. Metabolomics in Cancer Research and Emerging Applications in Clinical Oncology. *CA Cancer J Clin* (2021) 71:333–58. doi: 10.3322/caac.21670
16. Yu L, Lai Q, Feng Q, Li Y, Feng J, Xu B. Serum Metabolic Profiling Analysis of Chronic Gastritis and Gastric Cancer by Untargeted Metabolomics. *Front Oncol* (2021) 11:636917. doi: 10.3389/fonc.2021.636917
17. Huang H, Wei Y, Xia Y, Wei L, Chen X, Zhang R, et al. Child Marriage, Maternal Serum Metal Exposure, and Risk of Preterm Birth in Rural Bangladesh: Evidence From Mediation Analysis. *J Expo Sci Environ Epidemiol* (2021) 31:571–80. doi: 10.1038/s41370-021-00319-3
18. Deng W, Rao J, Chen X, Li D, Zhang Z, Liu D, et al. Metabolomics Study of Serum and Urine Samples Reveals Metabolic Pathways and Biomarkers Associated With Pelvic Organ Prolapse. *J Chromatogr B Analyt Technol BioMed Life Sci* (2020) 1136:121882. doi: 10.1016/j.jchromb.2019.121882
19. Parizadeh SM, Parizadeh SA, Alizade-Noghani M, Jafarzadeh-Esfehani R, Ghandehari M, Mottaghi-Moghaddam A, et al. Association Between non-Alcoholic Fatty Liver Disease and Colorectal Cancer. *Expert Rev Gastroenterol Hepatol* (2019) 13:633–41. doi: 10.1080/17474124.2019.1617696
20. Mikolasevic I, Orlic L, Stimac D, Hrstic I, Jakopcic I, Milic S. Non-Alcoholic Fatty Liver Disease and Colorectal Cancer. *Postgrad Med J* (2017) 93:153–8. doi: 10.1136/postgradmedj-2016-134383

21. Probst-Hensch NM, Yuan JM, Stanczyk FZ, Gao YT, Ross RK, Yu MC. IGF-1, IGF-2 and IGFBP-3 in Prediagnostic Serum: Association With Colorectal Cancer in a Cohort of Chinese Men in Shanghai. *Br J Cancer* (2001) 85:1695–9. doi: 10.1054/bjoc.2001.2172
22. Peters G, Gongoll S, Langner C, Mengel M, Piso P, Klempnauer J, et al. IGF-1r, IGF-1 and IGF-2 Expression as Potential Prognostic and Predictive Markers in Colorectal-Cancer. *Virchows Arch* (2003) 443:139–45. doi: 10.1007/s00428-003-0856-5
23. Zhang J, Li S, Zhang X, Li C, Zhang J, Zhou W. LncRNA HLA-F-AS1 Promotes Colorectal Cancer Metastasis by Inducing PFN1 in Colorectal Cancer-Derived Extracellular Vesicles and Mediating Macrophage Polarization. *Cancer Gene Ther* (2021) 28:1269–84. doi: 10.1038/s41417-020-00276-3
24. Ding R, Li G, Yao Y, Zhang L, Zhang X, Li J, et al. Transgelin-2 Interacts With CD44 to Regulate Notch1 Signaling Pathway and Participates in Colorectal Cancer Proliferation and Migration. *J Physiol Biochem* (2022) 78:99–108. doi: 10.1007/s13105-021-00843-8
25. Huang B, Song B, Xu C. Cholesterol Metabolism in Cancer: Mechanisms and Therapeutic Opportunities. *Nat Metab* (2020) 2:132–41. doi: 10.1038/s42255-020-0174-0
26. Vincenzi B, Santini D, Galluzzo S, Russo A, Fulfaro F, Silletta M, et al. Early Magnesium Reduction in Advanced Colorectal Cancer Patients Treated With Cetuximab Plus Irinotecan as Predictive Factor of Efficacy and Outcome. *Clin Cancer Res* (2008) 14:4219–24. doi: 10.1158/1078-0432.CCR-08-0077
27. Rayssiguier Y, Gueux E, Weiser D. Effect of Magnesium Deficiency on Lipid Metabolism in Rats Fed a High Carbohydrate Diet. *J Nutr* (1981) 111:1876–83. doi: 10.1093/jn/111.11.1876
28. Tejpar S, Piessevaux H, Claes K, Piront P, Hoenderop JG, Verslype C, et al. Magnesium Wasting Associated With Epidermal-Growth-Factor Receptor-Targeting Antibodies in Colorectal Cancer: A Prospective Study. *Lancet Oncol* (2007) 8:387–94. doi: 10.1016/S1470-2045(07)70108-0
29. Teng L, Zhang J, Dai M, Wang F, Yang H. Correlation Between Traditional Chinese Medicine Symptom Patterns and Serum Concentration of Zinc, Iron, Copper and Magnesium in Patients With Hepatitis B and Associated Liver Cirrhosis. *J Tradit Chin Med* (2015) 35:546–50. doi: 10.1016/s0254-6272(15)30137-0
30. Pehkonen H, de Curtis I, Monni O. Liprins in Oncogenic Signaling and Cancer Cell Adhesion. *Oncogene* (2021) 40:6406–16. doi: 10.1038/s41388-021-02048-1
31. Han Q, Han C, Liao X, Huang K, Wang X, Yu T, et al. Prognostic Value of Kinesin-4 Family Genes mRNA Expression in Early-Stage Pancreatic Ductal Adenocarcinoma Patients After Pancreaticoduodenectomy. *Cancer Med* (2019) 8:6487–502. doi: 10.1002/cam4.2524
32. Nakagomi T, Hirotsu Y, Goto T, Shikata D, Yokoyama Y, Higuchi R, et al. Clinical Implications of Noncoding Indels in the Surfactant-Encoding Genes in Lung Cancer. *Cancers (Basel)* (2019) 11:552. doi: 10.3390/cancers11040552
33. Sun Y, Han Y, Song M, Charoensinphon N, Zheng J, Qiu P, et al. Inhibitory Effects of Nobiletin and its Major Metabolites on Lung Tumorigenesis. *Food Funct* (2019) 10:7444–52. doi: 10.1039/c9fo01966a
34. Wu X, Song M, Qiu P, Li F, Wang M, Zheng J, et al. A Metabolite of Nobiletin, 4'-Demethylnobiletin and Atorvastatin Synergistically Inhibits Human Colon Cancer Cell Growth by Inducing G0/G1 Cell Cycle Arrest and Apoptosis. *Food Funct* (2018) 9:87–95. doi: 10.1039/c7fo01155e

Conflict of Interest: The authors declare that the research was conducted in the absence of any commercial or financial relationships that could be construed as a potential conflict of interest.

Publisher's Note: All claims expressed in this article are solely those of the authors and do not necessarily represent those of their affiliated organizations, or those of the publisher, the editors and the reviewers. Any product that may be evaluated in this article, or claim that may be made by its manufacturer, is not guaranteed or endorsed by the publisher.

frontiers | Frontiers in Immunology

ORIGINAL RESEARCH
published: 10 June 2022
doi: 10.3389/fimmu.2022.916933

Endotoxins Induced ECM-Receptor Interaction Pathway Signal Effect on the Function of MUC2 in Caco2/HT29 Co-Culture Cells

Wenxiang Hu[1†], Ping Feng[2†], Mingming Zhang[1†], Tian Tian[1], Shengxiang Wang[1], Baoyu Zhao[1], Yajie Li[1], Shuo Wang[1] and Chenchen Wu[1]*

[1] College of Animal Veterinary Medicine, Northwest A & F University, Yanling City, China, [2] College of Life Sciences, Yulin University, Yulin, China

OPEN ACCESS

Edited by:
Mengyao Guo,
Northeast Agricultural University, China

Reviewed by:
Lin Wang,
Shandong Agricultural University, China
Peng Liao,
Institute of Subtropical Agriculture (CAS), China
Sen Xie,
Wageningen University and Research, Netherlands

***Correspondence:**
Chenchen Wu
wucen95888@163.com

[†]These authors have contributed equally to this work

Specialty section:
This article was submitted to Nutritional Immunology, a section of the journal Frontiers in Immunology

Received: 10 April 2022
Accepted: 04 May 2022
Published: 10 June 2022

Citation:
Hu W, Feng P, Zhang M, Tian T, Wang S, Zhao B, Li Y, Wang S and Wu C (2022) Endotoxins Induced ECM-Receptor Interaction Pathway Signal Effect on the Function of MUC2 in Caco2/HT29 Co-Culture Cells. Front. Immunol. 13:916933. doi: 10.3389/fimmu.2022.916933

Endotoxins are toxic substances that widely exist in the environment and can enter the intestine with food and other substances. Intestinal epithelial cells are protected by a mucus layer that contains MUC2 as its main structural component. However, a detailed understanding of the mechanisms involved in the function of the mucus barrier in endotoxin penetration is lacking. Here, we established the most suitable proportion of Caco-2/HT-29 co-culture cells as a powerful tool to evaluate the intestinal mucus layer. Our findings significantly advance current knowledge as focal adhesion and ECM-receptor interaction were identified as the two most significantly implicated pathways in MUC2 small interfering RNA (siRNA)-transfected Caco-2/HT-29 co-culture cells after 24 h of LPS stimulation. When the mucus layer was not intact, LPS was found to damage the tight junctions of Caco-2/HT29 co-cultured cells. Furthermore, LPS was demonstrated to inhibit the integrin-mediated focal adhesion structure and damage the matrix network structure of the extracellular and actin microfilament skeletons. Ultimately, LPS inhibited the interactive communication between the extracellular matrix and the cytoskeleton for 24 h in the siMUC2 group compared with the LPS(+) and LPS(-) groups. Overall, we recognized the potential of MUC2 as a tool for barrier function in several intestinal bacterial diseases.

Keywords: lipopolysaccharide (LPS), Caco2/HT-29 cells, mucins, focal adhesion pathway, ECM receptor interaction pathway

Abbreviations: FN1, Fibronecin; ITGAV, integrin subunit alpha V; ITGB3, integrin beta 3; COL6A2, Collagen alpha-2(VI) chain VI; HSPG2, heparan sulfate proteoglycan 2; LAMC1, laminin subunit gamma 1; LAMA5, laminin subunit alpha 5; LAMB2, laminin subunit beta 2; CD44, CD44 molecule (Indian blood group); DAG1, dystroglycan 1; SRC, SRC proto-oncogene, non-receptor tyrosine kinase; ITGB4, integrin subunit beta 4; RhoA, ras homolog family member A; ROCK1, Rho associated coiled-coil containing protein kinase 1; ROCK2, Rho associated coiled-coil containing protein kinase 2; ACTB-G1, actin beta/gamma 1; ARHGAP5, Rho GTPase activating protein 5; ITGA2, integrin subunit alpha 2; AGRN, Agrin.

INTRODUCTION

Bacterial endotoxins are toxic substances found on the cell walls of gram-negative bacteria. Lipopolysaccharide (LPS) is the main toxic substance of endotoxins, which are released by the death and rupture of gram-negative bacteria (1, 2). As endotoxins are more stable, they are widely distributed in a variety of environments. The human gastrointestinal tract has a large and complex array of commensal and harmful gram-negative bacteria that cannot damage the intestinal lumen when the intestinal mucosal barrier is intact (3, 4). However, when the intestinal mucosal immune barrier is damaged, many endotoxins translocate to the blood, causing endotoxemia. Ensuring the integrity of the intestinal mucosal barrier is thus key to preventing endotoxin translocation. The intestinal mucus layer shields host epithelial cells of the gastrointestinal tract from both normal microbiota and enteric pathogens (5–7). The main component of the intestinal mucus layer is MUC2 (mucin-2), which is produced by goblet cells and forms a highly organized glycoprotein network (8). The density of the mucus layer rapidly expands and attaches to the epithelial layer. Owing to the mucus layer, lumen bacteria, which are isolated from epithelial cells, cannot reach the surface of epithelial cells (9–11). Previous studies revealed that endotoxins do not damage intestinal epithelial cells in the presence of the mucus layer (12, 13). We hypothesized that the lack of the mucus layer is caused by the translocation of endotoxins to intestinal epithelial cells. However, the structures and functions of epithelial cells that are first damaged by endotoxins in the absence of the mucus layer are unclear. Here, a model of Caco-2 and HT-29 co-culture cells was established on 2D Transwell inserts to mechanistically investigate the endotoxin on the intestinal mucus layer based on intestinal barrier function. Further, the proliferation, structure, function, and mechanism of Caco-2/HT-29 cell co-culture after LPS treatment was evaluated using siRNA transfection analysis, RNA-seq, qPCR, ELISA, and immunofluorescence analysis. The differences in resource utilization reflect the regulatory mechanism of the endotoxin effect on the intestinal mucous barrier, providing insights into intestinal mucosal immune barrier function.

MATERIAL AND METHODS

Cell Culture and Cell Co-Culture

Caco-2 (BNCC Bio-350769, China) and HT-29 (BNCC Bio-350769, China) cells were seeded at density of of 1×10^5 cells/cm^2. Cells were grown in tissue culture flasks at 37°C, 5% CO_2, and 90% relative humidity. All cell lines were cultured in DMEM-H medium (containing glutamine and sodium pyruvate) supplemented with 10% fetal bovine serum and 1% penicillin-streptomycin. Caco-2 and HT-29 cells were counted using a blood cell counter, mixed evenly in different proportions (Caco-2:HT-29 = 3:1 and 9:1), and seeded into the apical chambers of 24-well Transwell inserts (Corning, USA) at a final density of 1×10^5 cells/cm^2 in each insert. Cells were cultured in the same atmosphere described above, and allowed to grow for 15 days. The medium (500 μL in the upper compartment and 1500 μL in the lower compartment) was refreshed every other day. All samples were tested in six times repeat in this study (14, 15).

Cell Viability Assay

The Cell Counting Kit-8 was used to quantify cell viability according to the manufacturer's instructions. Briefly, 1 mL of a 3:1 (Caco-2: HT-29) cell suspension was seeded into 24-well plates at a density of 1×10^5 cells/cm^2 for 7 days. LPS was dissolved in DMEM-H and prepared in solutions of different concentrations (0, 100, 200, 400, and 800 μg/mL). LPS medium with different concentrations was added to a 24-well plate with 1 mL added to each well. Each dose group was assigned 24 wells. Six parallel wells for each dose group were exposed to LPS for 12 h, 24 h, 36 h, and 48 h. Blank wells were also established (no cells, only medium). The 24-well plates were removed at specific time points, the original culture medium. Thereafter, 100 μL of diluted CCK-8 reagent was added. After 1 h of incubation, the OD value of each well at a wavelength of 450 nm was measured using an automatic microplate reader (BioTek, USA); the measurement was repeated three times to calculate cell viability. Cell viability (%) =(OD value of experimental group OD value of blank group)/(OD value of control group OD value of blank group)×100.

Alcian Blue/Periodic Acid-Schiff Stain

Acidic mucin and mucopolysaccharide produced by HT-29 cells in the control and LPS groups (400 μg/mL at 12 h, 24 h, 36 h, 48 h) were determined by Alcian blue and periodic acid-Schiff (PAS) staining. For Alcian staining, the cells were fixed with 4% paraformaldehyde for 30 min, soaked in Alcian acidification solution for 3 min, stained with Alcian staining solution for 30 min, and washed with running water. For PAS staining, the cells were fixed with PAS fixative (75% ethanol solution) for 10 min, oxidized in 1.0% periodic acid solution for 5 min in the dark, and then stained with Schiff's reagent for 1 h at 37°C. After the addition of Schiff's reagent, the samples were washed three times with sulfite solution for 1 min each. Nuclei were then stained with hematoxylin for 1 min, and the cells were imaged using an inverted microscope (Nikon, Japan).

Immunofluorescence Analysis

The intercellular junctions of the LPS(-) and LPS(+) groups (400 μg/mL at 12 h, 24 h, 36 h, 48 h) were observed by immunofluorescence. The cells were seeded on glass coverslips, fixed for 30 min at 4°C with 4% paraformaldehyde, washed with PBS (three washes of 5 min each), permeabilized with 0.1% Triton-X-100 for 30 min at room temperature (RT), and rinsed with PBS at RT. To evaluate intercellular adhesion, cells were pre-incubated for 1 h with normal goat serum (5%, diluted in PBS) at RT to saturate non-specific binding sites. Incubation with the primary antibody, occludin (4°C overnight), and the secondary antibody, goat anti-rabbit IgG 488 (4 h at RT) was subsequently performed. Nuclei were stained with 10 g/mL DAPI for 5 min at RT. For each antibody, a technical negative control was used by replacing the primary antibody with PBS.

ELISA

A total of 50 μL of the diluted standard was added to the standard wells and 40 μL of the diluent was added to each of the sample wells. Thereafter, 10 μL of the sample was mixed *via* gentle shaking, and 50 μL of the biotin antigen working solution was added. The plate membrane was covered, sealed, and then incubated for 1 h in a 37°C incubator. The sealing membrane was carefully removed, and the liquid was discarded. After the plate membrane was spin dried, each well was filled with washing solution, which was allowed to stand for 30 s. The solution was then discarded, and the process was repeated 5 times. Thereafter, the membrane was pat dried. A total of 50 μL of chromogen reagent A was added to the membrane, followed by 50 μL of chromogenic reagent B. After gentle mixing, the color was allowed to develop at 37°C for 15 min in the dark. Fifty μL of stop solution was then added to each well to stop the reaction, and the absorbance of each well was measured sequentially with a microplate reader at a wavelength of 450 nm.

Small Interfering RNA Transfection

To prepare DNA-Hieff TransTM Liposome Nucleic Acid Transfection Reagent Complex, serum-free DMEM-H medium was mixed with MUC2 siRNA or negative control siRNA to a final concentration of 50 nM. Serum-free DMEM-H medium was also mixed with liposomal transfection reagent (liposomal transfection reagent: siRNA =3:1) and incubated for 3 min at RT. The diluted DNA and liposomal transfection reagent were gently mixed and incubated at RT for 20 min to form the DNA-liposome complex.

For cell transfection, 3:1 Caco-2 and HT-29 cells were seeded in 6-well plates at a seeding density of 1×10^5 cells/cm^2 before transfection. Thereafter, the co-cultured cells were transfected at a density of 90%-95% using antibiotic-free media plates. The DNA-Hieff Trans^{TM} complex was added to each well of the cell culture plate, followed by incomplete DMEM-H medium to a total volume of 2 mL. The culture plate was then gently shaken and mixed. After 6 h of culture at 37°C in a 5% CO_2 incubator, the growth medium was replaced. Further, after 48 h of culture, RNA was extracted, and the expression of the MUC2 gene in the transfection group and the LPS(-) group was detected by fluorescence quantitative PCR. FAM-negative control siRNA cells were transfected for 48 h and the transfection efficiency was evaluated under a fluorescence microscope.For challenged cells after transfection (LPS(+)+siRNA group), the transfection was performed for 48h according to the above steps. After 48h, the culture medium was discarded, washed with PBS twice, and 1.5mL medium containing 400 μg/mL LPS was added to continue culture for 24h in the incubator. For challenged cells after transfection (LPS(+)+siRNA group), the transfection was performed for 48h according to the above steps. After 48h, the culture medium was discarded, washed with PBS twice, and 1.5mL medium containing 400 μg/mL LPS was added to continue culture for 24h in the incubator.

MUC2 siRNA primer sequence F: 5`-GGAACAUGCAGAAG AUCAATT-3`

R: 5`-UUGAUCUUCUGCAUGUUCCTT-3`

FAM negative control sequence F: 5`-UUCUCCGAACGUGUC ACGUTT-3`

R: 5`-ACGUGACACGUUCGGAGAATT-3`

RNA-seq

The following three groups were established: LPS(-), LPS(+) (LPS 400 μg/mL, 24 h), and LPS(+)+siMUC2 (exposed to 400 μg/mL LPS for 24 h after transfection for 48 h). Total RNA was extracted from the three groups of cell samples, and the concentration, purity, and integrity of RNA were determined. mRNA was isolated from the total RNA, and double-stranded cDNA was synthesized. The adapter products were ligated, purified, and fragmented, and the final library was obtained using the Illumina TruSeq RNA Sample Prep Kit. High-throughput sequencing was then performed using the Illumina HiSeq 2500 system. The raw data were compared with the human genome, and differentially expressed genes were selected according to the criteria of $|\log2FC| \geq 1$ and p-value <0.05.

Occludin (*OCLN*), Claudin (*CLDN1*), *JAMA*, Desmosome, E-cadherin, and Zona occludens (*ZO1*) were selected as genes of tight-junction components. In addition, *FN1*, *ITGAV*, *ITGB3*, *COL6A2*, *HSPG2*, *LAMC1*, *LAMA5*, *LAMB2*, *CD44, DAG1*, and *SRC* genes in the ECM receptor interaction pathway, and *ITGB4*, *RhoA*, *ROCK1*, *ROCK2*, *ACTB-G1*, *ARHGAP5*, *ITGA2*, and *AGRN* in the focal adhesion pathway were selected. GAPDH was used as a housekeeping control.

Real-Time PCR

RNA extraction and RT-PCR were performed according to previously published studies. Total RNA was extracted from the samples according to the instructions of the RNA extraction kit. Thereafter, the concentration, purity, and integrity of RNA were determined. The 5 All-In-one RT MasterMix kit (including additional gDNA removal steps) was used to reverse transcribe the RNA into cDNA according to the manufacturer's instructions. Diluted cDNA was used as template DNA to assess gene expression levels. According to the human gene sequence, primers were designed using NCBI. The synthesized primers were then used for PCR amplification of the sample target fragment. RT-PCR was performed with an UltraSYBR Mixture on a fluorescence quantitative gene amplifier with three replicates per sample. GAPDH was used as a housekeeping gene to standardize the expression levels of the target genes. The relative expression levels of the target genes were calculated using the $2^{-\Delta\Delta CT}$ method. All genes mRNA expression of LPS(-) group are "1" by analyse in the test.

Gene	Primer name	Sequence	Product size (bp)
MUC2	F	ACCCGCACTATGTCACCTTC	151
	R	GGACAGGACACCTTGTCGTT	
MUC5AC	F	ACGGGAAGCAATACACGG	281
	R	GGTCTGGGCGATGATGAA	
ALPi	F	CCTGGTTGGGAAATAAGCACTC	136

(Continued)

Continued

Gene	Primer name	Sequence	Product size (bp)
	R	TTCAGAGGGAGGTCAGAAACAC	
FN1	F	GAGAATAAGCTGTACCATCGCAA	200
	R	CGACCACATAGGAAGTCCCAG	
ITGAV	F	GGCTGCATATTTCGGATTTTCTG	183
	R	CCATTCAGCTTTGTCGTCTGG	
ITGB3	F	AGTAACCTGCGGATTGGCTTC	164
	R	GTCACCTGGTCAGTTAGCGT	
COL6A2	F	AGCCTACGGAGAGTGCTACA	173
	R	GTCCTGGGAATCCAATGGGG	
LAMC1	F	CTGCAAAGAAGGGACGGGAT	139
	R	ATGGTCTGGTTGATGGCAGG	
LAMA5	F	GGGGTGTCTGTATCGACTGC	204
	R	ACCGCTCCCCAGAGAAGTT	
LAMB2	F	GGAACGCTCAGCAGACTTTG	131
	R	AGCGGGACTCACAGACTACAT	
CD44	F	CTGCCGCTTTGCAGGTGTA	109
	R	CATTGTGGGCAAGGTGCTATT	
ARGN	F	GACTTCAACGGCTTCTCCCA	134
	R	TTCTGCCCGTTGTAGAGCAG	
HSPG2	F	CCAAATGCGCTGGACACATTC	206
	R	CGGACACCTCTCGGAACTCT	
DAG1	F	TCAAGGCCAAGTTTGTGGGT	139
	R	GAGCCCCGGGTGATATTCTG	
ITGA2	F	GGGAATCAGTATTACACAACGGG	112
	R	CCACAACATCTATGAGGGAAGGG	
ITGB4	F	TGTCCATCCCCATCATCCCT	106
	R	CCCGATGGAGAGCGTAGAAC	
SRC	F	TGGCAAGATCACCAGACGG	100
	R	GGCACCTTTCGTGGTCTCAC	
ARHGAP5	F	ACCGAAGGACTCTACCGTGT	211
	R	CCGGGATTTTTGCTGCTTCC	
RhoA	F	GAGCCGGTGAAACCTGAAGA	146
	R	TTCCCACGTCTAGCTTGCAG	
ROCK1	F	CCAATTGTGATGCCTGTGCC	281
	R	AGAAAGCGTTCGAGGGGAAG	
ROCK2	F	AGTTGGTTCGTCACAAGGCA	207
	R	CTCCACCAGGCATGTACTCC	
ACTB-P1	F	CATGTACGTTGCTATCCAGGC	250
	R	CTCCTTAATGTCACGCACGAT	
TPJ1	F	ACCAGTAAGTCGTCCTGATCC	128
	R	TCGGCCAAATCTTCTCACTCC	
CLDN1	F	GAGGTGCCCTACTTTGCTGT	102
	R	ACACGTAGTCTTTCCCGCTG	
F11R	F	CCAAGGAGACACCACCAGAC	184
	R	GAGCTTGACCTTGACCTCCC	
DSC3	F	GGAGGGCAGGAAACCATTGA	94
	R	TGCAGGAGTCCAGGGTATGA	
OCLD	F	AGCAGCGGTGGTAACTTTGA	113
	R	CCGCCAGTTGTGTAGTCTGT	
GAPDH	F	CATCAAGAAGGTGGTGAAGCAG	120
	R	GCGTCAAAGGTGGAGGAGTG	

Statistical Analysis

Statistical analyses were performed using GraphPad Prism 7, and the data are expressed as mean ± SD. Statistical analyses were performed using the Statistical Package for Social Sciences (SPSS, USA) software, and a two-pair test followed by Student's t-test was performed to determine statistical significance between means. * Statistical difference between co-culture Caco2/HT-29 cells in the LPS(+) and LPS(+)+siMUC2 groups for the same factors ($P < 0.05$).

RESULTS

Determination of the Optimal Mucus Layer of the Caco-2/HT-29 Co-Culture Model in Transwell

HT-29 cells are often used as a goblet cell model *in vitro*, and can produce mucin secretions, forming an extracellular mucus layer. Herein, the combination of Caco-2 and HT-29 co-culture cells in the transwell compartment was selected to ensure that the established intestinal epithelial model had a mucus layer; this was determined by measuring epithelial monolayer integrity and mucus production (**Figure 1A**). In other studies, Caco-2:HT-29 ratios of 9:1 and 3:1 showed similar results; the TEER values also reached 400 $\Omega \times cm^2$ at the end of the 15-day differentiation process (14). Therefore, at the end of 15 days of differentiation, the optimal Caco-2: HT-29 ratios were 3:1 and 9:1, respectively. ALPi is a marker of Caco-2 cell differentiation, MUC5AC is a marker of HT-29 cell differentiation, and MUC2 is the main component that forms the mucus layer skeleton. Here, MUC2 and MUC5AC mRNA expression in Caco-2/HT-29 (3:1) co-culture markedly increased relative to that in the Caco-2/HT-29 (9:1) co-culture at the end of the 15-day differentiation process (**Figures 1B, C**). These combined data indicate that the Caco-2: HT-29 ratio of 3:1 led to the best mucus barrier at the end of the 15-day differentiation in the Transwell compartment.

PAS/Alcian Blue Staining and Immunofluorescence Analysis of Mucus Secretion and Occludin Expression in Caco-2/HT-29 Co-Culture Cell

To confirm the effect of the best time and dose of LPS on the mucus barrier function, we used 100, 200, 400, 800, and 1000 μg/mL LPS to stimulate Caco-2/HT-29 (3:1) co-culture cells at 12, 24, 36, and 48 h, respectively, after 15 days of Caco-2/HT-29 (3:1) co-culture differentiation. Cell viability was found to be highest after 24 h of LPS stimulation; thereafter, cell viability began to decline. Stimulation of Caco-2/HT29 (3:1) co-culture cells with 800 and 1000 μg/mL LPS caused cell death at 48 h. Therefore, 400 μg/mL LPS was selected to stimulatCaco-2/HT-29 (3:1) co-culture cells in the next test (**Figure 2A**). Based on PAS and Alcian Blue staining, mucin secretion by Caco-2/HT-29 cell was significantly increased at 24 h compared with 36 h and 48 h in the LPS(-) group. Further, the LPS(+) group displayed remarkable increases in mucin secretion compared with LPS(-) group after LPS stimulation for 12, 24, 36, and 48 h (**Figures 2B, C**). Using immunofluorescence, we evaluated the expression of occludin transmembrane proteins in Caco-2/HT-29 (3:1) co-cultured cells at different time points to assess the presence of tight junctions (**Figure 2D**). Caco-2/HT-29 cells in the LPS(-) group had good cell membrane connectivity at 24, 36, and 48 h. In contrast, the connection of the cell membrane for LPS stimulation was damaged in the LPS(+) group at 24, 36, and 48 h. Taken together, these results indicate that mucin secretion and occludin expression in Caco-2/HT29 (3:1) co-culture cells markedly increased in the LPS(-) and LPS(+) groups after 24 h of LPS stimulation.

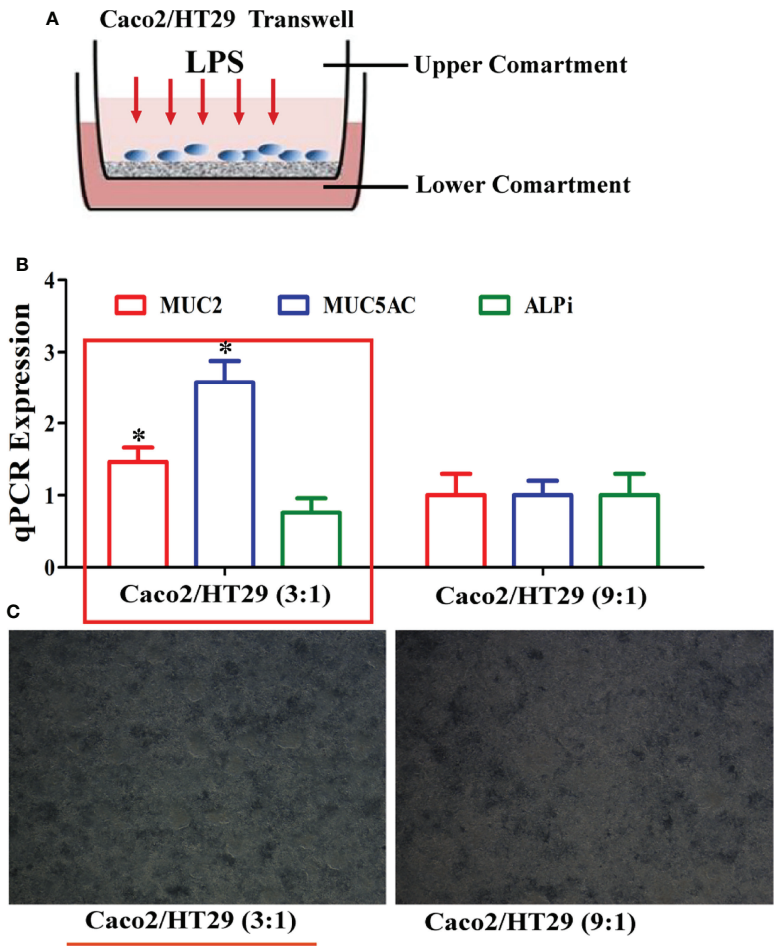

FIGURE 1 | Establishment of the Caco2/HT-29 cell co-culture model. **(A)**, Transwell of the Caco-2/HT-29 co-culture cell model; **(B)**, MUC2, MUC5AC, and ALPi mRNA expression of the Caco-2/HT-29 co-culture cell at two cell seeding ratios (N=6); **(C)**, Image of the Caco-2/HT-29 co-culture cell at two cell seeding ratios (×200).* Statistical difference between co-culture Caco2/HT-29 cells (3:1) compare to co-culture Caco2/HT-29 cells (9:1) for the same factor (P<0.05).

RNA Interference for MUC2 Gene Silencing in Caco-2/HT-29 (3:1) Co-Culture Cell

To understand the function of the mucus layer, we used RNA interference (RNAi) to silence the *MUC2* gene (the main component of the mucus layer) in Caco-2/HT-29 (3:1) co-cultured cells. First, we evaluated MUC2 mRNA and protein expression using qPCR and ELISA, respectively. After 15 days of Caco-2/HT-29 (3:1) co-culture differentiation, cells were stimulated with LPS(LPS+) or 0.0 1M PBS (LPS-) at 24, 36, 48, and 60 h. The expression levels of MUC2 mRNA and protein in the LPS(+) and LPS(-) groups were higher at 24 h than at other time points. Therefore, Caco-2/HT-29 (3:1) co-culture cells were transfected with siRNA MUC2 constructs using Lipofectamine ™ 2000 **before** stimulation with LPS for 24 h (**Figures 3A, B**). MUC2 mRNA expression was significantly decreased after transfection with MUC2 siRNA. A green fluorescent negative control was used to determine the transfection efficiency (**Figures 3C, D**). These combined results indicate the significant increase in MUC2 mRNA expression after transfection with siRNA and LPS stimulation for 24 h. All co-cultured cells were divided into three groups, namely LPS (-), LPS (+), and siMUC2 +LPS(+) in the following test.

Analysis of the Different Genes and KEGG Enrichment Pathways for the LPS (-), LPS (+), and siMUC2 +LPS(+) Groups by RNA-seq

To provide insights into how the regulatory mechanism of LPS affects the mucus layer, the different genes and KEGG enrichment pathways in the LPS (-), LPS (+), and siMUC2 +LPS(+) groups were analyzed using RNA-seq techniques. A total of 1,161 upregulated genes and 1,379 differentially expressed genes were found in the LPS (+) and siMUC2 +LPS(+) groups. Further, 1,417 and 1,904 genes were upregulated and downregulated, respectively, in the LPS (-) vs. siMUC2 +LPS(+) group, and 71 different genes were upregulated and 82 genes were downregulated in the LPS (-) vs. LPS(+) group (**Figure 4A**). A total of 1,953

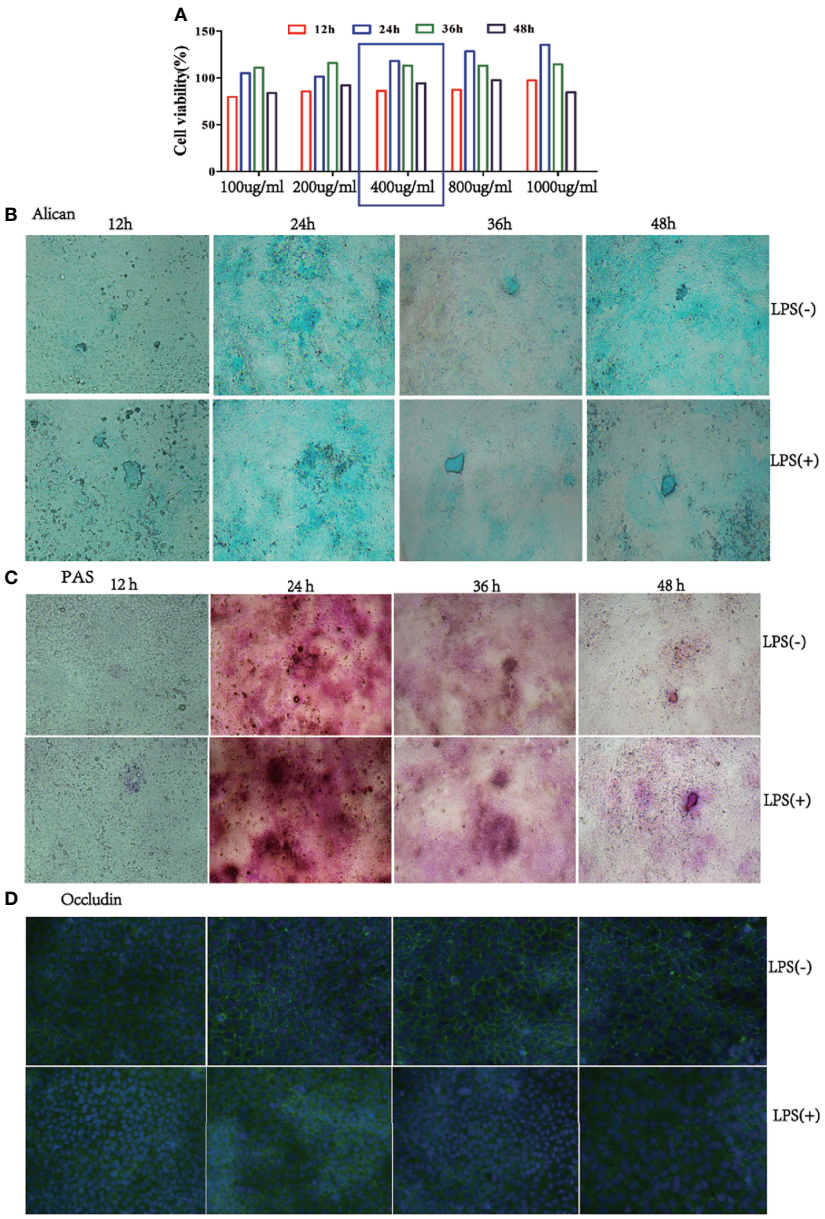

FIGURE 2 | Mucus expression in the co-culture model at a 3:1 ratio of Caco-2/HT-29 cells. **(A)**, Viability of the Caco-2/HT-29 co-culture cell (3:1) was determined using CCK-8 after stimulation with 100, 200, 400, 800, and 1000 μg/mL LPS for 12 h, 24 h, 36 h, and 48 h (N=6); **(B)**, Alcian Blue staining of Caco-2 and HT-29 co-culture cell stimulated with LPS for 12 h, 24 h, 36 h, and 48 h. Blue areas indicate mucus deposition (Nikon Plan 10× objective lens); **(C)**, Periodic Acid-Schiff staining (PAS) on Caco-2/HT-29 co-culture cell stimulated with LPS for 12 h, 24 h, 36 h, and 48 h. Fuchsia areas indicate mucus deposition (Nikon Plan 10× objective lens); **(D)**, Occludin expression of Caco-2/HT-29 co-culture cell was analyzed by immunofluorescence. The green color represents the occludin expression of Caco-2 and HT-29 co-culture cells; blue color indicates the nucleus of Caco-2/HT-29 co-culture cell (×100).

differentially expressed genes were found between the LPS (-) vs siMUC2+LPS group and LPS (+) vs siMUC2 +LPS group (**Figure 4B**). The first 20 signaling pathways were measured by KEGG enrichment analysis between the LPS (-) vs. siMUC2+LPS (+) group and LPS (+) vs. siMUC2+LPS group (**Figure 4C**). The cell extracellular matrix (ECM) receptor interaction and focal adhesion signaling pathways were used to further study the mechanism of mucus layer function.

Expression of Different Genes in ECM-Receptor Interaction and the Focal Adhesion Signal Pathway and Intercellular Linker

To understand the different genes involved in ECM-receptor interactions and the focal adhesion pathway, we measured the mRNA expression of these factors in the LPS (+) and siMUC2 +LPS(+) groups using qPCR. After 15 days of Caco-2/HT-29

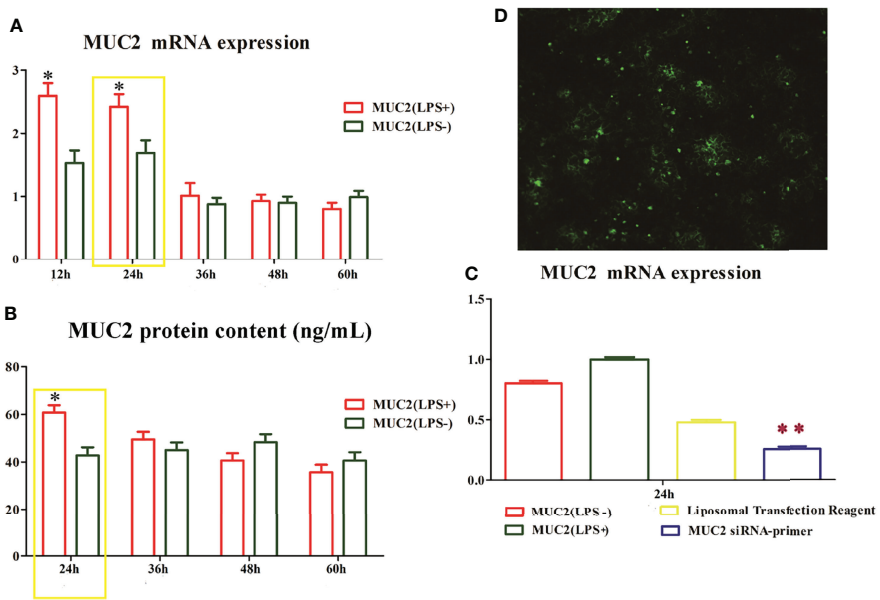

FIGURE 3 | The time and dose screen of small RNA interference. **(A)**, MUC2 mRNA expression in Caco-2/HT-29 co-culture cells after LPS stimulation for 12 h, 24 h, 36 h, 48 h, and 60 h; The highest level of MUC2 mRNA expression in Caco-2/HT-29 co-culture cells is observed at 24 h after LPS stimulation (N=6); **(B)**, MUC2 protein content in the supernatant of Caco-2/HT-29 co-culture cells after LPS stimulation for 24 h, 36 h, 48 h, and 60 h (N=6); the highest level of MUC2 protein content in Caco-2/HT-29 co-culture cells is observed at 24 h after LPS stimulation; * Statistical difference between co-culture Caco2/HT-29 cells in the LPS(+) compare to LPS(-) groups for the same time (P<0.05); **(C)**, After LPS stimulation for 24 h, the Caco-2/HT-29 co-culture cells were transfected with 50 nM MUC2 siRNA or 50 nM negative control siRNA (siNC) using Liposomal Transfection Reagent. The MUC2 mRNA expression of MUC2 siRNA group was significantly decreased compare with that of the MUC2(LPS+) and MUC2(LPS-) groups (N=6); ** Statistical difference between co-culture Caco2/HT-29 cells in the MUC2 siRNA-primer compare to LPS(+) and LPS(-) groups (P <0.01); **(D),** Small interfering RNA transfection rate, the green point indicates positive signal of MUC2 small interfering RNA transfection.

(3:1) co-culture differentiation, the cells were stimulated with LPS for 24 h, and total RNA was extracted from cells in the LPS (+) and siMUC2+LPS(+) groups. The mRNA expression levels of Claudin-1, ZO-1, JAMA, Desmosome, Occludin, and E-cadherin were significantly increased in the LPS (+) group compared with the siMUC2 +LPS group (P<0.05). Further, the mRNA expression levels of FN1, ITGAV, COL6A2, LAMC1, LAMA5, LAMB2, AGRN, ROCK1, ITGB2, ITGB4, ACTB-P1, CD44, ARHGAP5, HSPG2, DAG1, and SRC were significantly increased in the LPS (+) group, compared with siMUC2 +LPS(+) group (P<0.05). There was no difference in the mRNA expression of ITGB3, ROCK2, and RhoA between the LPS (+) group and siMUC2 +LPS(+) group (P>0.05) (**Figure 5**).

DISCUSSION

The combination of Caco2/HT-29 cells is an already-described *in vitro* epithelial barrier model in the real environment of the human intestine, and has been proposed as a predictive tool to evaluate the permeability of endotoxins (16–18). In this study, we employed the co-culture model and identified that 3:1 (Caco-2: HT-29) was the optimal ratio for cell seeding compared to 9:1 (Caco-2:HT-29) after 15 days of Caco-2/HT-29 co-culture. The use of a wide set of gene markers (MUC5AC and ALPi) was also found to be appropriate for evaluating the integrity of the co-culture cell model. The mRNA expression of MUC2 corresponded to the *in vivo* human colonic epithelium after 15 days of Caco-2/HT-29 co-culture. Herein, 400 μg/mL LPS was selected to stimulate co-cultured cells for 12 h, 24 h, 36 h, and 48 h.

To choose a time that will ensure that Caco-2 and HT-29 cells have a well-established mucus shed, Alcian Blue and PAS staining was performed on the co-cultured cells. Mucin secretion was identified to be the highest in the LPS(+) and LPS(-) group after 24 h. Further, confocal microscopy was verified as a powerful tool for visualizing the tight junctions of cells in these barriers. After 15 days of Caco-2/HT-29 co-culture, the tight junction function of co-culture cells in the LPS(-) group was found to be better after 24 h of PBS stimulation; however, the tight junction function of co-culture cells in the LPS(+) group was damaged by LPS stimulation for 24 h. Additionally, the mRNA and protein expression levels of MUC2 were the highest following LPS stimulation for 24 h relative to the other times investigated. Taken together, after 15 days of Caco-2/HT-29 co-culture, the highest value of MUC2 secretion was obtained 24 h after LPS stimulation.

Based on the above results, we opted to silence the MUC2 gene in the co-culture cells *via* small interfering RNA transfection for LPS stimulation at 24 h after 15 days of Caco-2/HT-29 co-culture.

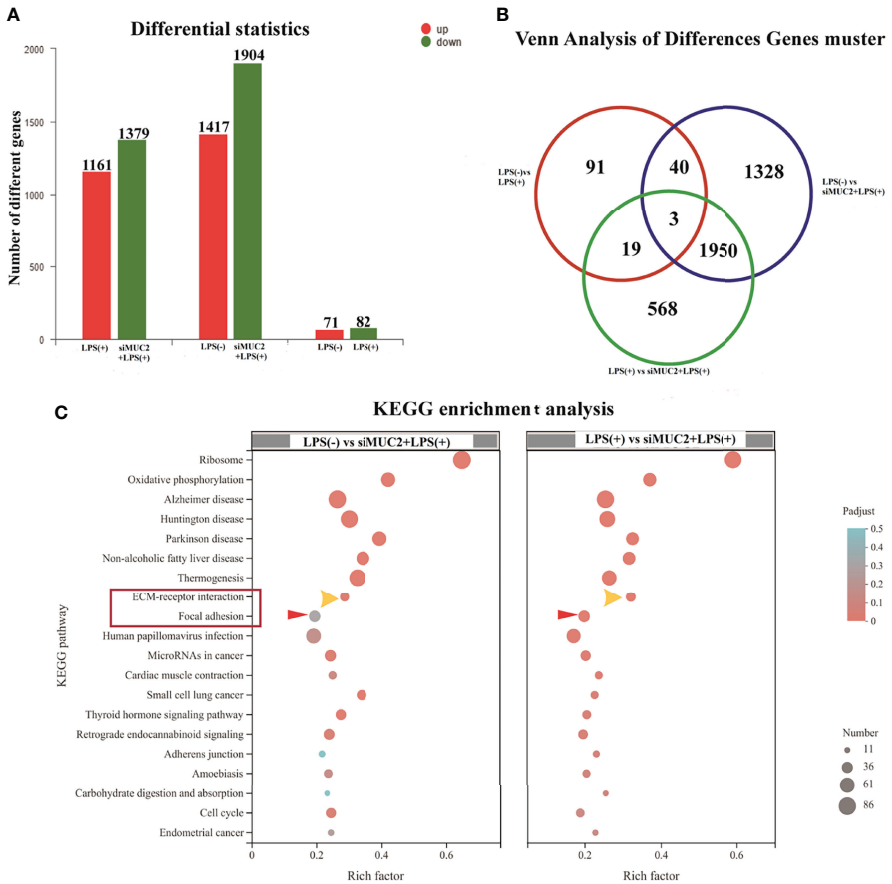

FIGURE 4 | RNA-seq of the LPS(+) group, LPS(-) group, and siMUC2+LPS(+) group. **(A),** the number of different genes in the LPS(+) vs siMUC2+LPS(+) group, LPS(-) vs siMUC2+LPS(+) group, and LPS(-) vs LPS(+) group; red color indicated upregulated gene and blue color indicates downregulated gene (N=6); **(B)**, Venn analysis of different gene clusters in the LPS(+) vs siMUC2+LPS(+) group, LPS(-) vs siMUC2+LPS(+) group, and LPS(-) vs LPS(+) group; Three genes were found between the LPS(+) vs siMUC2+LPS(+) group, LPS(-) vs siMUC2+LPS(+) group, and LPS(-) vs LPS(+) group; 43 genes were found between the LPS(-) vs siMUC2 +LPS(+) group and LPS(-) vs LPS(+) group; 22 genes were found between the LPS(-) vs LPS(+) group and LPS(+) vs siMUC2+LPS(+) group; and 1,953 genes were found between the LPS(+) vs siMUC2+LPS(+) group and LPS(-) vs siMUC2+LPS(+) group (N=6); **(C),** KEGG enrichment analysis of the LPS(+) vs siMUC2+LPS(+) group (right column) and LPS(-) vs siMUC2+LPS(+) group (left column); the first 20 signaling pathways with differentially expressed genes are listed in the figure.

MUC2 mRNA expression was significantly inhibited. Therefore, the co-cultured cells were divided into three groups (LPS(+), LPS(-), and LPS(+)+siMUC2 groups) for the subsequent experiment. The usefulness of RNA-seq to demonstrate the effect of LPS on the mucus layer in an *in vitro* intestinal model was evaluated. A total of 1,161 upregulated genes and 1,379 downregulated genes were found in the LPS(+) vs. LPS(+)+siMUC2 group; 1,417 upregulated genes and 1,904 downregulated genes were found in the LPS(-) vs. LPS(+) +siMUC2 group; and 71 upregulated genes and 82 downregulated genes were found in the LPS(+) vs. LPS(-) group. LPS stimulation for 24 h led to very few differential genes that had an impact on the integrity of the mucus barrier of Caco-2/HT-29 co-culture cells. Further, LPS did not disrupt the mucus barrier to penetrate the epithelial cells. Nonetheless, significant changes in a large number of genes were found in the LPS(-) and LPS(+) groups when the MUC2 gene was silenced by LPS stimulation for 24 h. The intestinal mucus layer may primarily act as a barrier that protects epithelial cells from LPS stimulation (19–22).

From top to bottom, the complete intestinal mucosal barrier is composed of the mucus layer, epithelial cell layer, and muscle layer (23–25). Further, the mucins of the mucus layer are fused with water and digestive juice in the intestinal tract, which together form the first barrier of intestinal mucosa against pathogenic microbial and toxic substances (26). Both the junctional network and the mucous layer protect the integrity of the intestinal epithelium (27). The intestinal mucus layer is a mechanical barrier comprising intestinal epithelial cells and various intercellular connections (28). Intestinal epithelial integrity is dependent on the organization of cell-cell adhesion and cell matrix adhesion complexes, including occluding junctions, anchoring junctions, and communication junctions (29). The most important way of occluding junctions is tight junctions (TJs), which include claudins and occludins, which interact with each other on their extracellular sides to promote junction assembly (30). In this study, the mRNA expression levels of claudins, JAMA, E-cadherin, and occludin were

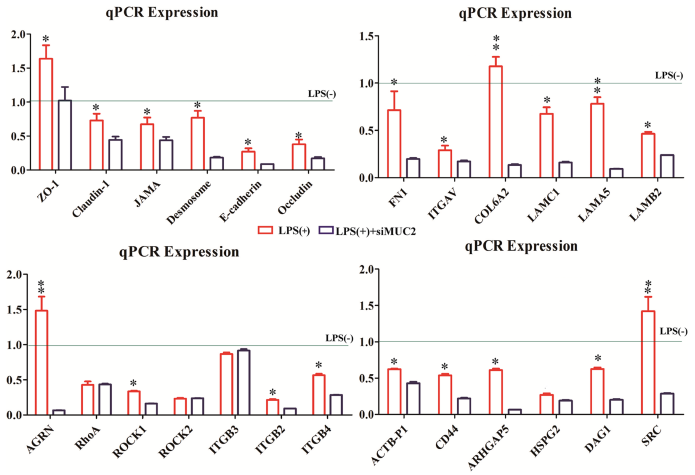

FIGURE 5 | The expression of different genes in the LPS(+), LPS(+)+siMUC2, and LPS(-) groups.Statistical analyses were performed using the Statistical Package for Social Sciences (SPSS, USA) software, and a two-pair test followed by Student's t-test was performed to determine statistical significance between means (N=6). The relative expression levels of the target genes were calculated using the $2^{-\Delta\Delta CT}$ method. The factors mRNA expression of LPS(-) group are "1" (gray line).* Statistical difference between co-culture Caco2/HT-29 cells in the LPS(+) and LPS(+)+siMUC2 groups for the same factors (P<0.05). ** Statistical difference between co-culture Caco2/HT-29 cells in the LPS(+) and LPS(+)+siMUC2 groups for the same factors (P <0.01).

significantly increased in the LPS(+) group compared to the LPS (+) +siMUC2 group. E-cadherin is the most essential cadherin present on the epithelial surface and is responsible for the formation of adhesion junctions. E-cadherin hinges on the neighboring cell through another E-cadherin. *via* Based on our results, LPS disrupts the tight junctions and penetration barriers in epithelial cells after MUC2 gene silencing in co-culture cells (**Figure 6A**).

LPS acts on the anchoring junction, which mainly connects with intermediate fibers such as desmosomes and hemidesmosomes, through tight junctions (31–33). Further, the anchoring junction connected with actin fibers mainly includes focal adhesion and adhesion belts.In this study, desmosome mRNA expression was significantly higher in the LPS(+) group than in the LPS(+) +siMUC2 group. Using the differential gene lists, focal adhesion and ECM-receptor interaction were identified as the two most significantly implicated pathways by KEGG analysis. Cell-ECM interactions are crucial for cell survival and normal cellular functions, such as cell adhesion, spreading, and migration, and regulate the establishment and maintenance of development and homeostasis (34). ECM is a complex network structure composed of cell synthesis and biomacromolecules on the cell surface or between cells. As the ECM-receptor interactions play a critical role in focal adhesion, genes related to ECM-mediated focal adhesion are of particular interest as potential transcriptomic markers of the intestinal mucus layer (35). In addition to controlling cell movement and migration, focal adhesions physically adhere to the external environment by attaching themselves to the ECM (36). In our study, gene expression related to ECM-mediated focal adhesion was mixed, and adhesion glycoproteins (THBS1), fibronectin (FN1), and other ECM molecules can directly and indirectly bind to cell surface receptors. The ECM, through cell surface receptors, transmits extracellular to intracellular signals, which together affect cell function. Integrins are the main receptors for ECM proteins. Integrins (ITGAV, ITGB3,4 and ITGA2) of cell surface receptors are used as "bridges" to connect ECM, and the intracellular cytoskeleton formed an organic body, mediating intracellular signal transduction (37). In our experiment, the expression levels of THBS, IBSP, and FN1 were downregulated in the LPS(+)+siMUC2 group compared to the LPS(+) group. they are high affinity ligand for ITGB4, ITGAV, ITGA2 of cell membrane, were found to be downregulated in the co-culture cell. Integrins can activate SRC kinase; however, SRC expression in the LPS(+)+siMUC2 group was downregulated compared with that in the LPS(+)group, and was inhibited downstream of the ECM-mediated focal adhesion pathway. SRC is specifically phosphorylated and inhibited by ARHGAP5 and RhoA expression (38). Coiled-coil-forming protein kinase (ROCK1,2) downstream of RhoA is well known for its inability to regulate the stability of filamentous actin (ACTB-G1) in the LPS(+) +siMUC2 group compared to the LPS(+) group (**Figure 6B**). Actin provides mechanical support to cells and a transport pathway through the cytoplasm to assist with the rapid assembly and disassembly of the signal transduction actin network, enabling cell migration. Cells connect the ECM network to the intracellular actin microfilament skeleton through integrin-mediated focal adhesion structures (39). The extracellular mechanical force activates SRC kinase through focal adhesions and promotes further maturation of the focal adhesion structure. Further, the intracellular mechanical force generated by actin contraction is transmitted to the focal adhesion through adaptor proteins. Actin contraction drives the movement of integrins along the microfilament cytoskeleton, from focal adhesions at the cell edge to fibrillar adhesions in the middle

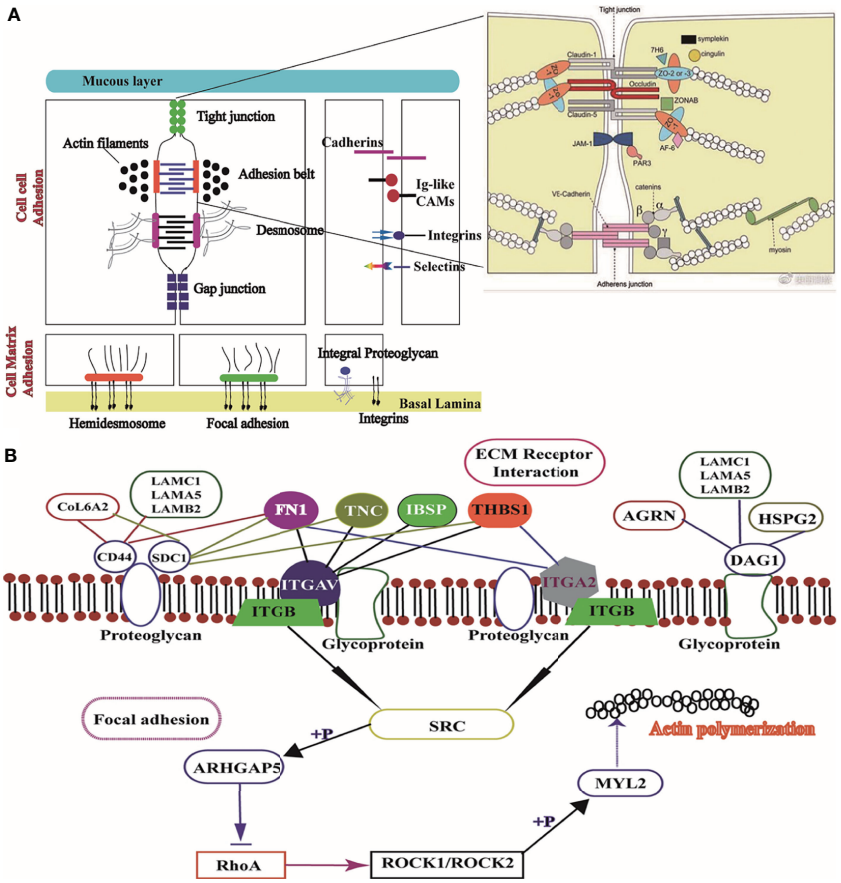

FIGURE 6 | Image of ECM receptor interaction and the focal adhesion signaling pathway. **(A),** Structure of the mucus layer, cell-cell adhesion, and cell-matrix adhesion of intestinal epithelial cells; **(B)**, Interaction mechanism of the difference factor for ECM receptor interaction and the focal adhesion signaling pathway.

of the cell body (40). According to our results, when only the ECM integrin-mediated focal adhesion-action is connected, integrins play a role in signal transduction. When the connection between the adaptor protein and actin is disrupted, integrin slides on the surface of the cell membrane without signal transmission.

This study also sought to elucidate the usefulness of KEGG to demonstrate the impact of LAMB2, COL6A2, and FN1 downregulation on ECM binding to CD44 of proteoglycan receptor on the cell membrane. The downregulation of CD44 in the LPS(+)+siMUC2 group was found to inhibit the proteoglycan of the cell membrane. The ECM membrane receptor, CD44, can integrate ECM signals and regulate cell adhesion, migration, and proliferation (31). LAMB2 and AGRN bind to DAG1 and promote glycoprotein secretion by the cell membrane (40). However, when the MUC2 gene was silenced in the co-culture cells, the decrease in glycoprotein secretion of the ECM due to LAMB2, AGRN, and DAG1 mRNA expression was reduced (**Figure 6B**). Transmembrane-linked glycoproteins of mesenchymal cells, which are linked to attachment proteins in the intracellular portion, interact with transmembrane-linked glycoproteins of adjacent cells or the ECM in the extracellular portion (41). Cell surface glycoproteins are membrane surface glycoproteins that mediate adhesion between cells, and between cells and the ECM (39). These glycoproteins influence the spatial organization and function of the transmembrane receptors. A small amount of glycoproteins and proteoglycan inhibited the adhesion of integrins and altered the integrin state by applying tension to matrix-bound integrins, independent of actomyosin contractility (41).

CONCLUSION

In summary, in addition to the data that enabled the establishment of the proposed Caco-2/HT-29 model, we defend its use as a powerful tool for evaluating the intestinal mucus barrier. LPS (400 μg/mL) was found to disrupt the regulatory mechanism of the ECM-mediated focal adhesion signaling pathway under MUC2 gene silencing in co-cultured cells after 24 h of LPS stimulation. When the mucus layer is not intact, LPS first damages the tight junctions of epithelial cells, regulates the integrin of cell surface receptors through the ECM transmitted to downstream signals, and inhibits the integrin-

mediated focal adhesion structure, further damaging the ECM network structure and intracellular actin microfilament skeleton. Ultimately, LPS inhibits the interaction between the ECM and cytoskeleton. By combining these data, the protective function of the mucus barrier is expected to be well characterized in the future.

DATA AVAILABILITY STATEMENT

The original contributions presented in the study are included in the article/supplementary material. Further inquiries can be directed to the corresponding author.

AUTHOR CONTRIBUTIONS

CW and PF conceived and designed the experiments. WH, MZ, YL and ShuW performed the experiments. WH and TT analyzed the data and wrote the manuscript. All authors contributed to the article and approved the submitted version.

FUNDING

This study was supported by the Shaanxi province Key research projects (2020NY-020) and the National Natural Science Foundation of Shaanxi (K4030220016).

REFERENCES

1. Radicioni G, Cao R, Carpenter J, Ford AA, Wang TT, Li Y, et al. The Innate Immune Properties of Airway Mucosalsurfaces are Regulated by Dynamic Interactions Between Mucins and Interacting Proteins: The Mucin Interactome. *Mucosal Immunol* (2016) 9:1442–54. doi: 10.1038/mi.2016.27
2. Kesimer M, Ehre C, Burns KA, Davis CW, Sheehan JK, Pickles RJ. Molecular Organization of the Mucins and Glycocalyx Underlying Mucus Transport Over Mucosal Surfaces of the Airways. *Mucosal Immunol* (2013) 6:379–92. doi: 10.1038/mi.2012.81
3. Ridley C, Kouvatsos N, Raynal BD, Howard M, Thornton DJ. Assembly of the Respiratory Mucin MUC5B: A New Model for a Gel-Forming Mucin. *J Biol Chem* (2014) 289:16409–20. doi: 10.1074/jbc.M114.566679
4. Schneider H, Pelaseyed T, Svensson F, Johansson MEV. Study of Mucin Turnover in the Small Intestine by *In Vivo* Labeling. *Sci Rep* (2018) 8:5760. doi: 10.1038/s41598-018-24148-x
5. Rodriguez-Pineiro AM, Bergstrom JH, Ermund A, Gustafsson JK, Schiitte A, Johansson MEV, et al. Studies of Mucus in Mouse Stomach, Small Intestine, and Colon. II. Gastrointestinal Mucus Proteome Reveals Muc2 and Muc5ac Accompanied by a Set of Core Proteins. *Am J Physiol Gastrointest Liver Physiol* (2013) 305:G348–56. doi: 10.1152/ajpgi.00047.2013
6. Schneider H, Pelaseyed T, Svensson F, Johansson MEV. Three-Dimensional Intestinal Villi Epithelium Enhances Protection of Human Intestinal Cells From Bacterial Infection by Inducing Mucin Expression. *Integr Biol (Camb)* (2014) 6:1122–31. doi: 10.1016/j.jcf.2004.05.012
7. Johansson ME, Denning PW. Fast renewal of the distal colonic mucus layers by the surface goblet cells as measured by *in vivo* labeling of mucin glycoproteins. *PloS One* (2012) 7:e41009. doi: 10.1371/journal.pone.0041009
8. Li H, Limenitakis JP, Fuhrer T, Geuking MB, Lawson MA, Wyss M, et al. The Outer Mucus Layer Hosts a Distinct Intestinal Microbial Niche. *Nat Commun* (2015) 6:1038 –45. doi: 10.1038/ncomms9292
9. Jakobsson HE, Rodríguez-Piñeiro AM, Schütte A, Ermund A, Boysen P, Bemark M, et al. The Composition of the Gut Microbiota Shapes the Colon Mucus Barrier. *EMBO Rep* (2015) 16:164–77. doi: 10.15252/embr.201439263
10. Johansson ME. Fast Renewal of the Distal Colonic Mucus Layers by the Surface Goblet Cells as Measured by *In Vivo* Labeling of Mucin Glycoproteins. *PloS One* (2012) 7:e41009. doi: 10.1371/journal.pone.0041009
11. Schroeder BO. Fight Them or Feed Them: How the Intestinal Mucus Layer Manages the Gut Microbiota. *Gastroenterol Rep* (2019) 7(1):3–12. doi: 10.1093/gastro/goy052
12. Swidsinski A, Loening-Baucke V, Theissig F, Engelhardt H, Bengmark S, Koch S, et al. Comparative Study of the Intestinal Mucus Barrier in Normal and Inflamed Colon. *Gut* (2007) 56:343–50. doi: 10.15252/embr.201439263
13. Johansson MEV, Hansson GC. Immunological Aspects of Intestinal Mucus and Mucins. *Nat Rev Immunol* (2016) 16:639–49. doi: 10.1038/nri.2016.88
14. Puqiao L, Saskia B, Soheil V, Harry J W, Gert F. Hypoxia and Heat Stress Affect Epithelial Integrity in a Caco-2/HT-29 Co-Culture. *Sci Rep* (2021) 11:131–6. doi: 10.1038/s41598-021-92574-5
15. García-Rodrígueza A, Vilaa L, Cortésa C, Hernándeza A, Marcos R. Exploring the Usefulness of the Complex *In Vitro* Intestinal Epithelial Model Caco-2/HT29/Raji-B in Nanotoxicology. *Food Chem Toxicol* (2018) 113:162–70. doi: 10.1016/j.fct.2018.01.042
16. Ferraretto A, Bottani M, De Luca1 P, Cornaghi L, Arnaboldi F, Maggioni M, et al. Morphofunctional Properties of a Differentiated Caco2/HT-29 Co-Culture as an *In Vitro* Model of Human Intestinal Epithelium. *Biosci Rep* (2018) 38:147–50. doi: 10.1042/BSR20171497
17. Antunes F, Andrade F, Araújo F, Ferreira D, Sarmento B. Establishment of a Triple Co-Culture *In Vitro* Cell Models to Study Intestinal Absorption of Peptide Drugs. *Eur J Pharm Biopharm* (2013) 83:427–35. doi: 10.1016/j.ejpb.2012.10.003
18. Imai S, Morishita Y, Hata T, Kondoh M, Yagi K, Gao JQ, et al. Cellular Internalization, Transcellular Transport, and Cellular Effects of Silver Nanoparticles in Polarized Caco-2 Cells Following Apical or Basolateral Exposure. *Biochem Biophys Res Commun* (2017) 484:543–9. doi: 10.1016/j.bbrc.2017.01.114
19. Lozoya-Agullo I, Araújo F, González-Álvarez I, Merino-Sanjuán M, González-Álvarez M, Bermejo M, et al. Usefulness of Caco-2/HT29-MTX and Caco-2/HT29-MTX/Raji B Coculture Models to Predict Intestinal and Colonic Permeability Compared to Caco-2 Monoculture. *Mol Pharm* (2017) 14:1264–70. doi: 10.1021/acs.molpharmaceut.6b01165
20. Mahler GJ, Shuler ML, Glahn RP. Characterization of Caco-2 and HT29-MTX Co-Cultures in an *In Vitro* Digestion/Cell Culture Model Used to Predict Iron Bioavailability. *J Nutr Biochem* (2009) 20:494–502. doi: 10.1016/j.jnutbio.2008.05.006
21. Xin H, Gao Y, Li S, Wu C, Wang J. Modulation of Mucin (MUC2, MUC5AC and MUC5B) mRNA Expression and Protein Production and Secretion in Caco-2/HT29-MTX Co-Cultures Following Exposure to Individual and Combined Afatoxin M1 and Ochratoxin A. *Toxins* (2019) 11:132. doi: 10.3390/toxins11020132
22. Corfield AP. The Interaction of the Gut Microbiota With the Mucus Barrier in Health and Disease in Human. *Microorganisms* (2018) 6:78. doi: 10.3390/microorganisms6030078
23. Ottman N, Davids M, Suarez-Diez M, Boeren S, Schaap PJ, Martins VAP, et al. Genome-Scale Model and Omics Analysis of Metabolic Capacities of Akkermansia Muciniphila Reveal a Preferential Mucin-Degrading Lifestyle. *Appl Environ Microbiol* (2017) 83:e01014-17. doi: 10.1128/aem.01014-17
24. Yan Y, Meng F, Wei Y, Zhang H, Zhao W, Pei Z, et al. Research Progress on Intestinal Tight Junction. *Chin J Anim Sci* (2022) 58:01–10. doi: 10.1080/17450390512331342377
25. Boivin MA, Ye D, Kennedy JC, Alsadi R, Shepela C, Ma TY. Mechanism of Glucocorticoid Regulation of the Intestinal Tight Junction Barrier. *Am J Physiol Gastrointest Liver Physiol* (2007) 292:G590–8. doi: 10.1152/ajpgi.00252.2006
26. Van Itallie CM, Anderson JM. Architecture of Tight Junctions and Principles of Molecular Composition. *Semin Cell Dev Biol* (2014) 36:157–65. doi: 10.1046/j.1523-1747.2002.01774.x
27. Tsukita S, Tanaka H, Tamura A. The Claudins: From Tight Junctions to Biological Systems. *Trends Biochem Sci* (2019) 44(2):141–52. doi: 10.1016/j.tibs.2018.09.008
28. Van Itallie CM, Anderson JM. Claudin Interactions in and Out of the Tight Junction. *Tissue Barriers* (2013) 1(3):e25247. doi: 10.1152/ajplung.00182.2003

29. Basler K, Brandner JM. Tight Junctions in Skin Inflammation. *Pflugers Arch* (2017) 469(1):3–14. doi: 10.1007/s00424-016-1903-9
30. Curry SM, Schwartz KJ, Yoon KJ, Gabler NK, Burrough ER. Effects of Porcine Epidemic Diarrhea Virus Infection on Tight Junction Protein Gene Expression and Morphology of the Intestinal Mucosa in Pigs. *Pol J Vet Sci* (2019) 22(2):345–53. doi: 10.1016/j.vetmic.2017.09.021
31. Wu Y, Ge G. Progress of Extracellular Matrix. *Chin J Cell Biol* (2019) 41 (3):415–22. doi: 10.1038/jid.1989.34
32. Liu X-S, Luo H-J, Yang H, Wang L, Kong H, Jin Y-E, et al. Palladin Regulates Cell and Extracellular Matrix Interaction Through Maintaining Normal Actin Cytoskeleton Architecture and Stabilizing Beta1-Integrin. *J Cell Biochem* (2007) 100:1288–300. doi: 10.1002/jcb.21126
33. Brakebusch C, Hirsch E, Potocnik A, Fassler R. Genetic Analysis of Beta1 Integrin Function: Confirmed, New and Revised Roles for a Crucial Family of Cell Adhesion Molecules. *J Cell Sci* (1997) 110:2895–904. doi: 10.1242/jcs.110.23.2895
34. Calderwood DA. Integrin Activation. *J Cell Sci* (2004) 117:657–66. doi: 10.1042/BST0360229
35. Stamper BD, Park SS, Beyer RP, Bammler TK, Farin FM, Mecham B, et al. Differential Expression of Extracellular Matrix-Mediated Pathways in Single-Suture Craniosynostosis. *PloS One* (2011) 6:e26557. doi: 10.1371/journal.pone.0026557
36. Zhong-Gui G, Yuan Z, Zhen-Yong W, Rui-Feng F, Zong-Ping L, Lin W. Epigenetic Regulator BRD4 is Involved in Cadmium-Induced Acute Kidney Injury *via* Contributing to Lysosomal Dysfunction, Autophagy Blockade and Oxidative Stress. *J Hazard Mater* (2022) 423:127–40. doi: 10.1016/j.jhazmat.2021.127110
37. Geiger B, Bershadsky A, Pankov R, Yamada KM. Transmembrane Crosstalk Between the Extracellular Matrix–Cytoskeleton Crosstalk. *Nat Rev Mol Cell Biol* (2001) 2:793–805. doi: 10.1038/35099066
38. Liu J-B, Li Z-F, Lu L, Wang Z-Y, Wang L. Glyphosate Damages Blood-Testis Barrier *via* NOX1-Triggered Oxidative Stress in Rats: Long-Term Exposure as a Potential Risk for Male Reproductive Health. *Environ Int* (2022) 159:107–38. doi: 10.1016/j.envint.2021.107038
39. Paszek MJ, DuFort CC, Rossier O, Bainer R, Mouw JK, Godula K, et al. The Cancer Glycocalyx Mechanically Primes Integrin-Mediated Growth and Survival. *Nature* (2014) 511(7509):319–25. doi: 10.1038/nature13535
40. Lakins JN, Chin AR, Weaver VM. Exploring the Link Between Human Embryonic Stem Cell Organization and Fate Using Tension-Calibrated Extracellular Matrix Functionalized Polyacrylamide Gels. *Methods Mol Biol* (2012) 916:317–50. doi: 10.1007/978-1-61779-980-8_24
41. Grashoff C, Hoffman BD, Brenner MD, Zhou R, Parsons M, Yang MT, et al. Measuring Mechanical Tension Across Vinculin Reveals Regulation of Focal Adhesion Dynamics. *Nature* (2010) 466(7303):263–6. doi: 10.1038/nature09198

Conflict of Interest: The authors declare that the research was conducted in the absence of any commercial or financial relationships that could be construed as a potential conflict of interest.

Publisher's Note: All claims expressed in this article are solely those of the authors and do not necessarily represent those of their affiliated organizations, or those of the publisher, the editors and the reviewers. Any product that may be evaluated in this article, or claim that may be made by its manufacturer, is not guaranteed or endorsed by the publisher.

frontiers | Frontiers in Immunology

ORIGINAL RESEARCH
published: 30 June 2022
doi: 10.3389/fimmu.2022.934084

Effect of *Platycodon grandiflorus* Polysaccharide on M1 Polarization Induced by Autophagy Degradation of SOCS1/2 Proteins in 3D4/21 Cells

Liping Li[1,2†], *Xufang Chen*[1†], *Meiyun Lv*[1], *Ziqiang Cheng*[1], *Fang Liu*[1], *Ying Wang*[1], *Aiqin Zhou*[1], *Jianzhu Liu*[3*] and *Xiaona Zhao*[1*]

[1] College of Veterinary Medicine, Shandong Agricultural University, Tai'an, China, [2] Qingdao Animal Disease Prevention and Control Center,Qingdao Municipal Bureau of Agriculture and Rural Affairs, Qingdao, China, [3] Research Center for Animal Disease Control Engineering, Shandong Agricultural University, Tai'an, China

M1-polarized macrophages can improve the body's immune function. This study aimed to explore the mechanism of *Platycodon grandiflorus* polysaccharide ($PGPS_t$) degrading SOCS1/2 protein through autophagy and promoting M1 polarization in 3D4/21 cells. Immunoprecipitation, confocal laser scanning microscopy, flow cytometry, and intracellular co-localization were used to detect the expression of related phenotypic proteins and cytokines in M1-polarized cells. The results showed that $PGPS_t$ significantly promoted the mRNA expression of IL-6, IL-12, and TNF-α and enhanced the protein expression of IL-6, IL-12, TNF-α, IL-1β, iNOS, CD80, and CD86, indicating that $PGPS_t$ promoted M1 polarization in 3D4/21 cells. Next, the effect of the $PGPS_t$ autophagy degradation of SOCS1/2 on the M1 polarization of 3D4/21 cells was detected. The results showed that $PGPS_t$ significantly downregulated the expression level of SOCS1/2 protein, but had no obvious effect on the mRNA expression level of SOCS1/2, indicating that $PGPS_t$ degraded SOCS1/2 protein by activating the lysosome system. Further research found that under the action of 3-MA and BafA1, $PGPS_t$ upregulated LC3B II and downregulated SOCS1/2 protein expression, which increased the possibility of LC3B, the key component of autophagy, bridging this connection and degrading SOCS1/2. The interaction between SOCS1/2 and LC3 was identified by indirect immunofluorescence and Co-IP. The results showed that the co-localization percentage of the two proteins increased significantly after $PGPS_t$ treatment, and LC3 interacted with SOCS1 and SOCS2. This provides a theoretical basis for the application of $PGPS_t$ in the treatment or improvement of diseases related to macrophage polarization by regulating the autophagy level.

Keywords: ***Platycodon grandiflorus*** **polysaccharide, 3D4/21 cells, autophagy degradation, SOCS1/2 proteins, M1 polarization**

OPEN ACCESS

Edited by:
Mengyao Guo,
Northeast Agricultural University, China

Reviewed by:
Yi Wu,
Nanjing Agricultural University, China
Ranran Hou,
Qingdao Agricultural University, China
Tao Qin,
Fujian Agriculture and Forestry University, China
Mi Wang,
Chinese Academy of Agricultural Sciences, China

***Correspondence:**
Xiaona Zhao
zhaoxn@sdau.edu.cn
Jianzhu Liu
liujz@sdau.edu.cn

†These authors have contributed equally to this work

Specialty section:
This article was submitted to Nutritional Immunology, a section of the journal Frontiers in Immunology

Received: *02 May 2022*
Accepted: *24 May 2022*
Published: *30 June 2022*

Citation:
Li L, Chen X, Lv M, Cheng Z, Liu F, Wang Y, Zhou A, Liu J and Zhao X (2022) Effect of Platycodon grandiflorus Polysaccharide on M1 Polarization Induced by Autophagy Degradation of SOCS1/2 Proteins in 3D4/21 Cells. Front. Immunol. 13:934084. doi: 10.3389/fimmu.2022.934084

INTRODUCTION

A tremendous amount of scientific work has confirmed the medicinal values of traditional Chinese medicine (TCM). One of the representative TCMs is *Platycodon grandiflorus*, which has been used to treat viral diseases for several centuries in China. *P. grandiflorus* (the rhizome of *P. grandiflorus*) are well-known, commonly used TCM preparations. According to anecdotal evidence passed down for over 2,000 years by the practitioners of the TCM system, *P. grandiflorus* can promote health and homeostasis. In recent decades, the investigations of *P. grandiflorus* have focused on its biological activities, including its anti-tumor, hepatoprotective, immunoregulatory, and antioxidant effects. These studies have resulted in the isolation of saponins, flavonoids, anthocyanins, phenolics, and polysaccharides, among other compounds, from the plant (1). Polysaccharide is the main immunologically active substance in PG, which has an obvious immunomodulatory effect. It is the material basis for "strengthening and restoring effects" and enhancing immune function. In order to explore the immune mechanism of the *P. grandiflorus* polysaccharide ($PGPS_t$), our research group has identified the polysaccharide structure of $PGPS_t$ and evaluated its immune regulation activities on 3D4/21 cells, chicken peritoneal macrophages, and lymphocytes. Studies have found that $PGPS_t$ can enhance the phagocytosis and proliferation activity of chicken peritoneal macrophages, induce the expression of costimulatory molecules (CD80 and CD86), promote the secretion of cytokines and the release of NO, and induce macrophage polarization to the M1 type (2). In addition, $PGPS_t$ can promote lymphocyte proliferation, increase the ratio of CD4 +/CD8 + subsets, and promote cells to enter the DNA synthesis phase (3). PG, a polysaccharide isolated from *P. grandiflorum*, could induce macrophage activation through the TLR4/NF-κB signaling pathway and activate MAPK and AP-1, which suggested that PG induces nitric oxide (NO) production and the mRNA expression of iNOS in RAW 264.7 cells (4). Yeo Dae Yoon et al. demonstrated that a polysaccharide isolated from *P. grandiflorums* electively activates B cells and macrophages but not T cells (5).

Macrophages have long been considered to be important immune effector cells. Macrophage polarization refers to an estimate of macrophage activation at a given point in space and time. Polarization is not fixed, as macrophages are sufficiently plastic to integrate multiple signals, such as those from microbes, damaged tissues, and the normal tissue environment. Macrophages can acquire distinct morphological and functional properties in different microenvironments. Different inflammatory stimuli can temporarily induce distinct subsets of macrophages with polarized inflammatory phenotypes. The M1 phenotype is characterized by a high capacity to present antigen, high levels of inflammatory cytokine (TNF-α, IL-6) secretion and increased levels of NO production, an enhanced capacity to kill intracellular pathogens and tumor cells, and the promotion of polarized h1 immune responses (6). Polarized macrophages can further affect the local immune response, and coordinate with various factors to regulate pathogenic microbial infection and tumor immunity, and participate in immune regulation (7). It has been reported that the polarization of macrophages toward the M1 type is very important for effective antiviral immune response. In acute and chronic HIV infection, M1 macrophages in parenchymal tissue play an important role in the early antiviral immune response and subsequent recovery response (8). In addition, some scholars have found that polarized M1 porcine alveolar macrophages (PAMs) have a significant inhibitory effect on the replication and proliferation of PRRSV (9).

Autophagy can activate innate immune cells, and the substrate of autophagy can be presented as an antigen to adaptive immune cells to start adaptive immune response. In recent years, studies on a variety of chronic inflammatory disease models have shown that autophagy may participate in the regulation of macrophage polarization. It has been reported that autophagy occurs in many physiological and pathological situations and is a key component of development and differentiation (10). Some studies suggest that autophagy plays a vital role in viral infection and immunosuppression (11, 12).

Autophagy has recently been considered important in macrophage polarization. Autophagy may be involved in the regulation of macrophage polarization by regulating inflammatory response, reactive oxygen species (ROS), and apoptosis (13). Baicalin promotes the transformation of tumor-associated macrophages (TAMs) from M2- to M1-like phenotypes through the autophagy degradation of TRAF2 to exert anti-tumor effects (14). USP19 inhibits inflammation and promotes M2-like macrophage polarization by regulating NLRP3 function through autophagy (15). The inhibition of USP14 can promote the autophagy of M1-like macrophages and alleviate sepsis caused by CLP (16). It has been found that the IFN-γ/JAK-STAT1 pathway is a key component of the macrophage M1 polarization regulator. The SOCS protein family is a very important regulator of macrophage polarization (17). The expression of STAT, a key protein in the polarization pathway, is affected by the cytokine signal transduction inhibitor SOCS protein (18). For M1 macrophages, SOCS1 protein reduces the secretion of some pro-inflammatory mediators in M1 macrophages (19). After SOCS1 protein expression was downregulated, the proportion of M1 type cells increased significantly, while the proportion of M2 cells did not change significantly. SOCS2 protein knockout macrophages highly express M1 markers (20). In addition, studies have shown that SOCS2 protein can interact with LC3 protein and promote the differentiation of astrocytes through the autophagy degradation of SOCS2 protein (21). These results provide a partial basis for the autophagy degradation of SOCS protein.

In this study, co-immunoprecipitation, laser confocal, flow cytometry, and intracellular co-localization techniques were used to detect the changes in the expression of related phenotypic proteins and cytokines in M1-polarized cells and to determine the degree of polarization of 3D4/21 cells induced by $PGPS_t$. The effect of $PGPS_t$-induced autophagy degradation of SOCS1/2 on M1 polarization in 3D4/21 cells was studied to clarify the

relationship between autophagy and polarization. The co-localization of SOCS1/2 with autophagosomes and autolysosomes was observed. The interaction between SOCS1/2 and LC3 was identified by Co-IP to verify that SOCS1/2 autophagy degradation was mediated by LC3 protein. The purpose of this study was to explore the mechanism of $PGPS_t$ inducing the autophagy degradation of SOCS1/2 protein and promoting the M1 polarization of 3D4/21 cells and to provide a theoretical basis for the application of $PGPS_t$ in the prevention and treatment of viral infection diseases.

MATERIALS AND METHODS

Reagents and Antibodies

Total $PGPS_t$ was prepared in our laboratory, and the polysaccharide content of $PGPS_t$ was 76.76%. The information on the extraction methods and structure identification of the polysaccharide has been determined in our previous study (2).

Recombinant porcine interferon-gamma (IFN-?) (985-PI-050) was purchased from R&D Systems (Minneapolis, MN, USA). Lipopolysaccharide (LPS) (L8880) was purchased from Solarbio (Beijing, China). MG-132, chloroquine (CQ), 3-methyladenine (3-MA), and bafilomycin A1 (Baf A1) were delivered by Med Chem Express (Shanghai, China). The Hoechst 33342 kit (C1026) and Nitric Oxide Synthase (iNOS) Assay kit (S0025) were provided by Beyotime Institute of Biotechnology (Haimen, China). The modified RPMI-1640 medium was purchased from Gibco (Shanghai, China). Penicillin-Streptomycin Amphotericin B (03-033-1B/C) and Certified FBS (04-001-1ACS) were purchased from Biological Industries (Kibbutz Beit Haemek, Israel).

Anti-LC3B (ab229327) and SOCS1 (ab9870) were purchased from Abcam (Shanghai, China). Anti-SOCS2 (#2779) and anti-LC3B (#83506) were obtained from Cell Signaling Technology (Shanghai, China). Anti-SOCS3 (14025-1-AP), anti-CD80 (66406-1-lg), anti-α-tubulin (66031-1-lg), anti-SQSTM1/p62 (18420-1-AP), anti-GAPDH (60004-1-lg), HRP-conjugated Affinipure Rabbit Anti-Goat IgG (H+L) (SA00001-4), HRP-conjugated Affinipure Goat Anti-Mouse IgG (H+L) (SA00001-1), HRP-conjugated Affinipure Goat Anti-Rabbit IgG (H+L) (SA00001-2), and CoraLite488-conjugated Affinipure Goat Anti-Mouse IgG (H+L) (SA00013-1) were purchased from Proteintech (Wuhan, China). Cy3-conjugated Goat Anti-rabbit IgG (H+L) (GB21303) was purchased from Servicebio (Wuhan, China). Anti-CD86 (abs120515) was purchased from Absin (Shanghai, China). IFkine™ Red Donkey Anti-Goat IgG (A24431) and IFkine™ Green Donkey Anti-Rabbit IgG (A24221) was provided by Abbkine (Shanghai, China).

Cell Culture

Porcine alveolar macrophage cell line 3D4/21 cells were obtained from iCell Bioscience (Shanghai, China) and cultured in the modified RPMI-1640 medium adjusted to contain with 2 mM L-glutamine, 1.5 g/L sodium bicarbonate, 4.5 g/L glucose, 10 mM HEPES, 1.0 mM sodium pyruvate supplemented with 0.1 mM nonessential amino acids, 10% fetal bovine serum, and 1% Penicillin-Streptomycin Amphotericin B at 37°C in 5% CO_2 atmosphere.

Experimental Treatments

To obtain differentiated macrophages, 3D4/21 cells were stimulated with LPS (150 ng/ml) and IFN-γ (50 g/ml), to promote M1 polarization when grown to 70%–80% confluence in six-well plates; the dosage refers to the study of Wang et al. (22). Then, $PGPS_t$ (100 μg/ml) was added to the tested wells; the dosage refers to our previous study (23). To inhibit autophagy, cells were pretreated for 8 h with 3-MA (100 μM) and BafA1 (60 nM), respectively, before $PGPS_t$. After different treatments, cells or supernatants were harvested for analyses. In order to study the degradation pathway of SOCS protein, MG-132 (100 nM) and CQ (20 μM) were respectively used in the experiment.

ELISA Analysis

At indicated time points, the concentration of IL-6, IL-12, TNF-α, and IL-1β in supernatants were measured by ELISA according to manufacturer's instruction (Porcine IL-6 ELISA Kit, Porcine IL-12 ELISA Kit, Porcine TNF-α ELISA Kit, Porcine IL-1β ELISA Kit, Shanghai, China).

Real-Time Fluorescence Quantitative Polymerase Chain Reaction

Total RNA was extracted using the RNAiso Plus reagent(Takara, Dalian, China), and then genomic DNA Contaminated gDNA was removed as follows: 2 μL (1 μg) total RNA, 1 μL gDNA Eraser, 2 μL 5× gDNA Eraser Buffer, 5 μL RNase free water were mixed in PCR tube, the reaction was incubated at 42°C for 2 min. Afterwards, 1 μL PrimeScript RT Enzyme Mix I, 1 μL RT Primer Mix, 4 μL 5× PrimeScript Buffer 2, 4 μL RNase free water were added to the tube. The mixture was incubated at 37°C for 15 min, 85°C for 5 s. The cDNA was stored at −20°C for later use. was removed and reverse-transcribed in a BIO-RAD Mastercycler (BIO-RAD, California, USA), using a PrimeScript™ RT reagent Kit (Takara, Dalian, China) with gDNA Eraser according to the manufacturers' instructions. PCR was performed in triplicate in a LightCycler®96 system(Roche Diagnostics GmbH, Mannheim, Germany). The sequences of the specific primers are shown in **Table 1** and were purchased from Takara. After using the threshold cycle value to normalize the expression changes of the gene of interest to the housekeeping gene GAPDH, the folding changes are calculated.

Protein Isolation and Western Blotting

After different treatments, cells were lysed with the RIPA buffer containing a protease inhibitor cocktail for protein analysis. Then, protein concentration was measured by the BCA Protein Assay Kit (CWBIO, Beijing, China). Equal amounts of protein samples were size-separated by 12% SDS-PAGE and blotted onto the polyvinylidene fluoride membrane. After blocking, membranes were exposed to antibodies that recognized P62/SQSTM1, LC3B, SOCS1, SOCS2, SOCS3, CD80, and CD86 at 4° Covernight. Then, the membranes were incubated with the

TABLE 1 | Primer sequences for real-time PCR analysis.

Gene	Primer	
TNF-α	Forward:	5'-AGAGCATGATCCGAGACGTG -3'
	Reverse:	5'-CAGTAGGCAGAAGAGCGTGGT -3'
IL-6	Forward:	5'-AATAAGGGAAATGTCGAGGCTGT -3'
	Reverse:	5'-GGCATTTGTGGTGGGGTTAG -3'
IL-12	Forward:	5'-TCATCAGGGACATCATCAAACC -3'
	Reverse:	5'-GAACACCAAACATCAGGGAAAAG -3'
SOCS1	Forward:	5'-CCGTCCTCCGCGATTACTTGA -3'
	Reverse:	5'-CCTCCAACCCACATGGTTCCAA -3'
SOCS2	Forward:	5'-GGCACCGTTCACCTCTATCTG -3'
	Reverse:	5'-TAGTCTTGTTGGTAAAGGCAGTCC -3'
GAPDH	Forward:	5'-CACTGGTGTCTTCACGACCAT -3'
	Reverse:	5'-TTCACGCCCATCACAAACA -3'

corresponding horseradish peroxidase (HRP)–conjugated IgG secondary antibody at room temperature for 1 h. The reactive bands were visualized using the enhanced chemiluminescence detection system and analyzed with Image J software. The relative protein expression levels were normalized to GAPDH or α-tubulin.

Confocal Microscopy Analysis

The iNOS protein expression levels of the 3D4/21 cells were evaluated by confocal immunofluorescence microscopy according to the iNOS manufacturer's instruction. In order to observe the morphology of macrophages under different treatment conditions, indirect immunofluorescence was performed using the anti-GAPDH antibody. To elucidate the cytosolic localization of SOCS1 and LC3B, SOCS2, and LC3B, indirect immunofluorescence was performed using the anti-SOCS1 antibody, anti-SOCS2 antibody, and anti-LC3B antibody. Briefly, the 3D4/21 cells were incubated with antibodies overnight at 4°C and then with the corresponding fluorescent dye–conjugated secondary antibodies for 1 h. After washing with PBS, the cells were permeabilized with Hoechst 33342 for 10 min and examined with a Leica TCS SPE confocal microscope (Heidelberg, Baden-Württemberg, Germany).

Co-Immunoprecipitation

Cell samples were lysed and centrifuged. The supernatant was added to 100 μl of Protein A+G agarose beads and rotated at 4°C for 1 h to remove non-specific binding proteins for further use. The LC3B antibody and corresponding amount of normal IgG were diluted according to the instructions, and 100 μl of Protein A+G agarose beads were added, respectively, rotated for 2 h at 4°C, and then centrifuged for 5 min at 1,000 g and 4°C. The prepared supernatant was added to Protein A+G agarose beads conjugated with antibody or normal IgG, and rotated overnight at 4°C, to bind the protein to the antibody. After removing the supernatant, the supernatant was washed with PBS four times, 1 ml each time. The eluted protein was added to 100 μL 1× loading buffer, boiled for 5 min, and centrifuged for 5 min at 1,000 g, and the supernatant was taken for Western blot detection.

Statistical Analysis

All data were obtained from three repeated experiments and expressed as mean ± standard deviation (SD). All statistical calculations were performed using SPSS 24.0 software (IBM, Armonk, NY, USA). Differences between groups were analyzed using one-way analysis of variance (ANOVA). The levels of significance were as follows: $P< 0.05$ is signified by *; $P< 0.01$ is signified by **.

RESULTS AND DISCUSSION

Morphological Changes of M1 Polarization in 3D4/21 Cells

After stimulation with LPS/IFN-γ for 24 h, the morphology of 3D4/21 cells changed. Compared with the control group (M0), the nucleus of 3D4/21 cells became larger after polarization, the nucleus became irregular, the cell outline became rounded, and the tubulin became disorderly (**Figure 1**).

Macrophages are stimulated by different environmental factors to differentiate into different phenotypes that can adapt to the internal environment. Macrophages stimulated by IFN-γ and LPS polarize toward the classically activated M1 phenotype macrophages and can trigger an inflammatory response and kill pathogens in the cell (24). Most viruses with monocyte tropism, such as human immunodeficiency virus (HIV), respiratory syncytial virus (RSV), and severe acute respiratory syndrome virus (SARS), may affect macrophages after infection and in turn cause immune suppression of the host, which reduces the body's immune system's ability to recognize and eliminate the virus, leading to serious secondary infections (25–27). Tumor-secreted Pros1 inhibits macrophage M1 polarization to reduce antitumor immune response (7, 7). It is imperative to activate macrophages to polarize M1 in diseases such as viral infections,

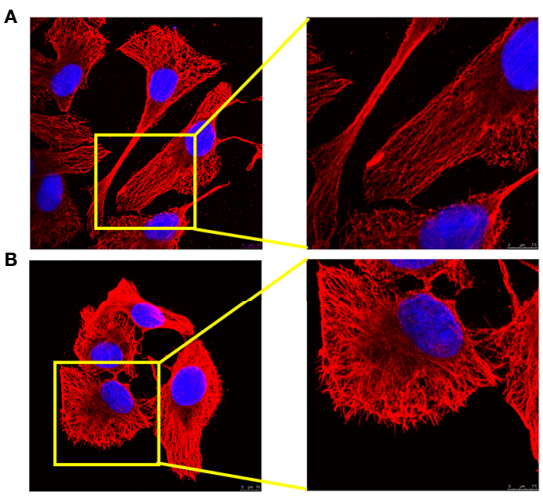

FIGURE 1 | Analysis of 3D4/21-cell morphology under different activation methods. **(A)** Morphology of (M0) 3D4/21 cells incubated in RPMI-1640 for 24 h. **(B)** The morphology of (M1) 3D4/21 cells treated with IFN-γ/LPS was examined by confocal microscopy. M0-type 3D4/21 cells were a non-polarized control group.

immunosuppression, and tumors. In this study, an *in vitro* M1 polarization model of 3D4/21 cells was established.

In recent years, with the deepening understanding of the function of macrophages, some studies have begun to explore their immune activity from the effect of polysaccharides on the polarization of macrophages.

Changes in the Expression of M1 Genes in Stimulated 3D4/21 Cells

In order to confirm the effectiveness of the selected treatment for inducing M1 polarization, qRT-PCR was used to detect the expression of important M1 biomarkers. It is noteworthy that the expression of IL-6, IL-12, and TNF-α in the LPS/IFN-γ treatment group was significantly higher than that in the control group. The mRNA expression of $PGPS_t$ was significantly higher than that in LPS/IFN-γ treatment group (**Figures 2A–C**). As shown in **Figures 2D, E**, LPS/IFN-γ can also enhance the mRNA expression level of SOCS1/2, but $PGPS_t$ seems to have no effect. These results indicated that LPS/IFN-γ induced the macrophage transformation into the M1 phenotype, in accordance with the ones found in the roots of *Actinidia eriantha* (28).

Inducible nitric oxide synthase (iNOS) is an important factor expressed by M1 macrophages, which catalyzes the production of nitric oxide (NO) from the L-arginine substrate. IL-6, IL-12, TNF-α, IL-1β, and iNOS are the markers of M1 macrophages (1). Therefore, the expression levels of these cytokines can be used to evaluate the activation of macrophages. As shown in **Figures 3A–D, L**, compared with the control group, the LPS/IFN-γ treatment group significantly increased the expression levels of IL-6, IL-12, TNF-α, IL-1β, and iNOS. Importantly, the expression of these markers in the $PGPS_t$ group was significantly increased compared to the LPS/IFN-γ treatment group alone, which confirmed that $PGPS_t$ could promote the production of IL-6, IL-12, TNF-α, IL-1β, and iNOS. An interesting phenomenon was discovered here, that is, $PGPS_t$ could downregulate the protein level rather than the mRNA level of polarization pathway inhibitor SOCS1/2. This indicates that $PGPS_t$ induces the degradation of SOCS1/2 proteins.

CD80 and CD86 are expressed in activated B and T lymphocytes, macrophages, peripheral blood mononuclear cells, and dendritic cells, which are essential membrane antigens for macrophage activation. In addition, CD80 is the most robust phenotypic marker for human MΦ (IFN-γ) (29). In **Figures 3E, G, H**, the expression levels of CD80 and CD86 in the $PGPS_t$ group were significantly higher than those in other groups. Furthermore, the expression of SOCS3, which inhibited M2 polarization, was increased by $PGPS_t$ (**Figures 3E, F**). These results further proved that $PGPS_t$ could promote LPS/IFN-γ-induced macrophage transformation to the M1 phenotype.

SOCS family is a negative regulator associated with CNS immune inflammatory response. For M1 macrophages, SOCS1 protein attenuates the secretion of certain proinflammatory mediators in M1 macrophages (19). After the downregulation of SOCS1 protein expression, the proportion of M1-type cells increased significantly, while the proportion of M2-type cells did not change significantly; SOCS2 protein knockout macrophages highly expressed M1-type markers (20). SOCS1/2 is likely to become a rational target for therapeutic regimens against various

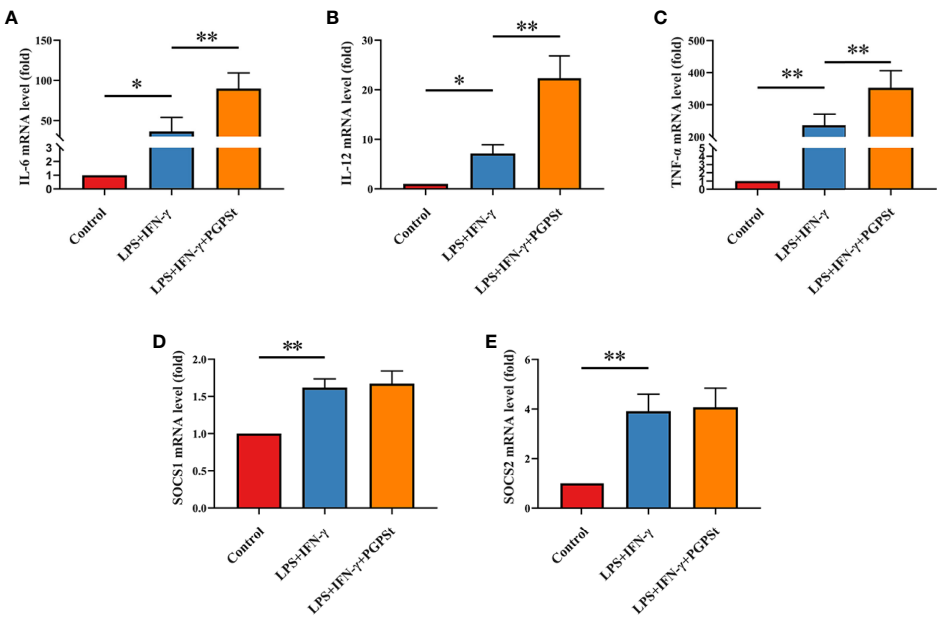

FIGURE 2 | qRT-PCR analysis to determine 3D4/21 cell polarization. After treatment with various reagents, the mRNA levels of M1-type 3D4/21 cells were monitored by qRT-PCR. After incubation for 24 h, these images showed the expression of polarization markers in M1-type 3D4/21 cells, such as **(A)** IL-6, **(B)** IL-12, and **(C)** TNF-α. The expression of regulatory factors **(D)** SOCS1 and **(E)** SOCS2 in the polarization pathway of M1-type 3D4/21 cells. Means ± SD are indicated (n = 3). * indicates $P < 0.05$; ** indicates $P < 0.01$.

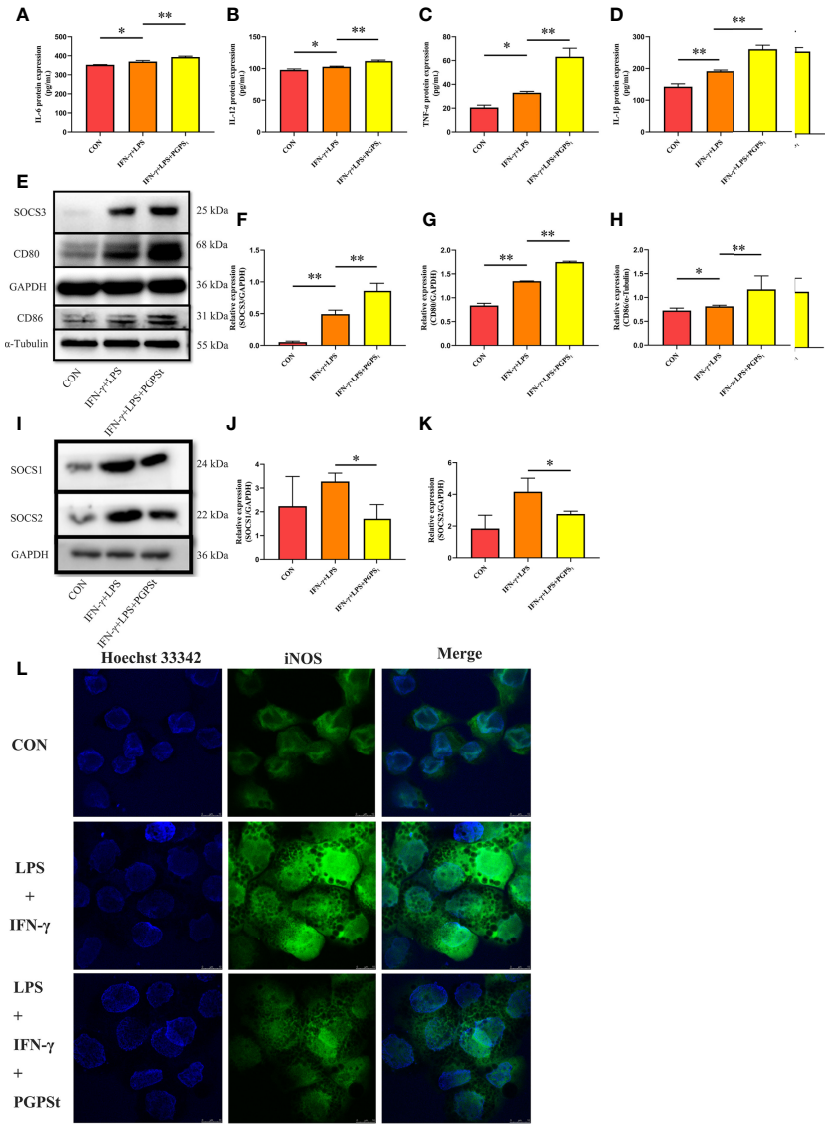

FIGURE 3 | Expression changes of M1 marker protein in 3D4/21 cells treated with LPS/IFN-γ or $PGPS_t$ for 24 h. **(A–D)** The expression of M1 marker proteins in different activated 3D4/21 cells was analyzed by the ELISA kit. **(E–H)** 24 h after stimulation, Western blot analysis of M1 marker protein expression in 3D4/21 cells; **(I–K)** Western blot analysis of protein expression regulated by the polarization pathway in 3D4/21 cells. **(L)** Approximately 24 h after stimulation, the proportion of cells expressing iNOS (the marker of M1-type 3D4/21 cells) was monitored by a laser confocal microscope. Means ± SD are indicated (n = 3). * indicates $P < 0.05$; ** indicates $P < 0.01$.

immune diseases that occur on the basis of the overshooting of the immune system, such as immunodeficiency and immunosuppressive diseases. An interesting phenomenon can be observed here; LPS/IFN-γ could increase the expression level of SOCS1/2 protein. However, $PGPS_t$ reduced the protein level of SOCS1/2 (**Figures 3I–K**). The inhibitor of cytokine signaling (SOCS) proteins act as feedback inhibitors in the JAK/STAT signaling pathway, which can terminate innate and adaptive immune responses (18). The results indicated that $PGPS_t$ promoted LPS/IFN-γ-induced M1 polarization by reducing the inhibitory protein SOCS1/2 in the JAK/STAT signal transduction pathway of M1 polarization.

SOCS1/2 Was Degraded Through the Lysosomal Pathway

To explore the degradation pathway of SOCS1/2, the classical proteasome pathway inhibitor MG-132 and lysosome inhibitor CQ were used. As shown in **Figures 4A–C**, $PGPS_t$ decreased the expression level of SOCS1/2 proteins. When treated with MG-132, $PGPS_t$ can still reduce the expression of SOCS1/2. Conversely, CQ prevented the effect of $PGPS_t$ on SOCS1/2. These results indicated that $PGPS_t$ could degrade SOCS1/2 proteins by activating the lysosomal pathway. Studies have shown that SOCS2 protein can interact with LC3 protein to degrade SOCS2 protein through autophagy to promote the differentiation of astrocytes (21).

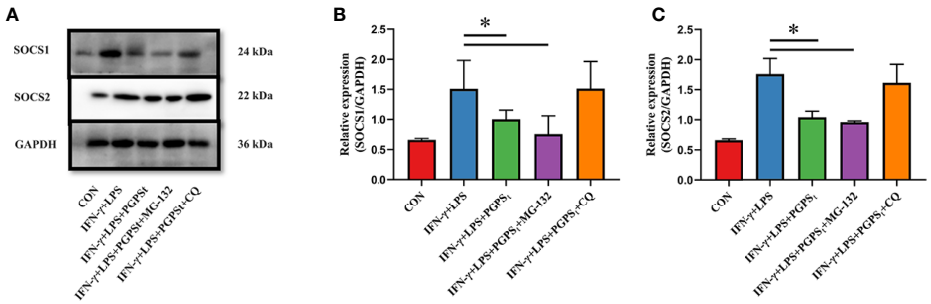

FIGURE 4 | Effects of MG-132 and CQ on SOCS1 and SOCS2 expression in M1-type 3D4/21 cells. **(A–C)** Western blot analysis of the expression of SOCS1 and SOCS2 proteins in M1-type 3D4/21 cell polarization pathway regulators. Means ± SD are indicated (n = 3). * indicates $P < 0.05$.

Therefore, we speculate that the reduction of SOCS1/2 protein is related to autophagy.

Regulation of Autophagy by $PGPS_t$ Affected the Expression of SOCS1/2

The above experimental results mentioned that $PGPS_t$ degraded SOCS1/2 proteins by activating the lysosomal pathway, which indicates that autophagy might be involved in this process. It can be seen from **Figures 5A–C** that $PGPS_t$ significantly increased the content of intracellular LC3B II and decreased the content of P62. With the effect of the autophagy inhibitor 3-MA, $PGPS_t$ promoted the significant reduction of LC3B II and blocked the downregulation of SOCS1/2 protein by $PGPS_t$. In addition, with the effect of BafA1, $PGPS_t$ promoted the accumulation of LC3B II and P62, and the autophagy flow was blocked. The SOCS1/2 protein is no longer downregulated by $PGPS_t$ (**Figures 5D, E**). It can be reasonably assumed that the loss of SOCS1 and SOCS2 on macrophages was due to the enhanced autophagy induced by $PGPS_t$. The results showed that under the condition of smooth autophagy, $PGPS_t$ upregulated LC3B II and downregulated

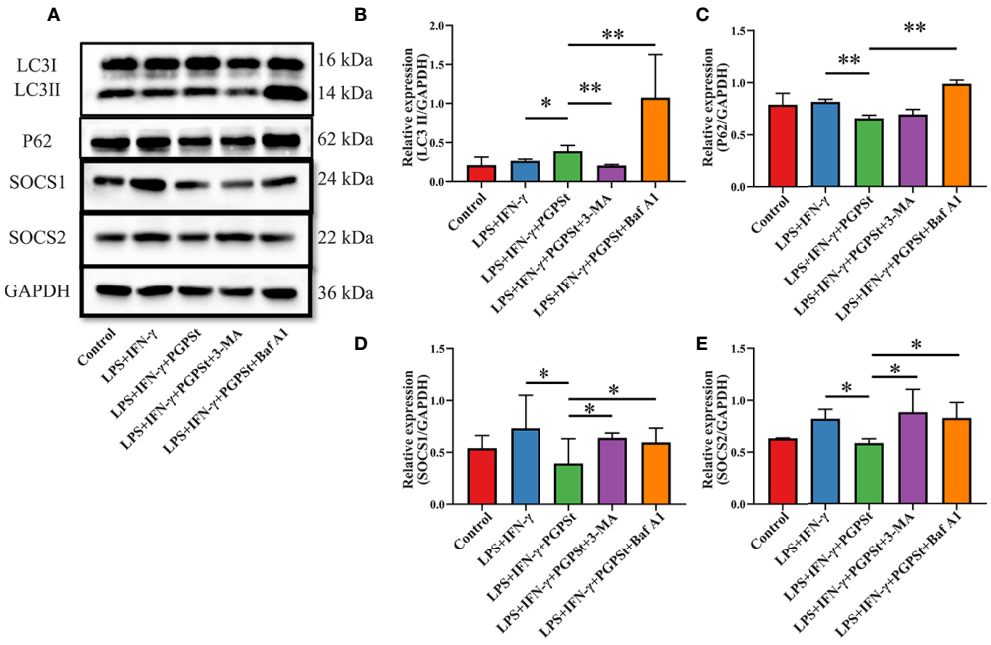

FIGURE 5 | Effect of $PGPS_t$ on SOCS1/2 expression through autophagy regulation. **(A)** Western blot analysis of LC3, P62, and SOCS1/2 in 3D4/21 cells in the presence or absence of 3-MA or bafilomycin A1; **(B)** Western blot analysis of LC3II/GAPDH expression; **(C)** Western blot analysis of P62/GAPDH expression; **(D)** Western blot analysis of SOCS1/GAPDH expression; **(E)** Western blot analysis of SOCS2/GAPDH expression. Means ± SD are indicated (n = 3). * indicates $P < 0.05$; ** indicates $P < 0.01$.

SOCS1/2 protein expression, which increased the possibility of LC3B, the key component of autophagy, bridging this connection and degrading SOCS1/2.

The previous observations raise fundamental questions: what is the relationship between autophagic machinery and SOCS1/2 degradation? If a relationship exists, what is the functional role of this interaction? The questions indicate a new research field for further investigation of these processes.

Interaction Between LC3B and SOCS1, LC3B and SOCS2

The above results indicated that $PGPS_t$ downregulated SOCS1/2 and increased the possibility that LC3B, the key component of autophagy, might bridge this connection and degrade SOCS1/2. To verify this possibility, the interaction between LC3 and SOCS1/2 was investigated by indirect immunofluorescence and co-immunoprecipitation experiments.

Compared with the control group, the co-localization percentage of the two proteins increased significantly after adding $PGPS_t$ (**Figures 6A, B**). The resolution limit of optical microscope means that the physical size and position of small objects in a two-dimensional space or even three-dimensional space are uncertain. The relationship between the two proteins cannot be proved by a single immunofluorescence test. Therefore, the two proteins were detected by immunoprecipitation.

NAs shown in **Figure 6C**, the results showed that LC3, SOCS1, and SOCS2 could be normally detected in the input group, indicating that the expression of three proteins in the cell lysate was normal. The LC3 antibody beads IP complex can detect LC3 expression, while IgG antibody beads IP complex cannot detect LC3 expression, indicating that the LC3 antibody can specifically bind to LC3 protein. The expressions of SOCS1 and SOCS2 could be detected in the LC3 antibody bead IP complex, while the expressions of SOCS1 and SOCS2 were not detected in the IgG bead IP complex, indicating that LC3 might interact with SOCS1 and SOCS2. These data suggest that $PGPS_t$ regulated SOCS1/2 protein through the interaction between LC3B and SOCS1/2 protein and that $PGPS_t$ was mediated by autophagy in macrophage polarization to M1.

Autophagy participates in the pathophysiological process of many diseases. Through the study of chronic inflammatory disease models, the effect of autophagy on the polarization of macrophages has gradually been confirmed, but under different disease states, the effect of autophagy on the polarization of macrophages is different. Impaired macrophage autophagy promotes proinflammatory macrophage polarization (30). Autophagy promotes M2 macrophage through upregulating ID3

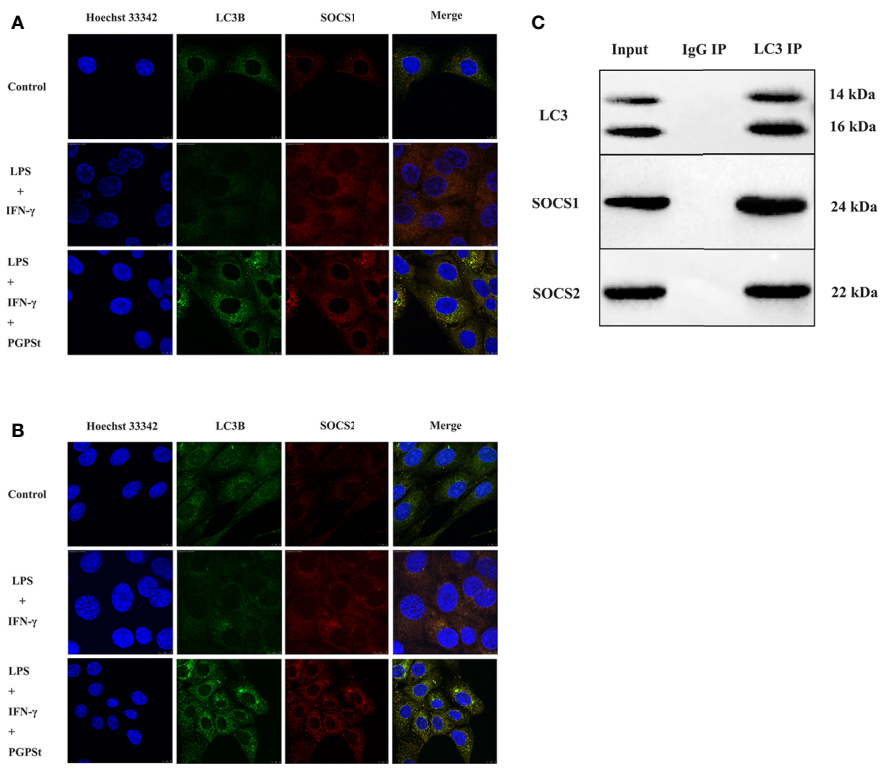

FIGURE 6 | The confocal and co-IP confirmed the co-localization between LC3 and SOCS1, LC3, and SOCS2 in 3D4/21 cells. **(A)** Co-location of SOCS1 and LC3. **(B)** Co-location of SOCS2 and LC3. **(C)** Protein interactions between SOCS1 and LC3, SOCS2, and LC3.

(31). Increased autophagy induces macrophage polarization into M1 with an elevated CD11c population and the gene expressions of proinflammatory cytokines to impair cutaneous wound healing (13).

In view of the important role of macrophages in a variety of diseases and the influence of autophagy on the polarization of macrophages, the research and development of Chinese medicine ingredients to regulate autophagy activity and thereby change the functional state of macrophages is expected to provide new strategies and new ideas for the treatment of related diseases.

In summary, $PGPS_t$ promotes the M1 polarization of 3D4/21 cells and enhances the immunoregulatory activity by increasing the autophagy level. As a macromolecular active substance, $PGPS_t$ has a complex structure that plays a huge role in immune regulation. Most of the polysaccharides with prominent biological activity are linked by (1→3) glycosidic bonds, with the main chain structure of β (1→3)-D-glucan, which is consistent with the main chain structure of $PGPS_t$ (32, 33). The active polysaccharides have a certain molecular weight range. The molecular weight of subpolysaccharides is too large, which is not conducive to their biological activity across the cell membrane into the organism, while the molecular weight is too low, and there is no activity (34). The number-average molecular weight of $PGPS_t$ is 1.72×10^3–1.66×10^5 Da, the weight-average molecular weight is 2.05×10^3-2.67×10^5 Da, and the distribution width is 1.19–1.60, indicating that the molecular weight distribution is relatively narrow and the biological activity is better. Polysaccharides are composed of a variety of monosaccharides with more branched chains. Lo et al. (35) studied lentinan (LNT) and found that xylose, mannose, galactose, and their molar ratios are closely related to the biological activity of LNT. Although glucose is an important part of polysaccharides, it has little effect on the biological activity of polysaccharides. $PGPS_t$ contains more mannose and xylose, which is consistent with many studies.

CONCLUSION

$PGPS_t$ promotes the M1 polarization of porcine alveolar macrophages by degrading SOCS1/2 proteins through autophagy and improves the immune function of macrophages.

DATA AVAILABILITY STATEMENT

The original contributions presented in the study are included in the article/supplementary material. Further inquiries can be directed to the corresponding authors.

AUTHOR CONTRIBUTIONS

LL: designed and executed experiments, data curation, data analysis, writing—original draft preparation. XC: data curation, data analysis, writing—original draft preparation. ML, ZC, FL, YW, and AZ: data curation. JL: writing—reviewing and editing, supervision, and project administration. XZ: writing—reviewing and editing, supervision, funding acquisition, and project administration. All authors have revised the manuscript and approved the final version of the paper to be published.

FUNDING

This project was supported by the Key Research and Development Program of Shandong Province (Important Science and Technology Innovation Project) (2019JZZY010735), the Natural Science Foundation of Shandong Province, China (ZR2021MC088) and the technology Project of Tai`an science and technology correspondent (2021TPY034).

REFERENCES

1. Moghaddam AS, Mohammadian S, Vazini H, Taghadosi M, Esmaeili SA, Mardani F, et al. Macrophage Plasticity, Polarization, and Function in Health and Disease. *J Cell Physiol* (2018) 233(9):6425–40. doi: 10.1002/jcp.26429
2. Zheng P, Fan W, Wang S, Hao P, Wang Y, Wan H, et al. Characterization of Polysaccharides Extracted From Platycodon Grandiflorus (Jacq.) A.Dc. *Affecting Activation Chicken Peritoneal Macrophages Int J Biol Macromol* (2017) 96:775–85. doi: 10.1016/j.ijbiomac.2016.12.077
3. Zhao X, Wang Y, Peng Y, Cheng G, Wang C, Geng N, et al. Effects of Polysaccharides from Platycodon Grandiflorum on Immunity-Enhancing Activity *in Vitro*. *Molecules* (2017) 22(11):1918. doi: 10.3390/molecules22111918
4. Yoon YD, Han SB, Kang JS, Lee CW, Park SK, Lee HS, et al. Toll-Like Receptor 4-Dependent Activation of Macrophages by Polysaccharide Isolated From the Radix of Platycodon Grandiflorum. *Int Immunopharmacol* (2003) 3 (13–14):1873–82. doi: 10.1016/j.intimp.2003.09.005
5. Han SB, Park SH, Lee KH, Lee CW, Lee SH, Kim HC, et al. Polysaccharide Isolated From the Radix of Platycodon Grandiflorum Selectively Activates B Cells and Macrophages But Not T Cells. *Int Immunopharmacol* (2001) 1 (11):1969–78. doi: 10.1016/S1567-5769(01)00124-2
6. Qin H, Holdbrooks AT, Liu Y, Reynolds SL, Yanagisawa LL, Benveniste EN. Socs3 Deficiency Promotes M1 Macrophage Polarization and Inflammation. *J Immunol* (2012) 189(7):3439–48. doi: 10.4049/jimmunol.1201168
7. Ubil E, Caskey L, Holtzhausen A, Hunter D, Story C, Earp HS. Tumor-Secreted Pros1 Inhibits Macrophage M1 Polarization to Reduce Antitumor Immune Response. *J Clin Invest* (2018) 128(6):2356–69. doi: 10.1172/JCI97354
8. Burdo TH, Walker J, Williams KC. Macrophage Polarization in Aids: Dynamic Interface Between Anti-Viral and Anti-Inflammatory Macrophages During Acute and Chronic Infection. *J Clin Cell Immunol* (2015) 6(3):333.
9. Konttinen YT, Pajarinen J, Takakubo Y, Gallo J, Nich C, Takagi M, et al. Macrophage Polarization and Activation in Response to Implant Debris: Influence by "Particle Disease" and "Ion Disease". *J Long Term Eff Med Implants* (2014) 24(4):267–81. doi: 10.1615/JLongTermEffMedImplants.2014011355
10. Levine B, Kroemer G. Autophagy in the Pathogenesis of Disease. *Cells* (2008) 132(1):27–42. doi: 10.1016/j.cell.2007.12.018
11. Abhilash C, Nathan B, Ralf B. Divergent Roles of Autophagy in Virus Infection. *Cells* (2013) 2(1):83–104. doi: 10.3390/cells2010083
12. Ren C, Hui Z, Wu TT, Yao YM. Autophagy: A Potential Therapeutic Target for Reversing Sepsis-Induced Immunosuppression. *Front Immunol* (2017) 8:1832. doi: 10.3389/fimmu.2017.01832
13. Guo Y, Lin C, Xu P, Wu S, Fu X, Xia W, et al. Ages Induced Autophagy Impairs Cutaneous Wound Healing Via Stimulating Macrophage Polarization to M1 in Diabetes. *Sci Rep* (2016) 6:36416. doi: 10.1038/srep36416

14. Tan HY, Wang N, Man K, Tsao SW, Che CM, Feng Y, et al. Autophagy-Induced Relb/P52 Activation Mediates Tumour-Associated Macrophage Repolarisation and Suppression of Hepatocellular Carcinoma by Natural Compound Baicalin. *Cell Death Dis* (2015) 6(10):. doi: 10.1038/cddis.2015.271
15. Liu T, Wang L, Liang P, Wang X, Cui JJC, Immunology M. Usp19 Suppresses Inflammation and Promotes M2-Like Macrophage Polarization by Manipulating Nlrp3 Function Via Autophagy. *Cell Mol Immunol* (2020) 18 (10):2431–42. doi: 10.1038/s41423-020-00567-7
16. Xu F, Ma Y, Huang W, Gao J, Guo M, Li J, et al. Typically Inhibiting Usp14 Promotes Autophagy in M1-Like Macrophages and Alleviates Clp-Induced Sepsis. (2020) 11(8):666. Disease. doi: 10.1038/s41419-020-02898-9
17. Arndt L, Dokas J, Gericke M, Kutzner CE, Müller S, Jeromin F, et al. Tribbles Homolog 1 Deficiency Modulates Function and Polarization of Murine Bone Marrow-Derived Macrophages. (2018) 293(29):11527–36. doi: 10.1074/jbc.RA117.000703
18. Dalpke A, Heeg K, Bartz H, Baetz A. Regulation of Innate Immunity by Suppressor of Cytokine Signaling (Socs) Proteins. *Immunobiology* (2008) 213 (3-4):225–35. doi: 10.1016/j.imbio.2007.10.008
19. Gordon P, Okai B, Hoare JI, Erwig L, Wilson HM. Socs3 Is a Modulator of Human Macrophage Phagocytosis. *J Leukoc Biol* (2016) 100(4):771–80. doi: 10.1189/jlb.3A1215-554RR
20. Liang YB, Tang H, Chen ZB, Zeng LJ, Wu JG, Yang W, et al. Downregulated Socs1 Expression Activates the Jak1/Stat1 Pathway and Promotes Polarization of Macrophages Into M1 Type. *Mol Med Rep* (2017) 16(5):6405. doi: 10.3892/mmr.2017.7384
21. Wang S, Li B, Qiao H, Lv X, Liang Q, Shi Z, et al. Autophagy-Related Gene Atg5 Is Essential for Astrocyte Differentiation in the Developing Mouse Cortex. *EMBO Rep* (2013) 15(10):1053–61. doi: 10.15252/embr.201338343
22. Yang W, Li Y, Li H, Song H, Zhai N, Lou L, et al. Brucella Dysregulates Monocytes and Inhibits Macrophage Polarization Through Lc3-Dependent Autophagy. *Front Immunol* (2017) 8. doi: 10.3389/fimmu.2017.00691
23. Cheng WA, Gc A, Sy B, Ll A, Yz C, Xz A, et al. Protective Effects of Platycodon Grandiflorus Polysaccharides Against Apoptosis Induced by Carbonyl Cyanide 3-Chlorophenylhydrazone in 3d4/21 Cells. *Int J Biol Macromol* (2019) 141:1220–7. doi: 10.1016/j.ijbiomac.2019.09.086
24. Gordon S, Martinez FO. Alternative Activation of Macrophages: Mechanism and Functions. *Immunity* (2010) 32(5):593–604. doi: 10.1016/j.immuni.2010.05.007
25. Brown GD, Meintjes G, Kolls JK, Gray C, Horsnell WJ. Aids-Related Mycoses: The Way Forward. *Sci Soc* (2014) 22(3):107–9. doi: 10.1016/j.tim.2013.12.008
26. Mccullers JA. The Co-Pathogenesis of Influenza Viruses With Bacteria in the Lung. *Nat Rev Microbiol* (2014) 12(4):252. doi: 10.1038/nrmicro3231
27. Zanoni BC, Gandhi RT. Update on Opportunistic Infections in the Era of Effective Antiretroviral Therapy. *Infect Dis Clin North Am* (2014) 28(3):501–18. doi: 10.1016/j.idc.2014.05.002
28. Sun H, Zhang J, Chen F, Chen X, Zhou Z, Wang H. Activation of Raw264.7 Macrophages by the Polysaccharide From the Roots of Actinidia Eriantha and Its Molecular Mechanisms. *Carbohydr Polym* (2015) 121:388–402. doi: 10.1016/j.carbpol.2014.12.023
29. Ambarus CA, Krausz S, van Eijk M, Hamann J, Radstake TR, Reedquist KA, et al. Systematic Validation of Specific Phenotypic Markers for in Vitro Polarized Human Macrophages. *J Immunol Methods* (2012) 375(1-2):196–206. doi: 10.1016/j.jim.2011.10.013
30. Liu K, Zhao E, Ilyas G, Lalazar G, Lin Y, Haseeb M, et al. Impaired Macrophage Autophagy Increases the Immune Response in Obese Mice by Promoting Proinflammatory Macrophage Polarization. *Autophagy* (2015) 11 (2):271–84. doi: 10.1080/15548627.2015.1009787
31. Lucía S, Gemma A, Érica T, Núria A, Carolina A, Daniel L, et al. Cd5l Promotes M2 Macrophage Polarization Through Autophagy-Mediated Upregulation of Id3. *Front Immunol* (2018) 9. doi: 10.3389/fimmu.2018.00480
32. Surenjav U, Zhang L, Xu X, Zhang X, Zeng F. Effects of Molecular Structure on Antitumor Activities of (1→3)-B-D-Glucans From Different Lentinus Edodes. *Carbohydr Polym* (2006) 63(1):97–104. doi: 10.1016/j.carbpol.2005.08.011
33. Wu M, Wu Y, Zhou J, Pan Y. Structural Characterisation of a Water-Soluble Polysaccharide With High Branches From the Leaves of Taxus Chinensis Var. Mairei. *Food Chem* (2009) 113(4):1020–4. doi: 10.1016/j.foodchem.2008.08.055
34. Liu W, Wang H, Pang X, Yao W, Gao X. Characterization and Antioxidant Activity of Two Low-Molecular-Weight Polysaccharides Purified From the Fruiting Bodies of Ganoderma Lucidum. *Int J Biol Macromol* (2010) 46 (4):451–7. doi: 10.1016/j.ijbiomac.2010.02.006
35. Lo T, Yi HJ, Chao A, Cheng A. Use of Statistical Methods to Find the Polysaccharide Structural Characteristics and the Relationships Between Monosaccharide Composition Ratio and Macrophage Stimulatory Activity of Regionally Different Strains of Lentinula Edodes. *Anal Chim Acta* (2007) 584(1):50–6. doi: 10.1016/j.aca.2006.10.051

Conflict of Interest: The authors declare that the research was conducted in the absence of any commercial or financial relationships that could be construed as a potential conflict of interest.

frontiers | Frontiers in Immunology

ORIGINAL RESEARCH
published: 06 July 2022
doi: 10.3389/fimmu.2022.947655

Selenium Deficiency Leads to Inflammation, Autophagy, Endoplasmic Reticulum Stress, Apoptosis and Contraction Abnormalities *via* Affecting Intestinal Flora in Intestinal Smooth Muscle of Mice

Fuhan Wang, Ni Sun, Hanqin Zeng, Yuan Gao, Naisheng Zhang and Wenlong Zhang**

College of Veterinary Medicine, Jilin University, Changchun, China

Selenium (Se) is a micronutrient that plays a predominant role in various physiological processes in humans and animals. Long-term lack of Se will lead to many metabolic diseases. Studies have found that chronic Se deficiency can cause chronic diarrhea. The gut flora is closely related to the health of the body. Changes in environmental factors can cause changes in the intestinal flora. Our study found that Se deficiency can disrupt intestinal flora. Through 16s high-throughput sequencing analysis of small intestinal contents of mice, we found that compared with CSe group, the abundance of Lactobacillus, Bifidobacterium, and Ileibacterium in the low selenium group was significantly increased, while Romboutsia abundance was significantly decreased. Histological analysis showed that compared with CSe group, the small intestine tissues of the LSe group had obvious pathological changes. We examined mRNA expression levels in the small intestine associated with inflammation, autophagy, endoplasmic reticulum stress, apoptosis, tight junctions, and smooth muscle contraction. The mRNA levels of *NF-κB*, *IκB*, *p38*, *IL-1β*, *TNF-α*, *Beclin*, *ATG7*, *ATG5*, *LC3α*, *BaK*, *Pum*, *Caspase-3*, *RIP1*, *RIPK3*, *PERK*, *IRE1*, *eIF2α*, *GRP78*, *CHOP2*, *ZO-1*, *ZO-2*, *Occludin*, *E-cadherin*, *CaM*, *MLC*, *MLCK*, *Rho*, and *RhoA* in the LSe group were significantly increased. The mRNA levels of *IL-10*, *p62 BcL-2* and *BcL-w* were significantly decreased in the LSe group compared with the CSe group. These results suggest that changes in the abundance of Lactobacillus, bifidobacterium, ileum, and Romboutsia may be associated with cellular inflammation, autophagy, endoplasmic reticulum stress, apoptosis, tight junction, and abnormal smooth muscle contraction. Intestinal flora may play an important role in chronic diarrhea caused by selenium deficiency.

Keywords: intestinal flora, inflammatory, autophagy, tight junction, apoptosis, ERS, smooth muscle contraction, selenium

OPEN ACCESS

Edited by:
Ziwei Zhang,
Northeast Agricultural University, China

Reviewed by:
Ganzhen Deng,
Huazhong Agricultural University, China
Jin Cui,
University of Illinois at Urbana–Champaign, United States
Zi-gong Wei,
Hubei University, China

****Correspondence:***
Naisheng Zhang
zhangns0628@126.com
Wenlong Zhang
zwenlong123@126.com

Specialty section:
This article was submitted to Nutritional Immunology, a section of the journal Frontiers in Immunology

Received: *19 May 2022*
Accepted: *07 June 2022*
Published: *06 July 2022*

Citation:
Wang F, Sun N, Zeng H, Gao Y, Zhang N and Zhang W (2022) Selenium Deficiency Leads to Inflammation, Autophagy, Endoplasmic Reticulum Stress, Apoptosis and Contraction Abnormalities via Affecting Intestinal Flora in Intestinal Smooth Muscle of Mice. Front. Immunol. 13:947655. doi: 10.3389/fimmu.2022.947655

1 INTRODUCTION

Selenium (Se) is a micronutrient that plays a vital role in various physiological processes in humans and animals. Lots of previous research have confirmed the biological effects of Se. Se has antioxidant properties, anti-cancer, enhances immunity, and other efficacy (1–3). Humans and animals need to continuously obtain nutrients from the external world to maintain normal physiological processes. Se is one of them. The body must maintain a balanced Se concentration (4). Long-term Se deficiency can lead to many diseases, such as cancer, liver disease, cardiovascular disease, pancreatic disease, cataracts, diabetes, and other diseases (5–13). Some studies have found that many animals with selenium deficiency develop diarrhea symptoms (14–16). Previous studies have shown that environmental factors can cause changes in the intestinal flora in the body (17–19). Does Se deficiency cause changes in intestinal flora? Is it because of this change that diarrhea develops? What is the mechanism?

The various bacteria that live in the gut are called the gut microbiome, and there are about 10 trillion of them. It contains 100 to 1000 bacterial species and 50 phyla. The gut microbiota is called the second gene (20). With the continuous progress of genome sequencing, culture omics, and other technologies, people are increasingly exploring the structure and function of intestinal flora (21). The regular operation of the intestinal tract must keep the dynamic and relative proportional balance among various microorganisms in the intestinal tract (22). According to their different roles in the gut, they are classified as beneficial, opportunistic, and pathogenic bacteria (23). Intestinal flora is a symbiotic relationship with human beings and plays a very important role in human life and health (24). They play an important role in the immune system, metabolic system, nervous system, and so on (25–27). When the composition of the gut microbiome changes, its function may change, which in turn affects the health of animals. This condition, called intestinal microbiome disorder, can cause diseases of the digestive, nervous, respiratory, and vascular systems (28–31). In recent years, intestinal flora has become a new hot research field. The interaction between intestinal flora and Se in food mainly focuses on the composition of symbiotic flora, the regulation of the metabolic process, and the function of the intestinal mucosal barrier (32, 33). Exploring the relationship between intestinal flora and dietary selenium can provide a theoretical basis for the treatment of intestinal diseases.

Diarrhea is associated with intestinal inflammation, disruption of the intestinal mucosal barrier, and abnormal contraction of the intestinal smooth muscle (34–37). Previous studies have found that bacterial enteritis is associated with disruption of intestinal barrier function (38). Intestinal inflammatory diseases are characterized by intestinal inflammation and the damage of the intestinal mucosa to varying degrees. Widespread epithelial cell death is one of them (39, 40). The release of inflammatory factors can induce apoptosis, necrosis, and autophagy of intestinal tissue cells. Under the action of various stimulating factors, such as infection and oxidative stress, the endoplasmic reticulum will become dysfunctional, leading to endoplasmic reticulum stresses (ERS) (41). Studies have shown that the intestinal biodiversity of ulcerative colitis (UC) and Crohn's disease patients decreased, and the dominant flora and opportunistic pathogens changed (42, 43). Abnormal contraction of intestinal smooth muscle can cause diarrhea with intestinal motility disorder (44).

An intact intestinal mucosal barrier is essential for maintaining the host's physiological barrier and innate immune function (45). It plays an important role in the epithelial transport of nutrients and metabolites and in the defense of penetrating microbiota (46). Intestinal barrier function depends primarily on the integrity of the epithelium and adjacent cell-to-cell connections (47). These connections are primary adhesion and tight adhesion complexes (48). A tight junction is usually between two adjacent cells at the top of the epithelium, where the plasma membrane is almost fused and tightly joined. Tight junctions, located at the top of intestinal epithelial cells, are the most important type of junctions between cells (49). When tight junctions are lost, intercellular permeability increases significantly, resulting in disruption of the intestinal epithelial barrier (50). *ZO-1*, *ZO-2*, and *Occludin* are classic tight junction proteins and can be used as common indicators to observe tight junction damage (51).

Smooth muscle contractions occur in two main ways. The calcium-dependent pathway mainly involves Ca^{2+} binding to calmodulin (*CaM*) to form a Ca^{2+}-CaM complex (52). It can activate myosin light chain kinase (*MLCK*) in the cytoplasm. The non-calcium-dependent pathway is associated with *RhoA/Rho* kinase (*ROCK*) signaling pathway (53). The key signaling molecules of the *RhoA/ROCK* pathway include *RhoA*, myosin light chain kinase (*MLCK*), and myosin light chain (*MLC*) (54). Many studies have confirmed that gut microbiota is closely related to gastrointestinal dynamics, and a healthy gut microecology helps promote intestinal motility (55). The imbalance of intestinal flora may be the key factor in intestinal barrier dysfunction and intestinal motility dysfunction.

In this study, we sequenced the intestinal microflora of the mouse model. This study investigated the effect of selenium deficiency on intestinal epithelial cell tight junction, intestinal inflammation, and intestinal smooth muscle contraction due to changes in the intestinal flora. It provides theoretical guidance for the follow-up research.

2 MATERIALS AND METHODS

2.1 Animals and Group

Female c57 mice aged 4-5 weeks (n = 40,18g body weight) were selected. These mice were divided randomly into two groups and 20 mice in each group. The environmental parameters such as temperature, relative humidity, wind speed, and the illumination of each group were controlled and kept consistent. Low selenium group (LG): 20 mice were fed with Se-deficient mouse diet (Se content: 0.01mg Se/kg). Normal Se group (NG): 20 mice were fed with normal Se content mouse diet (Se content: 0.15mg Se/kg). Rat food is customized for selenium deficiency rat food and

normal rat food from Trophic Animal Feed High-tech Company, China. The mice were free to eat and drink. The mice died of cervical dislocation after being fed at room temperature for 50 days and were quickly sampled and stored in a -80°C refrigerator. The animal study was reviewed and approved by the Institutional Animal Care and Use Committee (IACUC) of Jilin University.

2.2 Histopathology Staining

Small intestinal tissue was fixed in 4% paraformaldehyde and paraffin-embedded overnight. The small intestine sections were cut into two μm thick and soaked overnight in ZGSJ (Masson A). The small intestine sections were stained with Weigert's hematoxylin (Masson A and Masson B in equal amounts) for 1 minute, differentiated by 1% acid ethanol, Then it was stained in scarlet magenta solution (Masson D) for 6 min, differentiated in phospho-molybdenum-phosphotungstate solution (Masson E) for 1 min, and transferred directly (without rinsing) to aniline blue solution (Masson F) for 2-30s. Then, rinse briefly in distilled water for 2-5 minutes. Finally, dehydration through anhydrous ethanol, xylene transparent, and neutral sealant. The sections were scanned by Pannoramic 250 slide scanner (3D HISTECH). Micrographs were analyzed by the blind method. Collagen volume fraction (CVF) was observed by image analysis system software (HALO, Indica Labs, American). Technical support was provided by Servicebio, Inc. (Wuhan, China).

2.3 Evaluation of the Degree of Apoptosis in Late Apoptotic Cells

Chromosomal DNA double-strand or single-strand breaks produce sticky 3'-OH ends. Under the catalysis of deoxyribonucleotide terminal transferase (DTT), dUTP with fluorescein molecule is labeled to the 3'end of DNA. Observe the stained apoptotic cells through a fluorescence microscope. Dewax the paraffin sections to water, break the membranes, incubate the Tunel reaction solution, microwave repair, incubate the primary antibody overnight at 4°C, add the secondary antibody, DAPI staining the nucleus, anti-fluorescence quenching and mounting, microscopic examination and taking pictures, and observe the results.

2.4 Real-Time PCR

Total RNA was extracted from frozen intestinal tissue. The concentration and purity of RNA solution were determined by UV spectrophotometry at 260nm and 280nm. Targeting specific primers were synthesized by reverse transcription design of glyceraldehyde 3-phosphate dehydrogenase (GAPDH) based on known sequences. The ABI PRISM7700 processing system was used for real-time quantitative PCR. For each gene to be measured, the cDNA template and sample cDNA of the expressed gene is selected for PCR reaction. There are 40 cycles, such as 94°C for 30 seconds, 94°C for 5 seconds, and 60°C for 30 seconds. Each experiment was repeated three times, and each sample was repeated three times. GAPDH was used as an endogenous internal standard control. The primers were purchased from Sangon Biotech, Shanghai. Primer sequences are shown in **Table 1**.

2.5 Intestinal Flora Assay

In this study, genomic DNA was extracted from intestinal contents by CTAB or SDS. After that, agarose gel electrophoresis was used to detect the purity and concentration of DNA. An appropriate amount of DNA was taken into the centrifuge tube and diluted to 1ng/μ L with sterile water. Using diluted genomic DNA as a template, specific primers with barcodes were used according to the 16S V3-V4 region of the sequencing area. New England Biolabs Phusion® High Fidelity PCR Master Mix with GC Buffer and High Fidelity enzyme for PCR amplification efficiency and accuracy. PCR products were detected by electrophoresis with 2% agarose gel. The qualified PCR products were purified by magnetic beads, quantified by enzyme standard, and mixed in equal quantities according to the concentration of PCR products. After full mixing, PCR products were detected by 2% agarose gel electrophoresis, and the target bands were recovered using gel recovery kits provided by Qiagen. TruSeq® DNA PCR-free Sample Preparation Kit was used for library construction. The constructed library was quantified by Qubit and Q-PCR. After the library was qualified, NovaSeq6000 was used for machine sequencing. Each sample data was separated from the off-machine data according to the Barcode sequence and PCR primer sequence. Qiime software (Version 1.9.1) was used to calculate and analyze the data. This experiment was commissioned by Novogene Tianjin Company.

2.6 Statistical Analysis

SPSS 22.0 statistical software was used for statistical analysis. All data were expressed as ± standard deviation (SD) measurements. The data were compared by the T-test method. The significance of the difference criterion is $P<0.05$.

3 RESULT

3.1 Se Deficiency Resulted in Changes in the Composition and Structure of Intestinal Flora in Mice

3.1.1 Species Lightning Strike Curve

The species accumulation curve is used to determine whether the available sample size is sufficient for a high-throughput community analysis of the species. If the upward trend of this curve is always steep, it indicates that the sample size is too small to support the following analysis. As the number of samples increases, the upward trend of the curve is relatively gentle, indicating that the original sample size is large. Therefore, it is necessary to measure the cumulative curve of species before all kinds of analyses of fecal flora. If the cumulative curve always shows an upward trend, it indicates that the sample size is insufficient to support the analysis of species composition

TABLE 1 | Primer sequence list.

IL-1β	Forward: 5′- TTCCCA TTAGACAACTGC-3′
	Reverse: 5′- CTGTAGTGTTGTATGTGATC -3′
IL-6	Forward: 5′- CAGAACCGCAGTGAAGAG -3′
	Reverse: 5′- CAGAACCGCAGTGAAGAG -3′
TNF-α	Forward:5′- CTCA TTCCTGCTTGTGGC -3′
	Reverse: 5′- CACTTGGTGGTTTGCTACG -3′
IL-10	Forward: 5′- CAGAGCCAAAGCAGTGAGC -3′
	Reverse: 5′- TGACCCAGTCCATCCAGAG -3′
NF-κB	Forward:5′-CCATAGCCATAGTTGCGGTCCTTC-3′
	Reverse: 5′- CGTTCTTCCCTCCCTTTTCCTTTCC-3′
IκB-α	Forward:5′-GAATCACCAGAACATCGTGAAG-3′
	Reverse: 5′- CAGTACTCCATGATTAGCACCT-3′
p38	Forward:5′-GCCGCTTAGTCACATACC-3′
	Reverse: 5′-GCCGCTTAGTCACATACC-3′
ATG7	Forward:5′-GTGTACGATCCCTGTAACCTAG-3′
	Reverse: 5′- GATGCTATGTGTCACGTCTCTA-3′
ATG5	Forward:5′-AGTCAAGTGATCAACGAAATGC-3′
	Reverse: 5′- TATTCCATGAGTTTCCGGTTGA-3′
p62	Forward:5′-GAACACAGCAAGCTCATCTTTC-3′
	Reverse: 5′- AAAGTGTCCATGTTTCAGCTTC-3′
Beclin	Forward:5′-TAATAGCTTCACTCTGATCGGG-3′
	Reverse: 5′- CAAACAGCGTTTGTAGTTCTGA-3′
LC3α	Forward:5′-CTGTCCTGGATAAGACCAAGTT-3′
	Reverse: 5′- GTCTTCATCCTTCTCCTGTTCA-3′
PERK	Forward:5′-GTAGCCACGACCTTCATC-3′
	Reverse: 5′-GTAGCCACGACCTTCATC-3′
IRE1	Forward:5′-TTGAAGTGGACAGTGAAGG-3′
	Reverse: 5′-TTGAAGTGGACAGTGAAGG-3′
eIF2α	Forward:5′-TGGTGGTTATCCGTGTTG-3′
	Reverse: 5′-CCGATTGCTTGAAGATGTC-3′
GRP78	Forward:5′-GTCAGGGAGAGGAGGAAT-3′
	Reverse: 5′-TGGTGTCACTTATGGTAGAA-3′
CHOP2	Forward:5′-TACACCACCACACCTGAA-3′
	Reverse: 5′-GCACCACTACACCTGATAG-3′
BcL-2	Forward:5′-CCTCCAATACTCACTCTGTC-3′
	Reverse: 5′-TACCTGCGTTCTCCTCTC-3′
BcL-w	Forward:5′-CCGTCTTGTGGCATTCTT-3′
	Reverse: 5′-AGCACTGTCCTCACTGAT-3′
Pum	Forward:5′-GATTCGGAAGCAGCAGTT-3′
	Reverse: 5′-GGAGCAGCAGAGATGTATC-3′
p53	Forward:5′-TGGAAGACAGGCAGACTT-3′
	Reverse: 5′-GTGATGATGGTAAGGATAGGT-3′
Bak	Forward:5′-GGAATGCCTACGAACTCTT-3′
	Reverse: 5′-CCAACAGAACCACACCAA-3′
Caspase3	Forward:5′-TGGTTGACGCAGTAGAGA-3′
	Reverse: 5′-GACGCCTTCACACTTCAT-3′
RIP1	Forward:5′-TGGTTGACGCAGTAGAGA-3′
	Reverse: 5′-GACGCCTTCACACTTCAT-3′
RIPK3	Forward:5′-TGCCTTGACCTACTGATTG-3′
	Reverse: 5′-TTCCGTGACATAACTTGACA-3′
ZO-1	Forward:5′- AACCCGAAACTGATGCTGTGGATAG -3′
	Reverse:5′- CGCCCTTGGAATGTATGTGGAGAG -3′
ZO-2	Forward:5′- CATGTCTCTAACGGATGCTCGGAAG -3′
	Reverse:5′- GTTTAGGGCTGGGATGTTGATGAGG -3′
Occludin	Forward:5′- TGGAGGCTATGGCTATGGCTATGG-3′
	Reverse:5′- TTACTAAGGAAGCGATGAAGCAGAAGG-3′
E-cadherin	Forward: 5′- ACCAGCAGTTCGTTGTCGTCAC-3′
	Reverse: 5′- GTTCCTCGTTCTCCACTCTCACATG-3′
CaM	Forward:5′-ACAAGGATGGGAATGGTTACAT-3′
	Reverse: 5′- TGCAGTCATCATCTGTACGAAT-3′
MLC	Forward:5′-GATAGCCATCAGCAGCCTCACATC-3′
	Reverse: 5′- GCAACAGGAGCAGCAGGAGAAC-3′
MLCK	Forward:5′-GGGCTGCCTCTCATCATCAATACG-3′
	Reverse: 5′- TGGATTCTGCTTCTGTGGGTAGGG-3′
RhoA	Forward:5′-ACGGTGTTTGAAAACTATGTGG-3′
	Reverse: 5′- GACAGAAATGCTTGACTTCTGG-3′
Rho	Forward:5′-GTCTGATCTTCGTGGTAGACTG-3′
	Reverse: 5′- CTCATCTCCCGGTCATTGATAA-3′
GAPDH	Forward: 5′-CCCAGAAGACTGTGGATGG-3′
	Reverse: 5′- ACACATTGGGGGTAGGAACA-3′

structure. On the contrary, if the curve rises gently with the increase of samples, it indicates that the sample size is sufficient to reflect the species composition of the community. It can be seen in **Figure 1** that the species accumulation curve of mouse intestinal contents collected in this experiment rises gently, indicating that the collected feces samples are sufficient for species composition analysis in this experiment.

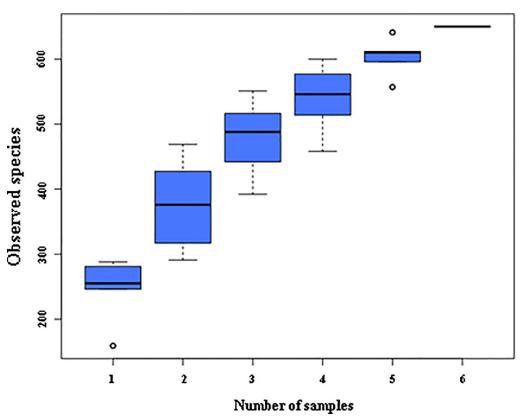

FIGURE 1 | Species accumulation box plot. The abscissa is the sample size; The y-coordinate is the number of OTU after sampling.

3.2 Analysis of Relative Abundance of Species

Figures 2A, B is a species composition analysis of all samples at the genus level. When analyzed by group, it could be seen that the composition of fecal flora changed significantly after the LSe group. The most abundant strains in the CSe were Dubosiella (25.4976%), Lactobacillus (12.2355%), and Romboutsia (18.7987%) Faecalibaculum (11.1052%). The bacteria with the highest abundance in LSe group were Dubosiella (22.8274%), Lactobacillus (18.7323%), Bifidobacterium (20.2125%) and Ileibacterium (11.0841%). The abundance of Lactobacillus, Bifidobacterium, and Ileibacterium in the LSe group was higher than in the CSe. Romboutsia abundance in the LSe group was significantly lower than that in CSe. **Figures 2C, D** shows the species composition analysis of all samples at the species level. The abundance of Lactobacillus_johnsonii, Bifidobacterium_pseudolongum, and Ileibacterium_valens in the LSe group was significantly higher than that in the CSe group. The abundance of all other bacteria was lower or none in the CSe group.

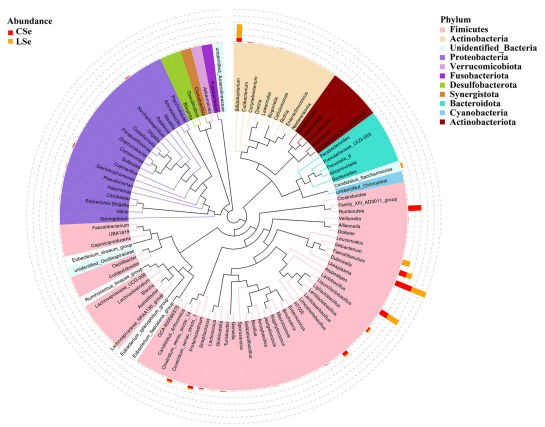

FIGURE 3 | Phylogenetic tree analysis of genus level species.

3.3 Phylogenetic Tree Analysis of Genus Level Species

The representative sequences of the top100 genera were obtained by multiple sequences alignment to further study the phylogenetic relationships of genus-level species. The resulting display was shown in **Figure 3**. The phylogenetic tree was constructed by the representative sequences of the horizontal species of the genus. The colors of branches and fan-shaped segments represented the corresponding phylum, and the accumulation histogram outside the fan ring represented the abundance distribution information of the genus in different samples. The relative dominant genus and phylum of LSe could be identified. Firmicutes phylum Ileibacterium is the most obvious bacterium.

3.4 Alpha Diversity Index Analysis

3.4.1 Analysis of Differences in Alpha Diversity Index Between Groups

Figure 4 shows the analysis results of Alpha Diversity index. The repeatability among three samples was poor in the LSe group. Chao1 index reflects the presence of low abundance species, and the CSe group is higher than the LSe group. The species richness of the LSe group was lower than that of the CSe group. Simpson index and Shannon index indicated that the diversity and evenness of species distribution of the CSe group were better than that of the LSe group. ACE index and Observed species index reflect the number of randomly selected bacterial community species in the CSe group is more than that in the LSe group. PD index indicated that species in the LSe group had more complex genetic relationships and longer evolutionary distances. Good's Coverage index reflects the sequencing depth.

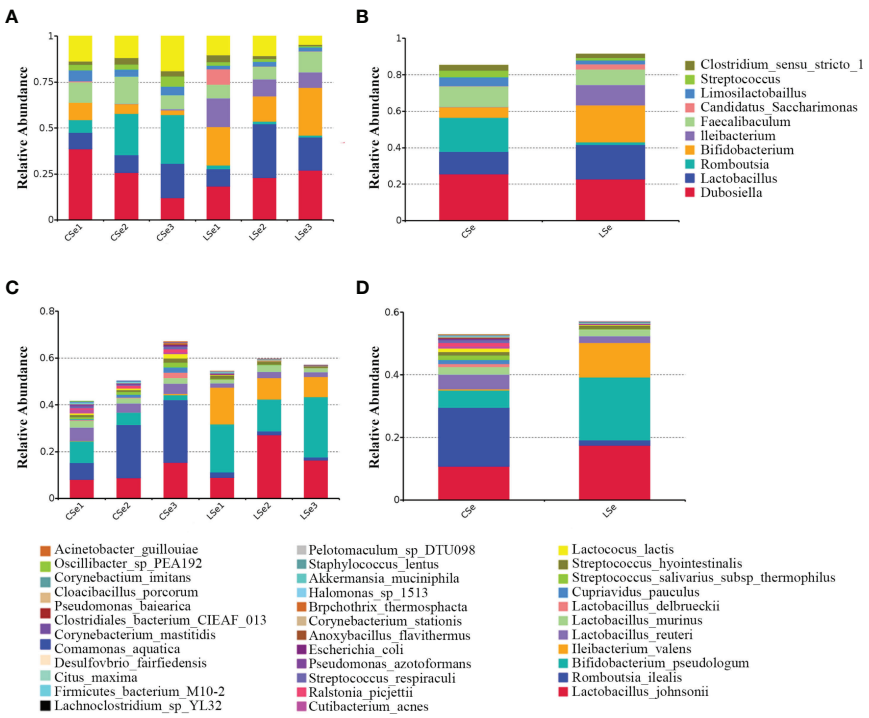

FIGURE 2 | Histogram of relative abundance of species. **(A)** Histogram of relative abundance of sample species (Top 10, Genus). **(B)** Histogram of relative abundance of grouped species (Top 10, Genus). **(C)** Histogram of relative abundance of sample species (Top 35, Species). **(D)** Histogram of relative abundance of grouped species (Top 35, Species).

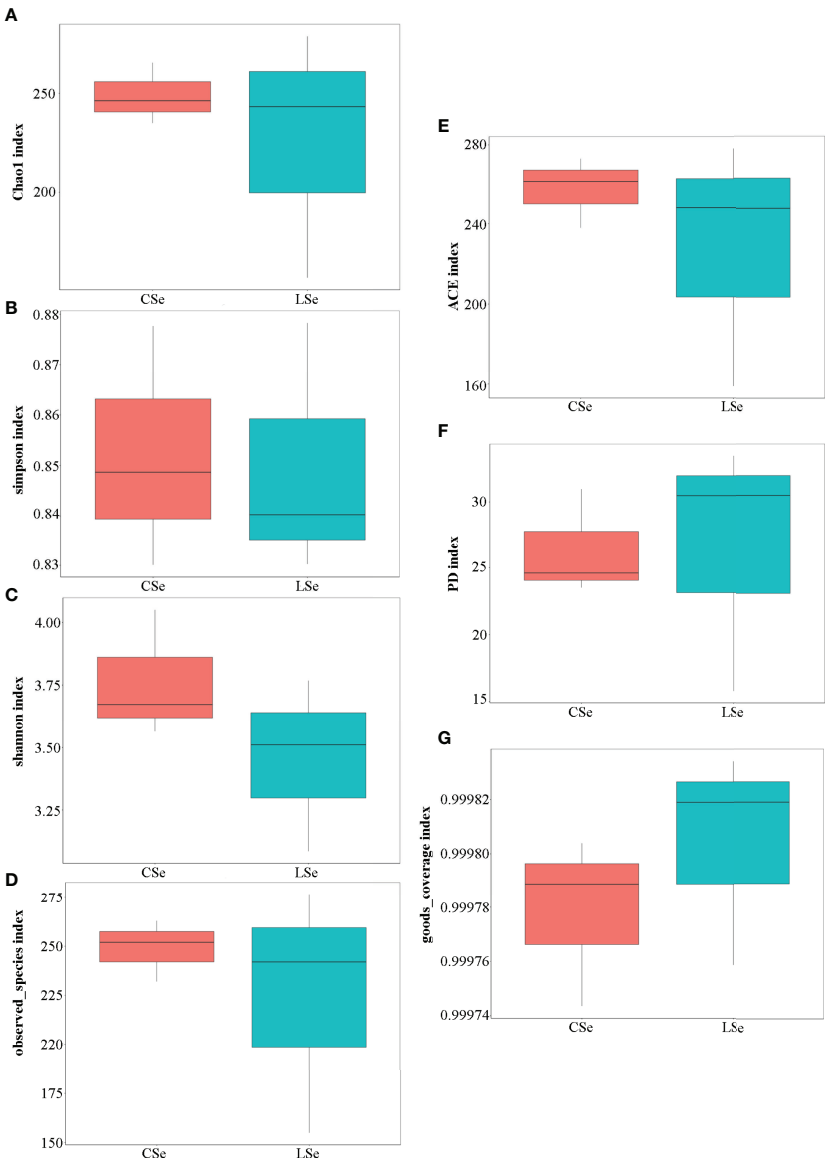

FIGURE 4 | Alpha Diversity index analysis. **(A)** Chao1 index; **(B)** Simpson index; **(C)** Shannon index; **(D)** Observed species index; **(E)** ACE index; **(F)** PD index **(G)** Good's Coverage index.

3.4.2 Analysis of species diversity curve

The rarefaction Curve and Rank Abundance curve are usually describing the diversity of samples within groups. In **Figures 5A, B**). The dilution curve reflects the rationality of the two groups of sequencing data, and indirectly reflects the richness of species in the samples. When the curve tends to be flat, the sequencing data amount is progressive and reasonable, and more data amount will only produce a few new species. The rank Abundance curve in **Figures 5C, D** can intuitively reflect the Abundance and evenness of species in samples. The greater the span of the curve along the horizontal axis, the higher the species richness. In the vertical direction, the smoothness of the curve reflects the uniformity of species in the sample. Vertically, the smoothness of the curve reflects the uniformity of species in the sample. The flatter the curve, the more evenly distributed the species. In general, the species richness and evenness of the CSe group were better than that of the LSe group.

3.5 Analysis of Differences in Beta Diversity Index Between Groups

3.5.1 Beta Diversity Analysis

Beta Diversity is a comparative analysis of microbial community composition of different samples. As shown in **Figures 6A, B**, Unifrac distance is a method to calculate the distance between

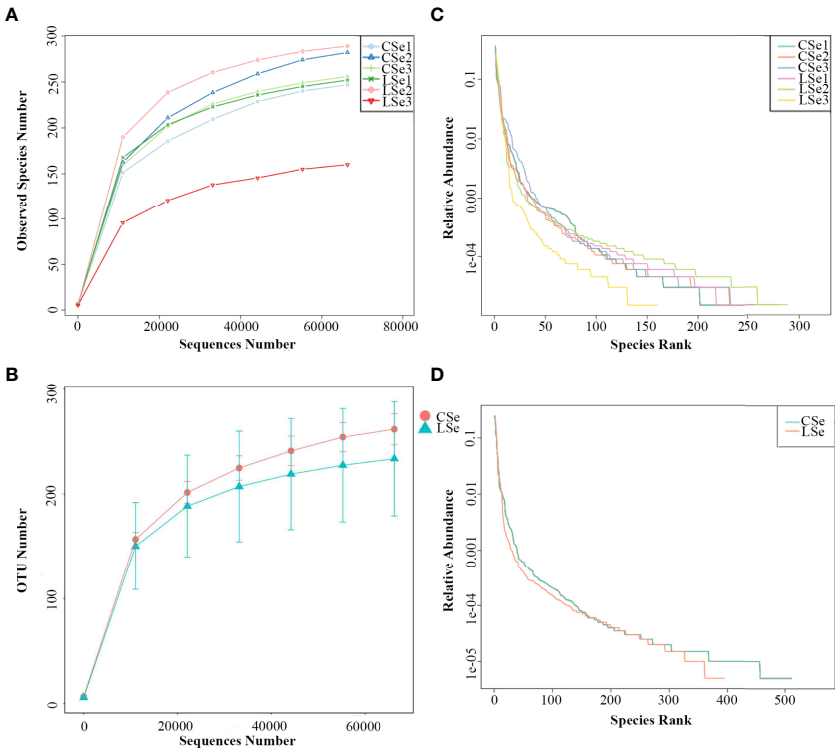

FIGURE 5 | Species dilution curve. **(A)** rarefaction Curve (Simple); **(B)** Rank Abundance (Simple);(C) rarefaction Curve (Group); **(D)** Rank Abundance (Group).

samples by using the evolutionary information between microbial sequences in each group. Weighted Unifrac distance and Unweighted Unifrac distance were used to measure species diversity differences between the two samples. The results showed that the diversity difference between the CSe group was smaller than that of the LSe group.

3.5.2 Principal Component Analysis

PCA (Principal Component Analysis) is a method to extract the most important elements and structures in data based on Euclidean Distances. PCA analysis can extract two coordinate axes that reflect the difference between samples to the greatest extent. The differences in multi-dimensional data are reflected in the two-dimensional coordinate graph, and the simple rules under the complex data background are revealed. The more similar the community composition of the samples is, the closer they are to the PCA diagram. As shown in **Figure 6C**, at the genus level, the community composition of the LSe group samples was more similar.

3.5.3 Principal Coordinate Analysis

To characterize the overall differences in the gut microbiome between groups, we performed a principal coordinate analysis (PCoA) of unweighted UniFrac distances. There were significant differences between the LSe group and CG (**Figure 6D**). The results also showed that the bacterial community structure in the feces of mice was significantly changed by Se deficiency.

3.5.4 Non-Metric Multi-Dimensional Scaling (NMDS)

NMDS (non-metric multi-dimensional Scaling) is a ranking method suitable for ecological studies. NMDS is a nonlinear model based on bray-Curtis distance, which is reflected in a two-dimensional plane in the form of points according to the species information contained in the sample. It can better reflect the nonlinear structure of ecological data. NMDS analysis can reflect the differences between and within groups of samples. NMDS analysis results based on OTU level are shown in **Figure 6E**. There are significant differences between the two groups of samples.

3.6 LefSe Analysis of Bacterial Community Structure in Small Intestinal Contents of Mice

LEfSe is used to detect OTUs or bacterial system types (phylum to order level) in different feeding groups. In **Figure 7**, Actinobacteria and Ileibacterium_valens in the LSe group were significantly higher than those in the CG group, which might be the reason for the change in intestinal mucosal barrier in mice.

3.7 Tax4Fun Function Predictive Analysis

Tax4Fun function prediction is used by the nearest neighbor method based on the minimum 16SrRNA sequence similarity. The specific method was to extract the 16S rRNA gene sequence of the whole genome of prokaryotes from the KEGG database and compare it with the SILVA SSU Ref NR database (BLAST

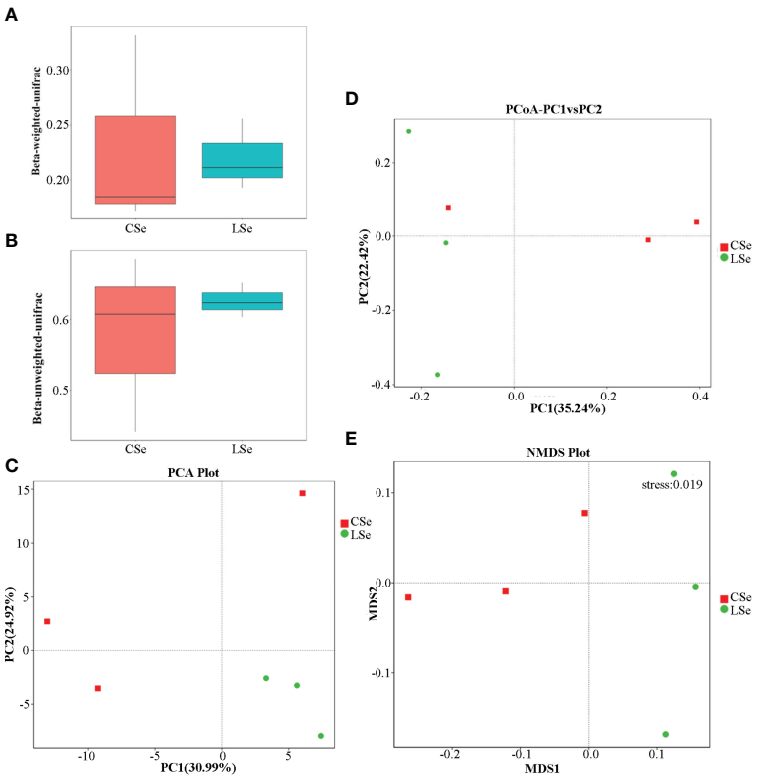

FIGURE 6 | Analysis of differences in Beta diversity index between groups. **(A)** Beta-weighted-unifrac index; **(B)** Beta-unweighted-unifrac index; **(C)** PCA (Principal Component Analysis); **(D)** PCoA (principal coordinate analysis); **(E)** NMDS (non-metric multi-dimensional Scaling).

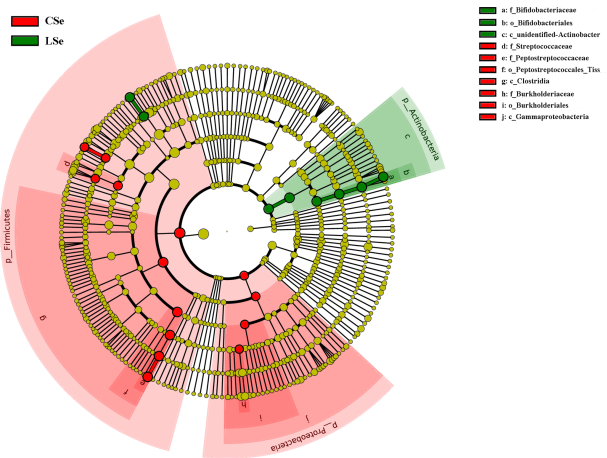

FIGURE 7 | LefSe analysis of bacterial community structure in small intestinal contents of mice.

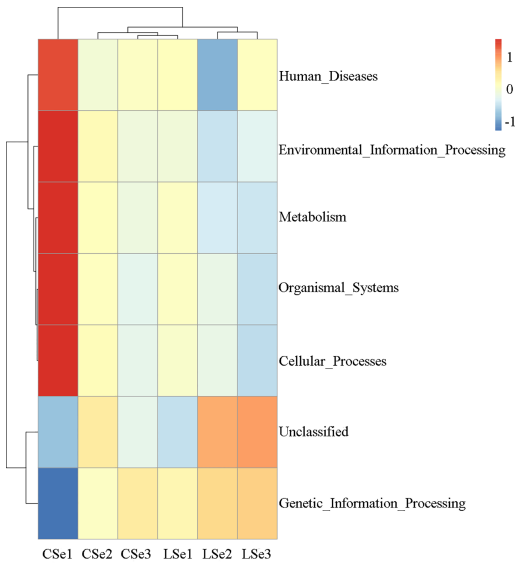

FIGURE 8 | Tax4Fun function predictive analysis. According to the functional notes and abundance information of samples in the database, the top 35 functions and their abundance information in each sample were selected to draw a heat map. And cluster from the level of functional difference. The abscissa is the sample name and the ordinate is the feature comment.

bitscore >1500) using the BLASTN algorithm to establish a correlation matrix. The whole-genome functional information of prokaryotes annotated by UProC and PAUDA in the KEGG database was corresponding to the SILVA database to realize the

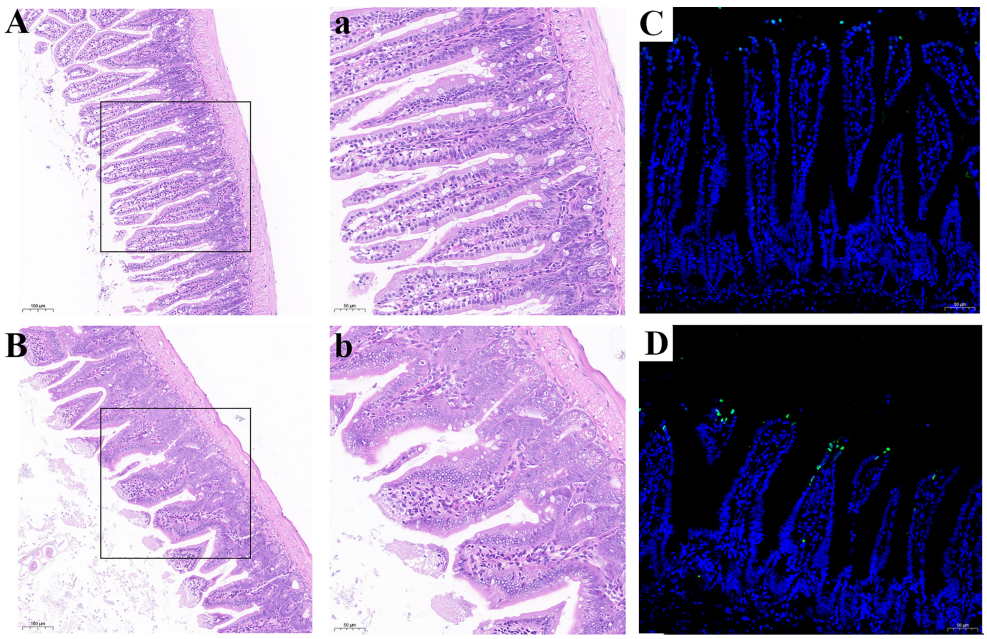

FIGURE 9 | Se deficiency caused apoptosis and injury of small intestine in mice. **(A, B)** Histopathology of small intestine. **(A)** CSe group; (a) An enlarged image of CSe Group; **(B)** LSe group; (b) An enlarged image of LSe group; **(C, D)** TUNEL analysis of small intestinal tissue; **(C)** CSe group; **(D)** LSe group.

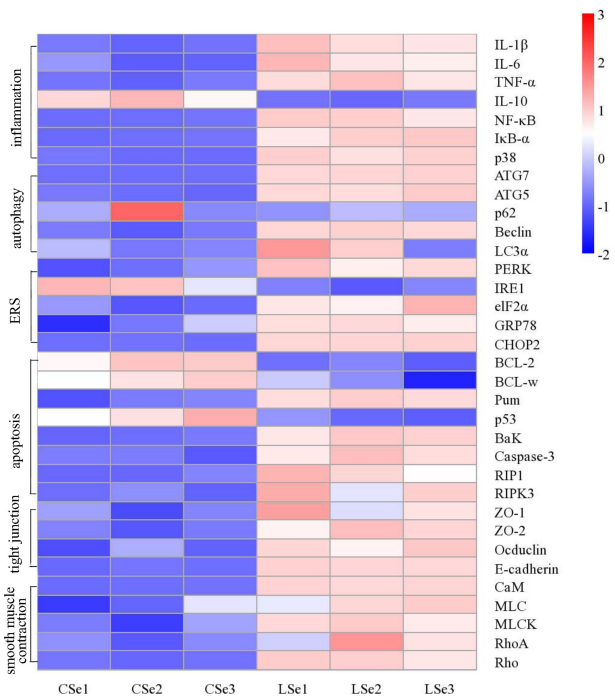

FIGURE 10 | Analysis of mRNA expression level in small intestine tissue. The Ct values measured by PCR were calculated by 2-△△ Ct and then standardized. The abscissa is the sample name and the ordinate is the gene name. $p < 0.05$.

functional annotation of the SILVA database. SILVA database sequence was used as a reference sequence to cluster OTU and obtain functional annotation information. Changes of Intestinal microflora induced by Selenium Deficiency and their relationship with Human Diseases, Environmental Information Processing, Metabolism, Organismal Systems, Cellular Processes Genetic information processing. The result of the annotation is shown in **Figure 8**.

3.8 Se Deficiency Caused Apoptosis and Injury of Small Intestine in Mice

Histological analysis was shown in **Figures 9A, B**. Compared with the CSe group, the LSe group had lower villi height and even fractures. Goblet cells are reduced. The mucosa and muscular arrange the cells lose. TUNEL test results are shown in **Figures 9 C, D**, and the green fluorescence intensity of the LSe group is significantly higher than that of the CSe group. It suggests that selenium deficiency promotes apoptosis of small intestinal cells.

3.9 Selenium Deficiency Leads to Inflammation, Autophagy, Endoplasmic Reticulum Stress, Apoptosis, Tight Junctions and Smooth Muscle Contraction in Small Intestinal Tissues of Mice

We examined gene levels in the small intestine related to inflammation, autophagy, endoplasmic reticulum stress, apoptosis, tight junctions and smooth muscle contraction. The results were shown in **Figure 10**. The mRNA levels of *NF-κB, IκBα*, *p38, IL-1β*, and *TNF-α* in the LSe group were significantly increased, while the mRNA levels of *IL-10* were significantly decreased. It is evidence of inflammation in the small intestine. The mRNA levels of *Beclin, ATG7, ATG5*, and *LC3α* were significantly increased in the LSe group, while the mRNA levels of *p62* were slightly decreased compared with the CSe group. It indicates that the cells of the small intestine are autophagy. Compared with CSe, mRNA levels of *PERK, IRE1, elF2α*, *GRP78*, and *CHOP2* were significantly increased. It indicates endoplasmic reticulum stress in the cells of the small intestine. The mRNA levels of *BaK*, *Pum*, *Caspase-3*, *RIP1*, and *RIPK3* were significantly increased in the LSe group, while the mRNA levels of *BcL-2* and *BcL-w* were significantly decreased in the LSe group compared with the CSe group. It indicates that the cells of the small intestine have undergone apoptosis. The mRNA levels of tight junction proteins such as *ZO-1, ZO-2, Occludin*, and *E-cadherin* were significantly increased. It suggests that the tight junctions of the small intestine were broken in the LSe group. The expression of LSe smooth muscle contraction-related genes such as *CaM*, *MLC*, *MLCK*, *Rho*, and *RhoA* increased. It indicates abnormal contraction of the small intestine smooth muscle.

4 DISCUSSION

Se is a micronutrient. It has biological functions such as anti-oxidation, anti-cancer, and enhancing immunity (2, 3). Se deficiency can cause weakened immunity, muscle atrophy, arrhythmia, and other symptoms. Previous studies have shown that Se regulates gut microbiota. Some studies have also found that chronic Se deficiency can cause chronic diarrhea (56). Our study shows that Se deficiency does cause intestinal inflammation in mice. It confirms this view. What is the cause of Se deficiency leading to diarrhea? Is it related to changes in gut flora?

Intestinal flora has become a new hot research field. The interaction between intestinal flora and Se in food mainly focuses on the composition of symbiotic flora, the regulation of the metabolic process, and the function of the intestinal mucosal barrier. To further evaluate the effects of Se deficiency on intestinal microbiota in mice, we extracted the contents of the small intestine for 16S high-throughput sequencing analysis. The results showed that the intestinal microbiota of the LSe group changed significantly compared with that of CG. The strains with the highest abundance in the CG were Dubosiella, Romboutsia, Lactobacillus, and Faecalibaculum. Dubosiella, Bifidobacterium, Lactobacillus, and Ileibacterium had the highest abundance in the LSe group. The composition of microflora changed obviously. Compared with CG, the abundance of Lactobacillus, Bifidobacterium, and Ileibacterium with LSe significantly increased, while the abundance of Romboutsia significantly decreased or almost disappeared. The abundance changes of Ileibacterium and Romboutsia are the most obvious. The abundance changes of these two bacteria likely cause the abundance changes of Dubosiella and Lactobacillus. But this still needs to be further studied. The result suggests that selenium deficiency can lead to changes in the composition of intestinal flora.

Our study showed significant pathological changes in small intestinal tissues of mice in the LSe group compared with CSe. The studies on gene levels showed that cytokines *IL-1β, TNF-α*, and *IL-6* were significantly elevated. The LSe group also significantly increased the expression of *NF-κB* and the *IκBα* gene in the classic inflammatory signaling pathway. This confirmed that selenium deficiency can cause inflammation of the small intestine through intestinal flora.

Autophagy plays an important role in regulating cell death. *Beclin* is an autophagy-related gene and participates in the formation of autophagosomes (57). *ATG5* and *ATG7*, *LC3α* play a key role in autophagy elongation (58). *p62* is considered one of the markers of autophagy ability (59). The result was found that the mRNA levels of *Beclin*, *ATG5*, *ATG7*, and *LC3α* in the LSe group were significantly increased, while the mRNA levels of *p62* were significantly decreased. It proves that selenium deficiency promotes autophagy through intestinal flora.

ER is one of the most important organelles in the cell, which is mainly involved in protein processing and modification, guiding its correct folding and assembly. ERS may be affected by various stimuli such as infection and oxidative stress. *PERK*, *IRE1*, *elF2α*, *GRP78*, and *CHOP2* are key genes in er stress (60). PCR analysis showed that the mRNA levels of *PERK*, *IRE1*, *elF2α*, *GRP78*, and *CHOP2* were increased in the LSe group. Other studies have shown that dysbiosis can cause er stress. This proves that

selenium deficiency promotes endoplasmic reticulum stress through intestinal flora.

TUNEL analysis showed that the apoptosis level of LSe intestinal epithelial cells was increased. *BaK* induces apoptosis through mitochondrial pathway activation of *Caspase-3* (61). p53 can promote cell apoptosis by blocking cell cycle activation of *Caspase-3* (62). *Pum* gene can promote cell apoptosis, *BcL-2* and *BcL-w* have an anti-apoptotic effect (63). *RIP1* and *RIPK3* play an important role in necrotic apoptosis (64). It was confirmed that the mRNA levels of *BaK*, *Pum*, *Caspase-3*, *RIP1*, and *RIPK3* were significantly increased in the LSe group, while the mRNA levels of *BcL-2* and *BcL-w* were significantly decreased in the LSe group compared with the CSe group. It indicates that the cells of the small intestine have undergone apoptosis. Selenium deficiency induces apoptosis of intestinal epithelial cells through intestinal flora.

Tight junction is an important structure to maintain a balance of intestinal mucosal barrier function. *ZO-1*, *ZO-2*, *Occludin*, and e-cadherin are important components of tight junction. The mRNA levels of tight junction proteins *ZO-1*, *ZO-2*, *Occludin*, and *E-cadherin* were significantly increased in the LSe group. The result suggests that the tight junctions of the small intestine were broken in the LSe group. It Indicates that selenium deficiency can disrupt the intestinal flora by tightly connecting them.

Abnormal contraction of intestinal smooth muscle can cause diarrhea with intestinal motility disorder. The expression of smooth muscle contractile related genes such as *CaM*, *MLC*, *MLCK*, *Rho* and *RhoA* increased. The result confirmed abnormal contraction of small intestinal smooth muscle in the LSe group. Selenium deficiency can cause abnormal contraction of intestinal smooth muscle through the intestinal flora.

In general, the changes in the abundance of Lactobacillus, Bifidobacterium, Ileibacterium and Romboutsia may be related to intestinal tissue cell inflammation, autophagy, endoplasmic reticulum stress, apoptosis, tight junction and abnormal smooth muscle contraction. Romboutsia is a bacterium that needs selenium to thrive properly. But the specific role each of these bacteria plays in selenium deficiency-induced intestinal inflammation is unknown. That remains to be explored.

In conclusion, long-term dietary Se deficiency does lead to changes in the composition of intestinal flora. Se deficiency can cause significant changes in species abundance of Lactobacillus, Bifidobacterium, Ileibacterium and Romboutsia. Species abundance of Lactobacillus, Bifidobacterium and Ileibacterium may be positively correlated with intestinal inflammation. Romboutsia was negatively correlated with intestinal inflammation. Intestinal microflora may play an important role in the response of intestinal tissue cell inflammation, autophagy, endoplasmic reticulum stress, apoptosis, tight junction, and abnormal smooth muscle contraction induced by selenium deficiency.

DATA AVAILABILITY STATEMENT

The original contributions presented in the study are included in the article/supplementary material. Further inquiries can be directed to the corresponding authors.

ETHICS STATEMENT

The animal study was reviewed and approved by Institutional Animal Care and Use Committee (IACUC) of Jilin University.

AUTHOR CONTRIBUTIONS

FW, NS, and WZ conceived and designed the research; FW, NS, HZ, and YG performed the research and acquired the data, and FW analyzed and interpreted the data and wrote sections of the manuscript. All authors contributed to manuscript revision, read, and approved the submitted version.

ACKNOWLEDGMENTS

The authors gratefully acknowledge NZ from Jilin University for his theoretical guidance. The authors gratefully acknowledge Professor Meng-yao Guo from Northeast Agricultural University for providing experimental technical analysis for this study.

REFERENCES

1. Liu GX, Jiang GZ, Lu KL, Li XF, Zhou M, Zhang DD, et al. Effects of Dietary Selenium on the Growth, Selenium Status, Antioxidant Activities, Muscle Composition and Meat Quality of Blunt Snout Bream, Megalobrama Amblycephala. *Aquacult Nutr* (2017) 23:777–87. doi: 10.1111/anu.12444
2. Dehghani M, Shokrgozar N, Ramzi M, Kalani M, Golmoghaddam H, Arandi N. The Impact of Selenium on Regulatory T Cell Frequency and Immune Checkpoint Receptor Expression in Patients With Diffuse Large B Cell Lymphoma (DLBCL). *Cancer Immunol Immunother* (2021) 70:2961–9. doi: 10.1007/s00262-021-02889-5
3. Li Q, Chen G, Wang W, Zhang W, Ding Y, Zhao T, et al. A Novel Se-Polysaccharide From Se-Enriched G. Frondosa Protects Against Immunosuppression and Low Se Status in Se-Deficient Mice. *Int J Biol Macromol* (2018) 117:878–89. doi: 10.1016/j.ijbiomac.2018.05.180
4. Lee SH, Park BY, Yeo JM, Lee SS, Lee JH, Ha JK, et al. Effects of Different Selenium Sources on Performance, Carcass Characteristics, Plasma Glutathione Peroxidase Activity and Selenium Deposition in Finishing Hanwoo Steers. *Asian-Australasian J Anim Sci* (2007) 20:229–36. doi: 10.5713/ajas.2007.229
5. Sunde RA, Raines AM. Selenium Regulation of the Selenoprotein and Nonselenoprotein Transcriptomes in Rodents. *Adv Nutr* (2011) 2:138–50. doi: 10.3945/an.110.000240
6. Lymbury R, Tinggi U, Griffiths L, Rosenfeldt F, Perkins AV. Selenium Status of the Australian Population: Effect of Age, Gender and Cardiovascular Disease. *Biol Trace Element Res* (2008) 126:S1–S10. doi: 10.1007/s12011-008-8208-6
7. Li S, Zhao Q, Zhang K, Sun W, Li J, Guo X, et al. Selenium Deficiency-Induced Pancreatic Pathology Is Associated With Oxidative Stress and Energy Metabolism Disequilibrium. *Biol Trace Element Res* (2021) 199:154–65. doi: 10.1007/s12011-020-02140-9

8. Zhang Y, Xu Y, Chen B, Zhao B, Gao X-j. Selenium Deficiency Promotes Oxidative Stress-Induced Mastitis via Activating the NF-kappa B and MAPK Pathways in Dairy Cow. *Biological Trace Element Research 200* (2022) 2716–2726. doi: 10.1007/s12011-021-02882-0
9. Ubesie AC, Kocoshis SA, Mezoff AG, Henderson CJ, Helmrath MA, Cole CR, et al. Multiple Micronutrient Deficiencies Among Patients With Intestinal Failure During and After Transition to Enteral Nutrition. *J Pediatr* (2013) 163 (6):1692–6. doi: 10.1016/j.jpeds.2013.07.015
10. Carmean CM, Mimoto M, Landeche M, Ruiz D, Chellan B, Zhao L, et al. Dietary Selenium Deficiency Partially Mimics the Metabolic Effects of Arsenic. *Nutrients* (2021) 13(8):2894. doi: 10.3390/nu13082894
11. Zadeh MH, Farsani GM, Zamaninour N. Selenium Status After Roux-En-Y Gastric Bypass: Interventions and Recommendations. *Obes Surg* (2019) 29:3743–8. doi: 10.1007/s11695-019-04148-0
12. Murphy P, Kanwar A, Stell D, Briggs C, Bowles M, Aroori S. The Prevalence of Micronutrient Deficiency in Patients With Suspected Pancreatico-Biliary Malignancy: Results From a Specialist Hepato-Biliary and Pancreatic Unit. *Ejso* (2021) 47:1750–5. doi: 10.1016/j.ejso.2021.03.227
13. Flohe L. Selenium, Selenoproteins and Vision. *Developments Ophthalmol* (2005) 38:89–102. doi: 10.1159/000082770
14. Wang J, Liu Z, He X, Lian S, Liang J, Yu D, et al. Selenium Deficiency Induces Duodenal Villi Cell Apoptosis *via* an Oxidative Stress-Induced Mitochondrial Apoptosis Pathway and an Inflammatory Signaling-Induced Death Receptor Pathway. *Metallomics* (2018) 10(10):1390–1400. doi: 10.1039/C8MT00142A
15. Dermauw V, Yisehak K, Dierenfeld ES, Du Laing G, Buyse J, Wuyts B, et al. Effects of Trace Element Supplementation on Apparent Nutrient Digestibility and Utilisation in Grass-Fed Zebu (Bos Indicus) Cattle. *Livestock Sci* (2013) 155:255–61. doi: 10.1016/j.livsci.2013.05.027
16. Chen Y, Yang J, Huang Z, Jing H, Yin B, Guo S, et al. Exosomal Lnc-AFTR as a Novel Translation Regulator of FAS Ameliorates Staphylococcus Aureus-Induced Mastitis. *Biofactors* (2022) 48(1):148–63. doi: 10.1002/biof.1806
17. Liu Y-T, Qi S-L, Sun K-W. Traditional Chinese Medicine, Liver Fibrosis, Intestinal Flora: Is There Any Connection?-a Narrative Review. *Ann Palliative Med* (2021) 10:4846–57. doi: 10.21037/apm-20-2129
18. Luo X, Yang Z. Research Progress on Correlation Between Intestinal Flora and Cardiovascular Diseases. *Chin Pharmacol Bull* (2018) 34:1037–41. doi: 1001-1978(2018)34:8<1037:CDJQYX>2.0.TX;2-T
19. Yang G, Xing X. Advances in the Study on the Interaction Between Helminths and Intestinal Flora. *Chin J Microecology* (2017) 29:1087–9. doi: 1005-376X (2017)29:9<1087:RCGRYC>2.0.TX;2-C
20. Li C, Pi G, Li F. The Role of Intestinal Flora in the Regulation of Bone Homeostasis. *Front Cell Infect Microbiol* (2021) 11. doi: 10.3389/fcimb.2021.579323
21. Hu J, Zhong X, Yan J, Zhou D, Qin D, Xiao X, et al. High-Throughput Sequencing Analysis of Intestinal Flora Changes in ESRD and CKD Patients. *BMC Nephrol* (2020) 21(1):12. doi: 10.1186/s12882-019-1668-4
22. Gu Z, Wu Y, Wang Y, Sun H, You Y, Piao C, et al. Lactobacillus Rhamnosus Granules Dose-Dependently Balance Intestinal Microbiome Disorders and Ameliorate Chronic Alcohol-Induced Liver Injury. *J Medicinal Food* (2020) 23:114–24. doi: 10.1089/jmf.2018.4357
23. Tomasello G, Sorce A, Damiani P, Sinagra E, Carini F. The Importance of Intestinal Microbial Flora (Microbiota) and Role of Diet. *Prog Nutr* (2017) 19:342–4. doi: 10.23751/pn.v19i3.4495
24. Jing H, Wang S, Wang Y, Shen N, Gao XJ. Environmental Contaminant Ammonia Triggers Epithelial-to-Mesenchymal Transition-Mediated Jejunal Fibrosis With the Disassembly of Epithelial Cell-Cell Contacts in Chicken. *Sci Total Environ* (2020) 726:138686. doi: 10.1016/j.scitotenv.2020.138686
25. Zhou B, Yuan Y, Zhang S, Guo C, Li X, Li G, et al. Intestinal Flora and Disease Mutually Shape the Regional Immune System in the Intestinal Tract. *Front Immunol* (2020) 11. doi: 10.3389/fimmu.2020.00575
26. Liu J, Zhao F, Wang T, Xu Y, Qiu J, Qian Y. Host Metabolic Disorders Induced by Alterations in Intestinal Flora Under Dietary Pesticide Exposure. *J Agric Food Chem* (2021) 69:6303–17. doi: 10.1021/acs.jafc.1c00273
27. Tang Q, Cao L. Intestinal Flora and Neurological Disorders. *Sheng wu gong cheng xue bao* (2021) 37:3757–80. doi: 10.13345/j.cjb.210253
28. Tremblay A, Lingrand L, Maillard M, Feuz B, Tompkins TA. The Effects of Psychobiotics on the Microbiota-Gut-Brain Axis in Early-Life Stress and Neuropsychiatric Disorders. *Prog Neuropsychopharmacol Biol Psychiatry* (2021) 105:110142. doi: 10.1016/j.pnpbp.2020.110142
29. Wang L, Zhou J, Gober H-J, Leung WT, Huang Z, Pan X, et al. Alterations in the Intestinal Microbiome Associated With PCOS Affect the Clinical Phenotype. *Biomed Pharmacother* (2021) 133:110958. doi: 10.1016/j.biopha.2020.110958
30. Zhou R, Fan X, Schnabl B. Role of the Intestinal Microbiome in Liver Fibrosis Development and New Treatment Strategies. *Trans Res* (2019) 209:22–38. doi: 10.1016/j.trsl.2019.02.005
31. Zaher S. Nutrition and the Gut Microbiome During Critical Illness: A New Insight of Nutritional Therapy. *Saudi J Gastroenterol* (2020) 26:290–8. doi: 10.4103/sjg.SJG_352_20
32. Zhu H, Zhou Y, Qi Y, Ji R, Zhang J, Qian Z, et al. Preparation and Characterization of Selenium Enriched-Bifidobacterium Longum DD98, and Its Repairing Effects on Antibiotic-Induced Intestinal Dysbacteriosis in Mice. *Food Funct* (2019) 10:4975–84. doi: 10.1039/C9FO00960D
33. Li H, Che H, Xie J, Dong X, Song L, Xie W, et al. Supplementary Selenium in the Form of Selenylation Alpha-D-1,6-Glucan Ameliorates Dextran Sulfate Sodium Induced Colitis *In Vivo*. *Int J Biol Macromol* (2022) 195:67–74. doi: 10.1016/j.ijbiomac.2021.11.189
34. Istrate C, Hagbom M, Vikstrom E, Magnusson K-E, Svensson L. Rotavirus Infection Increases Intestinal Motility But Not Permeability at the Onset of Diarrhea. *J Virol* (2014) 88:3161–9. doi: 10.1128/JVI.02927-13
35. Zhang Y, Yang C, Han Y, Chen Y, Wang Z, Cao J, et al. Effect of 5-Hydroxytryptamine on the Intestine Histological Structure of Weaning Diarrhea Pups. *J China Agric Univ* (2017) 22:80–6. doi: 1007-4333(2017) 22:2<80:5QSADD>2.0.TX;2-I
36. Reisinger EC, Fritzsche C, Krause R, Krejs GJ. Diarrhea Caused by Primarily non-Gastrointestinal Infections. *Nat Clin Pract Gastroenterol Hepatol* (2005) 2:216–22. doi: 10.1038/ncpgasthep0167
37. Gai X, Wang H, Li Y, Zhao H, He C, Wang Z, et al. Fecal Microbiota Transplantation Protects the Intestinal Mucosal Barrier by Reconstructing the Gut Microbiota in a Murine Model of Sepsis. *Front Cell Infect Microbiol* (2021) 11. doi: 10.3389/fcimb.2021.736204
38. Lamb-Rosteski JM, Kalischuk LD, Inglis GD, Buret AG. Epidermal Growth Factor Inhibits Campylobacter Jejuni-Induced Claudin-4 Disruption, Loss of Epithelial Barrier Function, and Escherichia Coli Translocation. *Infect Immun* (2008) 76:3390–8. doi: 10.1128/IAI.01698-07
39. Rojo E, Casanova MJ, Gisbert JP. Treatment of Microscopic Colitis: The Role of Budesonide and New Alternatives for Refractory Patients. *Rev Esp Enferm Dig* (2020) 112(1):53–58. doi: 10.17235/reed.2019.6655/2019
40. Chu C, Rotondo-Trivette S, Michail S. Chronic Diarrhea. *Curr Probl Pediatr Adolesc Health Care* (2020) 50(8):100841. doi: 10.1016/j.cppeds.2020.100841
41. Cao P, Chen Y, Chen Y, Su W, Zhan N, Dong W. Fusobacterium Nucleatum Activates Endoplasmic Reticulum Stress to Promote Crohn's Disease Development *via* the Upregulation of CARD3 Expression. *Front Pharmacol* (2020) 11. doi: 10.3389/fphar.2020.00106
42. Guo XY, Liu XJ, Hao JY. Gut Microbiota in Ulcerative Colitis: Insights on Pathogenesis and Treatment. *J Digest Dis* (2020) 21:147–59. doi: 10.1111/1751-2980.12849
43. van Hoek MJA, Merks RMH. Emergence of Microbial Diversity Due to Cross-Feeding Interactions in a Spatial Model of Gut Microbial Metabolism. *BMC Syst Biol* (2017) 11(1):56. doi: 10.1186/s12918-017-0430-4
44. Chen D, Xiong Y, Lin Y, Tang Z, Wang J, Wang L, et al. Capsaicin Alleviates Abnormal Intestinal Motility Through Regulation of Enteric Motor Neurons and MLCK Activity: Relevance to Intestinal Motility Disorders. *Mol Nutr Food Res* (2015) 59:1482–90. doi: 10.1002/mnfr.201500039
45. Zhang H, Ran C, Teame T, Ding Q, Hoseinifar SH, Xie M, et al. Research Progress on Gut Health of Farmers Teleost Fish: A Viewpoint Concerning the Intestinal Mucosal Barrier and the Impact of its Damage. *Rev Fish Biol Fish* (2020) 30:569–86. doi: 10.1007/s11160-020-09614-y
46. Albert-Bayo M, Paracuellos I, Gonzalez-Castro AM, Rodriguez-Urrutia A, Rodriguez-Lagunas MJ, Alonso-Cotoner C, et al. Intestinal Mucosal Mast Cells: Key Modulators of Barrier Function and Homeostasis. *Cells* (2019) 8 (2):135. doi: 10.3390/cells8020135
47. Gonzalez-Castro AM, Martinez C, Salvo-Romero E, Fortea M, Pardo-Camacho C, Perez-Berezo T, et al. Mucosal Pathobiology and Molecular Signature of Epithelial Barrier Dysfunction in the Small Intestine in Irritable

Bowel Syndrome. *J Gastroenterol Hepatol* (2017) 32:53–63. doi: 10.1111/jgh.13417
48. Saia RS, Ribeiro AB, Giusti H. Cholecystokinin Modulates the Mucosal Inflammatory Response and Prevents the Lipopolysaccharide-Induced Intestinal Epithelial Barrier Dysfunction. *Shock* (2020) 53:242–51. doi: 10.1097/SHK.0000000000001355
49. Zou L, Liu K, Zhu H-F, Feng S. Protective Effect of Catalpolon Destruction of Tight Junctions of High Glucose Induced BMECs. *Zhongguo Zhong yao za zhi* (2018) 43:4118–24. doi: 10.19540/j.cnki.cjcmm.20180510.001
50. Slifer ZM, Blikslager AT. The Integral Role of Tight Junction Proteins in the Repair of Injured Intestinal Epithelium. *Int J Mol Sci* (2020) 21(3):972. doi: 10.3390/ijms21030972
51. Lynn KS, Easley KF, Martinez FJ, Reed RC, Schlingmann B, Koval M. Asymmetric Distribution of Dynamin-2 and Beta-Catenin Relative to Tight Junction Spikes in Alveolar Epithelial Cells. *Tissue Barriers* (2021) 9 (3):1929786. doi: 10.1080/21688370.2021.1929786
52. Wang FH, Peng X, Chen Y, Wang Y, Yang M, Guo MY. Se Regulates the Contractile Ability of Uterine Smooth Muscle *via* Selenoprotein N, Selenoprotein T, and Selenoprotein W in Mice. *Biol Trace Element Res* (2019) 192:196–205. doi: 10.1007/s12011-019-1647-4
53. Rattan S. Ca2+/calmodulin/MLCK Pathway Initiates, and RhoA/ROCK Maintains, the Internal Anal Sphincter Smooth Muscle Tone. *Am J Physiol Gastrointest Liver Physiol* (2017) 312:G63–6. doi: 10.1152/ajpgi.00370.2016
54. Tong L, Ao J-P, Lu H-L, Huang X, Zang J-Y, Liu S-H, et al. Tyrosine Kinase Pyk2 is Involved in Colonic Smooth Muscle Contraction *via* the RhoA/ROCK Pathway. *Physiol Res* (2019) 68:89–98. doi: 10.33549/physiolres.933857
55. Muller PA, Koscso B, Rajani GM, Stevanovic K, Berres M-L, Hashimoto D, et al. Crosstalk Between Muscularis Macrophages and Enteric Neurons Regulates Gastrointestinal Motility. *Cell* (2014) 158:300–13. doi: 10.1016/j.cell.2014.04.050
56. Zimmermann MB, Köhrle J. The Impact of Iron and Selenium Deficiencies on Iodine and Thyroid Metabolism: Biochemistry and Relevance to Public Health. *Thyroid* (2002) 12(10):867–78. doi: 10.1089/105072502761016494
57. Yang F, Zhao L, Mei D, Jiang L, Geng C, Li Q, et al. HMGA2 Plays an Important Role in Cr (VI)-Induced Autophagy. *Int J Cancer* (2017) 141:986–97. doi: 10.1002/ijc.30789
58. Arakawa S, Honda S, Yamaguchi H, Shimizu S. Molecular Mechanisms and Physiological Roles of Atg5/Atg7-Independent Alternative Autophagy. *Proc Japan Acad Ser B Physical Biol Sci* (2017) 93:378–85. doi: 10.2183/pjab.93.023
59. Zhu C, Du J, Yao Y, Wu D, Yuan M, Gan L, et al. Inhibiting Autophagy by Silencing ATG5 and ATG7 Enhances Inhibitory Effect of DDP on DDP-Resistant I-10 Testicular Cancer Cells. *Nan fang yi ke da xue xue bao* (2021) 41:657–63. doi: 10.12122/j.issn.1673-4254.2021.05.04
60. Han X, Kang KA, Piao MJ, Zhen AX, Hyun YJ, Kim HM, et al. Shikonin Exerts Cytotoxic Effects in Human Colon Cancers by Inducing Apoptotic Cell Death *via* the Endoplasmic Reticulum and Mitochondria-Mediated Pathways. *Biomolecules Ther* (2019) 27:41–7. doi: 10.4062/biomolther.2018.047
61. Azad A, Storey A. BAK Multimerization for Apoptosis, But Not Bid Binding, is Inhibited by Negatively Charged Residue in the BAK Hydrophobic Groove. *Mol Cancer* (2013) 12:65. doi: 10.1186/1476-4598-12-65
62. Degenhardt K, Chen GH, Lindsten T, White E. BAX and BAK Mediate P53-Independent Suppression of Tumorigenesis. *Cancer Cell* (2002) 2:193–203. doi: 10.1016/S1535-6108(02)00126-5
63. Almawi WY, Melemedjian OK, Abou Jaoude MM. On the Link Between Bcl-2 Family Proteins and Glucocorticoid-Induced Apoptosis. *J Leukocyte Biol* (2004) 76:7–14. doi: 10.1189/jlb.0903450
64. Moquin DM, McQuade T, Chan FK-M. CYLD Deubiquitinates RIP1 in the TNF Alpha-Induced Necrosome to Facilitate Kinase Activation and Programmed Necrosis. *PLos One* (2013) 8(10):e76841. doi: 10.1371/journal.pone.0076841

Conflict of Interest: The authors declare that the research was conducted in the absence of any commercial or financial relationships that could be construed as a potential conflict of interest.

Publisher's Note: All claims expressed in this article are solely those of the authors and do not necessarily represent those of their affiliated organizations, or those of the publisher, the editors and the reviewers. Any product that may be evaluated in this article, or claim that may be made by its manufacturer, is not guaranteed or endorsed by the publisher.

frontiers | Frontiers in Immunology

ORIGINAL RESEARCH
published: 22 July 2022
doi: 10.3389/fimmu.2022.952639

Hexavalent Chromium Exposure Induces Intestinal Barrier Damage *via* Activation of the NF-κB Signaling Pathway and NLRP3 Inflammasome in Ducks

Chenghong Xing[1†], Fan Yang[1†], Yiqun Lin[1], Jiyi Shan[1], Xin Yi[1], Farah Ali[2], Yibo Zhu[1], Chang Wang[1], Caiying Zhang[1], Yu Zhuang[1], Huabin Cao[1] and Guoliang Hu[1*]*

[1] Jiangxi Provincial Key Laboratory for Animal Health, Institute of Animal Population Health, College of Animal Science and Technology, Jiangxi Agricultural University, Nanchang, China, [2] Department of Theriogenology, Islamia University of Bahawalpur, Bahawalpur, Pakistan

Hexavalent chromium [Cr(VI)] is a dangerous heavy metal which can impair the gastrointestinal system in various species; however, the processes behind Cr(VI)-induced intestinal barrier damage are unknown. Forty-eight healthy 1-day-old ducks were stochastically assigned to four groups and fed a basal ration containing various Cr(VI) dosages for 49 days. Results of the study suggested that Cr(VI) exposure could significantly increase the content of Cr(VI) in the jejunum, increase the level of diamine oxidase (DAO) in serum, affect the production performance, cause histological abnormalities (shortening of the intestinal villi, deepening of the crypt depth, reduction and fragmentation of microvilli) and significantly reduced the mRNA levels of intestinal barrier-related genes (ZO-1, occludin, claudin-1, and MUC2) and protein levels of ZO-1, occludin, cand laudin-1, resulting in intestinal barrier damage. Furthermore, Cr(VI) intake could increase the contents of hydrogen peroxide (H_2O_2) and malondialdehyde (MDA), tumor necrosis factor-α (TNF-α), interleukin-1β (IL-1β), and interleukin-18 (IL-18) but decrease the activities of total superoxide dismutase (T-SOD), catalase (CAT), and glutathione reductase (GR), as well as up-regulate the mRNA levels of TLR4, MyD88, NF-κB, TNFα, IL-6, NLRP3, caspase-1, ASC, IL-1β, and IL-18 and protein levels of TLR4, MyD88, NF-κB, NLRP3, caspase-1, ASC, IL-1β, and IL-18 in the jejunum. In conclusion, Cr(VI) could cause intestinal oxidative damage and inflammation in duck jejunum by activating the NF-κB signaling pathway and the NLRP3 inflammasome.

Keywords: hexavalent chromium, intestinal barrier, NF-κB, NLRP3, duck

OPEN ACCESS

Edited by:
Mengyao Guo, Northeast Agricultural University, China

Reviewed by:
Jianzhu Liu, Shandong Agricultural University, China
Honggang Fan, Northeast Agricultural University, China

***Correspondence:**
Guoliang Hu
hgljx3818@jxau.edu.cn
Huabin Cao
chbin20020804@jxau.edu.cn

[†]These authors have contributed equally to this work

Specialty section:
This article was submitted to Nutritional Immunology, a section of the journal Frontiers in Immunology

Received: *25 May 2022*
Accepted: *23 June 2022*
Published: *22 July 2022*

Citation:
Xing C, Yang F, Lin Y, Shan J, Yi X, Ali F, Zhu Y, Wang C, Zhang C, Zhuang Y, Cao H and Hu G (2022) Hexavalent Chromium Exposure Induces Intestinal Barrier Damage via Activation of the NF-κB Signaling Pathway and NLRP3 Inflammasome in Ducks. Front. Immunol. 13:952639. doi: 10.3389/fimmu.2022.952639

INTRODUCTION

Chromium (Cr) is a crudely occurring element that can be found in diverse environmental media such as soils, water, air, and sediments (1, 2). It exists in an amount of oxidation states ranging from -2 to +6. Trivalent chromium [Cr(III)] and hexavalent chromium [Cr(VI)] are the most common valence states (3).

Cr(III) is a relatively stable essential trace element that plays a critical role in human carbohydrate, lipid, and protein metabolism (4). Unlike Cr(III), Cr(VI) is highly mobile in soil and exceedingly hazardous to living creatures and is designated as a carcinogen by the World Health Organization (WHO) (5). With the widespread use of Cr(VI) in wood preservation, leather tanning, chrome plating, dye production, and alloy manufacturing, large amounts of Cr(VI) are mined/produced globally each year, resulting in environmental pollution (6–8). The total amount of Cr(VI) discharged in soil, water, and air globally per year is estimated to be 896,000, 142,000, and 30,000 metric tons, respectively (9), which is well above the international guideline (50–100 kg/year) (10). Cr(VI) has well-known solubility, mobility, and responsiveness that can easily enter animal and human bodies through the skin, gastrointestinal tract, or respiratory tract, thus leading to Cr(VI) poisoning (11). Previous studies have indicated that Cr(VI) exposure could induce immunotoxicity, dermatotoxicity, genotoxicity, neurotoxicity, and carcinogenicity in different tissues of animals and humans (12, 13).

The intestine not only is responsible for the digestion and absorption of nutrients but also is the largest immune organ that is closely related to the health of animals (14, 15). It plays a crucial role in resisting the invasion of pathogenic bacteria and the entry of xenobiotics (16). Intestinal environment homeostasis is maintained by the epithelial cell integrity, intestinal mucosal immunity, and complex interaction between the intestinal microbiota and nutrients (17, 18). Numerous investigations have shown that heavy metal exposure negatively impacts gut function (19, 20). Zhang et al. demonstrated that lead exposure in carp altered gut microbiota and destroyed intestinal structural integrity by inhibiting the expression of intestinal epithelial tight-junction proteins (21). Zhong et al. demonstrated that arsenic trioxide could cause jejunum inflammation *via* increasing the production of pro-inflammatory cytokines in ducks (22). Furthermore, Zhou et al. discovered that subchronic mercury exposure led to gut microbiota dysbiosis and metabolic disturbances in chickens (23). These studies illustrated that heavy metal exposure could induce intestinal toxicity by destroying the intestinal barrier in different ways. In recent years, many studies have also shown that long-term exposure to Cr(VI) could cause intestinal damage and adversely affect the intestinal immunity of chickens (24, 25). Nevertheless, the mechanism by which Cr(VI) induced intestinal toxicity remains unknown. Proverbially, oxidative stress is one of the most crucial mechanisms of Cr(VI)-induced tissue injury (26). When Cr(VI) enters the cell, it acts as a strong oxidant and can produce additional reactive oxygen species (ROS) (27). The body's antioxidants are greatly reduced as ROS continues to accumulate. The cells are then attacked, resulting in cellular injury, which then produces inflammatory cytokines, which activate immune cells, resulting in inflammation that eventually causes tissue damage (28–32). A slew of recent studies has suggested that inflammation is linked to the activation of the NF-κB signaling pathway and the NLRP3 inflammasome (33, 34). However, the activation mechanism of Cr(VI)-induced intestinal inflammation remains uncertain. Therefore, the mechanism of Cr(VI)-induced intestinal barrier damage in ducks *via* activation of the oxidative stress-mediated NF-κB signaling pathway and the NLRP3 inflammasome needs to be further investigated.

Ducks are more susceptible to Cr(VI) toxicity than other animals due to ingestion of Cr(VI)-contaminated water and soil. Ducks better reflect the toxic effects of Cr(VI). Hence, ducks were used in this study to assist the researchers in better understanding the potential mechanisms of Cr(VI)-induced intestinal barrier damage and lay the groundwork for future research.

MATERIALS AND METHODS

Experiment Animals and Management

The experimental procedures were in favor of the animal ethics committee of Jiangxi Agricultural University (Approval ID: JXAULL-2022003). Ducks were purchased from Nanchang Miaowang Industrial Co., Ltd. (Nanchang, China), and fed with the standard rations as recommended by the National Research Council (NRC), which cited Ren et al. (35). **Table 1** displays the basic diet. The experimental animals were housed in a controlled environment with free access to water and a duck basal diet.

Determination of Lethal Dose 50 (LD_{50})

The source of Cr(VI) was analytical-grade potassium dichromate ($K_2Cr_2O_7$) (Sigma-Aldrich, St. Louis, CA, USA, 99% purity). For the determination of LD_{50}, 16 healthy Tianfu meat ducks (1 day old) were stochastically assigned to four groups of four ducks each. Different doses of Cr(VI) were administered to these groups that were infected *via* oral gavage, namely, 0.215, 0.464, 1.0, and 2.15 g/kg body weight. The gavage volume was calculated as 1% of body weight, fasting before gavage lasted 6 h, drinking water was not restricted, and the observation lasted 14 days. According to the Horn Table (the People's Republic of China's national standard acute toxicity test), the LD_{50} of $K_2Cr_2O_7$ in ducks was 0.464 g/kg, with a 95% confidence limit of 0.298–0.723 g/kg.

Toxicity Trials and Sample Collection

Before the experiment, 48 Tianfu meat ducks (1 day old) were housed in an appropriate environment for 7 days. Then ducks were divided into four groups and given Cr(VI) in doses of 0 (Control), 9.28 (LCr), 46.4 (MCr), and 232 (HCr) mg/kg body weight for 49 days. All ducks were weighed, and blood samples were collected from each duck's wing vein and separated serum on day 49. The jejuna were removed from each group of 12 ducks promptly after euthanasia. The length and weight of the jejunum tissues were measured. Then, the jejunum was cut into small pieces and rinsed repeatedly with 0.9% NaCl until there was no stool. A part of jejunum specimens was stored at -20°C for determining contents of Cr(VI), and a part of jejunum specimens was fixed in 10% formalin and 2.5% glutaraldehyde for histopathological and ultrastructural observation, and the rest of the jejuna were stored at -80°C for RNA isolation and total protein extraction.

TABLE 1 | The composition and nutritional levels of the basal diet.

Item (%, unless noted)	Content
Corn	47
Wheat bran	13
Rice bran	9
Soybean meal, 43%	9
Rapeseed meal	9
Cottonseed meal	6
Rapeseed oil	2.88
Calcium corbonate	0.96
Dicalcium plosphate, $2H_2O$	1.275
L-Lysine-HCl	0.37
D, L-Methionine	0.226
Threonine, 98.5%	0.044
Tryptophan, 98.5%	0.032
Sodium chloride	0.4
Choline chloride, 50%	0.2
Bentonite	0.913
Mineral premix1	0.4
Vitamin premix2	0.2
Analyzed nutrient content	
ME (Kcal/kg, calculated)	2914
CP (analyzed)	17.12
Calcium (analyzed)	0.94
Total phosphorus (analyzed)	0.84
Nonphytate phosphorus (calculated)	0.478

[1]*Dietary supply per kilogram: copper, 8 mg; iron, 80 mg; zinc, 90 mg; manganese, 70 mg; selenium, 0.3 mg; iodine, 0.4 mg.*

[2]*Dietary supply per kilogram: vitamin A, 15,000 IU; vitamin D_3, 5000 IU; vitamin K_3, 5 mg; vitamin E, 80 mg; vitamin B_1, 3 mg; vitamin B_2, 9 mg; vitamin B_6, 7 mg; vitamin B_{12}, 0.04 mg; nicotine acid, 80 mg; pantothenic acid, 15 mg; biotin, 0.15 mg; folic acid, 2 mg; vitamin C, 200 mg; 25-hydroxycholecalciferol, 0.069 mg.*

Histopathological Examination

The jejunum tissues were fixed in 10% formalin for 24 h, then dehydrated, embedded, sliced, and stained for microscopy (36). TissueFAXS was applied to measure and analyze villus length and crypt depth (TissueFAXS Plus, Vienna, Austria).

The effect of Cr(VI) on jejunum tissues was studied using periodic acid–Schiff (PAS) staining. PAS staining was performed according to the instructions provided by the manufacturer of the PAS Kit (Cat # G1049, Service, Wuhan, China). TissueFAXS was used to count the number of goblet cells in all of the sections (TissueFAXS Plus, Austria).

Transmission Electron Microscopy

Transmission electron microscopy (TEM) was carried out in accordance with the protocol previously described (37, 38). After collecting jejunum tissues, they were processed and examined using a TEM HT7800 (Hitachi, Tokyo, Japan). The ultrastructural pathological changes in the jejunum were observed and compared to the control group counterparts.

Determination of Cr(VI) Contents in Jejunum Tissues

The jejunum tissues were digested with HNO_3 (65%) and H_2O_2 (30%) before being diluted to 10 ml with deionized water. Following that, the samples were digested and analyzed using a microwave system and inductively coupled plasma mass spectrometry (ICP-MS) (NexION 350, Watertown, MA, USA).

Determination of Diamine Oxidase and Oxidative Stress Index Content

Commercially available diagnostic kits (Jiancheng Biotech, Nanjing, China) were applied to detect the concentrations of diamine oxidase (DAO) in serum. Additionally, H_2O_2 and MDA concentrations and T-SOD, CAT, and GR activities in jejunum tissues were also detected as previously described (39).

Determination of Inflammation Cytokines

TNF-α, IL-1β, and IL-18 levels were detected in jejunum tissues using a commercial kit (mlbio, Shanghai, China). All operation steps were carried out according to the manual.

Real-Time Quantitative PCR

Total RNA was isolated from jejunum tissues using TRIzol reagent (Takara, Shiga, Japan) and reverse transcribed, as directed by the manufacturer. Then, the reverse transcription product was used for RT-PCR. The gene sequences for duck ZO-1, occludin, claudin-1, MUC2, TLR4, MyD88, NF-κB, TNFα, IL-6, NLRP3, caspase-1, ASC, IL-1β, IL-18, and GAPDH are shown in **Table 2**. Primers were designed with Primer Express 3.0 software and synthesized by Beijing Qingke Biotechnology Co., Ltd. The experiment was carried out on a CFX384 Touch+CFX PCR instrument (Bio-Rad, Hercules, CA, USA). Pre-denaturation was at 95°C for 30 s, denaturation at 95°C for 5 s, annealing at 60°C for 34 s, 40 cycles. The data were normalized to GAPDH expression and analyzed using the $2^{-\triangle\triangle}$CT method.

Western Blot

Jejunum tissues were homogenized at 4°C in RIPA lysis buffer which contained protease inhibitors (PMSF) (Beyotime, Shanghai, China), and concentrations were determined using a BCA assay (35). Samples were further diluted, and 5× SDS-PAGE loading buffer was added and boiled for 5 min. Equal amounts of protein (10 μg) were loaded onto 12% SDS-polyacrylamide denaturing gels before being transferred to polyvinylidene fluoride (PVDF) membranes. After blocking with tris-buffered saline Tween (TBST) containing 5% non-fat milk powder for 1 h at room temperature, the membrane was incubated overnight with diluted primary antibodies against ZO-1 (1:1,000; ABclonal, Wuhan, China), occludin (1:1,000; Selleck Chemicals, USA), claudin-1 (1:1,000; ABclonal, China), TLR4 (1:500; Proteintech, Wuhan, China), MyD88 (1:500; Wanleibio, Shenyang, China), NF-κB (1:500; Wanleibio, China), NLRP3 (1:1,000; Wanleibio, China), ASC (1:500; Santa Cruz Biotechnology, Dallas, TX, USA), caspase-1 (1:500; Wanleibio, China), IL-1β (1:500; Wanleibio, China), IL-18 (1:1,000; Wanleibio, China), and GAPDH (1:5,000; Proteintech, China). Electrochemiluminescence liquid (ECL) (Tanon, Shanghai, China) was used to detect the signal. ImageJ software was used to assess protein levels. The target protein levels were normalized to GAPDH, and the radioactivity was compared with the control group.

Immunofluorescence Analysis

MUC2 secretion was investigated using immunofluorescence analysis. A previous report provided detailed descriptions of

TABLE 2 | Premier sequences used for real-time PCR.

Gene	5'-Primer (F)	3'-Primer (R)
ZO-1	ACGCTGGTGAAATCAAGGAAGAA	AGGGACATTCAACAGCGTGGC
Occludin	CAGGATGTGGCAGAGGAATACAA	CCTTGTCGTAGTCGCTCACCAT
Claudin-1	CACACGAGCTTTGATGGTGG	ACCAATGCTGACAAACCTGCAA
MUC2	ATGGAGAGCGTTGTGTTTGC	GTGAAGACCAGTTCGGGGAG
TLR4	CACCAGTTTCACTTCCCCTTGT	GCTTTGCTAGGGATGACCTCCAA
MyD88	GCTTATAGAAAGGAGGTGTCGG	TGAAAGTCGCATTCGTCGCT
NF-κB	ACAACGTCCTTCATTTAGCAA	TCTGATAAAGGTCGTTCCTCA
TNFα	TCAGATCATTCAGCGTCACC	GACACCATCACAAAGTTTCTGC
IL-6	GGTCATCCCAGATTCAGCTAC	CCCTCACGGTTTTCTCCATAA
NLRP3	CCAGCCTGAAGATCGGAGACCT	AGGAGCCACCCTAGAGGAGAGT
Caspase-1	CTATCCCATACTCTTGCCACG	TCCTTCACATCCACTTCAGC
ASC	CAGCATTCTGGATCGGCTCT	ATTTTCTCCTGCCTGATGCTT
IL-1β	TCATCTTCTACCGCCTGGAC	TAGCTTGTAGGTGGCGATGT
IL-18	ACCTCTGCCTCTATTTTGCTG	TTCAAAAGCTGCCATGTTCAG
GAPDH	TGATGCTCCCATGTTCGTGA	CTTTTCCCACAGCCTTAGCAG

F, forward; R, reverse

the procedure (40). In brief, the prepared slides were incubated at 4°C for 16 h with the primary antibodies MUC2 (1:200; Service, Wuhan, China). The sections were then incubated for 1 h at 37°C with FITC-conjugated goat anti-rabbit Ig G (1:300; Service, Wuhan, China). Finally, the nucleus was stained for 10 min with DAPI. A fluorescence microscope was used to observe and capture the fluorescence patterns (Nikon, Japan).

Statistical Analysis

The data were presented as the standard error of mean (SEM). Microsoft Excel 2016 and GraphPad Prism 8.0 (GraphPad Inc., La Jolla, CA, USA) was applied for data analysis and graphing. To compare differences with the control group, one-way ANOVA and multiple comparisons were used. The *P*-values of 0.05, 0.01, 0.005, and 0.001 were regarded as statistically significant.

RESULTS

Cr(VI) Accumulation in the Jejunum and Its Effect on Growth Indexes and Histopathology

As shown in **Figure 1A**, when compared to the control group, the Cr(VI) content in the jejunum tissues of the HCr group was significantly higher ($P < 0.001$). To investigate the effects of Cr(VI) exposure on intestinal injury, anatomical pathological and histological changes were identified. The changes in growth indexes are shown in **Figures 1B–D**, and the body weight in all Cr(VI)-treated groups was observably lower than in the control group ($P < 0.005$ or $P < 0.001$). The jejunum weight in all Cr(VI)-treated groups was observably lower compared with the control group ($P < 0.05$ or $P < 0.001$). The length of the jejunum in the MCr and HCr groups was noticeably shortened compared with the control group ($P < 0.05$ or $P < 0.001$). H&E staining revealed normal morphology, clear borders, and well-arranged epithelial cells in the control group. Nevertheless, the jejunum was injured in the MCr and HCr groups, with the shedding of the apical epithelium of the intestinal villi (green arrows) and destruction of the mucosal layer (blue arrows). In addition, we also observed intestinal villus breakage (red arrows) in the HCr group (**Figure 1E**). The length of the intestinal villus was significantly shorter in the HCr group compared with the control group ($P < 0.005$). The crypt depth (black arrows) was deepened ($P > 0.05$), while the ratio of villus height to crypt depth (VH/CD) in the HCr group was noticeably decreased compared with the control group ($P < 0.05$) (**Figures 1F–H**). The experiment data showed that Cr(VI) could lead to jejunum damage, thereby affecting the digestion and absorption of nutrients.

The Effects of Cr(VI) Exposure on the Intestinal Barrier Function

To explore whether Cr(VI) exposure could cause intestinal barrier damage, we examined the number of goblet cells (**Figure 2A**), the ultrastructural pathological changes (**Figure 2B**), and the mRNA and protein levels of intestinal barrier-related factors (**Figures 2C–G**). PAS staining showed that goblet cells reduced in a dose-dependent manner with increasing Cr(VI) concentration. TEM results showed that the microvilli of intestinal epithelial cells were shed, the number of microvilli was reduced, and the TJ structure of intestinal epithelial cells was damaged in the MCr and HCr groups. Compared with the control group, the ZO-1, occludin, claudin-1, and MUC2 mRNA levels were observably down-regulated in the HCr group ($P < 0.05$ or $P < 0.01$ or $P < 0.005$). Furthermore, the mRNA levels of occludin and claudin-1 in the LCr and MCr groups were significantly lower than those in the control group ($P < 0.05$ or $P < 0.01$) and the mRNA level of MUC2 in the MCr group was significantly lower than those in the control group ($P < 0.05$). Likewise, ZO-1, occludin, and claudin-1 protein levels were significantly down-regulated in all Cr(VI)-exposed groups compared to the control group ($P < 0.01$, $P < 0.005$, or $P < 0.001$). Meanwhile, MUC2 immunofluorescence results showed that Cr(VI) reduced the MUC2 fluorescence intensity (**Figure 2H, J**). DAO was also measured as a marker of intestinal epithelial cell maturity, integrity, and function, and the results revealed that DAO levels in serum were observably elevated in all Cr(VI)-exposure groups ($P < 0.005$ or $P < 0.001$) compared with the control group (**Figure 2I**).

The Effects of Cr(VI) Exposure on Cytokines and Oxidative Stress Indices in the Jejunum

The contents of cytokines in the jejunum are presented in **Figures 3A–C**. The TNF-α and IL-1β levels in jejunum were dramatically increased dose-dependently ($P < 0.01$ or $P < 0.005$ or $P < 0.001$) in all Cr(VI)-exposure groups in comparison with the control group. The level of IL-18 in the jejunum was observably elevated ($P < 0.001$) in the MCr and HCr groups compared with the control group. Additionally, oxidative stress indicators were measured in jejunum tissues to assess the extent of oxidative damage to ducks caused by Cr(VI) (**Figures 3D–H**).

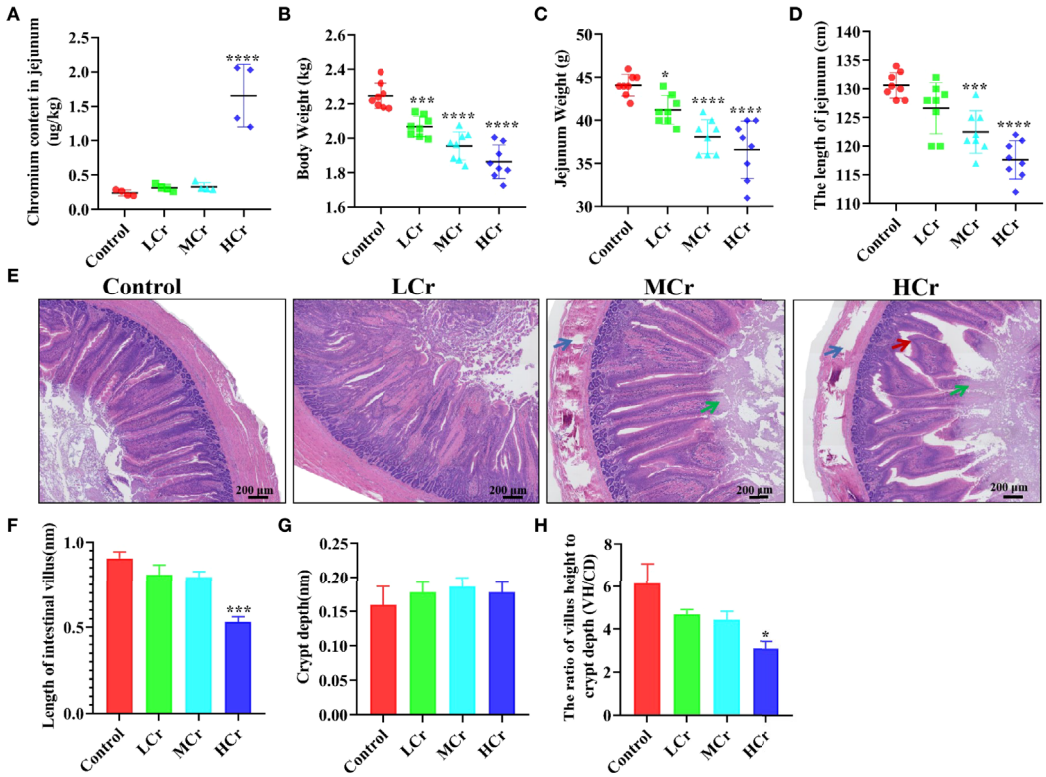

FIGURE 1 | Cr(VI) exposure induced intestinal damage. **(A)** Cr(VI) content in jejunum tissues. **(B)** Body weight. **(C)** Jejunum weight. **(D)** The length of jejunum. **(E)** Histopathological variation in jejunum tissues (scale bar = 200 μm). **(F)** Length of intestinal villus. **(G)** Crypt depth. **(H)** The ratio of villus height to crypt depth (VH/CD). All data were presented as mean ± SEM; n ≥ 3 for each group. The symbol "*" denotes a statistically significant difference from the control group (*$P < 0.05$, ***$P < 0.005$ and ****$P < 0.001$).

In comparison to the control group, H_2O_2 and MDA concentrations were observably elevated, while T-SOD, CAT, and GR activities were observably decreased ($P < 0.01$, $P < 0.005$, or $P < 0.001$) in the MCr and HCr groups.

The Influence of Cr(VI) on the NF-κB Signaling Pathway in Jejunum Tissues

To determine whether Cr(VI) induced inflammation in jejunum tissues, we measured the mRNA and protein levels of NF-κB signaling pathway-related factors. TLR4, MyD88, NF-κB, TNF-α, and IL-6 mRNA levels were observably up-regulated in the MCr and HCr groups compared to the control group ($P < 0.05$, $P < 0.01$, $P < 0.005$, or $P < 0.001$), while TNF-α and IL-6 mRNA levels were observably up-regulated ($P < 0.05$) in the LCr group (**Figure 4A**). TLR4, MyD88, and NF-κB protein levels were also markedly up-regulated in the MCr and HCr groups compared to the control group ($P < 0.05$, $P < 0.01$, $P < 0.005$, or $P < 0.001$), and the protein level of MyD88 was markedly up-regulated ($P < 0.05$) in the LCr group (**Figures 4B, C**). The heatmap visually depicts the changes in these genes and proteins (**Figure 4D**). These findings suggested that Cr(VI) exposure activated the NF-κB signaling pathway in the jejunum, which was more pronounced in the HCr group.

The Effects of Cr(VI) Exposure on the Activation of the NLRP3 Inflammasome in Jejunum Tissues

As shown in **Figure 5A**, NLRP3, caspase-1, ASC, IL-1β, and IL-18 mRNA levels were observably up-regulated in the HCr group compared with the control group ($P < 0.05$ or $P < 0.01$) and NLRP3 mRNA level was also observably up-regulated in the MCr group compared with the control group ($P < 0.05$). Simultaneously, NLRP3, caspase-1, ASC, IL-1β, and IL-18 protein levels were also observably up-regulated in the HCr group compared to the control group ($P < 0.05$, $P < 0.005$, or $P < 0.001$) and ASC, IL-1β, and IL-18 protein levels were observably up-regulated ($P < 0.005$ or $P < 0.001$) in the MCr group and IL-1β and IL-18 protein levels were observably up-regulated ($P < 0.01$ or $P < 0.001$) in the LCr group ($P < 0.005$) (**Figures 5B, C**). A heatmap was created to show the changes in these genes and proteins (**Figure 5D**). Experimental results indicated that Cr(VI) exposure activated the NLRP3 inflammasome in duck jejunum tissues.

DISCUSSION

Cr(VI) is a naturally occurring heavy metal that can be found in air, water, soil, and food. It is classified as highly toxic because it

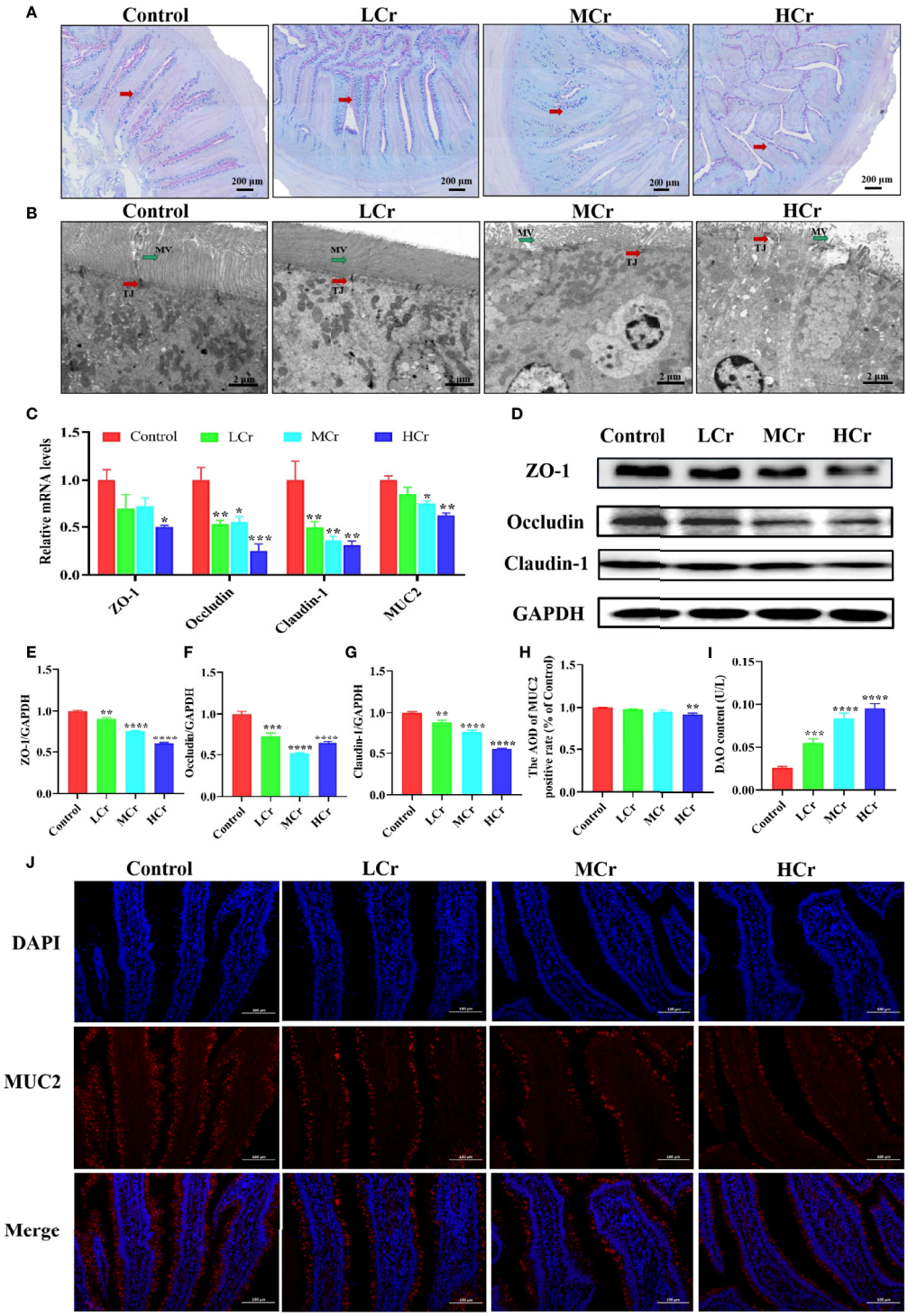

FIGURE 2 | Effects of Cr(VI) exposure on intestinal epithelial barrier function. **(A)** PAS staining was used to determine the distribution of goblet cells (red arrows) in the intestine (scale bar = 200 μm). **(B)** Ultrastructure of the jejunum (scale bar = 2 μm). The red and green arrows represent changes in tight connections and microvilli, respectively. TJ stands for tight connection; MV stands for microvilli. **(C)** mRNA levels of genes related to the intestinal barrier. **(D–G)** Effects of Cr(VI) exposure on tight-junction protein expression levels in the duck jejunum. **(E)** ZO-1/GAPDH. **(F)** Occludin/GAPDH. **(G)** Claudin-1/GAPDH. **(H)** ImageJ analysis of MUC2 immunofluorescent staining results. **(I)** DAO content. **(J)** Immunofluorescence staining of MUC2 protein expression in jejunum tissue. The symbol "*" denotes a statistically significant difference from the control group (*$P < 0.05$, **$P < 0.01$, ***$P < 0.005$ and ****$P < 0.001$).

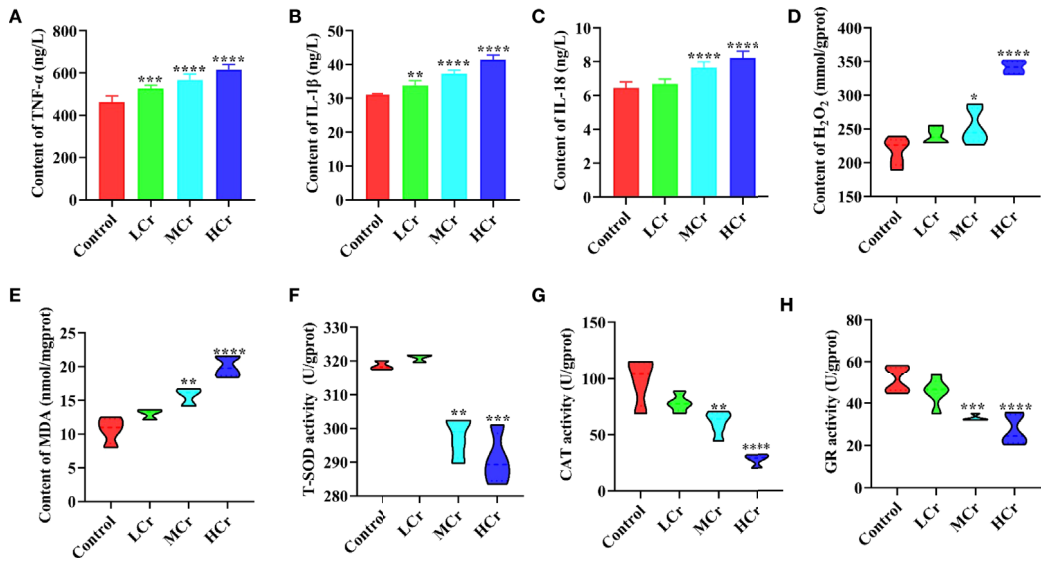

FIGURE 3 | The effects of Cr(VI) on inflammation and oxidative stress in the jejunum. **(A)** TNF-α concentration. **(B)** IL-1β concentrations. **(C)** IL-18 concentrations. **(D)** H_2O_2 concentrations. **(E)** MDA concentrations. **(F)** T-SOD activity. **(G)** CAT activity. **(H)** GR activity. The symbol "*" denotes a statistically significant difference from the control group (*$P < 0.05$, **$P < 0.01$, ***$P < 0.005$ and ****$P < 0.001$).

causes severe symptoms in humans and animals such as diarrhea, ulcers, eye and skin irritations, kidney dysfunction, and lung carcinoma (41, 42). As a result, many scientists have concentrated on the negative effects of Cr(VI) on human and animal health (43). Previous studies have found that long-term exposure to high concentrations of Cr(VI) in mice can lead to gastric mucosal bleeding, ulcers, weight loss, and severe effects on intestinal morphology and function (44, 45). However, its potential impact on the waterfowl intestine is unknown. We used a Cr(VI) poisoning model in this study to investigate the effects of Cr(VI)-induced jejunum damage in ducks and the underlying toxic mechanisms.

Intestines are crucial digestive organs, and damage to them can lead to nutrient absorption problems and an insufficient supply of nutrients to the body (46). In the current study, we noticed that the content of Cr(VI) was dramatically increased in the jejunum tissue. Additionally, the weight and length of the jejunum and the body weight of ducks were significantly decreased with increasing doses of Cr(VI) in the diet, which may be caused by damage to the intestinal epithelium. The epithelium of the small intestine is composed of abundant crypt–villus units. The intestinal villus is the crucial part in the increase in the mucosal surface area and then enhancement in the absorption of nutrients. Crypts are known as the home to a population of energetically reproducing epithelial cells, fueling the active intestinal epithelium. The VH/CD value was believed to be a sensitive indicator of the absorptive capacity of the small intestine (47). Therefore, changes in villus or intestinal gland anatomy have a direct impact on nutrient absorption. Accumulating evidence indicated that heavy metal exposure could cause shortening of intestinal villi, increase in recess depth and VH/CD values, and weight loss (48, 49). Similarly, Cr(VI) exposure resulted in Cr(VI) accumulation, shortening of the height of the jejunum gland, deepening in the crypt depth, and decrease in VH/CD values in the jejunum. These findings confirmed that continuous Cr(VI) accumulation in the jejunum caused significant damage to the intestinal epithelium, which may affect nutrient digestion and absorption in the ducks, resulting in poor growth performance.

Besides ingestion and absorption, the small intestine also has a barrier function that protects the body from hazardous substance such as toxins, pathogens, and foodborne antigens. MUC2 is the main protein component of the intestinal mucous layer that is secreted into the lumen of the large intestine from goblet cells in the epithelial lining. It forms a gel with small amounts of related mucins, forming an insoluble mucus barrier that protects intestinal epithelial cells (50). A previous study showed that by gavage of ducks with 80 mg/kg, goblet cells were significantly reduced, and at the same time, the mRNA and protein levels of MUC2 were also significantly reduced (22). Our results showed that with the increase in Cr(VI) concentration, the number of goblet cells was significantly reduced and the mRNA and protein levels of MUC2 were observably down-regulated. Tight-junction proteins are located between adjacent epithelial cells and play a crucial role in maintaining tight junctions in intestinal epithelial cells to form a physical barrier to enhance the intestinal protective function (51). DAO is a highly active intracellular enzyme in all mammalian intestinal mucosal epithelial cells, and DAO activity in serum can be used to assess the maturity, integrity, and functional status of intestinal epithelial cells (52). Once the barrier function was compromised, intestinal permeability increased, resulting in "leaky gut," and DAO entered the bloodstream *via* the damaged mucosa, increasing the DAO levels in serum (53). Cr(VI) has been demonstrated to damage the intestinal epithelial TJ structure and decrease the levels of tight-junction proteins in mice by Zhu et al.

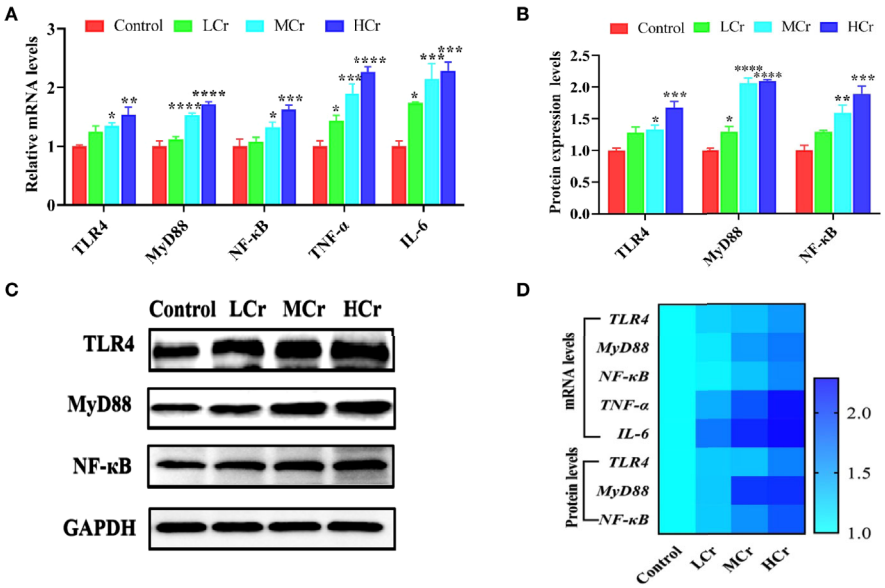

FIGURE 4 | The influence of Cr(VI) on the NF-κB signaling pathway in jejunum tissues. **(A)** mRNA levels of genes involved in the NF-κB signaling pathway. **(B)** Quantitative analysis of NF-κB signaling pathway-related protein expression. **(C)** Western blot reveals that expression levels of NF-κB signaling pathway-related proteins. **(D)** A heatmap depicts the relationship between NF-κB signaling pathway-related mRNA and protein levels in jejunum tissues. The symbol "*" denotes a statistically significant difference from the control group (*$P < 0.05$, **$P < 0.01$, ***$P < 0.005$ and ****$P < 0.001$).

(54). In the current study, we observed the effects of Cr(VI) on intestinal epithelial cell microvilli and TJ protein by using TEM and found that Cr(VI) exposure caused intestinal epithelial cell microvilli to fall off, the number of microvilli decreased, and the intestinal epithelial cell TJ structure was damaged. Meanwhile, the tight-junction proteins were detected, and the results indicated that Cr(VI) exposure decreased the mRNA and protein levels of ZO-1, occludin, and claudin-1 in the jejunum. To further verify the damage to the intestinal barrier, the level of DAO in serum was evaluated to check whether Cr(VI) exposure caused the "leaky gut". Our result showed that Cr(VI) exposure increased the level of DAO in serum. These findings suggested that Cr(VI) exposure caused gut

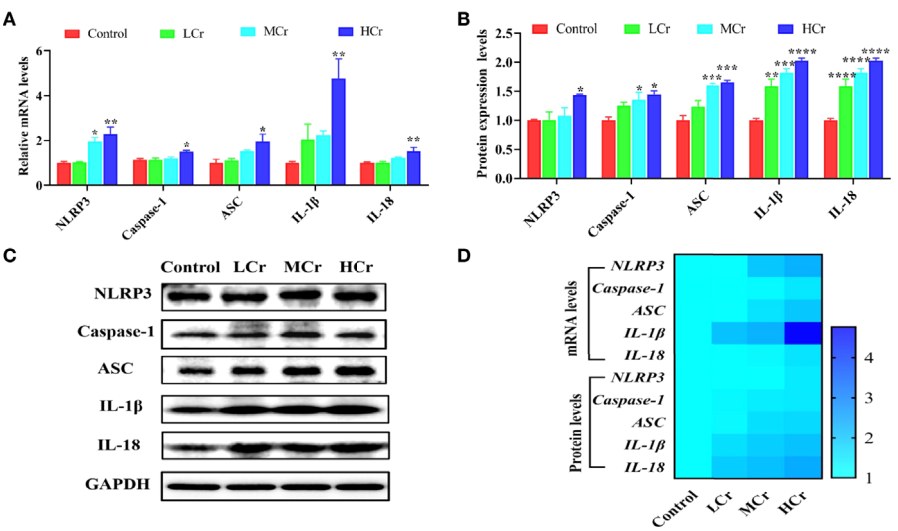

FIGURE 5 | Effects of Cr(VI) exposure on NLRP3 inflammasome activation in jejunum tissues. **(A)** Pyroptosis-related gene mRNA levels. **(B)** Quantitative analysis of pyroptosis-related factor protein levels. **(C)** Western blot demonstrates pyroptosis-related protein expression. **(D)** A heatmap depicts the relationship between the expression of pyroptosis-related genes and proteins in jejunum tissues. The symbol "*" denotes a statistically significant difference from the control group (*$P < 0.05$, **$P < 0.01$, ***$P < 0.005$ and ****$P < 0.001$).

physicochemical barrier damage and increased jejunum permeability, resulting in more severe intestinal barrier destruction in ducks.

Substantial evidence suggests that intestinal epithelial barrier disruption and increased intestinal epithelial permeability increase exposure to bacteria and toxins, resulting in intestinal immune cell hyperstimulation and mucosal inflammation (55, 56). Furthermore, intestinal inflammation can cause intestinal epithelial barrier dysfunction and increased permeability (57). It has been reported that trichlorfon exposure decreased the expression levels of ZO-1, occludin, and claudin-2 in common carp accompanied by significantly increased expression levels of IL-1β and TNF-α (58). Moreover, high levels of TNF-α could disrupt the barrier function of Caco2 cells and increase intestinal permeability (59). IL-1β is a cytokine that has been linked to epithelial barrier dysfunction in the gut and has been shown to suppress the expression of claudin-3 in Caco2 cells (60). In a colitis model, IL-18 is critical in driving the pathological breakdown of intestinal barrier integrity; deletion of IL-18 conferred protection from colitis and mucosal damage in mice (61). In this study, TNF-α, IL-1β, and IL-18 concentrations were elevated with the increasing level of Cr(VI), which represented that Cr(VI) exposure induced inflammation in duck jejunum tissues. Many studies indicated that the production of pro-inflammatory factors is strongly related to oxidative stress (62). Thus, in the current study, we further investigated the redox state of the jejunum by measuring antioxidant enzymes and peroxidation products. T-SOD is a crucial antioxidant enzyme that converts superoxide $O_2^{\bullet-}$ into H_2O_2, protecting the structure and function of cells from oxidative damage, H_2O_2 is then converted into water and oxygen *via* CAT catalysis (63, 64). Similarly, GR is important for detoxifying active metabolites and maintaining intracellular redox balance (65). Additionally, the accumulation of peroxidation product H_2O_2 could cause cell structure damage as well as gene damage and mutation. MDA is a by-product of lipid peroxidation that could promote cross-linking and polymerization of living macromolecules such as proteins and nucleic acids, resulting in cytotoxicity (66). Our results found that excessive dietary Cr(VI) significantly increased the contents of H_2O_2 and MDA and decreased the activities of SOD, CAT, and GR, which indicated that Cr(VI) exposure could induce oxidative stress in the jejunum of duck. In line with our results, Zhu et al. reported that excessive Cr (VI) could damage the intestine by inducing oxidative stress and inflammation (54).

The NLRP3 inflammasome has been shown to be a novel mechanism for intestinal inflammation, and it can be activated by ROS (67). The activation of the NLRP3 inflammasome triggers a series of immune responses, including the production of proinflammatory cytokines and chemokines and the recruitment of neutrophils and other immune cells, as well as cell death (68). However, activation of the NLRP3 inflammasome requires two steps: initiation and activation. TLRs recruit the signaling regulator MyD88 and a TIR domain-containing adaptor protein-induced interferon (TRIF) in the priming step to connect to signaling factors *via* NF-κB. This process promotes the transcription of NLRP3, pro-IL-1β, and pro-IL-18, as well as the production of multiple pro-inflammatory cytokines, including IL-1β, IL-6, and TNF-α (69). The inflammasome assembly step is triggered by several molecular and cellular events such as K+ efflux, Ca2+ signaling, and ROS generation. Procaspase-1 converts to cleaved-caspase-1 during the assembly of the NLRP3 inflammasome, promoting the cleavage of pro-IL-1β and pro-IL-18 precursors to IL-1β and IL-18 to induce inflammation (70, 71). Zhong et al. demonstrated that ATO exposure impaired intestinal barrier function and caused inflammatory injury in the duck jejunum by activating the LPS/TLR4/NF-κB signaling pathway (22). Similarly, Cr(VI) exposure increased the mRNA levels of TLR4, MyD88, NF-κB, TNF-α, and IL-6, as well as the protein expression levels of TLR4, MyD88, and NF-κB in jejunum tissues. Furthermore, Fan et al. demonstrated that zearalenone could activate the NLRP3 inflammasome *via* ROS, resulting in severe intestinal inflammation in mice. Our results also showed that Cr(VI) exposure elevated the mRNA and protein levels of NLRP3, ASC, caspase-1, IL-1β, and IL-18 in jejunum tissues. These findings suggested that Cr(VI), as a strong redox heavy metal, was involved in redox behavior and ROS generation, and induced jejunum inflammation by activating the NF-κB signaling pathway and the NLRP3 inflammasome. However, whether Cr(VI) induces intestinal barrier damage through ROS-mediated activation of the NF-κB signaling pathway and the NLRP3 inflammasome needs to be further verified by *in vitro* experiments.

CONCLUSIONS

Overall, our studies revealed the negative impact on bioaccumulation, digestion, intestinal barrier function, antioxidant capacity, and immune response of the ducks following exposure to Cr(VI), further indicating that Cr(VI) induced intestine injury, oxidative stress, and immunotoxicity in ducks. Furthermore, the immunotoxicity of Cr(VI) was associated with the activation of the NF-κB signaling pathway and NLRP3 inflammasome by oxidative stress.

DATA AVAILABILITY STATEMENT

The original contributions presented in the study are included in the article/supplementary material. Further inquiries can be directed to the corresponding authors.

ETHICS STATEMENT

The animal study was reviewed and approved by the animal ethics committee of Jiangxi Agricultural University (Approval ID: JXAULL-2022003).

AUTHOR CONTRIBUTIONS

GH, HC, and FY contributed to conception and design of the study. CX performed the statistical analysis and wrote the first draft of the manuscript. YL, JS, XY, YZ, and CW provided

substantial contribution to experimental operation and data acquisition, wrote sections of the manuscript. FA, CZ, and YZ contributed to the grammatical revision of the manuscript. All authors contributed to manuscript revision, read, and approved the submitted version.

FUNDING

This project was supported by the National Natural Science Foundation of China (No. 32060819; Beijing, P. R. China) awarded to GH.

REFERENCES

1. Zhang H, Wu X, Mehmood K, Chang Z, Li K, Jiang X, et al. Intestinal Epithelial Cell Injury Induced by Copper Containing Nanoparticles in Piglets. *Environ Toxicol Pharmacol* (2017) 56:151–6. doi: 10.1016/j.etap.2017.09.010
2. Tian X, Zhang H, Zhao Y, Mehmood K, Wu X, Chang Z, et al. Transcriptome Analysis Reveals the Molecular Mechanism of Hepatic Metabolism Disorder Caused by Chromium Poisoning in Chickens. *Environ Sci pollut Res Int* (2018) 25(16):15411–21. doi: 10.1007/s11356-018-1653-7
3. De Flora S, D'Agostini F, Balansky R, Micale R, Baluce B, Izzotti A. Lack of Genotoxic Effects in Hematopoietic and Gastrointestinal Cells of Mice Receiving Chromium(VI) With the Drinking Water. *Mutat Res* (2008) 659 (1-2):60–7. doi: 10.1016/j.mrrev.2007.11.005
4. Zhao Y, Zhang H, Wu X, Zhang T, Shen K, Li L, et al. Metabonomic Analysis of the Hepatic Injury Suffer From Hexavalent Chromium Poisoning in Broilers. *Environ Sci pollut Res Int* (2019) 26(18):18181–90. doi: 10.1007/s11356-019-05075-4
5. Tian X, Patel K, Ridpath JR, Chen Y, Zhou YH, Neo D, et al. Homologous Recombination and Translesion DNA Synthesis Play Critical Roles on Tolerating DNA Damage Caused by Trace Levels of Hexavalent Chromium. *PLoS One* (2016) 11(12):e167503. doi: 10.1371/journal.pone.0167503
6. Shahid M, Shamshad S, Rafiq M, Khalid S, Bibi I, Niazi NK, et al. Chromium Speciation, Bioavailability, Uptake, Toxicity and Detoxification in Soil-Plant System: A Review. *Chemosphere* (2017) 178:513–33. doi: 10.1016/j.chemosphere.2017.03.074
7. Singh P, Itankar N, Patil Y. Biomanagement of Hexavalent Chromium: Current Trends and Promising Perspectives. *J Environ Manage* (2021) 279:111547. doi: 10.1016/j.jenvman.2020.111547
8. Kong Z, Wu Z, Glick BR, He S, Huang C, Wu L. Co-Occurrence Patterns of Microbial Communities Affected by Inoculants of Plant Growth-Promoting Bacteria During Phytoremediation of Heavy Metal-Contaminated Soils. *Ecotoxicol Environ Saf* (2019) 183:109504. doi: 10.1016/j.ecoenv.2019.109504
9. Mohan D, Pittman CJ. Activated Carbons and Low Cost Adsorbents for Remediation of Tri- and Hexavalent Chromium From Water. *J Hazard Mater* (2006) 137(2):762–811. doi: 10.1016/j.jhazmat.2006.06.060
10. Gil-Cardeza ML, Ferri A, Cornejo P, Gomez E. Distribution of Chromium Species in a Cr-Polluted Soil: Presence of Cr(III) in Glomalin Related Protein Fraction. *Sci Total Environ* (2014) 493:828–33. doi: 10.1016/j.scitotenv.2014.06.080
11. Ukhurebor KE, Aigbe UO, Onyancha RB, Nwankwo W, Osibote OA, Paumo HK, et al. Effect of Hexavalent Chromium on the Environment and Removal Techniques: A Review. *J Environ Manage* (2021) 280:111809. doi: 10.1016/j.jenvman.2020.111809
12. Banerjee S, Joshi N, Mukherjee R, Singh PK, Baxi D, Ramachandran AV. Melatonin Protects Against Chromium (VI) Induced Hepatic Oxidative Stress and Toxicity: Duration Dependent Study With Realistic Dosage. *Interdiscip Toxicol* (2017) 10(1):20–9. doi: 10.1515/intox-2017-0003
13. Hegazy R, Mansour D, Salama A, Hassan A, Saleh D. Exposure to Intranasal Chromium Triggers Dose and Time-Dependent Behavioral and Neurotoxicological Defects in Rats. *Ecotoxicol Environ Saf* (2021) 216:112220. doi: 10.1016/j.ecoenv.2021.112220
14. Jin Y, Wu S, Zeng Z, Fu Z. Effects of Environmental Pollutants on Gut Microbiota. *Environ pollut* (2017) 222:1–9. doi: 10.1016/j.envpol.2016.11.045
15. Yuan X, Pan Z, Jin C, Ni Y, Fu Z, Jin Y. Gut Microbiota: An Underestimated and Unintended Recipient for Pesticide-Induced Toxicity. *Chemosphere* (2019) 227:425–34. doi: 10.1016/j.chemosphere.2019.04.088
16. Farhadi A, Banan A, Fields J, Keshavarzian A. Intestinal Barrier: An Interface Between Health and Disease. *J Gastroenterol Hepatol* (2003) 18(5):479–97. doi: 10.1046/j.1440-1746.2003.03032.x
17. Johansson ME, Ambort D, Pelaseyed T, Schutte A, Gustafsson JK, Ermund A, et al. Composition and Functional Role of the Mucus Layers in the Intestine. *Cell Mol Life Sci* (2011) 68(22):3635–41. doi: 10.1007/s00018-011-0822-3
18. Sommer F, Anderson JM, Bharti R, Raes J, Rosenstiel P. The Resilience of the Intestinal Microbiota Influences Health and Disease. *Nat Rev Microbiol* (2017) 15(10):630–8. doi: 10.1038/nrmicro.2017.58
19. Ninkov M, Popov AA, Demenesku J, Mirkov I, Mileusnic D, Petrovic A, et al. Toxicity of Oral Cadmium Intake: Impact on Gut Immunity. *Toxicol Lett* (2015) 237(2):89–99. doi: 10.1016/j.toxlet.2015.06.002
20. Chen X, Bi M, Yang J, Cai J, Zhang H, Zhu Y, et al. Cadmium Exposure Triggers Oxidative Stress, Necroptosis, Th1/Th2 Imbalance and Promotes Inflammation Through the TNF-Alpha/NF-kappaB Pathway in Swine Small Intestine. *J Hazard Mater* (2022) 421:126704. doi: 10.1016/j.jhazmat.2021.126704
21. Zhang Y, Zhang P, Shang X, Lu Y, Li Y. Exposure of Lead on Intestinal Structural Integrity and the Diversity of Gut Microbiota of Common Carp. *Comp Biochem Physiol C Toxicol Pharmacol* (2021) 239:108877. doi: 10.1016/j.cbpc.2020.108877
22. Zhong G, Wan F, Lan J, Jiang X, Wu S, Pan J, et al. Arsenic Exposure Induces Intestinal Barrier Damage and Consequent Activation of Gut-Liver Axis Leading to Inflammation and Pyroptosis of Liver in Ducks. *Sci Total Environ* (2021) 788:147780. doi: 10.1016/j.scitotenv.2021.147780
23. Zhou C, Xu P, Huang C, Liu G, Chen S, Hu G, et al. Effects of Subchronic Exposure of Mercuric Chloride on Intestinal Histology and Microbiota in the Cecum of Chicken. *Ecotoxicol Environ Saf* (2020) 188:109920. doi: 10.1016/j.ecoenv.2019.109920
24. Li A, Ding J, Shen T, Han Z, Zhang J, Abadeen ZU, et al. Environmental Hexavalent Chromium Exposure Induces Gut Microbial Dysbiosis in Chickens. *Ecotoxicol Environ Saf* (2021) 227:112871. doi: 10.1016/j.ecoenv.2021.112871
25. Yu Z, Xu SF, Zhao JL, Zhao L, Zhang AZ, Li MY. Toxic Effects of Hexavalent Chromium (Cr(6+)) on Bioaccumulation, Apoptosis, Oxidative Damage and Inflammatory Response in Channa Asiatica. *Environ Toxicol Pharmacol* (2021) 87:103725. doi: 10.1016/j.etap.2021.103725
26. Hao P, Zhu Y, Wang S, Wan H, Chen P, Wang Y, et al. Selenium Administration Alleviates Toxicity of Chromium(VI) in the Chicken Brain. *Biol Trace Elem Res* (2017) 178(1):127–35. doi: 10.1007/s12011-016-0915-9
27. Roy RV, Pratheeshkumar P, Son YO, Wang L, Hitron JA, Divya SP, et al. Different Roles of ROS and Nrf2 in Cr(VI)-Induced Inflammatory Responses in Normal and Cr(VI)-Transformed Cells. *Toxicol Appl Pharmacol* (2016) 307:81–90. doi: 10.1016/j.taap.2016.07.016
28. Lag M, Rodionov D, Ovrevik J, Bakke O, Schwarze PE, Refsnes M. Cadmium-Induced Inflammatory Responses in Cells Relevant for Lung Toxicity: Expression and Release of Cytokines in Fibroblasts, Epithelial Cells and Macrophages. *Toxicol Lett* (2010) 193(3):252–60. doi: 10.1016/j.toxlet.2010.01.015
29. Dong GH, Zhang YH, Zheng L, Liang ZF, Jin YH, He QC. Subchronic Effects of Perfluorooctanesulfonate Exposure on Inflammation in Adult Male C57BL/6 Mice. *Environ Toxicol* (2012) 27(5):285–96. doi: 10.1002/tox.20642
30. Park EJ, Park K. Oxidative Stress and Pro-Inflammatory Responses Induced by Silica Nanoparticles *In Vivo* and *In Vitro*. *Toxicol Lett* (2009) 184(1):18–25. doi: 10.1016/j.toxlet.2008.10.012
31. Liu SQ, Wang LY, Liu GH, Tang DZ, Fan XX, Zhao JP, et al. Leucine Alters Immunoglobulin a Secretion and Inflammatory Cytokine Expression Induced by Lipopolysaccharide *via* the Nuclear factor-kappaB Pathway in Intestine Of Chicken Embryos. *Animal* (2018) 12(9):1903–11. doi: 10.1017/S1751731117003342
32. Jing H, Wang F, Gao XJ. Lithium Intoxication Induced Pyroptosis *via* ROS/NF-Kappab/NLRP3 Inflammasome Regulatory Networks in Kidney of Mice. *Environ Toxicol* (2022) 37(4):825–35. doi: 10.1002/tox.23446

33. Fan W, Lv Y, Ren S, Shao M, Shen T, Huang K, et al. Zearalenone (ZEA)-Induced Intestinal Inflammation Is Mediated by the NLRP3 Inflammasome. *Chemosphere* (2018) 190:272–9. doi: 10.1016/j.chemosphere.2017.09.145
34. Shen J, Cheng J, Zhu S, Zhao J, Ye Q, Xu Y, et al. Regulating Effect of Baicalin on IKK/IKB/NF-kB Signaling Pathway and Apoptosis-Related Proteins in Rats With Ulcerative Colitis. *Int Immunopharmacol* (2019) 73:193–200. doi: 10.1016/j.intimp.2019.04.052
35. Ren ZZ, Zeng QF, Wang JP, Ding XM, Bai SP, Su ZW, et al. Effects of Maternal Dietary Canthaxanthin and 25-Hydroxycholecalciferol Supplementation on Antioxidant Status and Calcium-Phosphate Metabolism of Progeny Ducks. *Poult Sci* (2018) 97(4):1361–7. doi: 10.3382/ps/pex402
36. Zhang C, Wang X, Nie G, Wei Z, Pi S, Wang C, et al. *In Vivo* Assessment of Molybdenum and Cadmium Co-Induce Nephrotoxicity *via* NLRP3/Caspase-1-Mediated Pyroptosis in Ducks. *J Inorg Biochem* (2021) 224:111584. doi: 10.1016/j.jinorgbio.2021.111584
37. Liu G, Wang ZK, Wang ZY, Yang DB, Liu ZP, Wang L. Mitochondrial Permeability Transition and its Regulatory Components are Implicated in Apoptosis of Primary Cultures of Rat Proximal Tubular Cells Exposed to Lead. *Arch Toxicol* (2016) 90(5):1193–209. doi: 10.1007/s00204-015-1547-0
38. Zhang TY, Chen T, Hu WY, Li JC, Guo MY. Ammonia Induces Autophagy *via* Circ-IFNLR1/miR-2188-5p/RNF182 Axis in Tracheas of Chickens. *Biofactors* (2022) 48(2):416–27. doi: 10.1002/biof.1795
39. Bao BW, Kang Z, Zhang Y, Li K, Xu R, Guo MY. Selenium Deficiency Leads to Reduced Skeletal Muscle Cell Differentiation by Oxidative Stress in Mice. *Biol Trace Elem Res* (2022). doi: 10.1007/s12011-022-03288-2
40. Wan F, Zhong G, Ning Z, Liao J, Yu W, Wang C, et al. Long-Term Exposure to Copper Induces Autophagy and Apoptosis Through Oxidative Stress in Rat Kidneys. *Ecotoxicol Environ Saf* (2020) 190:110158. doi: 10.1016/j.ecoenv.2019.110158
41. Mishra S, Bharagava RN. Toxic and Genotoxic Effects of Hexavalent Chromium in Environment and its Bioremediation Strategies. *J Environ Sci Health C Environ Carcinog Ecotoxicol Rev* (2016) 34(1):1–32. doi: 10.1080/10590501.2015.1096883
42. Jobby R, Jha P, Yadav AK, Desai N. Biosorption and Biotransformation of Hexavalent Chromium [Cr(VI)]: A Comprehensive Review. *Chemosphere* (2018) 207:255–66. doi: 10.1016/j.chemosphere.2018.05.050
43. Zhang S, Zhao X, Hao J, Zhu Y, Wang Y, Wang L, et al. The Role of ATF6 in Cr(VI)-Induced Apoptosis in DF-1 Cells. *J Hazard Mater* (2021) 410:124607. doi: 10.1016/j.jhazmat.2020.124607
44. Zhang L, Jiang X, Li A, Waqas M, Gao X, Li K, et al. Characterization of the Microbial Community Structure in Intestinal Segments of Yak (Bos Grunniens). *Anaerobe* (2020) 61:102115. doi: 10.1016/j.anaerobe.2019.102115
45. Zhang Z, Cao H, Song N, Zhang L, Cao Y, Tai J. Long-Term Hexavalent Chromium Exposure Facilitates Colorectal Cancer in Mice Associated With Changes in Gut Microbiota Composition. *Food Chem Toxicol* (2020) 138:111237. doi: 10.1016/j.fct.2020.111237
46. Zhang W, Liu H, Liu C. Biopharmaceutics Classification and Intestinal Absorption of Chikusetsusaponin IVa. *Biopharm Drug Dispos* (2019) 40 (8):276–81. doi: 10.1002/bdd.2200
47. Clevers H. The Intestinal Crypt, a Prototype Stem Cell Compartment. *Cell* (2013) 154(2):274–84. doi: 10.1016/j.cell.2013.07.004
48. Zhao Y, Zhou C, Guo X, Hu G, Li G, Zhuang Y, et al. Exposed to Mercury-Induced Oxidative Stress, Changes of Intestinal Microflora, and Association Between Them in Mice. *Biol Trace Elem Res* (2021) 199(5):1900–7. doi: 10.1007/s12011-020-02300-x
49. Li M, Wang J, Wu P, Manthari RK, Zhao Y, Li W, et al. Self-Recovery Study of the Adverse Effects of Fluoride on Small Intestine: Involvement of Pyroptosis Induced Inflammation. *Sci Total Environ* (2020) 742:140533. doi: 10.1016/j.scitotenv.2020.140533
50. Maloy KJ, Powrie F. Intestinal Homeostasis and its Breakdown in Inflammatory Bowel Disease. *Nature* (2011) 474(7351):298–306. doi: 10.1038/nature10208
51. Slifer ZM, Blikslager AT. The Integral Role of Tight Junction Proteins in the Repair of Injured Intestinal Epithelium. *Int J Mol Sci* (2020) 21(3). doi: 10.3390/ijms21030972
52. Liu L, Wu C, Chen D, Yu B, Huang Z, Luo Y, et al. Selenium-Enriched Yeast Alleviates Oxidative Stress-Induced Intestinal Mucosa Disruption in Weaned Pigs. *Oxid Med Cell Longev* (2020) 2020:5490743. doi: 10.1155/2020/5490743
53. Salvo RE, Alonso CC, Pardo CC, Casado BM, Vicario M. The Intestinal Barrier Function and its Involvement in Digestive Disease. *Rev Esp Enferm Dig* (2015) 107(11):686–96. doi: 10.17235/reed.2015.3846/2015
54. Zhu Y, Wang L, Yu X, Jiang S, Wang X, Xing Y, et al. Cr(VI) Promotes Tight Joint and Oxidative Damage by Activating the Nrf2/ROS/Notch1 Axis. *Environ Toxicol Pharmacol* (2021) 85:103640. doi: 10.1016/j.etap.2021.103640
55. Pastorelli L, De Salvo C, Mercado JR, Vecchi M, Pizarro TT. Central Role of the Gut Epithelial Barrier in the Pathogenesis of Chronic Intestinal Inflammation: Lessons Learned From Animal Models and Human Genetics. *Front Immunol* (2013) 4:280. doi: 10.3389/fimmu.2013.00280
56. Barmeyer C, Schulzke JD, Fromm M. Claudin-Related Intestinal Diseases. *Semin Cell Dev Biol* (2015) 42:30–8. doi: 10.1016/j.semcdb.2015.05.006
57. Onyiah JC, Colgan SP. Cytokine Responses and Epithelial Function in the Intestinal Mucosa. *Cell Mol Life Sci* (2016) 73(22):4203–12. doi: 10.1007/s00018-016-2289-8
58. Chang X, Wang X, Feng J, Su X, Liang J, Li H, et al. Impact of Chronic Exposure to Trichlorfon on Intestinal Barrier, Oxidative Stress, Inflammatory Response and Intestinal Microbiome in Common Carp (Cyprinus Carpio L.). *Environ pollut* (2020) 259:113846. doi: 10.1016/j.envpol.2019.113846
59. Calatayud M, Gimeno-Alcaniz JV, Velez D, Devesa V. Trivalent Arsenic Species Induce Changes in Expression and Levels of Proinflammatory Cytokines in Intestinal Epithelial Cells. *Toxicol Lett* (2014) 224(1):40–6. doi: 10.1016/j.toxlet.2013.09.016
60. Haines RJ, Beard RJ, Chen L, Eitnier RA, Wu MH. Interleukin-1beta Mediates Beta-Catenin-Driven Downregulation of Claudin-3 and Barrier Dysfunction in Caco2 Cells. *Dig Dis Sci* (2016) 61(8):2252–61. doi: 10.1007/s10620-016-4145-y
61. Nowarski R, Jackson R, Gagliani N, de Zoete MR, Palm NW, Bailis W, et al. Epithelial IL-18 Equilibrium Controls Barrier Function in Colitis. *Cell* (2015) 163(6):1444–56. doi: 10.1016/j.cell.2015.10.072
62. Ma C, Yang X, Lv Q, Yan Z, Chen Z, Xu D, et al. Soluble Uric Acid Induces Inflammation *via* TLR4/NLRP3 Pathway in Intestinal Epithelial Cells. *Iran J Basic Med Sci* (2020) 23(6):744–50. doi: 10.22038/ijbms.2020.44948.10482
63. Fang Y, Xing C, Wang X, Cao H, Zhang C, Guo X, et al. Activation of the ROS/HO-1/NQO1 Signaling Pathway Contributes to the Copper-Induced Oxidative Stress and Autophagy in Duck Renal Tubular Epithelial Cells. *Sci Total Environ* (2021) 757:143753. doi: 10.1016/j.scitotenv.2020.143753
64. Zhang Y, Xu Y, Chen B, Zhao B, Gao XJ. Selenium Deficiency Promotes Oxidative Stress-Induced Mastitis *via* Activating the NF-kappaB and MAPK Pathways in Dairy Cow. *Biol Trace Elem Res* (2022) 200(6):2716–26. doi: 10.1007/s12011-021-02882-0
65. Jiang J, Yin L, Li JY, Li Q, Shi D, Feng L, et al. Glutamate Attenuates Lipopolysaccharide-Induced Oxidative Damage and mRNA Expression Changes of Tight Junction and Defensin Proteins, Inflammatory and Apoptosis Response Signaling Molecules in the Intestine of Fish. *Fish Shellfish Immunol* (2017) 70:473–84. doi: 10.1016/j.fsi.2017.09.035
66. Kohen R, Nyska A. Oxidation of Biological Systems: Oxidative Stress Phenomena, Antioxidants, Redox Reactions, and Methods for Their Quantification. *Toxicol Pathol* (2002) 30(6):620–50. doi: 10.1080/01926230290166724
67. Tschopp J, Schroder K. NLRP3 Inflammasome Activation: The Convergence of Multiple Signalling Pathways on ROS Production? *Nat Rev Immunol* (2010) 10(3):210–5. doi: 10.1038/nri2725
68. Wree A, Broderick L, Canbay A, Hoffman HM, Feldstein AE. From NAFLD to NASH to Cirrhosis-new Insights into Disease Mechanisms. *Nat Rev Gastroenterol Hepatol* (2013) 10(11):627–36. doi: 10.1038/nrgastro.2013.149
69. Xiao Y, Yan H, Diao H, Yu B, He J, Yu J, et al. Early Gut Microbiota Intervention Suppresses DSS-Induced Inflammatory Responses by Deactivating TLR/NLR Signalling in Pigs. *Sci Rep* (2017) 7(1):3224. doi: 10.1038/s41598-017-03161-6
70. Gan J, Huang M, Lan G, Liu L, Xu F. High Glucose Induces the Loss of Retinal Pericytes Partly *via* NLRP3-Caspase-1-GSDMD-Mediated Pyroptosis. *BioMed Res Int* (2020) 2020:4510628. doi: 10.1155/2020/4510628
71. Karmakar M, Minns M, Greenberg EN, Diaz-Aponte J, Pestonjamasp K, Johnson JL, et al. N-GSDMD Trafficking to Neutrophil Organelles Facilitates IL-1beta Release Independently of Plasma Membrane Pores

and Pyroptosis. *Nat Commun* (2020) 11(1):2212. doi: 10.1038/s41467-020-16043-9

Conflict of Interest: The authors declare that the research was conducted in the absence of any commercial or financial relationships that could be construed as a potential conflict of interest.

Publisher's Note: All claims expressed in this article are solely those of the authors and do not necessarily represent those of their affiliated organizations, or those of the publisher, the editors and the reviewers. Any product that may be evaluated in this article, or claim that may be made by its manufacturer, is not guaranteed or endorsed by the publisher.

frontiers | Frontiers in Immunology

TYPE Original Research
PUBLISHED 09 August 2022
DOI 10.3389/fimmu.2022.928865

OPEN ACCESS

EDITED BY
Mengyao Guo,
Northeast Agricultural University,
China

REVIEWED BY
Shiwen Xu,
Northeast Agricultural University,
China
Sankar Renu,
Upkara Inc., United States

*CORRESPONDENCE
Qiugang Ma
maqiugang@cau.edu.cn

†These authors have contributed equally to this work

SPECIALTY SECTION
This article was submitted to Nutritional Immunology, a section of the journal Frontiers in Immunology

RECEIVED 26 April 2022
ACCEPTED 15 June 2022
PUBLISHED 09 August 2022

CITATION
Kang R, Wang W, Liu Y, Huang S, Xu J, Zhao L, Zhang J, Ji C, Wang Z, Hu Y and Ma Q (2022) Dietary selenium sources alleviate immune challenge induced by *Salmonella Enteritidis* potentially through improving the host immune response and gut microbiota in laying hens.
Front. Immunol. 13:928865.
doi: 10.3389/fimmu.2022.928865

Dietary selenium sources alleviate immune challenge induced by *Salmonella Enteritidis* potentially through improving the host immune response and gut microbiota in laying hens

Ruifen Kang[1,2†], Weihan Wang[1†], Yafei Liu[1,2], Shimeng Huang[1,2], Jiawei Xu[3], Lihong Zhao[1,2], Jianyun Zhang[1,2], Cheng Ji[1], Zhong Wang[1], Yanxin Hu[3] and Qiugang Ma[1,2*]

[1]State Key Laboratory of Animal Nutrition, College of Animal Science and Technology, China Agricultural University, Beijing, China, [2]Feed Safety and Healthy Livestock, Beijing Jingwa Agricultural Innovation Center, Beijing, China, [3]College of Veterinary Medicine, China Agricultural University, Beijing, China

The aim of this study was to evaluate the effects of different selenium (Se) sources on the immune responses and gut microbiota of laying hens challenged with *Salmonella enteritidis* (*S. Enteritidis*). A total of 240 45-week-old layers were randomly divided into eight groups with six replicates per group according to a 4 × 2 factorial design, including a blank diet without Se supplementation (CON group) and three diets with 0.3 mg/kg Se supplementation from sodium selenite (IS group), yeast Se (YS group), and selenium-enriched yeast culture (SYC group), respectively. After 8 weeks of feeding, half of them were orally challenged with 1.0 ml suspension of 10^9 colony-forming units per milliliter of *S. Enteritidis* daily for 3 days. The serum was collected on days 3, 7, and 14, and the cecum content was collected on day 14 after challenge. There was no significant difference in laying performance among the eight groups before challenge. The *S. Enteritidis* challenge significantly decreased the laying performance, egg quality, GSH-Px, IgG, and IgM and increased the ratio of feed and egg, malondialdehyde (MDA), *Salmonella*-specific antibody (SA) titers, IL-6, IL-2, IL-1β, and INF-γ. However, SYC increased the level of GSH-Px and IgG and decreased IL-6, while YS decreased the level of IL-2 and IL-1β. What is more, Se supplementation decreased the SA titers to varying degrees and reduced the inflammatory cell infiltration in the lamina propria caused by *S. Enteritidis* infection. In addition, the *S. Enteritidis* challenge disrupted the intestinal flora balance by reducing the abundance of the genera *Clostridium innocuum*, *Lachnospiraceae*, and *Bifidobacterium* and increasing the genera *Butyricimonas* and *Brachyspira*, while Se supplementation increased the gut microbial alpha diversity whether

challenged or not. Under the *S. Enteritidis* challenge condition, the alteration of microbial composition by the administration of different Se sources mainly manifested as IS increased the relative abundance of the genera *Lachnospiraceae* and *Christensenellaceae*, YS increased the relative abundance of the genera *Megamonas* and *Sphingomonas*, and SYC increased the genera *Fusobacterium* and *Lactococcus*. The alteration of gut microbial composition had a close relationship with antioxidant or immune response. To summarize, different Se sources can improve the egg quality of layers challenged by *S. Enteritidis* that involves elevating the immunity level and regulating the intestinal microbiota.

KEYWORDS

selenium, laying hen, *Salmonella Enteritidis*, immune responses, gut microbiota, antioxidant

Introduction

Salmonella enterica serovar Enteritidis (*S. Enteritidis*) is a gram-negative enteric bacterium that is a major animal-infectious pathogen that can not only cause disease in poultry but also infect humans through the food chain, causing food poisoning and even death (1, 2). *S. Enteritidis* is the most important serotype of *Salmonella*, causing about 40–60% of *Salmonella* infections worldwide (3). Eggs and egg products are the main food carriers for *S. Enteritidis* to spread disease (4, 5). Although the alkaline pH value, high viscosity, and antibacterial protein in albumen create a complex antibacterial environment, *S. Enteritidis* can also be able to resist these stresses and proliferate in eggs, causing food poisoning (6, 7). In 2010, there was an outbreak of *S. Enteritidis* -contaminated eggs in the United States, with as many as 2,752 cases of infection, and more than 500 million defective eggs were recalled (8). Between 2015 and 2018, 16 European countries reported 1,209 large outbreaks of salmonellosis caused by the contaminated eggs of *S. Enteritidis* (9).. What is more, previous studies have found that the *S. Enteritidis* challenge reduced the antioxidant capacity and immune function of laying hens by increasing the serum levels of MDA, IL-1β, and IL-6 (10, 11). Thus, *S. Enteritidis* was a substantial problem for human and animal health, and some strategies are urgently needed to solve this problem.

Selenium (Se) is an essential trace element for the synthesis of some antioxidant enzymes and selenoproteins. It can clean up active oxidative substances in the body and has biological functions such as anti-oxidation, anti-stress, and improving immunity (12–15). Historically, sodium selenite (SS) was the most widely used inorganic Se in animal feed. However, organic Se has higher deposition efficiency and bioavailability, stronger biosafety, and lower toxicity than inorganic Se (16, 17). The sources of organic Se include microorganisms, plants, and animals that absorb inorganic Se and convert it to organic selenium (14, 18, 19). Liao *et al.* compared the effects of dietary supplementation of SS, yeast Se (YS), and selenoprotein on broiler chicks and found that YS was more effective in increasing Se retention in the liver and muscle than IS and selenoprotein (20). Sun *et al.* found that adding 1.0 mg/kg of selenium-enriched earthworms power to laying hens increased the levels of glutathione peroxidase, IgG, and IL-2, further promoting antioxidant activity and immune response (14).

However, there is little information about whether supplementation of different forms of Se could alleviate the adverse effect of laying hens caused by *S. Enteritidis*. The purpose of this experiment was to investigate the effects of dietary supplementation of different Se sources on the performance, immune response, and gut microbiota of laying hens challenged with *S. Enteritidis* to evaluate the effect of different Se sources in resisting the inflammatory response caused by *Salmonella* infection and provide a theoretical basis for Se to defend against *Salmonella* infection in the production practice of laying hens.

Materials and methods

Animal experimental ethics

The experiment was allowed by the China Agricultural University Animal Care and Use Committee (A0041011202-1-1, Beijing, China).

Chemicals and treatments

The common yeast culture and selenium-enriched yeast culture (SYC) used in this experiment were both fermented

from the same yeast strain (preservation number: ACCC20060), but with different levels of sodium selenite (Se content was 0 and 30 mg/kg, respectively) in their medium. Both cultures were air-dried at 60°C to inactivate the yeast. Common yeast culture was added to the diet to balance the effect of yeast culture in different treatment diets. The sodium selenite premix (IS), containing 1% of inorganic Se, was purchased from Hebei Yuanda Zhongzheng Biotechnology Co., Ltd. (Hebei, China). The yeast Se (YS), named Alkosel, contains 1,000 mg/kg of organic Se, which was extracted from inactivated whole cell yeast (Lallemand Inc., Montreal, Quebec, Canada). The *Salmonella Enteritidis* (*S. Enteritidis*) strain (preservation number CVCC3377) was purchased from China Institute of Veterinary Drug Control (Beijing, China).

Animals and experimental design

Before the feeding trial, a total of 240 45-week-old laying hens (Peking Pink, Huadu Yukou Poultry Industry Co., Ltd., Beijing) were confirmed as double-negative for *S. Enteritidis* by using PCR method and plate-agglutination assay to test the cloacal swab and serum samples, respectively (21, 22). The birds were randomly divided into eight groups, with six replicates in each group of five birds each, according to a 4 × 2 factorial design. The chickens were housed in wire cages (length, 45 cm × width, 45 cm × height, 45 cm), with one hen per cage, which were equipped with nipple water and a V-shaped feeding trough. The diets of different treatments consisted of a blank diet without Se supplementation (CON group) and three diets with 0.3-mg/kg Se supplementation, which was supplied from sodium selenite (IS group), yeast Se (YS group), and selenium-enriched yeast culture (SYC group), respectively. The whole experimental period consisted of 8 weeks of normal feeding, followed by a 3-day continuous challenge with 1.0 ml suspension of 10^9 colony-forming units (CFU)/ml (11, 23), or they received the same volume of physiological saline solution (PS), and then the samples were collected at 3, 7, and 14 days after challenge (Figure 1). In *S. Enteritidis*, in order to control the horizontal transmission of pathogenic microorganisms, the layer challenged with PS or *S. Enteritidis* was reared respectively in two houses with exactly the same conditions, with four groups of birds in each house. The feed and water were provided *ad libitum*, and the diet composition and nutrient levels are shown in Supplementary Table S1.

Laying performance and egg quality

The egg weight and the number of egg mass were recorded daily based on each replicate. Feed consumption was recorded weekly based on each replicate. The rate of egg production, the mean egg weight, the average feed intake, and the feed/egg ratio were then calculated. At the end of 3, 7, and 14 days after the *S. Enteritidis* challenge, three eggs of each replicate were randomly selected and collected to analyze the egg quality. Egg Haugh units (HU) and egg yolk color were measured by using an egg analyzer (EA-01, Orka Teachnology Ltd., Ramat Hasharon, Israel). The eggshell strength was determined by an egg force reader (EFR-01, Orka Teachnology Ltd., Ramat Hasharon, Israel). The eggshell thickness was determined by a digital egg tester (ESTG-1; Orka Technology Ltd., Ramat Hasharon, Israel)

Blood collection and serum analysis

At the end of 3, 7, and 14 days after the *S. Enteritidis* challenge, blood samples of five chicken hens in each replicate were collected into heparin treated tubes for 3 h and then centrifuged at 3,000 revolutions per minute for 20 min to get

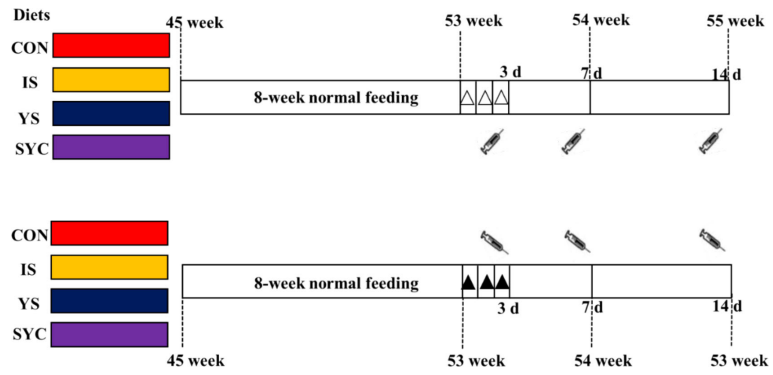

FIGURE 1
Experimental design for the timeline of supplementation of different Se sources and birds challenged with *S. Enteritidis*. : blood sampling at 3, 7, and 14 days after the challenge with *S. Enteritidis*, △: challenged with physiological saline solution, ▲: challenged with *S. Enteritidis*.

the sera, which were stored at -20°C for further analysis. All samples of five chickens in each replicate were mixed in equal proportions into one sample before analysis (24). The *S. Enteritidis* -specific antibody titer of the serum was determined by using avian *Salmonella* ELISA antibody test kit (catalog number SALS-5P, Biovetest Biotechnology Co., Ltd., Tianjin, China), following the instructions provided by the manufacturer. Serum MDA (catalog number A003-1-2), superoxide dismutase (SOD, catalog number A001-3-2), glutathione peroxidase (GSH-Px, catalog number A005-1-2), immunoglobulin A (IgA, catalog number H108-1-2), immunoglobulin G (IgG, catalog number H106), immunoglobulin M (IgM, catalog number H109), interleukin-1β (IL-1β, catalog number H002), interleukin-2 (IL-2, catalog number H003), interleukin-6 (IL-6, catalog number H007-1-2), and interferon-γ (IFN-γ, catalog number H025) were measured by using corresponding kits (Nanjing Jiancheng Biology Engineering Institute, Nanjing, China) according to instructions.

Histological examination

At 14 days after *S. Enteritidis* challenge, the duodenum, jejunum, and ileum of chicken were collected and fixed in 4% paraformaldehyde for 24 h. The method of histological examination referred to that in Li *et al.* (25). Images were collected by using the CaseViewer 2.4 software (3DHISTECH Ltd., Budapest, Hungary). The villus height and crypt depth were determined by ImageJ software.

Immunohistochemistry

The small intestine tissues were paraffin–embedded and cut into slices with a thickness of 4 μm. The slides were dewaxed, dehydrated, and then underwent antigen retrieval. The endogenous peroxidases were blocked with 3% H_2O_2 for 15 min at room temperature. The samples were incubated overnight at 4°C with a CD4 mouse-anti-chicken primary antibody (catalog number 8210-26, Southern Biotech; 1:2,000). After three washes, the samples were incubated with a goat-anti-mouse secondary antibody (Beyotime, Beijing, China) for 30 min at 37°C. Visualization was performed by using 3,3′-diaminobenzidine solution. After washing, the tissues were counterstained with hematoxylin (26).

16S rRNA gene sequencing

At 14 days after the *S. Enteritidis* challenge, the cecal contents of chicken were collected in tubes and stored at -80° C for further analysis. The cecal contents from five chicken in each replicate were also mixed in equal proportions into one sample (27) to make the microbiome correspond to the phenotypic indicators and serum indices. The total DNA was extracted by using the Omega Bio-tek stool DNA kit (Omega, Norcross, GA, USA) following the manufacturer's instructions. The V3–V4 region of the 16SrRNA gene was amplified with 338F (5′-ACTCCTACGGGAGGCAGCAG-3′) and 806R (5′-GGACTACHVGGGTWTCTAAT-3′). The PCR products were recovered by 2% agarose gel, purified using AxyPrep DNA Gel Extraction Kit (AxygenBiosciences, Union City, CA, USA), and quantified with QuantiFluor™-ST (Promega, USA). The purified PCR products were sequenced on the Illumina MiSeq PE300 platform (Shanghai MajorBio Biopharma Technology Co., Ltd., Shanghai, China).

Statistical analysis

The data were analyzed by using GraphPad Prism, version 7.01 (GraphPad Software, Inc., CA, USA). The results were analyzed by two-way ANOVA, followed by Duncan's multiple comparison when the data were in Gaussian distribution. Otherwise, the Kruskal–Wallis test, followed by Duncan's multiple comparison, was used for non-normally distributed data. The data were presented as mean ± SEM. P <0.05 was considered as significantly different.

The alpha-diversity of the microbiome was calculated by sampling-based OUT analysis by using the MOTHUR program (version v.1.30.1). The beta diversity of the microbiome was displayed by a principal coordinate analysis (PCoA), which was conducted based on the Bray–Curtis distance using QIIME (version 1.17). The difference of bacterial genera that were predominant in bacterial communities among different treatment groups was identified by linear discriminant analysis effect size (LEfSe).

Results

Effects of different SE sources on the laying performance of laying hens challenged with *S. Enteritidis*

During the 8-week normal feeding period, no differences of laying performance were observed among the different treatment groups (P > 0.05) (Table 1). As shown in Table 2, the egg production rate and egg mass at 0–3 and 4–7 days were reduced markedly, and the feed-to-egg ratio at 4–7 days was increased after the *S. Enteritidis* challenge (P < 0.05). In addition, compared to IS, SYC supplementation significantly increased the egg production rate from 8 to 14 days after the *S. Enteritidis* challenge (P < 0.05). There were no differences in the mean weight of eggs and average feed intake of laying hens during 0–3, 4–7, and 8–14 days among different treatment groups (P > 0.05).

TABLE 1 Effects of different selenium sources in diets on the performance of layers before challenge by *S. Enteritidis*.

Diets	Houses[a]	Egg production rate(%)	Egg mass(g/day/hen)	Mean weight of eggs(g)	Average feed intake(g)	Feed/egg ratio (g/g)
CON	A	86.67	50.88	58.45	108.92	2.15
CON	B	84.62	49.82	58.87	105.07	2.11
IS	A	86.19	50.06	57.98	105.54	2.12
IS	B	84.05	49.95	59.37	106.52	2.14
YS	A	89.95	51.89	57.98	109.50	2.10
YS	B	88.13	52.91	59.85	110.12	2.10
SYC	A	88.40	51.06	57.56	106.86	2.10
SYC	B	88.97	51.86	58.34	106.81	2.06
SEM		2.069	1.566	0.790	1.962	0.054
CON		85.65	50.35	58.66	107.00	2.13
IS		85.12	50.01	58.67	106.03	2.13
YS		89.04	52.40	58.91	109.81	2.10
SYC		88.69	51.46	57.95	106.84	2.08
SEM		1.463	1.107	0.559	1.387	0.038
	A	87.80	50.97	57.99	107.70	2.12
	B	86.44	51.14	59.11	107.13	2.11
SEM		1.034	0.783	0.395	0.981	0.027
P-values	House	0.367	0.885	0.063	0.685	0.733
	Diet	0.168	0.430	0.654	0.275	0.770
	House × diet	0.898	0.906	0.803	0.599	0.908

Different letters indicate statistically significant differences among different treatments ($P < 0.05$).
CON, basal diet; IS, sodium selenite; YS, yeast selenium; SYC, selenium-enriched yeast culture.
[a]The layers were reared respectively in two houses, with four groups of birds in each house.

Effects of different SE sources on the egg quality of laying hens challenged with *S. Enteritidis*

As demonstrated in Table 3, the *S. Enteritidis* challenge had no significant effect on eggshell strength, egg yolk color, egg yolk percent, and eggshell thickness at 3, 7, and 14 days ($P > 0.05$). The egg Haugh unit on day 3 was significantly reduced after the *S. Enteritidis* challenge ($P < 0.05$). However, YS supplementation significantly increased the egg yolk color compared to IS ($P < 0.05$), SYC supplementation significantly increased the egg yolk percent at 7 and 14 days, and IS increased the eggshell thickness at 7 days after the *S. Enteritidis* challenge compared to CON ($P < 0.05$).

Effects of different SE sources on the serum antioxidant status of laying hens challenged with *S. Enteritidis*

As shown in Figure 2, the serum GSH-Px at 7 days in the IS group was significantly higher than that in the IS+SE group ($P < 0.05$). The GSH-Px at 14 days in the IS group was significantly higher than that in CON, YS, and IS+SE groups ($P < 0.05$ and $P < 0.001$), and the GSH-Px in the SYC+SE group was significantly higher than that in the IS+SE group ($P < 0.05$). There was no obvious difference in the serum SOD of laying hens among the eight groups at 3, 7, and 14 days after the challenge with PS or *S. Enteritidis* ($P > 0.05$); however, the serum MDA at 7 days in the CON+SE group was significantly increased compared to that in the CON group ($P < 0.05$).

Effects of different SE sources on serum *Salmonella*-specific antibody titers of laying hens challenged with *S. Enteritidis*

As shown in Figure 3, the level of *Salmonella*-specific antibody (SA) titers at 3 days in the YS+SE group was significantly higher than that in the YS group ($P < 0.05$); however, no obvious difference was observed among the other groups ($P > 0.05$). The SA titers at 7 days in the CON +SE, IS+SE, and YS+SE groups were significantly higher than those in the CON, IS, and YS groups ($P < 0.001$), and the titer in SYC+SE was significantly lower than those in the CON+SE, IS+SE, and YS+SE groups ($P < 0.001$). The SA titers at 14 days

TABLE 2 Effects of different selenium sources in diets on the performance of layers challenged by *S. Enteritidis*.

Diets	SE	Egg production rate (%)			Egg mass(g/day/hen)			Mean weight of eggs (g)			Average feed intake (g)			Feed/egg ratio(g/g)		
		0–3 days	4–7 days	8–14 days	0–3 days	4–7 days	8–14 days	0–3 days	4–7 days	8–14 days	0–3 days	4–7 days	8–14 days	0–3 days	4–7 days	8–14 days
CON	–	86.67^{ab}	85.83	83.81^{ab}	51.08	50.90	48.78	58.91	59.27	58.18	114.90	100.30	98.19	2.26	1.98	2.02
CON	+	85.55^{ab}	83.33	83.81^{ab}	50.49	48.37	48.41	58.93	58.05	57.77	111.60	103.30	100.20	2.22	2.14	2.07
IS	–	92.22^{a}	89.17	80.00^{b}	53.45	51.96	46.07	57.99	58.26	57.59	96.89	101.20	98.29	1.82	1.95	2.14
IS	+	82.22^{b}	82.50	82.86^{ab}	49.21	48.81	48.89	59.84	59.14	59.01	106.00	105.30	97.05	2.15	2.16	1.98
YS	–	90.74^{a}	87.69	87.83^{ab}	52.55	50.94	50.39	57.91	58.12	57.31	105.53	98.43	101.80	2.01	1.94	2.02
YS	+	88.89^{ab}	83.33	85.71^{ab}	52.22	49.24	50.06	58.75	59.06	58.40	105.60	105.80	101.20	2.02	2.16	2.02
SYC	–	91.97^{a}	91.88	93.92^{a}	53.31	52.53	53.87	57.96	57.16	57.35	112.20	99.44	108.30	2.10	1.89	2.01
SYC	+	83.33^{b}	84.17	83.81^{ab}	48.39	48.90	47.99	58.09	58.12	57.30	98.89	100.70	100.50	2.05	2.06	2.10
SEM		1.535	2.612	2.492	1.309	1.725	1.637	0.778	0.790	0.723	4.729	2.883	3.159	0.117	0.059	0.07
CON		86.11^{b}	84.58	83.81^{ab}	50.78	49.63	48.60	58.92	58.66	57.97	113.22^{a}	101.79	99.19	2.24	2.06	2.05
IS		87.22^{ab}	85.83	81.43^{b}	51.33	50.39	47.48	58.92	58.70	58.30	101.44^{b}	103.25	97.67	1.99	2.05	2.06
YS		89.82^{a}	85.51	86.77^{ab}	52.39	50.09	50.22	58.33	58.59	57.85	105.54^{ab}	102.13	101.52	2.02	2.05	2.02
SYC		87.65^{ab}	88.02	88.87^{a}	50.85	50.71	50.93	58.02	57.64	57.33	105.55^{ab}	100.05	104.38	2.08	1.98	2.06
SEM		1.086	1.847	1.762	0.925	1.22	1.157	0.55	0.559	0.511	3.344	2.038	2.234	0.082	0.042	0.05
	–	90.40^{a}	88.64^{a}	86.39	52.60^{a}	51.58^{a}	49.78	58.19	58.20	57.61	107.38	99.82	101.64	2.05	1.94^{b}	2.05
	+	85.00^{b}	83.33^{b}	84.05	50.08^{b}	48.83^{b}	48.84	58.90	58.59	58.12	105.50	103.79	99.74	2.11	2.13^{a}	2.04
	SEM	0.768	1.306	1.246	0.654	0.863	0.818	0.389	0.395	0.362	2.365	1.441	1.580	0.058	0.030	0.035
	SE	< 0.001	0.011	0.202	0.015	0.038	0.428	0.216	0.495	0.332	0.582	0.069	0.408	0.442	< 0.001	0.934
P-values	Se	0.148	0.611	0.042	0.600	0.934	0.184	0.590	0.504	0.611	0.133	0.739	0.204	0.171	0.509	0.955
	SE × Se	0.019	0.754	0.097	0.211	0.949	0.102	0.633	0.452	0.544	0.167	0.752	0.476	0.329	0.941	0.361

Different letters indicate statistically significant differences among different treatments (P < 0.05).
CON, basal diet; IS, sodium selenite; YS, yeast selenium; SYC, selenium-enriched yeast culture; SE, Salmonella Enteritidis; –, with physiological saline solution challenge; +, with SE challenge.

in the four groups challenged with *S. Enteritidis* were significantly higher than those in the four groups challenged with PS ($P < 0.05$, $P < 0.01$, and $P < 0.001$), and the titers in the IS+SE group were significantly decreased compared to that in the CON+SE group ($P < 0.05$).

Effects of different SE sources on the immune response of laying hens challenged with *S. Enteritidis*

As shown in Figure 4, there was no obvious difference in the serum IgA of laying hens among the eight groups at 3, 7, and 14 days after the challenge with PS or *S. Enteritidis* ($P > 0.05$) (Figures 4A–C). The serum IgG in the SYC group was significantly higher than those in the CON, IS, and YS groups ($P < 0.05$). However, compared to SYC, the serum IgG at 14 days was significantly decreased in the SYC+SE group ($P < 0.05$) (Figure 4F). The serum IgM at 3 days in CON+SE was significantly decreased compared to that in CON ($P < 0.05$) (Figure 4G). The serum IgM at 14 days in YS+SE was significantly decreased compared to that in YS ($P < 0.05$) (Figure 4I). The serum IL-1β at 3 days in CON+SE was significantly higher than that in CON ($P < 0.05$) (Figure 4J). The serum IL-2 at 7 days in all groups challenged with *S. Enteritidis* was significantly higher than those challenged with PS ($P < 0.05$) (Figure 4N); however, only SYC+SE had significantly increased serum IL-2 at 14 days compared to SYC ($P < 0.05$) (Figure 4O). The serum IL-6 at 3 days in the CON, YS, and SYC groups of *S. Enteritidis* challenge was significantly higher than those challenged with PS ($P < 0.05$). IL-6 in SYC+SE was also significantly increased compared to that in the IS+SE group ($P < 0.05$) (Figure 4P). After the challenge with *S. Enteritidis*, the level of IL-6 at 14 days in IS+SE was significantly higher than those in the IS and SYC+SE groups ($P < 0.05$) (Figure 4R). The serum INF-γ at 3 days in SYC+SE was remarkably increased compared to that in the YS+SE group (Figure 4S), and the serum INF-γ at 7 days in SYC+SE was significantly higher than that in SYC group ($P < 0.05$) (Figure 4T). In addition, *S. Enteritidis* infection caused blue round particles in the lamina propria, which means that the infiltration of inflammatory cells is obvious. Se supplementation

TABLE 3 Effects of different selenium sources in diets on the quality of eggs challenged by *S. Enteritidis*.

Diets	SE	Eggshell strength (N)			Egg Haugh unit			Egg yolk color			Egg yolk percent (%)			Eggshell thickness (mm)		
		3 days	7 days	14 days	3 days	7 days	14 days	3 days	7 days	14 days	3 days	7 days	14 days	3 days	7 days	14 days
CON	–	35.69	35.13	30.51	76.64	76.21	76.65	3.67	2.89	3.11	26.57	27.16	26.98	0.39	0.38	0.36
CON	+	32.75	36.07	30.11	74.62	68.60	73.69	3.33	3.00	2.78	26.84	27.43	27.58	0.39	0.39	0.38
IS	–	33.43	32.56	34.06	71.13	75.94	68.47	3.56	3.00	2.95	28.24	26.77	27.68	0.38	0.43	0.38
IS	+	37.60	35.19	29.58	70.32	77.70	69.28	2.67	3.44	3.44	26.83	26.40	26.78	0.40	0.44	0.38
YS	–	35.74	32.80	32.22	74.00	75.67	72.35	3.89	3.89	3.44	27.81	28.04	27.96	0.39	0.42	0.35
YS	+	33.58	30.26	33.75	72.05	75.44	76.44	4.11	3.89	3.56	27.40	27.44	28.08	0.39	0.41	0.39
SYC	–	35.81	26.67	31.85	78.61	72.20	78.01	3.33	3.56	3.00	28.93	29.09	29.16	0.39	0.40	0.36
SYC	+	36.17	34.69	29.77	66.79	73.60	74.18	3.56	3.44	3.11	28.46	28.28	29.49	0.40	0.42	0.37
SEM		2.046	2.316	3.071	2.482	3.759	2.575	0.248	0.373	0.232	0.693	0.617	0.541	0.008	0.014	0.011
CON		34.22	35.60	30.31	75.63	72.41	75.17	3.50^{ab}	2.95	2.95	26.70	27.30^{b}	27.28^{b}	0.39	0.39^{b}	0.37
IS		35.52	33.87	31.82	70.73	76.82	68.88	3.11^{b}	3.22	3.20	27.54	26.59^{b}	27.23^{b}	0.39	0.43^{a}	0.38
YS		34.66	31.53	32.99	73.03	75.56	74.40	4.00^{a}	3.89	3.50	27.61	27.74^{ab}	28.02^{b}	0.39	0.42^{ab}	0.37
SYC		35.99	30.68	30.81	72.70	72.90	76.10	3.44^{ab}	3.50	3.06	28.69	28.68^{a}	29.33^{a}	0.39	0.41^{ab}	0.37
SEM		1.447	1.638	2.172	1.755	2.658	1.821	0.176	0.264	0.164	0.490	0.436	0.382	0.006	0.010	0.008
	–	35.17	31.79	32.16	75.10^{a}	75.01	73.87	3.61	3.33	3.13	27.89	27.76	27.95	0.39	0.41	0.36
	+	35.03	34.05	30.80	70.95^{b}	73.84	73.40	3.42	3.44	3.22	27.38	27.39	27.98	0.40	0.41	0.38
	SEM	1.023	1.158	1.536	1.241	1.879	1.288	0.124	0.186	0.116	0.347	0.309	0.270	0.004	0.007	0.006
	SE	0.924	0.187	0.541	0.031	0.666	0.798	0.288	0.688	0.629	0.321	0.401	0.921	0.320	0.594	0.057
P-values	Se	0.819	0.175	0.827	0.303	0.604	0.053	0.021	0.123	0.253	0.075	0.026	0.004	0.929	0.026	0.778
	Se × SE	0.333	0.186	0.793	0.134	0.578	0.417	0.116	0.896	0.539	0.694	0.833	0.542	0.676	0.739	0.401

Different letters indicated statistically significant differences among different treatments ($P < 0.05$).
CON, basal diet; IS, sodium selenite; YS, yeast selenium; SYC, selenium-enriched yeast culture; SE, Salmonella Enteritidis; –, with physiological saline solution challenge; +, with SE challenge.

reduced the inflammatory cell infiltration in the lamina propria (Figure 5).

Effects of different SE sources on the small intestine morphology of laying hens challenged with *S. Enteritidis*

The histopathological changes of the small intestine are shown in Figure 6 to analyze the effects of Se supplementation on the intestinal morphology of layers after the *S. Enteritidis* challenge. Hematoxylin–eosin (H&E) staining suggested that the morphology of the duodenum, jejunum, and ileum was destroyed by the *S. Enteritidis* challenge, as revealed by crypt atrophy and the adhesion or fusion of villi, whereas Se supplementation could alleviate the degree of intestinal damage caused by the *S. Enteritidis* challenge, which was demonstrated by the increase in villus height and the ratio of villi and crypt while the crypt depth of the duodenum, jejunum, and ileum decreased ($P < 0.05$) (Figure 7).

Effects of different SE sources on the gut microbial composition of laying hens challenged with *S. Enteritidis*

High-throughput 16S rRNA gene sequencing was conducted to investigate whether Se supplementation would affect the gut microbial composition in laying hens challenged with *S. Enteritidis*. As shown in Figure 8, significant differences were observed in alpha diversity among different groups, including Ace and Sobs. Compared to IS, the Ace and Sobs in the YS and SYC groups were significantly increased ($P < 0.05$). The Ace and Sobs in the YS+SE group were significantly higher than that in the CON+SE group ($P < 0.05$).

A PCoA was conducted to evaluate the differences among different groups. Our results suggested that Se supplementation and *S. Enteritidis* infection would not alter the β diversity of the gut microbial composition (Figures 9A–F). The most abundant cecal microbiota composition among different groups was revealed by phylogenetic analysis. At the phylum level, *Bacteroidota*, *Firmicutes*, *Desulfobacterota*, *Proteobacteria*, *Campilobacterota*, *Fusobacteriota*,

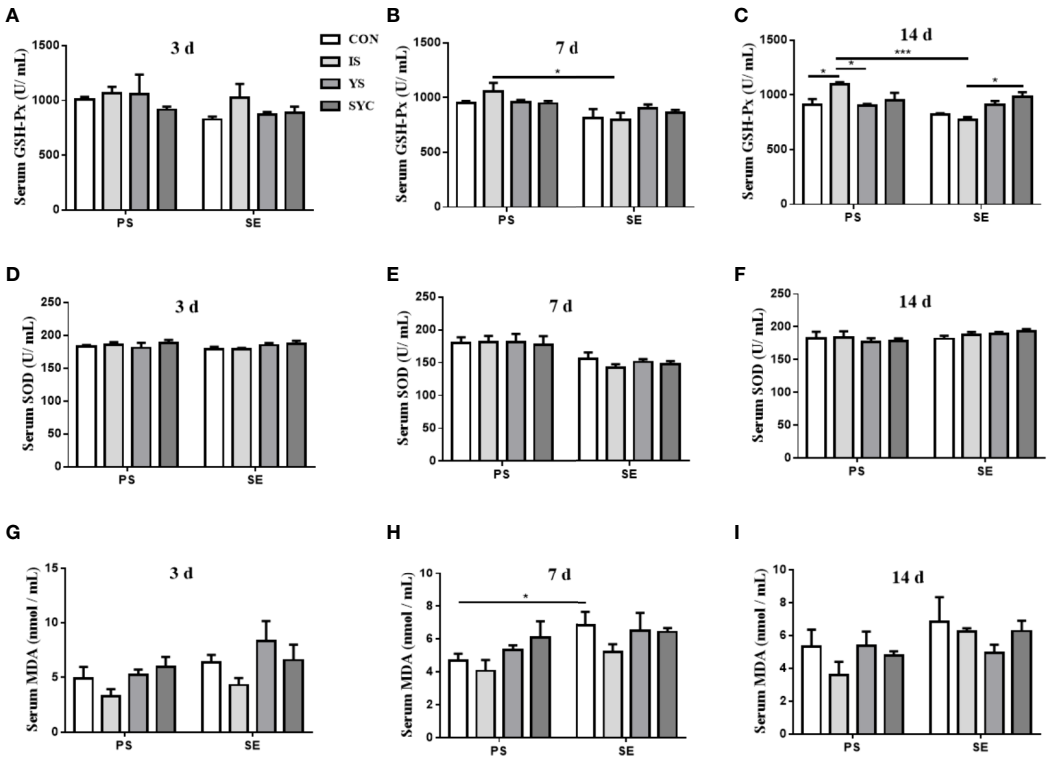

FIGURE 2
Effects of dietary supplementation with different Se sources on the serum antioxidant status of layers challenged with *S. Enteritidis*. CON, basal diet; IS, sodium selenite; YS, yeast selenium; SYC, selenium-enriched yeast culture; PS, challenged with physiological saline solution; SE, challenged with *S. Enteritidis*. The levels of serum GSH-Px, SOD, and MDA were measured among different periods and treatments **(A–I)**. The data were presented as mean ± SEM. Significance was compared with every other group; $^{*}P < 0.05$, $^{***}P < 0.001$.

and *Deferribacterota* were dominant (Figure 9G). The predominant genera were *Bacteroides*, *unclassified_o:Bacteroidales*, *Rikenellaceae_RC9_gut_group*, *norank_f:norank_o:Clostridia_UCG-014*, *Lactobacillus*, *Faecalibacterium*, *unclassified_f:Lachnospiraceae*, *Phascolarctobacterium*, *norank_f:norank_o:RF39*, *Desulfovibrio*, *Ruminococcus_torques_group*, *Alistipes*, *Parabacteroides*, and so on (Figure 9H).

As shown in Figure 10, the specific bacterial taxa associated with different Se sources and *S. Enteritidis* treatments were identified using LEfSe (LDA score > 2.0). Se supplementation

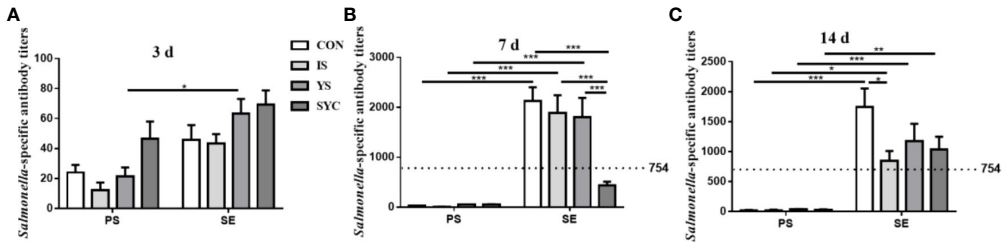

FIGURE 3
Effects of dietary supplementation with different Se sources on serum *Salmonella*-specific antibody titers of layers challenged with *S. Enteritidis*. CON, basal diet; IS, sodium selenite; YS, yeast selenium; SYC, selenium-enriched yeast culture; PS, challenged with physiological saline solution; SE, challenged with *S. Enteritidis*. The titers were measured among different periods and treatments **(A–C)**. When the antibody titer was >754, the immune status of *Salmonella* is positive, and when the antibody titer was ≤754, the immune status of *Salmonella* is negative. The data were presented as mean ± SEM. Significance was compared with every other group; $^{*}P < 0.05$, $^{**}P < 0.01$", $^{***}P < 0.001$.

10.3389/fimmu.2022.928865

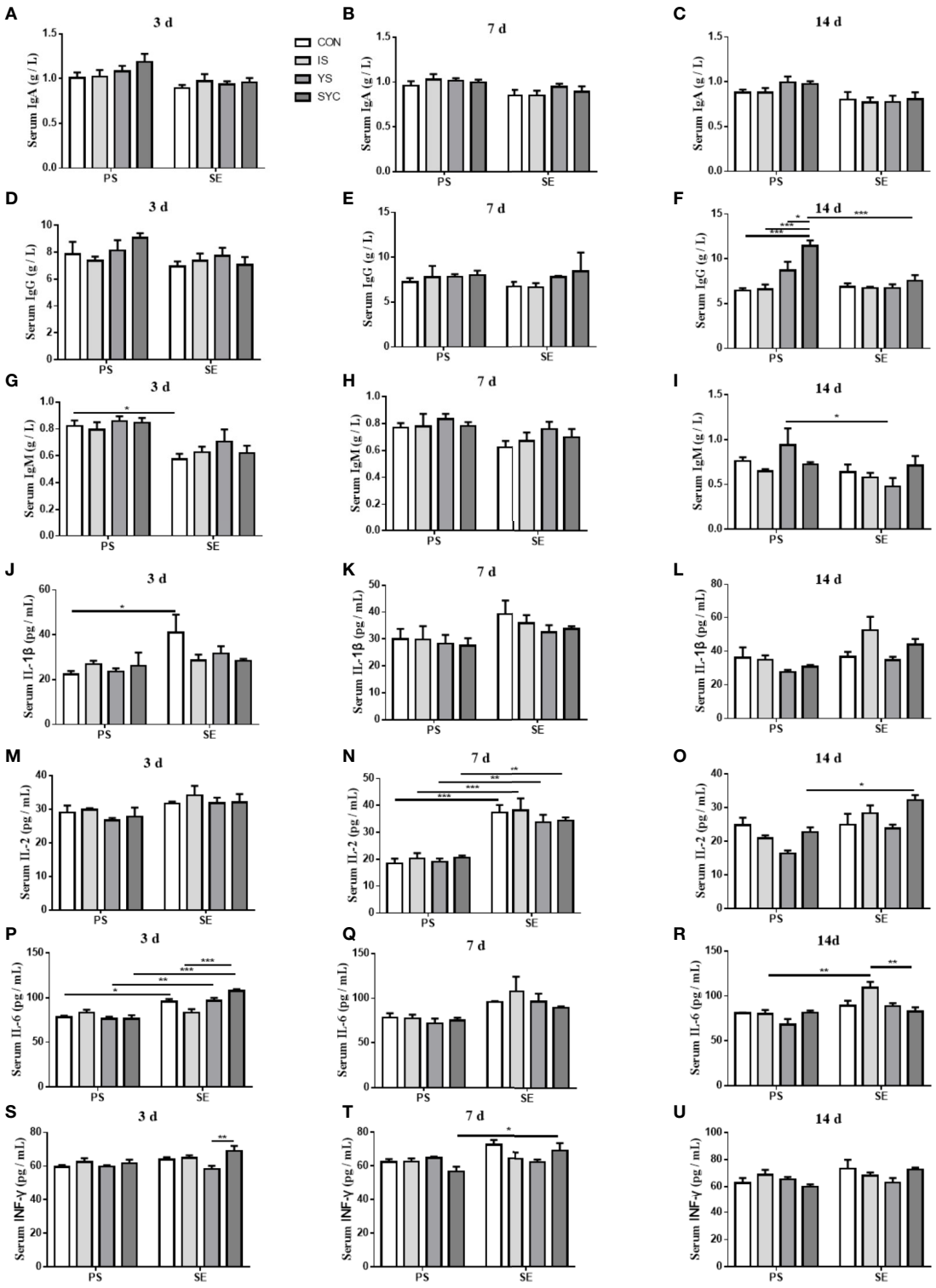

FIGURE 4
Effects of dietary supplementation with different Se sources on the serum parameters of layers challenged with *S. Enteritidis*. CON, basal diet; IS, sodium selenite; YS, yeast selenium; SYC, selenium-enriched yeast culture; PS, challenged with physiological saline solution; SE, challenged with *S. Enteritidis*. The levels of serum IgA, IgG, IgM, IL-2, Il-6, IL-β, and INF-γ were measured among different periods and treatments **(A–U)**. The data were presented as mean ± SEM. Significance was compared with every other group; $^{*}P < 0.05$, $^{**}P < 0.01$, $^{***}P < 0.001$.

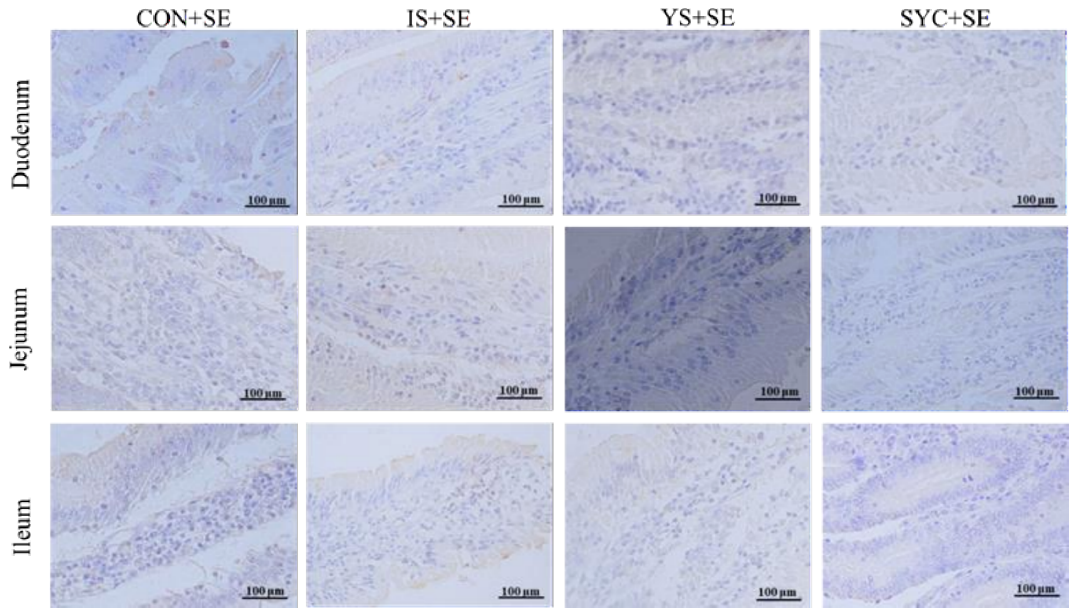

FIGURE 5
Effects of dietary supplementation with different Se sources on the small intestine immunoexpression of CD4 of laying hens challenged with *S. Enteritidis*. CON, basal diet; IS, sodium selenite; YS, yeast selenium; SYC, selenium-enriched yeast culture; SE, challenged with *S. Enteritidis*. Immunohistochemistry; total magnification ×400.

increased the abundance of gut microbial composition before or after the challenge with *S. Enteritidis* (Figures 10A, B). Compared to the CON, the relative abundance of *Butyricimonas* and *Brachyspira* was significantly increased, and the relative abundance of *unclassified_f:Tannerellaceae*, *norank_f:UCG_010*, *norank_f:Barnesiellaceae*, *Clostridium_innocuum_group*, *Coprobacter*, *CAG_352*, *norank_f:norank_o:norank_c:Clostridia*, *Lachnospiraceae_UCG_002*, and *Bifidobacterium*, respectively, was significantly decreased in the CON+SE group (Figure 10C). The dominant bacteria of the IS group were *unclassified_o:Bacteroidales*, *Clostridium_sensu_stricto_1*, and *Paraprevotella*, while the dominant bacteria in the IS+SE group were *Shuttleworthia*, *Lachnospiraceae_UCG_002*, *unclassified_f:Paludibacteraceae*, *unclassified_p:Firmicutes*, and *unclassified_o:Erysipelotrichales* (Figure 10D). The dominant bacteria in the YS group were also *unclassified_o:Bacteroidales*, *unclassified_f:Tannerellaceae*, *Barnesiella*, *Alcaligenes*, *Ochrobactrum*, *Aquabacterium*, *Ralstonia*, and so on, while the dominant bacteria in the YS+SE group were *Shuttleworthia*, *norank_f:norank_o:norank_c:norank_p:WPS_2*, *unclassified_f:Barnesiellaceae*, *Lachnoclostridium*, and *Helicobacter* (Figure 10E). In addition, the dominant bacteria in the SYC group were *unclassified_f:Tannerellaceae*, *Megasphaera*, *unclassified_f:Eggerthellaceae*, *Shewanella*, *CHKCI002*, *Ochrobactrum*, *Arthrobacter*, and so on, while the dominant bacteria in the SYC+SE group were *Phascolarctobacterium*, *DEV114*, *Intestinimonas*, and *Tyzzerella* (Figure 10F).

Effects of dietary supplementation with different SE sources on the difference of the gut microbiota and its correlation with the antioxidant and the immunity of laying hens challenged with *S. Enteritidis*

Spearman correlation was performed to predict the correlation among the intestinal microbial communities and the antioxidant and immunity of laying hens 14 days after the challenge with PS or *S. Enteritidis*. As shown in Figure 11A, at 14 days after the challenge with PS, *Lactobacillus* was negatively correlated with MDA and *Christensenellaceae_R-7_group* was positively correlated with IgA, but *Rikenellaceae_RC9_gut_group* was negatively correlated with IgA ($P < 0.05$). *Erysipelatoclostridium*, *Lachnoclostridium*, *Fournierella*, *Streptococcus*, *Fusobacterium*, *Barnesiella*, *Alistipes*, and *Faecalibacterium* were positively correlated with IgG ($P < 0.05$), while *Rikenellaceae_RC9_gut_group* was negatively correlated with IgG ($P < 0.05$). *Barnesiella* was positively correlated with IL-1β ($P < 0.05$), *Colidextribacter*, *Shuttleworthia*, and *Ruminococcus_torques_group* were positively correlated with IL-2 ($P < 0.05$), *Alloprevotella*, *Butyricicoccus*, and *Shuttleworthia* were positively correlated with IL-6 ($P < 0.05$), while *Parasutterella* and *NK4A214_group* were negatively correlated with INF-γ ($P < 0.05$).

As shown in Figure 11B, at 14 days after the challenge with *S. Enteritidis*, *Fusobacterium* was positively correlated with GSH-Px ($P < 0.05$) and *Ruminococcus_torques_group* and *Faecalibacterium* were negatively correlated with MDA. On

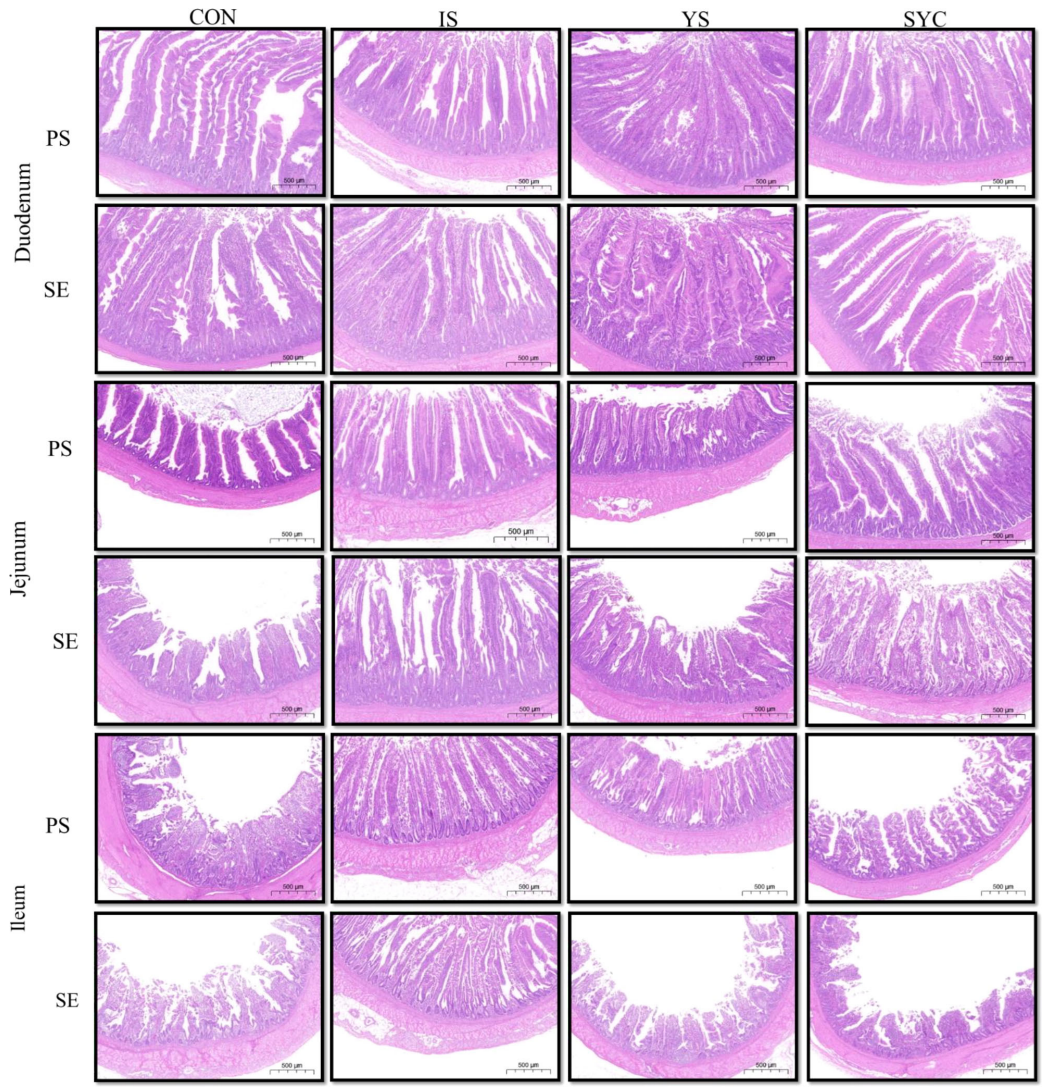

FIGURE 6
Effects of dietary supplementation with different Se sources on the small intestine histomorphology of laying hens challenged with *S. Enteritidis*. CON, basal diet; IS, sodium selenite; YS, yeast selenium; SYC, selenium-enriched yeast culture; PS, challenged with physiological saline solution; SE, challenged with *S. Enteritidis*. Hematoxylin and eosin staining of the duodenum, jejunum, and ileum of hens (bar = 500 μm).

the contrary, *Rikenellaceae_RC9_gut_group* was positively correlated with MDA ($P < 0.05$). *Parabacteroides* was negatively correlated with IgA, and *Lactobacillus* was negatively correlated with IgG and IgM ($P < 0.05$). *Campylobacter* and *Desulfovibrio* were positively correlated with IL-1β ($P < 0.05$). *Parasutterella* and *Phascolarcto bacterium* were positively correlated with IL-2. On the contrary, *Prevotellaceae_UCG-001* was negatively correlated with IL-2 ($P < 0.05$). *Lachnoclostridium*, *GCA-900066575*, *Shuttleworthia*, and *Ruminococcus_torques_group* were positively correlated with IL-6 ($P < 0.05$), while *Fusobacterium* and *Phascolarctobacterium* were negatively correlated with IL-6 ($P < 0.05$).

Discussion

S. Enteritidis was one of the major factors that affected laying performance for a long time. Previous studies have shown that the *S. Enteritidis* infection of laying hens reduced their feed intake, egg production rate, and body weight (28), which may be related to the colonization of *Salmonella* in the gut (29), disrupting the composition of gut microbiota (30), which, in turn, destroyed the gut barrier function and induced inflammation (31). In addition, oxidative stress is often accompanied by inflammation. When the body was infected by external pathogens, it activated the immune system to clear the infection, and this progress also generated oxidative stress

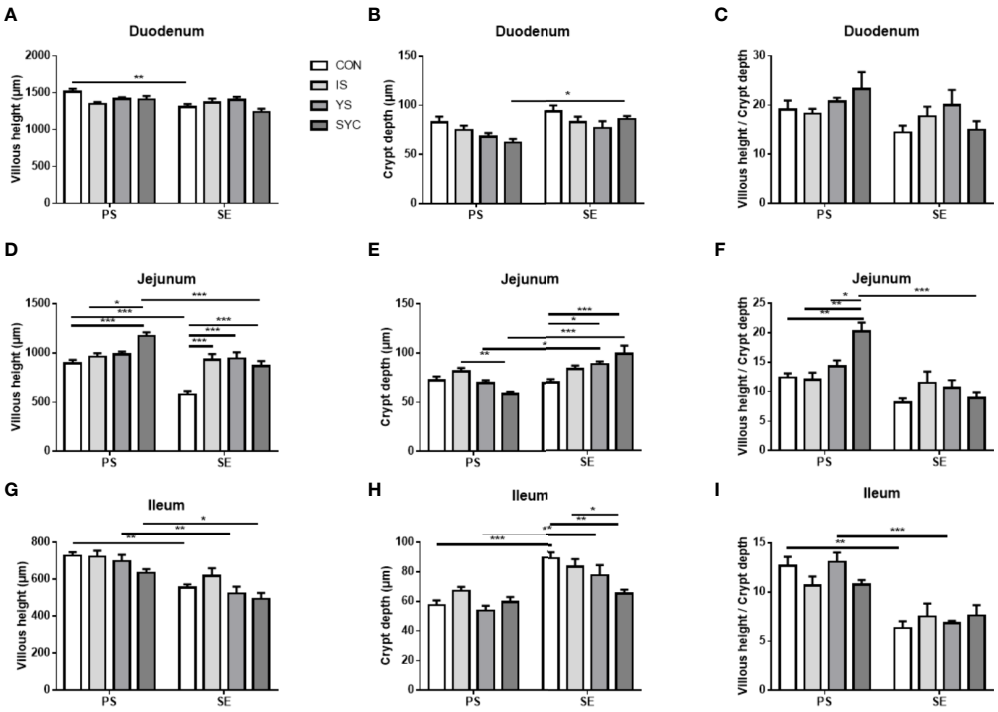

FIGURE 7
Effects of dietary supplementation with different Se sources on histomorphological measurements in the duodenum, jejunum, and ileum of hens challenged with *S. Enteritidis*. CON, basal diet; IS, sodium selenite; YS, yeast selenium; SYC, selenium-enriched yeast culture; PS, challenged with physiological saline solution; SE, challenged with *S. Enteritidis*. **(A–I)** The villus height, the crypt depth, and the villus/crypt ratio were measured randomly in each sample from different groups. The data were presented as mean ± SEM. Significance was compared with every other group; $^{*}P < 0.05$, $^{**}P < 0.01$, ***P < 0.001.

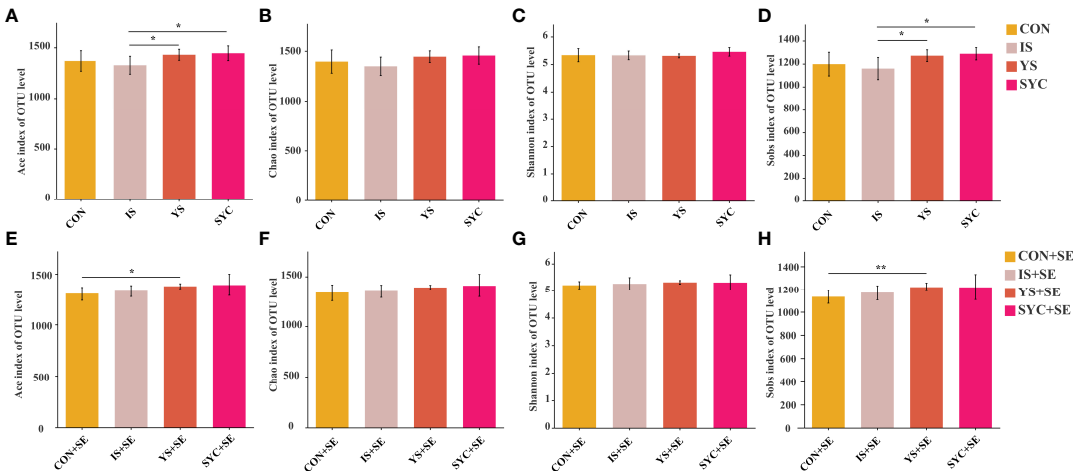

FIGURE 8
Effects of dietary supplementation with different Se sources on the alpha diversity of the cecal microbiota in layers challenged with *S. Enteritidis*. CON, basal diet; IS, sodium selenite; YS, yeast selenium; SYC, selenium-enriched yeast culture; CON+SE, IS+SE, YS+SE, and SYC+SE mean CON, IS, YS, and SYC challenged with *S. Enteritidis*, respectively. **(A, E)** Ace index of OUT level, **(B, F)** Chao index of OUT level, **(C, G)** Shannon index of OUT level, and **(D, H)** Sobs index of OUT level. The data were presented as means ± SEM. Significance was compared with every other group; $^{*}P < 0.05$, $^{**}P < 0.01$.

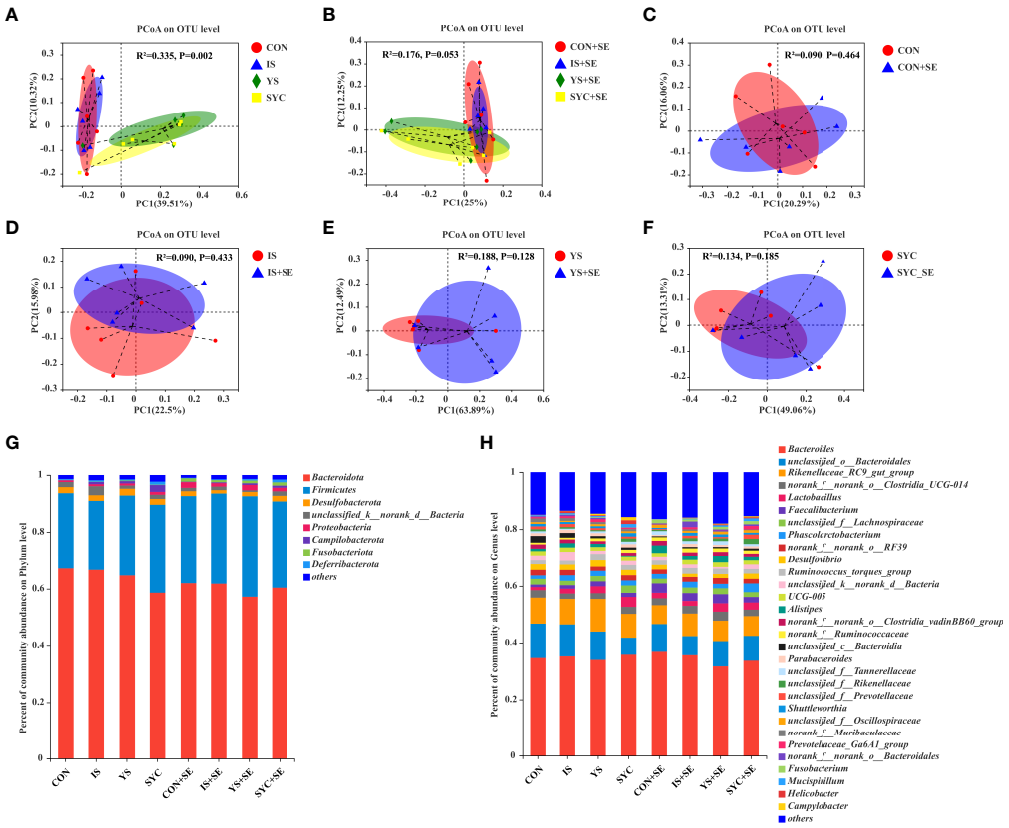

FIGURE 9
Effects of dietary supplementation with different Se sources on the principal coordinate analysis (PCoA) and the relative abundance in the cecal microbiota of laying hens challenged with *S. Enteritidis*. CON, basal diet; IS, sodium selenite; YS, yeast selenium; SYC, selenium-enriched yeast culture; CON+SE, IS+SE, YS+SE, and SYC+SE mean CON, IS, YS, and SYC challenged with *S. Enteritidis*, respectively. **(A)** PCoA in the CON, IS, YS, and SYC groups. **(B)** PCoA in the CON+SE, IS+SE, YS+SE, and SYC+SE groups. **(C)** PCoA in the CON and CON+SE groups. **(D)** PCoA in the IS and IS+SE groups. **(E)** PCoA in the YS and YS+SE groups. **(F)** PCoA in the SYC and SYC+SE groups. **(G)** Relative abundance of gut microbiota at the phylum level. **(H)** Relative abundance of gut microbiota at the genus level.

(32). Oxidative stress is mainly manifested as a decrease in antioxidant capacity, such as a decrease in the concentration of antioxidant enzymes such as T-SOD and GSH-PX, an increase in the concentration of MDA, and a further increase in the degree of lipid peroxidation (33). Liu *et al.* reported that *S. Enteritidis* infection significantly increased the level of MDA in the serum of laying hens, further causing oxidative stress (10). Se is an essential trace element and involved in the composition of several metabolic enzymes, such as glutathione peroxidase (GSH-Px) and type I iodothyronine deiodinase (34, 35), and plays a critical role in the application of GSH in resisting the oxidation of host cells (34). A previous study reported that both organic and inorganic Se supplementation could alleviate the heat stress-induced oxidative stress of layers, including increasing the serum concentration of GSH-Px and decreasing the MDA content (15). Se supplementation could increase the effectiveness of immune function through increasing the T cell response, mainly improving IL-2 receptor expression, and prevented immune cells from damage induced by oxidative stress (32). In our study, the *S. Enteritidis* challenge obviously increased the level of MDA, IL-2, IL-6, IL-β, and INF-γ and decreased the level of GSH-Px, IgG, and IgM, further disrupting the intestinal barrier and the balance of the intestinal flora, while Se supplementation alleviated these changes. Therefore, Se supplementation has the potential to be used in alleviating *Salmonella* infection in the production practice of laying hens.

It was worth noting that *Salmonella* infection did not cause changes in the apparent quality and freshness of eggs (4). In the present study, we have found that 10^9 CFU *S. Enteritidis* challenged for 3 days had no significant effect on the egg quality and laying performance of layers. Fan *et al.* reported that the dietary supplementation of 10^8 CFU *S. Enteritidis* had no significant effect on the egg quality and production performance of layers, which was consistent with our study. However, it deposited in the tissues and organs of layers, infected the forming eggs, and increased the serum levels of ALT and

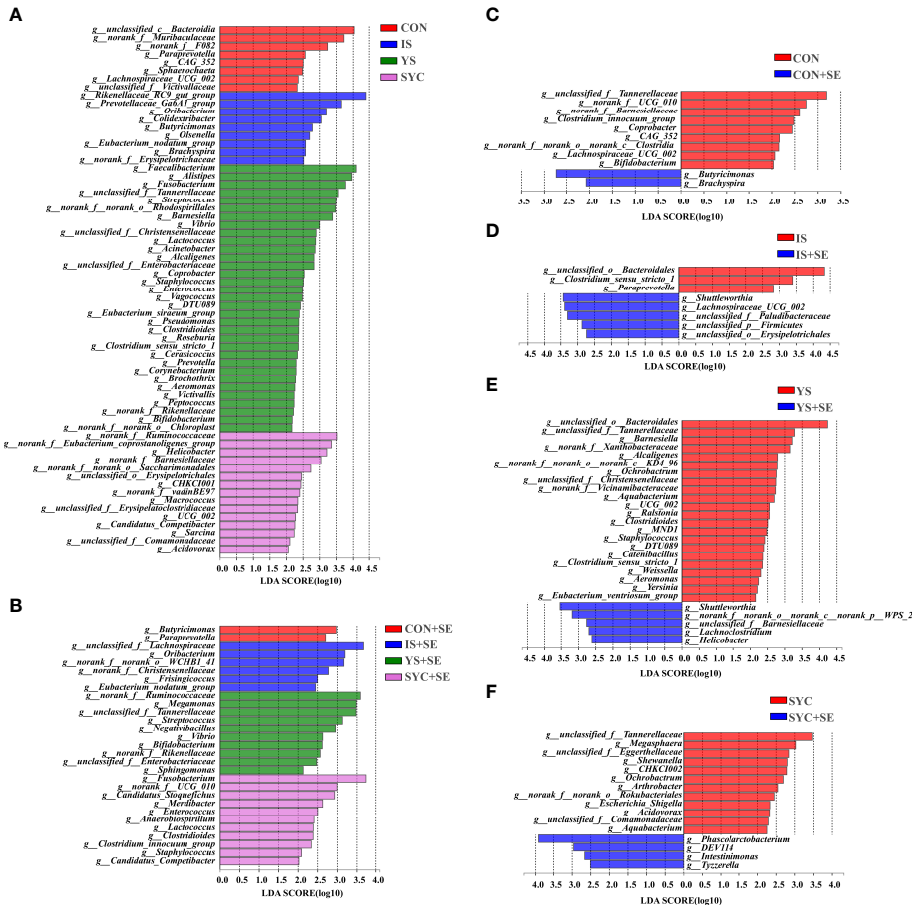

FIGURE 10
Differentially abundant genera in the gut microbiota of layers among different treatments. CON, basal diet; IS, sodium selenite; YS, yeast selenium; SYC, selenium-enriched yeast culture; CON+SE, IS+SE, YS+SE, and SYC+SE mean CON, IS, YS, and SYC challenged with *S. Enteritidis*, respectively. **(A)** LEfSe analysis of the gut microbiota in the CON, IS, YS, and SYC groups. **(B)** LEfSe analysis of the gut microbiota in the CON +SE, IS+SE, YS+SE, and SYC+SE groups. **(C)** LEfSe analysis of the gut microbiota in the CON and CON+SE groups. **(D)** LEfSe analysis of the gut microbiota in the IS and IS+SE groups. **(E)** LEfSe analysis of the gut microbiota in the YS and YS+SE groups. **(F)** LEfSe analysis of the gut microbiota in the SYC and SYC+SE groups.

AST (36). Although *Salmonella* does not affect the performance of birds, the infected *Salmonella* can continue to colonize the cecum and spread to other flocks as they grow (29). Thus, more attention should be paid to the detection of microorganisms in birds to prevent foodborne infections.

CD4 T cells play a critical role in immune protection by recruiting neutrophils, eosinophils, and basophils to the site of infection and responding to a full range of immune responses by producing cytokines and chemokines when the body was infected (37). Previous studies have reported that *Salmonella* infection activated the immune system of the host to conduct a series of immune responses (10, 38). Different cytokines that play important roles in regulating the body's immune responses resist *Salmonella* infection. The invasion of *Salmonella* onto intestinal epithelial cells caused the secretion of pro-inflammatory cytokines such as IL-6, IL-8, and IFN-γ, which induced systemic inflammation by recruiting immune cells (39, 40). In the present study, systemic inflammation was observed after *S. Enteritidis* infection, including significantly decreased IgM and an increased number of CD4 T cells and the level of IL-1β, IL-2, and IL-6, while IS, YS, and SYC supplementation reversed those changes in IgM, CD4 T cells, and IL-β. SYC also markedly increased the level of IgG compared to CON, IS, and YS. In addition, the level of IL-6 in SYC+SE was significantly higher than that in IS+SE, which is in line with a previous study suggesting that Se supplementation could increase the levels of IgM and IgG of birds, further increasing host immunity (41).

A specific antibody against *Salmonella* plays an important role in host resistance to *Salmonella* infection and directs the clearance of *Salmonella* infection (42). In the present study, we

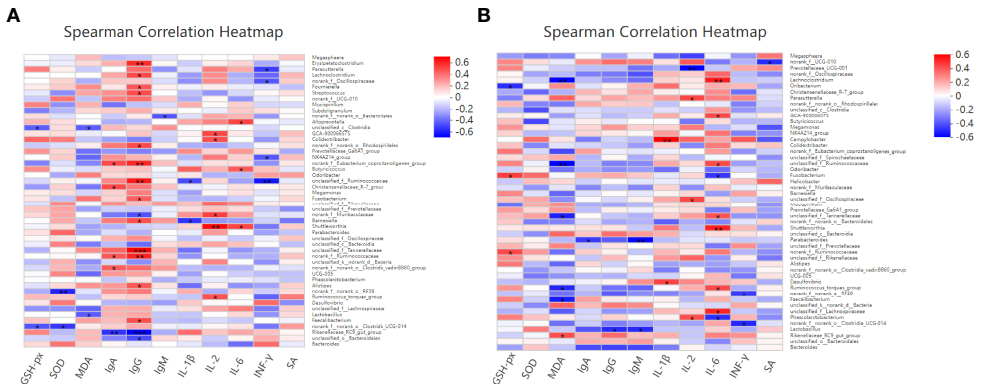

FIGURE 11
Effects of dietary supplementation with different Se sources on the difference of the gut microbiota and its correlation with the antioxidant and immunity of laying hens at 14 days after the challenge with physiological saline solution **(A)** or *S. Enteritidis* **(B)**. Asterisks indicate significant correlations: *$p \leq 0.05$, **$p \leq 0.01$, ***$p \leq 0.001$. Blue represents a significantly positive correlation ($p \leq 0.05$), red represents a significantly negative correlation ($p \leq 0.05$), and white represents no significant correlation ($p > 0.05$). SA, *Salmonella*-specific antibody.

found that *S. Enteritidis* infection significantly increased the specific antibody against *Salmonella* in peripheral serum during the pre-middle period of infection. In line with this outcome, a previous study has reported that *Salmonella* infection can induce high levels of anti-*Salmonella*-specific antibodies in chickens (43). In addition, the present study found that dietary supplementation of organic selenium and inorganic selenium decreased the anti-*Salmonella*-specific antibodies to varying degrees in the middle and late stages of infection. The amount of a specific antibody produced is proportional to the antigen content in the body. Lower levels of a specific antibody in the peripheral serum in the middle and late stages of infection were found in *S. Enteritidis*-infected layers fed with different Se sources, indicating that Se either directly inhibited the growth of *Salmonella* and killed it or SE stimulated the production of anti-*Salmonella*-specific antibodies, further decreasing the load of *Salmonella* in layers. The result suggested that both organic and inorganic Se supplementations could protect against *Salmonella* infection by regulating specific humoral immunity.

As we all know, the small intestine is the main site of nutrient absorption and the body's first barrier against external substances. It plays a critical role in maintaining gut homeostasis and keeping it healthy (44). Villus height and crypt depth—or the ratio of both (V/C)—were important indicators of intestinal function and maturity. An increase in villus height and V/C ratio indicated a healthy gut and better nutrient absorptive capacity. Conversely, with villus height becoming lower, the intestinal absorptive capacity becomes weaker (45–47). In the present study, *S. Enteritidis* infection significantly destroyed the villi and crypt of the small intestine, which were evidenced by crypt atrophy and villus adhesions. Interestingly, the addition of Se markedly increased the villus height and the ratio of villus and crypt and decreased the crypt depth of the small intestine of laying hens, which further alleviated the damages caused by *S. Enteritidis* infection. Thus, these results suggested that the integrity barrier of the duodenum, jejunum, and ileum of layers was destroyed by *S. Enteritidis* infection, whereas the supplementation of Se alleviated these changes through improving the immune response.

The intestinal flora constituted the intestinal microbial barrier, and a stable intestinal microbial barrier was essential in the digestion and absorption of nutrients and the maintenance of homeostasis in the intestinal environment (48). In the present study, both different organic Se supplementations (YS and SYC) and *S. Enteritidis* infection altered the gut microbial diversity, which was revealed by variations in α diversity, β diversity, and specific bacteria that occurred in different groups. In line with this outcome, a previous study has reported that, in 1-day-old chicks challenged with *Salmonella*, the diversity of the cecal microbiota was markedly decreased (49). Dietary Se supplementation also notably increased the α diversity and β diversity of microbiota in mice (50, 51). The changes of *Salmonella* to the gut microbial composition may be associated with the interaction between pathogen and commensal microbiota or the host mucosal immune response to pathogens or a combination of both of them (52). In addition, according to the LEfSe analyses, the microbial composition of layers was altered by both Se supplementation and *S. Enteritidis* infection. *S. Enteritidis* infection significantly decreased the relative abundance of microbial composition, which indicated that the gut homeostasis was disrupted and certain diseases may occur (53, 54), while Se supplementation reversed these negative effects. *S. Enteritidis* infection also significantly decreased the

abundance of *Lachnospiraceae* and *Clostridium*, which could utilize dietary carbohydrate and fiber metabolism to produce butyric acid, regulating both energy metabolism and the immune response of intestinal epithelial cells (55, 56). Butyric acid stimulated the intestinal cells to produce antimicrobial peptide substances that helped to resist the invasion and colonization of *Salmonella*, inhibiting the occurrence of intestinal inflammation and protecting intestinal health (57, 58). In addition, in the present study, YS and SYC supplementation markedly increased the abundance of *Barnesiella*. A previous study has reported that *Barnesiella* was able to clear the intestinal colonization of highly antibiotic-resistant bacteria (59). YS also increased the abundance of *Bacteroidales*, which was considered as an intestinal beneficial bacterial, which can increase immune function and improve intestinal health (60). Collectively, *S. Enteritidis* infection decreased the composition of intestinal microbiota, while Se supplementation could reverse these negative effects by increasing the relative abundance of microbes associated with anti-inflammation, further increasing intestinal homeostasis.

Conclusion

In conclusion, the present study suggested that selenium (Se) supplementation significantly increased egg production to resist the adverse effects caused by the *S. Enteritidis* challenge. These results also revealed that Se administration could alleviate the intestinal histopathologic damage caused by *S. Enteritidis* infection. In addition, *S. Enteritidis* infection significantly decreased the level of GSH-Px and IgM and increased the level of MDA, IL-1β, and *Salmonella*-specific antibody. However, Se addition reversed these outcomes. Moreover, yeast Se and selenium-enriched yeast culture supplementation maintained intestinal homeostasis through increasing the relative abundance of microbiota related to anti-inflammation, further alleviating the damage caused by *S. Enteritidis* infection.

Data availability statement

The data presented in the study are deposited in the NCBI repository, and the accession numbers can be found below: https://www.ncbi.nlm.nih.gov/sra/PRJNA849581.

Ethics statement

The animal study was reviewed and approved by the China Agricultural University Animal Care and Use Committee.

Author contributions

QM, JZ, CJ, SH, LZ, and ZW designed the study. WW conducted the experiments and collected the data. RK and WW performed the analysis of the experimental data. RK drafted the manuscript and finished the submission. RK, YL, JX and YH detected the samples. All authors contributed to the article and approved the submitted version.

Funding

This study was supported by the National Key Research and Development Programs of China (2021YFD1300204 and 2021YFD1300405), Special Fund for China Agricultural Research System program (CARS-40-K08), and the National Science Foundation of China (grant no. 31772621).

Acknowledgments

Special thanks to Professor Dan Liu of China Agricultural University for providing the immunohistochemical kits and to Mr. Yong Zhang of Shijiazhuang Tingrong Technology Co., Ltd. For helping with the emergency allocation of *Salmonella*-specific antibody kits. Without their help, it is impossible for us to complete the supplementary tests in time under the inconvenient condition caused by COVID-19.

Conflict of interest

The authors declare that the research was conducted in the absence of any commercial or financial relationships that could be construed as a potential conflict of interest.

Publisher's note

Supplementary material

The Supplementary Material for this article can be found online at: https://www.frontiersin.org/articles/10.3389/fimmu.2022.928865/full#supplementary-material

References

1. Dunkley KD, Callaway TR, Chalova VI, Mcreynolds ME, Hume CS, Dunkley LF, et al. Foodborne salmonella ecology in the avian gastrointestinal tract. *Anaerobe* (2009) 15(1-2):26–35. doi: 10.1016/j.anaerobe.2008.05.007

2. Howard ZR, O'Bryan CA, Crandall PG, Ricke SC. Salmonella enteritidis in shell eggs: current issues and prospects for control. *Food Res Int* (2012) 45(2):755–64. doi: 10.1016/j.foodres.2011.04.030

3. Pearce ME, Alikhan NF, Dallman TJ, Zhou Z, Grant K, Maiden MCJ. Comparative analysis of core genome MLST and SNP typing within a European salmonella serovar enteritidis outbreak. *Int J Food Microbio* (2018) 274:1–11. doi: 10.1016/j.ijfoodmicro.2018.02.023

4. Gantois I, Ducatelle R, Pasmans F, Haesebrouck F, Gast R, Humphrey TJ. Mechanisms of egg contamination by salmonella enteritidis. *FEMS Microbiol Rev* (2009) 33(4):718–38. doi: 10.1111/j.1574-6976.2008.00161.x

5. European Food Safety Authority and European Centre for Disease Prevention and Control. The European union summary report on trends and sources of zoonoses, zoonotic agents and food-borne outbreaks in 2011. *EFSA J* (2013) 11(4):3129. doi: 10.2903/j.efsa.2013.3129

6. Baron F, Nau F, Guérin-Dubiard C, Bonnassie S, Gautier M, Andrews SC, et al. Egg white versus salmonella enteritidis! a harsh medium meets a resilient pathogen. *Food Microbiol* (2016) 53:82–93. doi: 10.1016/j.fm.2015.09.009

7. Shen S, Fang FC. Integrated stress responses in salmonella. *Int J Food Microbiol* (2012) 152(3):75–81. doi: 10.1016/j.ijfoodmicro.2011.04.017

8. Zhang W, Zheng JX, Xu GY. Toward better control of salmonella contamination by taking advantage of the egg's self-defense system: A review. *J Food Sci* (2011) 76(3):R76–81. doi: 10.1111/j.1750-3841.2011.02053.x

9. Pijnacker R, Dallman TJ, Asl T, Hawkins G, Larkin L, Kotila SM, et al. An international outbreak of salmonella enterica serotype enteritidis linked to eggs from Poland: a microbiological and epidemiological study. *Lancet Infect Dis* (2019) 19(7):778–86. doi: 10.1016/S1473-3099(19)30047-7

10. Liu YJ, Zhao LH, Mosenthin R, Zhang JY, Ji C, Ma QG. Protective effect of vitamin e on laying performance, antioxidant capacity, and immunity in laying hens challenged with salmonella enteritidis. *Poultry Sci* (2019) 98(11):5847–54. doi: 10.3382/ps/pez227

11. Huang S, Rong X, Liu M, Liang Z, Geng Y, Wang X, et al. Intestinal mucosal immunity-mediated modulation of the gut microbiome by oral delivery of enterococcus faecium against salmonella enteritidis pathogenesis in a laying hen model. *Front Immuno* (2022) 13:853954. doi: 10.3389/fimmu.2022.853954

12. Han XJ, Qin P, Li WX, Ma QG, Ji C, Zhang JY, et al. Effect of sodium selenite and selenium yeast on performance, egg quality, antioxidant capacity, and selenium deposition of laying hens. *Poultry Sci* (2017) 96(11):3973–80. doi: 10.3382/ps/pex216

13. Nawaz F, Ashraf MY, Ahmad R, Waraich EA, Shabbir RN. Selenium (Se) regulates seedling growth in wheat under drought stress. *Adv Chem* (2014) 2014:1–7. doi: 10.1155/2014/143567

14. Sun X, Yue S, Qiao Y, Sun Z, Li H. Dietary supplementation with selenium-enriched earthworm powder improves antioxidative ability and immunity of laying hens. *Poultry Sci* (2020) 99(11):5344–9. doi: 10.1016/j.psj.2020.07.030

15. Wang W, Kang R, Liu M, Wang Z, Zhao L, Zhang J, et al. Effects of different selenium sources on the laying performance, egg quality, antioxidant, and immune responses of laying hens under normal and cyclic high temperatures. *Animals* (2022) 12(8):1006. doi: 10.3390/ani12081006

16. Kim YY, Mahan DC. Comparative effects of high dietary levels of organic and inorganic selenium on selenium toxicity of growing-finishing pigs. *J Anim Sci* (2001) 79(4):942–8. doi: 10.2527/2001.794942x

17. Lu J, Qu L, Ma M, Li YF, Wang XG, Yang Z, et al. Efficacy evaluation of selenium-enriched yeast in laying hens: effects on performance, egg quality, organ development, and selenium deposition. *Poultry Sci* (2020) 99(11):6267–77. doi: 10.1016/j.psj.2020.07.041

18. Skrivan M, Simane J, Dlouha G, Doucha J. Effect of dietary sodium selenite, Se-enriched yeast and Se-enriched chlorella on egg Se concentration, physical parameters of eggs and laying hen production. *Czech J Anim Sci* (2006) 51(4):163. doi: 10.1103/PhysRevD.78.034003

19. Chinrasri O, Chantiratikul P, Thosaikham W, Atiwetin P, Chantiratikul A. Effect of selenium-enriched bean sprout and other selenium sources on productivity and selenium concentration in eggs of laying hens. *Asian Austral J Anim* (2009) 22(12):1661–6. doi: 10.5713/ajas.2009.90220

20. Liao X, Lu L, Li S, Liu S, Zhang L, Wang G, et al. Effects of selenium source and level on growth performance, tissue selenium concentrations, antioxidation, and immune functions of heat-stressed broilers. *Biol Trace Elem Res* (2012) 150 (1):158–65. doi: 10.1007/s12011-012-9517-3

21. Williams JE, Whittemore AD. Serological diagnosis of pullorum disease with the microagglutination system. *Appl Microbiol* (1971) 21(3):394–9. doi: 10.1128/am.21.3.394-399.1971

22. Cohen ND, Mcgruder ED, Neibergs HL, Behle RW, Wallis DE, Hargis BM. Detection of salmonella enteritidis in feces from poultry using booster polymerase chain reaction and oligonucleotide primers specific for all members of the genus salmonella. *Poultry Sci* (1994) 73(2):354–7. doi: 10.3382/ps.0730354

23. Liu Y, Mosenthin R, Zhao L, Zhang J, Ma QG. Vitamin K alleviates bone calcium loss caused by salmonella enteritidis through carboxylation of osteocalcin. *J Anim Sci Biotechno* (2021) 12(1):1–10. doi: 10.1186/s40104-021-00604-z

24. Liao XD, Wang G, Lu L, Zhang LY, Lan YX, Li SF, et al. Effect of manganese source on manganese absorption and expression of related transporters in the small intestine of broilers. *Poultry Sci* (2019) 98(10):4994–5004. doi: 10.3382/ps/pez293

25. Li R, Song M, Li Z, Li Y, Watanabe G, Nagaoka K, et al. 4-nitrophenol exposure alters the AhR signaling pathway and related gene expression in the rat liver. *J Appl Toxicol* (2017) 37(2):150–8. doi: 10.1002/jat.3332

26. Stasikowska-Kanicka O, Wągrowska-Danilewicz M, Danilewicz M. Immunohistochemical analysis of Foxp3+, CD4+, CD8+ cell infiltrates and PD-L1 in oral squamous cell carcinoma. *Pathol Oncol Res* (2018) 24(3):497–505. doi: 10.1007/s12253-017-0270-y

27. Cao G, Zeng X, Liu J, Yan F, Yang C. Change of serum metabolome and cecal microflora in broiler chickens supplemented with grape seed extracts. *Front Immuno* (2020) 11:610934. doi: 10.3389/fimmu.2020.610934

28. Kulshreshtha G, Rathgeber B, MacIsaac J, Boulianne M, Brigitte L, Stratton G, et al. Feed supplementation with red seaweeds, chondrus crispus and sarcodiotheca gaudichaudii, reduce salmonella enteritidis in laying hens. *Front Microbiol* (2017) 8:567. doi: 10.3389/fmicb.2017.00567

29. Gast RK, Holt PS. Persistence of salmonella enteritidis from one day of age until maturity in experimentally infected layer chickens. *Poultry Sci* (1998) 77 (12):1759–62. doi: 10.1093/ps/77.12.1759

30. Varmuzova K, Kubasova T, Davidova-Gerzova L, Sisak F, Havlickova H, Sebkova A, et al. Composition of gut microbiota influences resistance of newly hatched chickens to salmonella enteritidis infection. *Front Microbiol* (2016) 7:957. doi: 10.3389/fmicb.2016.00957

31. Kamada N, Seo SU, Chen GY, Núez G. Role of the gut microbiota in immunity and inflammatory disease. *Nat Rev Immunol* (2013) 13(5):321–35. doi: 10.1038/nri3430

32. McKenzie RC, Rafferty TS, Beckett GJ. Selenium: an essential element for immune function. *Immunol Today* (1998) 19(8):342–5. doi: 10.1016/S0167-5699 (98)01294-8

33. Hou YJ, Zhao YY, Bo X, Cui XS, Kim NH, Xu YX, et al. Mycotoxin-containing diet causes oxidative stress in the mouse. *PloS One* (2013) 8(3):e60374. doi: 10.1371/journal.pone.0060374

34. Rotruck JT, Pope AL, Ganther HE, Swanson AB, Hoekstra D. Selenium: biochemical role as a component of glutathione peroxidase. *Science* (1973) 179 (4073):588–90. doi: 10.1126/science.179.4073.588

35. Berry MJ, Banu L, Larsen PR. Type I iodothyronine deiodinase is a selenocysteine-containing enzyme. *Nature* (1991) 349(6308):438–40. doi: 10.1038/349438a0

36. Fan S, Zheng J, Duan Z, Xu G. The influences of SE infection on layers' production performance, egg quality and blood biochemical indicators. *J Anim Sci Biotechno* (2014) 5(1):1–6. doi: 10.1186/2049-1891-5-4

37. Zhu J, Paul WE. CD4 T cells: fates, functions, and faults. *Blood* (2008) 112 (5):1557–69. doi: 10.1182/blood-2008-05-078154

38. Patel S, McCormick BA. Mucosal inflammatory response to salmonella typhimurium infection. *Front Immuno* (2014) 5:311. doi: 10.3389/fimmu.2014.00311

39. McCormick BA, Colgan SP, Delp-Archer C, Miller SI, Madara JL. Salmonella typhimurium attachment to human intestinal epithelial monolayers: transcellular signalling to subepithelial neutrophils. *J Cell Biol* (1993) 123(4):895–907. doi: 10.1083/jcb.123.4.895

40. Gal-Mor O, Suez J, Elhadad D, Porwollik S, Rahav G. Molecular and cellular characterization of a salmonella enterica serovar paratyphi a outbreak strain and the human immune response to infection. *Clin Vaccine Immunol* (2012) 19 (2):146–56. doi: 10.1128/CVI.05468-11

41. Cai SJ, Wu CX, Gong LM, Song T, Wu H, Zhang LY. Effects of nano-selenium on performance, meat quality, immune function, oxidation resistance, and tissue selenium content in broilers. *Poultry Sci* (2012) 91(10):2532–9. doi: 10.3382/ps.2012-02160

42. Beal RK, Smith AL. Antibody response to salmonella: its induction and role in protection against avian enteric salmonellosis. *Expert Rev Anti-infe* (2007) 5 (5):873–81. doi: 10.1586/14787210.5.5.873

43. Berthelot-Hérault F, Mompart F, Zygmunt MS, Dubray G, Duchet-Suchaux M. Antibody responses in the serum and gut of chicken lines differing in cecal carriage of salmonella enteritidis. *Vet Immunol Immunop* (2003) 96(1-2):43–52. doi: 10.1016/S0165-2427(03)00155-7

44. Barker N. Adult intestinal stem cells: critical drivers of epithelial homeostasis and regeneration. *Nat Rev Mol Cell Bio* (2014) 15(1):19–33. doi: 10.1038/nrm3721

45. Hampson DJ. Alterations in piglet small intestinal structure at weaning. *Res Vet Sci* (1986) 40(1):32–40. doi: 10.1016/S0034-5288(18)30482-X

46. Qin SM, Zhang KY, Ding XM, Bai SP, Zeng QF. Effect of dietary graded resistant potato starch levels on growth performance, plasma cytokines concentration, and intestinal health in meat ducks. *Poultry Sci* (2019) 98(9):3523–32. doi: 10.3382/ps/pez186

47. Turner JR. Intestinal mucosal barrier function in health and disease. *Nat Rev Immunol* (2009) 9(11):799–809. doi: 10.1038/nri2653

48. Bourlioux P, Koletzko B, Guarner F, Braesco V. The intestine and its microflora are partners for the protection of the host: report on the danone symposium "The intelligent intestine," held in Paris, June 14, 2002. *Am J Clin Nutr* (2003) 78(4):675–83. doi: 10.1093/ajcn/78.4.675

49. Mon K, Perot S, Halstead MM, Chanthavixay G, Chang HC, Garas L, et al. Salmonella enterica serovars enteritidis infection alters the indigenous microbiota diversity in young layer chicks. *Front Vet Sci* (2015) 2:61. doi: 10.3389/fvets.2015.00061

50. Kasaikina MV, Kravtsova MA, Lee BC, Seravalli J, Peterson DA, Walter J, et al. Dietary selenium affects host selenoproteome expression by influencing the gut microbiota. *FASEB J* (2011) 25(7):2492–9. doi: 10.1096/fj.11-181990

51. Zhu H, Lu C, Gao F, Qian Z, Yin Y, Kan S, et al. Selenium-enriched bifidobacterium longum DD98 attenuates irinotecan-induced intestinal and hepatic toxicity *in vitro* and *in vivo*. *BioMed Pharmacother* (2021) 143:112192. doi: 10.1016/j.biopha.2021.112192

52. Barman M, Unold D, Shifley K, Amir E, Hung K, Bos N, et al. Enteric salmonellosis disrupts the microbial ecology of the murine gastrointestinal tract. *Infect Immun* (2008) 76(3):907–15. doi: 10.1128/IAI.01432-07

53. Manichanh C, Rigottier-Gois L, Bonnaud E, Gloux K, Pelletier E, Frangeul L, et al. Reduced diversity of faecal microbiota in crohn's disease revealed by a metagenomic approach. *Gut* (2006) 55(2):205–11. doi: 10.1136/gut.2005.073817

54. Guo F, Geng Y, Abbas W, Zhen W, Wang S, Huang Y, et al. Vitamin D3 nutritional status affects gut health of salmonella-challenged laying hens. *Front Nutr* (2022) 9. doi: 10.3389/fnut.2022.888580

55. Donohoe DR, Garge N, Zhang X, Sun W, O'Connell TM, Bunger MK, et al. The microbiome and butyrate regulate energy metabolism and autophagy in the mammalian colon. *Cell Metab* (2011) 13(5):517–26. doi: 10.1016/j.cmet.2011.02.018

56. Xu B, Yan Y, Yin B, Zhang L, Qin W, Niu Y, et al. Dietary glycyl-glutamine supplementation ameliorates intestinal integrity, inflammatory response, and oxidative status in association with the gut microbiota in LPS-challenged piglets. *Food Funct* (2021) 12(8):3539–51. doi: 10.1039/D0FO03080E

57. Van Immerseel F, Boyen F, Gantois I, Timbermont L, Bohez L, Pasmans F, et al. Supplementation of coated butyric acid in the feed reduces colonization and shedding of salmonella in poultry. *Poultry Sci* (2005) 84(12):1851–6. doi: 10.1093/ps/84.12.1851

58. Fernández-Rubio C, Ordonez C, Abad-González J, Garcia-Gallego A, Honrubia MP, Mallo JJ, et al. Butyric acid-based feed additives help protect broiler chickens from salmonella enteritidis infection. *Poultry Sci* (2009) 88 (5):943–8. doi: 10.3382/ps.2008-00484

59. Ubeda C, Bucci V, Caballero S, Djukovic A, Toussaint NC, Equinda M, et al. Intestinal microbiota containing barnesiella species cures vancomycin-resistant enterococcus faecium colonization. *Infect Immun* (2013) 81(3):965–73. doi: 10.1128/IAI.01197-12

60. Delday M, Mulder I, Logan ET, Grant G. Bacteroides thetaiotaomicron ameliorates colon inflammation in preclinical models of crohn's disease. *Inflammation Bowel Dis* (2019) 25(1):85–96. doi: 10.1093/ibd/izy281

frontiers | Frontiers in Immunology

TYPE Original Research
PUBLISHED 18 August 2022
DOI 10.3389/fimmu.2022.952852

OPEN ACCESS

EDITED BY
Mengyao Guo,
Northeast Agricultural University, China

REVIEWED BY
Fu Chen,
Qingdao Agricultural University, China
Xinwei Li,
Jilin University, China
Guo Xiaoquan,
Jiangxi Agricultural University, China

*CORRESPONDENCE
Zhanyong Wei
zhanyong_wei@126.com

†These authors have contributed equally to this work

SPECIALTY SECTION
This article was submitted to Nutritional Immunology, a section of the journal Frontiers in Immunology

RECEIVED 26 May 2022
ACCEPTED 26 July 2022
PUBLISHED 18 August 2022

CITATION
Ren Z, Ding T, He H, Wei Z, Shi R and Deng J (2022) Mechanism of Selenomethionine inhibiting of PDCoV replication in LLC-PK1 cells based on STAT3/miR-125b-5p-1/HK2 signaling. *Front. Immunol.* 13:952852. doi: 10.3389/fimmu.2022.952852

Mechanism of selenomethionine inhibiting of PDCoV replication in LLC-PK1 cells based on STAT3/miR-125b-5p-1/HK2 signaling

Zhihua Ren[1,2†], Ting Ding[2†], Hongyi He[2†], Zhanyong Wei[1*], Riyi Shi[3] and Junliang Deng[2]

[1]College of Veterinary Medicine, Henan Agricultural University, Zhengzhou, China, [2]Key Laboratory of Animal Disease and Human Health of Sichuan Province, College of Veterinary Medicine, Sichuan Agricultural University, Chengdu, China, [3]Department of Basic Medical Sciences, College of Veterinary Medicine, Weldon School of Biomedical Engineering, Purdue University, West Lafayette, IN, United States

There are no licensed therapeutics or vaccines available against porcine delta coronavirus (PDCoV) to eliminate its potential for congenital disease. In the absence of effective treatments, it has led to significant economic losses in the swine industry worldwide. Similar to the current coronavirus disease 2019 (COVID-19) pandemic, PDCoV is trans-species transmissible and there is still a large desert for scientific exploration. We have reported that selenomethionine (SeMet) has potent antiviral activity against PDCoV. Here, we systematically investigated the endogenous immune mechanism of SeMet and found that STAT3/miR-125b-5p-1/HK2 signalling is essential for the exertion of SeMet anti-PDCoV replication function. Meanwhile, HK2, a key rate-limiting enzyme of the glycolytic pathway, was able to control PDCoV replication in LLC-PK1 cells, suggesting a strategy for viruses to evade innate immunity using glucose metabolism pathways. Overall, based on the ability of selenomethionine to control PDCoV infection and transmission, we provide a molecular basis for the development of new therapeutic approaches.

KEYWORDS

PDCoV, SeMet, STAT3, miR-125b-5p-1, HK2

Introduction

PDCoV is a novel porcine enteropathogenic coronavirus that infects intestinal epithelial cells and causes vomiting, diarrhea, dehydration and death in sows and piglets (1–3). It was first detected in Hong Kong in 2012 and its infection has subsequently been reported worldwide, posing a considerable threat to the global pig

industry (4–12). In addition, recent reports have shown that chickens and calves are also susceptible to PDCoV (13, 14), and even humans are susceptible (15), indicating that the novel virus has the possibility of cross-species transmission. However, there is no specific treatment for PDCoV infection, and prevention and treatment of PDCoV infection is an urgent problem.

Selenium is an essential trace element for plants and mammals (16). Generally speaking, selenium is classified into two types: inorganic and organic selenium. Compared to inorganic selenium, organic selenium is the most valuable type of selenium intake because it is more biologically active and less toxic than inorganic selenium, as well as being more readily absorbed and utilized by living organisms and abundant in variety (17). Selenomethionine (SeMet), the main chemical form of organic selenium in cereal diets, acts as a selenium-containing amino acid by itself or as a selenium-derived donor involved in selenoprotein synthesis for its antioxidant, immunomodulatory and antiviral effects (18–23). Previous studies found that knockdown of glutathione peroxidase 1 (GPx1) in selenoprotein promoted PCV2 replication and reversed the ability of SeMet to block hydrogen peroxide (H_2O_2)-induced PCV2 replication (20). Furthermore, in addition to these functions, selenium also affects the metabolic levels of the body. In mouse models, mice with either selenoprotein deficiency or high selenium levels exhibit dysregulated glucose homeostasis as well as insulin resistance (24, 25).

STAT3 was originally identified as an acute phase response factor and is a member of the signal transduction and transcriptional activator family (26, 27). At the transcriptional level, it is well known for regulating the transcription of target genes for various biologically important functions, such as energy metabolism, cell differentiation and immune response (28). Abnormal STAT3 function is commonly associated with disease development including viral development. For example, the X protein of HBV induces STAT3 phosphorylation (Y705) *via* JAK1 and downregulates the expression of miRNA let-7a, a negative regulator of STAT3, thereby promoting p-STAT3 dimer-specific binding to the core structural domain of HBV enhancer 1 and inducing viral gene expression (29–31).

miRNAs consist of a class evolutionarily conserved, endogenous non-coding small RNAs of approximately 9-24 nt in length (32). miRNAs function as post-transcriptional regulators of gene expression by acting on complementary target sequences in the mRNA-3'UTR to cleave mRNAs or repress protein translation (33). miRNAs redefine the ability of host-virus interactions is an emerging concept. For example, miR-144 can target and inhibit TRAF6 levels, impairing IRF7-mediated antiviral signalling and leading to dysregulation of antiviral gene expression in the host, thereby enhancing influenza A virus (IAV) replication (34).

Host cells possess the energy and molecular precursors required for viral infection and are the 'viral factories' that supply the resources for processing. It has been shown that HK2, a key rate-limiting enzyme of glycolysis, is involved in the activation of retinoic acid-inducible gene-I like receptors (RLRs) mediated innate immune signalling (35), and that hepatitis B virus can use HK2 to inhibit RLRs signalling and thus achieve immune escape (36). It is from the perspective of HK2 regulation of innate immune signaling that our experiment explores the molecular mechanism of SeMet inhibiting PDCoV replication. Our results show that HK2 promotes PDCoV replication in LLC-PK1 cells, while SeMet inhibits PDCoV replication by reducing HK2 expression. Further analysis at the transcriptional level revealed that STAT3/miR-125b-5p-1 is an intermediate link in the regulation of HK2 levels by SeMet and a key mechanism for SeMet inhibiting PDCoV replication.

Materials and methods

Reagents and antibodies

Antibodies for NF-κB p65 (#6956), p-NF-κB p65 (#3033) and β-Actin (#4970) (Cell Signaling Technology), p-TBK1 (#AF8190) and p-STAT3 (#AF3293) (Affinity Biosciences), STAT3 (#GB12176, Servicebio), HK2 (#22029-1-AP) and IRF3 (#11312-1-AP) (Proteintech Group), p-IRF3 (#MA5-14947, Invitrogen), TBK1 (#ab227182), Goat Anti-Rabbit IgG H&L (HRP) (#ab6721) and Rabbit Anti-Mouse IgG H&L(HRP) (#ab6728) (Abcam) were used for blotting. The anti-PDCoV-N antibodies were prepared in our laboratory. The Alexa Fluor 488-conjugated goat anti-mouse (#4408S) was purchased from Cell Signaling Technology. The STAT3 inhibitor static (#HY-13818) was purchased from Med Chem Express. The selenomethionine (SeMet) (#S3132) was purchased from Sigma. The miR-9-5p mimic, miR-125b-5p-1 mimic, and miR-125b-5p-1 inhibitor were purchased from Gene Pharma.

Cell culture and virus

The PDCoV strain-HNZK-04 (GenBank accession number MH708124) was isolated and identified by the laboratory and propagated in porcine kidney proximal tubular epithelial cell line (LLC-PK1, ATCC CL-101). LLC-PK1 cells were cultured at 37°C in 5% CO_2 minimum essential medium (MEM, Solarbio) containing 8% fetal bovine serum (FBS, Gibco), 1% HEPES (Solarbio) and 1% MEM-nonessential amino acids (NEAA, Solarbio). Passage 34 (P34) of PDCoV HNZK-04 was cultured in MEM supplemented with 1% HEPES and 3 μg/mL trypsin (Sigma).

Plasmids construction and transformation

The sequence of pcDNA3.1(+)-EGFP/RFP containing cloned HK2 gene (NM_001122987.1) or STAT3 gene

(NM_001044580.1) were designed and ordered from the Wuhan Gene Creat, China. The pcDNA3.1-HK2/STAT3 include Neomycin resistance gene as a known selectable marker of stable mammalian transfectants and β-lactamase (the Ampicillin resistance gene) as the selectable marker in the properly transformed prokaryotic hosts, and eucaryote expression vector pcDNA3.1 (+) and target products were digested with NheI and EcoRI. TOP10 competent cells were thawed on ice, then plasmid DNA was added, mixed gently, and the mixture incubated on ice for 30 min. Cells were then transferred to a 42°C water bath for 90 sec, then placed on ice for a further 2 min. Sterile SOC liquid medium (200 μL, Solarbio) without antibiotic was added, and the mixture was incubated for 45 min at 37°C in a shaker at 220 rpm/min to recover the cells. Cells were plated on solid LB containing agar and 50 mg/mL ampicillin (Sangon Biotech) and incubated at 37°C for 12–16 h. Single colonies were then picked into 100 mL LB and incubated at 37°C for 16 h in a shaker at 220 rpm/min.

siRNA-mediated silencing

LLC-PK1 cells [2×10 (5)] were seeded in 24-well plate for each well and allowed to grow for 12 hours. Then, cells were transfected with transfection reagent Lipofectamine 3000 (Invitrogen, #L3000015) and siRNA (HK2 and STAT3) or scrambled siRNA (siRNA-negative control, NC), Lipofectamine 3000: 3μL, 20μmol/L siRNA: 1.5μL for each well for 24 hours. The siRNA sequences are shown in Supplementary Table S1.

Quantitative real-time PCR

Total RNA of cells was extracted using Trizol reagent (Takara), according to the manufacturer's protocol. After reverse transcription by using TransScript All-in-One First-Strand cDNA Synthesis SuperMix for qPCR kit (Transgen) or Hairpin-it microRNAs RT reagent Kit (GenePharma), cDNAs were quantified in CFX Connect Real-Time PCR Detection System (BIO-RAD). Relative gene expression levels were calculated using the formula $2^{-(\Delta\Delta Ct)}$ (with β-actin or U6 used as the reference gene) and normalized as indicated. The information of primers are all listed in Supplementary Table S1.

Luciferase reporter assays

Luciferase constructs were generated by cloning porcine 3'UTR of HK2 (NM_001122987, 2941-3118 nt), HK2 promotor (NC_010445, -967 to -768 bp relative to the transcription start site), or miR-125b-1 promotor (NC_010451, -1059 to -1258 bp relative to the transcription start site) of firefly luciferase. Wild type and mutant miR-125b-5p-1 target sequences in the 3'UTR of HK2 were generated by containing predicted interaction sites, and cloning directly into the pmirGLO vectors. Similarly, wild type and mutant STAT3 target sequences in the HK2 or miR-125b-1 promotors were cloned into the pGL3 vectors. The cells were collected 48 hours after co-transfected with pmirGLO-HK2 and miR-125b mimic, pcDNA3.1-STAT3 and pGL3-HK2, as well as pcDNA3.1-STAT3 and pGL3-miR-125b-1 using Lipofectamine 2000 (Invitrogen). The luciferase activity was measured using the Dual-Luciferase Reporter Assay System (Promega). The results are expressed as relative luciferase activity (firefly luciferase/renilla luciferase).

Western immunoblotting

For the western blotting of the total lysates, we lysed cells in RIPA buffer (Servicebio) supplemented with phosphatase and protease inhibitors (Servicebio), which in turn subjected the lysates to protein quantification (Beyotime). The lysates were immunoblotted, electrophoresed on SDS-PAGE, transferred to PVDF membranes (Millipore), and probed with various antibodies. Chemiluminescent signals were detected by ChemiScope 6300 Touch (CLINX). Protein quantification was performed by Image J (NIH).

Immunofluorescence assay

Cells were fixed with 4% paraformaldehyde at room temperature for 20 minutes and washed with PBS three times. Cells were permeated with 0.05% Triton-x100 for 20 min and then washed with PBS three times. Cells were blocked (5% BSA sealing fluid) for 30 min and incubated with anti- PDCoV- N antibody for 12 hours at 4°C. Cells were then washed with PBS three times and incubated with FITC- conjugated secondary antibody for 30 min at 37°C. Thereafter, cells were incubated with 4′,6- diamidino- 2- phenylindole (DAPI, Solarbio) for 10 minutes after washing with PBS three times. The cells were examined using fluorescence microscope (Nikon).

Statistical analysis

All of the statistical data are presented as the mean ± s.e.m. Differences between mean values of normally distributed data were assessed by the one-way ANOVA test and Student's *t*-test. Statistical difference was accepted at $P < 0.05$. The software used are Excel (Microsoft Corporation), SPSS 25.0 software (SPSS Inc.), and Prism 8.0 (GraphPad Software Inc.).

Results

SeMet inhibits the infectivity of PDCoV

Previous assays obtained that no differences in cell morphology compared with control cells were observed cells at the maximum safe concentration with 256 μM of SeMet (data not shown). To evaluate whether SeMet inhibits PDCoV replication, LLC-PK1 cells were infected with PDCoV at 100 $TCID_{50}$ for 1.5 h and treated with 2-256 μM of SeMet for 48 h. The relative mRNA expression was detected by real-time quantitative PCR (qPCR). Treatment with 6.25-150 μM SeMet inhibited viral mRNA levels (Figure 1A), while treatment with 200-256 μM SeMet infected with PDCoV for 48 h resulted in almost no viable cells. IFA assays showed that the fluorescence signal was reduced in a dose-dependent manner following treatment of PDCOV-infected LLC-PK1 cells with 6.25-150 μM SeMet (Figure 1B). This indicated that SeMet significantly inhibited PDCoV replication in a dose-dependent manner, and we selected 150μM SeMet for further studies in subsequent assays.

To further elucidate the effect of SeMet on PDCoV, we performed analyses of SeMet treatment at different times. 6, 24 and 48 h after PDCoV infection were treated with SeMet. we observed a decrease in viral mRNA of PDCoV with increasing time of infection (Figure 1C), as well as a weakening of the IFA detection fluorescence signal (Figure 1D). This suggests that SeMet significantly inhibited PDCoV replication in a time-dependent manner.

HK2 plays an important role in PDCoV replication

We next explored how SeMet affects PDCoV replication. Our study found that SeMet treatment of cells infected with PDCoV resulted in a reduction in HK2 and lactate expression (Figures 2A, B). Previous studies have shown that lactate is critical for blocking RLRs signalling associated with viral infection, and that HK2 can influence the activation of RLRs signalling by regulating lactate production (35). We hypothesized that this role is precisely exploited by SeMet. Therefore, we knocked down the expression of HK2 (Figure 2C and Supplementary Figures S1A, B). We found that inhibition of HK2 expression attenuated the PDCoV-induced elevation of lactate (Figure 2D). Also, inhibition of HK2 expression reduced PDCoV replication at various times (Figure 2E), while restoration of HK2 expression attenuated the ability of SeMet inhibiting PDCoV replication (Figures 2F, G and Supplementary Figures S1C, D). These data suggest that SeMet inhibits PDCoV replication by reducing HK2 levels.

Considerable research has shown that PDCoV can achieve immune escape by inhibiting the activation of RLRs signalling (37–41). To further investigate the role of HK2 on the RLRs signalling pathway under the influence of PDCoV infection, we also examined the effect of HK2 inhibition on the total protein and phosphorylation of TBK1, IRF3 and p65, key proteins in RLRs signalling. We observed no significant changes in total protein expression in the three groups (Figure 2H), whereas knockdown of HK2 resulted in a significant increase in phosphorylation of TBK1, IRF3 and p65 in cells infected with PDCoV at different times (Figure 2H), suggesting that it promotes the expression of downstream signalling molecules in RLRs.

miR-125b-5p-1 is required for HK2-dependent SeMet inhibiting PDCoV replication

To elucidate the mechanism whereby SeMet inhibits PDCoV replication within LLC-PK1 cells *via* HK2, we compared the miRNA transcriptional profiles of PDCoV-infected or SeMet-supplemented cells with those of blank control cells, respectively. SeMet supplementation significantly increased the expression of 84 miRNAs and decreased the expression of 34 miRNAs in LLC-PK1 cells; while PDCoV infection upregulated the expression of 19 miRNAs (Figures 3A, B). Combining RNA-seq and TargetScan database predictions of miRNAs targeting the HK2 gene, we validated the differential expression of several characteristic and possible antiviral miRNAs (miR-143-3p, miR-9-5p, miR-125b-5p-1 and miR-125a-5p) by qRT-PCR (Figure 3C). We found that the addition of SeMet caused elevated expression of miR-9-5p and miR-125b-5p-1 at different time points (Figure 3D). So does SeMet inhibit PDCoV replication by increasing the expression of miR-9-5p and miR-125b-5p-1? Next, we synthesized miR-9-5p mimic and miR-125b-5p-1 mimic to increase their expression levels in LLC-PK1 cells (Figure 3E and Supplementary Figure S1E). Overexpression of miR-9-5p had no effect on PDCoV replication; whereas overexpression of miR-125b-5p-1 significantly inhibited PDCoV replication (Figure 3F). We further verified whether the antiviral effect of SeMet was dependent on the regulation of miR-125b-5p-1 and found that down-regulation of miR-125b-5p-1 expression attenuated the ability of SeMet to inhibit PDCoV replication (Figure 3G and Supplementary Figures S1F, G). These results suggest that miR-125b-5p-1 can negatively regulate PDCoV replication in LLC-PK1 cells and that SeMet inhibition of PDCoV replication is dependent on the positive regulation of miR-125b-5p-1.

Meanwhile, to determine whether HK2 is a direct target gene of miR-125b-5p-1, we constructed the porcine 3'UTR of HK2 luciferase reporter plasmid (Figure 3H). Reporter activity analysis showed that miR-125b-5p-1 mimic reduced the luciferase activity of the reporter containing 3'UTR of HK2 in

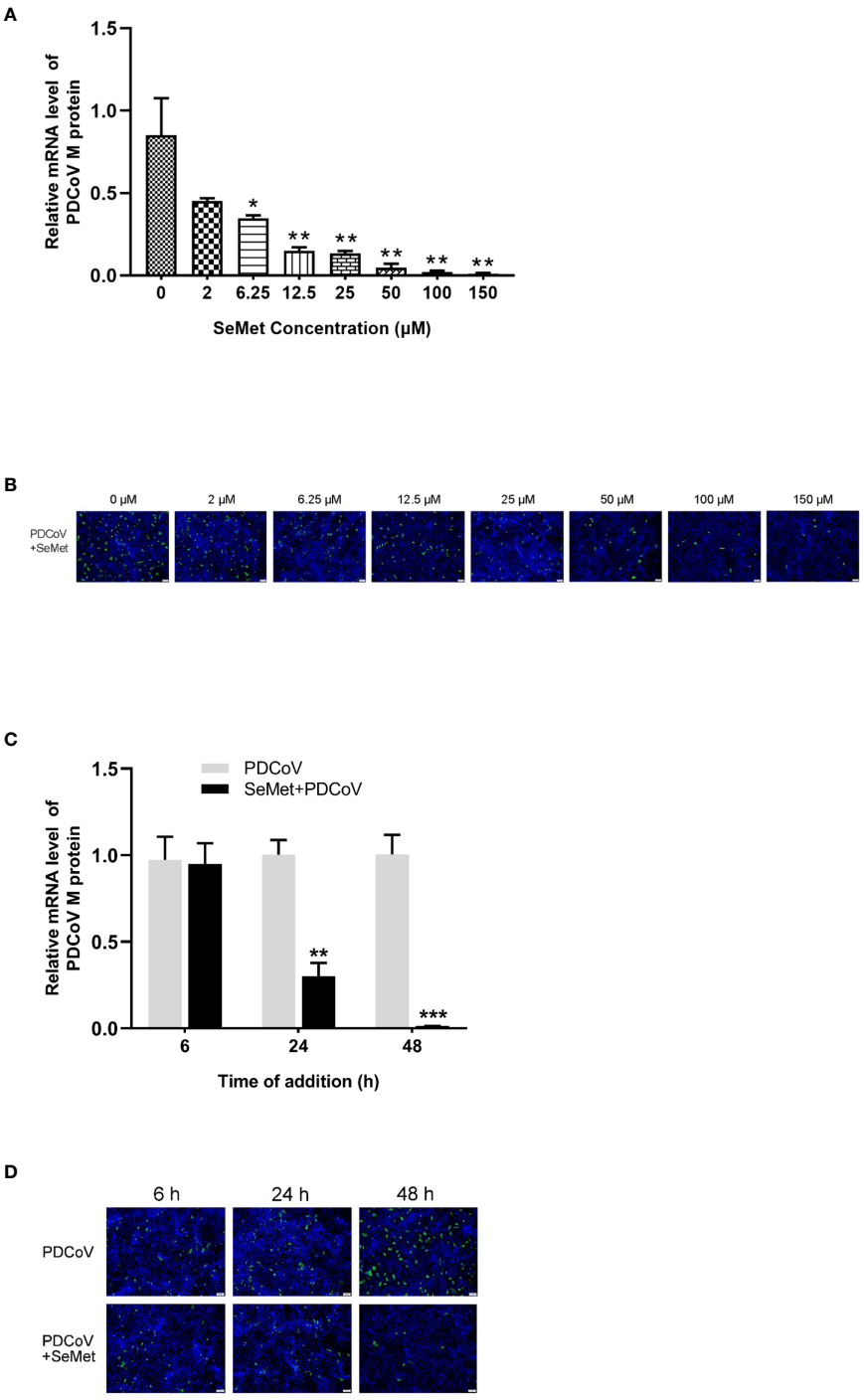

FIGURE 1
SeMet inhibits the infectivity of PDCoV. **(A)** LLC-PK1 were infected with PDCoV (100 $TCID_{50}$ = $10^{-2.15}$) for 1.5 h and treated with 0~150 μM of SeMet. Cells were collected after 48 h for qRT-PCR of viral M gene (n=6). **(B)** At 48 h treatment with SeMet, PDCoV (100 $TCID_{50}$) replication in LLC-PK1 cells was determined by indirect immunofluorescence assay (IFA). **(C)** LLC-PK1 cells were infected with PDCoV for 1.5 h and treated with SeMet (150 μM) for 6, 24, and 48 (h) Expression level of viral mRNAs was analyzed by qRT-PCR (n=6). **(D)** At 6~48 h treatment with SeMet, PDCoV replication in LLC-PK1 cells was determined by IFA. Means ± SD are shown. Statistical significance was determined by Student *t* test. ***, $P<0.001$; **, $P<0.01$; *, n.s, not significant. All experiments were repeated at least twice and representative results are shown.

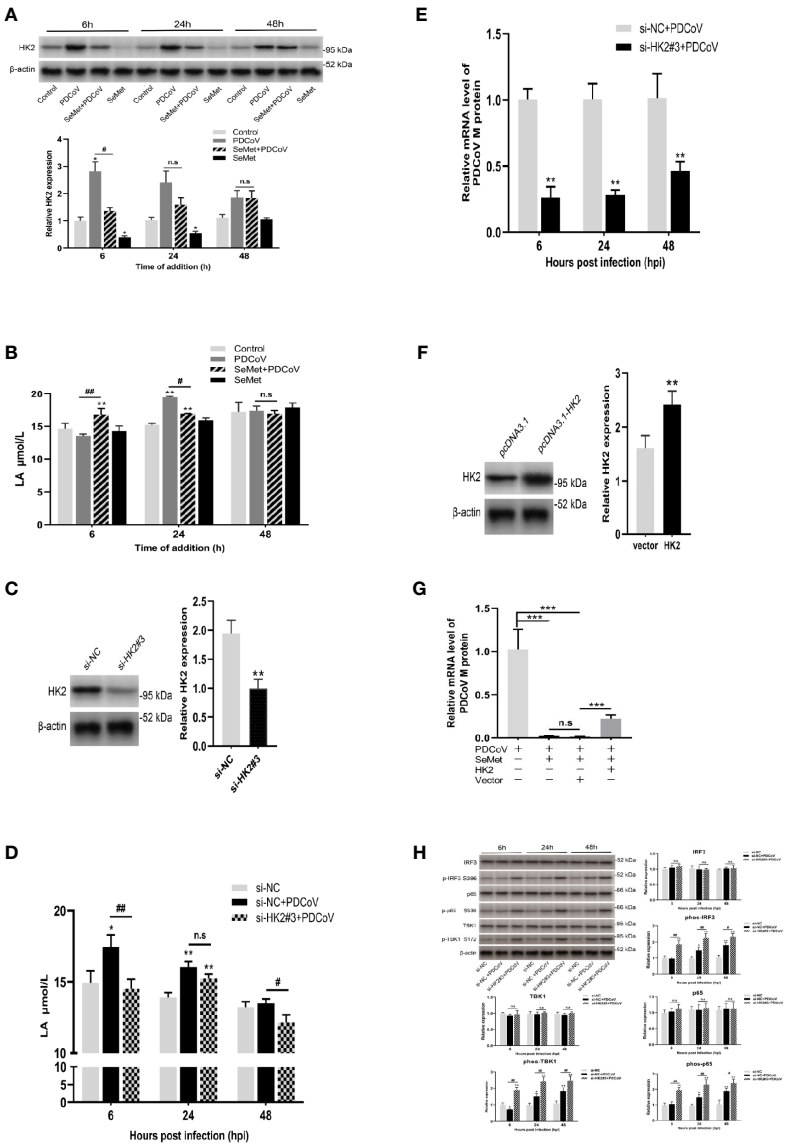

FIGURE 2
HK2 plays an important role in PDCoV replication. **(A)** LLC-PK1 cells were treated with PDCoV (100 $TCID_{50}$) and SeMet (150 μM) for 6, 24, and 48 h, and the level of HK2 was determined by and Western blot(n=3). **(B)** The LA level was measured by ELISA (n=3). **(C)** The HK2 protein expression was determined by Western blot in LLC-PK1 cells treated with siRNA-NC and siHK2 (n=3). **(D)** HK2 inhibition-induced LA expression after PDCoV infection. LA expression in LLC-PK1 cells was determined by ELISA (n=4). **(E)** Cells were infected with PDCoV for 6, 24, and 48 h post infection (hpi), after transfection with siRNA-NC or siHK2. Expression level of viral mRNAs was analyzed by qRT-PCR (n=8). **(F)** The HK2 protein expression was determined by Western blot in LLC-PK1 cells when transfected with pcDNA3.1-vector or pcDNA3.1-HK2 (n=3). **(G)** Cells were transfected with pcDNA3.1-vector or pcDNA3.1-HK2, followed by treatment with SeMet and PDCoV. Viral mRNA expression was analyzed by qRT-PCR (n=6). **(H)** HK2 inhibition-induced RLR signal proteins expression after PDCoV infection. The TBK1, phos-TBK1 (Ser172), IRF3, phos-IRF3 (Ser396), p65, or phos-p65 (Ser536) protein levels were analyzed by Western blot (n=3). Means ± SD are shown. Statistical significance was determined by Student *t* test. ***, $P<0.001$; **, $P<0.01$; *, $P<0.05$; $^{\#\#}$, $P<0.01$; $^{\#}$, $P<0.05$; n.s: not significant. All experiments were repeated at least twice and representative results are shown.

HEK293T cells but had no effect on the reporters with mutated 3'UTR of HK2 (Figure 3I), suggesting that HK2 is indeed a miR-125b-5p -1 target. We also demonstrated using qRT-PCR and Western blot that overexpression of miR-125b-5p-1 suppressed HK2 expression and knockdown of miR-125b-5p-1 promoted HK2 transcription and protein expression (Figures 3J, K). To further determine the effect of miR-125b-5p-1/HK2 on PDCoV infection, we performed a rescue experiment. Co-transfection of miR-125b-5p-1 mimic and HK2 overexpression plasmid showed that restoration of HK2 expression attenuated effects of

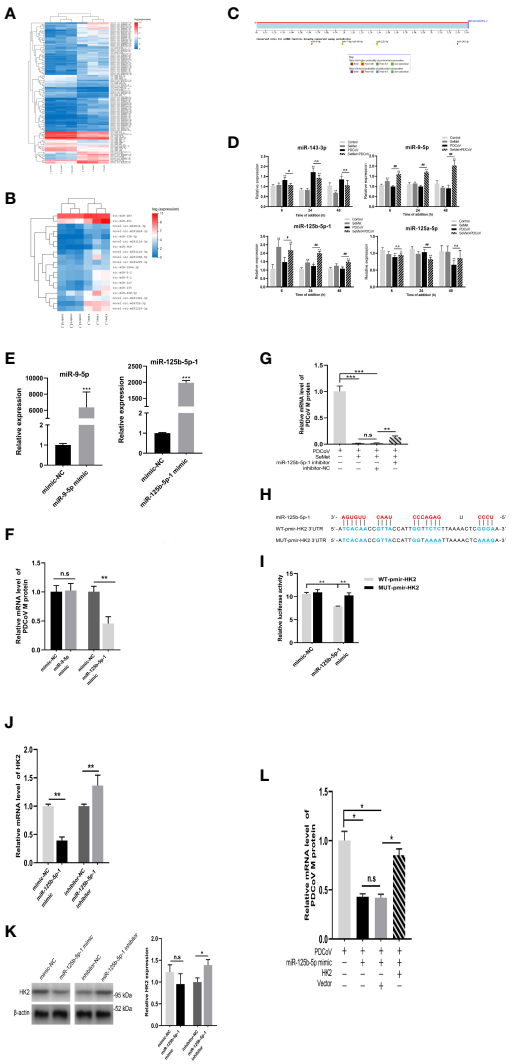

FIGURE 3
miR-125b-5p-1 is required for HK2-dependent SeMet inhibiting PDCoV replication. **(A, B)** Hierarchic clustering analyses of 118 miRNAs that were differentially expressed in the SeMet-supplemented LLC-PK1 cells by >2-fold compared with the mock-treated LLC-PK1 cells, and 19 miRNAs that were differentially expressed in the PDCoV-infected cells by >2-fold compared with the mock-treated cells. **(C)** Analysis of the TargetScanHuman (http://www.targetscan.org/vert_72/) website shows that miR-143-3p, miR-9-5p, miR-125b-5p-1, and miR-125a-5p can target the human 3'UTR of HK2. Binding sequences are highly conserved among species (including human and swine). **(D)** LLC-PK1 cells were treated with PDCoV (100 $TCID_{50}$) and SeMet (150 μM) for 6, 24, and 48 h, and the levels of miR-143-3p, miR-9-5p, miR-125b-5p-1, and miR-125a-5p were determined by qRT-PCR (n=6). **(E)** The miR-9-5p and miR-125b-5p-1 expressions were determined by qRT-PCR when transfected with mimic-NC, miR-9-5p mimic, and miR-125b-5p-1 mimic (n=4). **(F)** Viral mRNA in the LLC-PK1 cells transfected with miR-9-5p mimic or miR-125b-5p-1 mimic was quantified by qRT-PCR after 48 h (n=6-8). **(G)** Cells were transfected with miR-125b-5p-1 inhibitor, followed by treatment with SeMet and PDCoV. Viral mRNA expression was analyzed by qRT-PCR (n=6). **(H)** The miR-125b-5p-1 targets the base sequence and mutant sequence of the 3'UTR of HK2. **(I)** The miR-125b-5p-1 mimic or mimic-NC and WT-pmirGLO-HK2 or MUT-pmirGLO-HK2 were co-transfected into HEK293T cells. The luciferase reporter assay was used to detect whether miR-125b-5p-1 targeted to bind to the 3'UTR of HK2 (n=5). **(J, K)** The HK2 mRNA and protein expressions were determined by qRT-PCR and Western blot in LLC-PK1 cells when transfected with miR-125b-5p-1 mimic or inhibitor (n=3-6). **(L)** LLC-PK1 cells were transfected with miR-125b-5p-1 mimic and pcDNA3.1-HK2, followed by infection with PDCoV. Viral mRNA expression was analyzed by qRT-PCR (n=6). Means ± SD are shown. Statistical significance was determined by Student *t* test. ***, $P<0.001$; **, $P<0.01$; *, $P<0.05$; $^{\#\#}$, $P<0.01$; $^{\#}$, $P<0.05$; n.s: not significant. All experiments were repeated at least twice and representative results are shown.

overexpression of miR-125b-5p-1 in inhibiting PDCoV replication (Figure 3L). These data suggest that miR-125b-5p-1 inhibition of PDCoV replication in LLC-PK1 cells is dependent on the negative regulation of the HK2 gene.

STAT3 directly regulates miR-125b-5p-1 expression

We found that in LLC-PK1 cells infected with PDCoV, SeMet treatment resulted in a significant increase in STAT3 expression levels in the early stages and a decrease in the middle and late stages (Figures 4A, B). Next, we further analyzed the miR-125b-1 promoter sequence and identified interaction sites at -1059 to -1258 of the miR-125b-1 transcriptional start, which are STAT3 binding sites. We constructed a luciferase reporter plasmid containing the miR-125b-1 promoter (Figure 4C) and a STAT3 overexpression plasmid vector (Figure 4D and Supplementary Figures S1H, I). The pcDNA-STAT3 plasmid or empty vector was cotransfected with WT-pGL3-miR-125b-1 plasmid or mutant plasmid. The results of reporter gene activity analysis showed that STAT3 reduced luciferase activity in the miR-125b-1 promoter, but had no effect on the reporter gene mutated in the miR-125b-1 promoter (Figure 4E), suggesting that miR-125b-5p-1 is indeed a target of STAT3. The qRT-PCR results also showed that overexpression of STAT3 reduced the activity of miR-125b-5p-1 expression levels, while inhibition of STAT3 levels increased miR-125b-5p-1 expression (Figures 4F, G and Supplementary Figures S1J, K). These data suggest that STAT3 directly regulates the expression of miR-125b-5p-1.

Similarly, we identified interaction sites with STAT3 at -967 to -768 of the HK2 transcription start site and constructed a luciferase reporter plasmid containing the HK2 promoter (Figure 4H). Analysis of reporter gene activity showed that STAT3 reduced the luciferase activity of the HK2 promoter and that the luciferase activity of the mutant was also reduced (Figure 4I). We also demonstrated that overexpression of STAT3 inhibited HK2 transcription and protein expression and that inhibition of STAT3 expression promoted HK2 transcription and protein levels (Figures 4J, K). These data suggest that the -967 to -768 sites in the HK2 promoter sequence are not targets of STAT3 and that other interaction sites or potential regulators may exist.

In our study, we found that miR-125b-5p-1 could target and inhibit the expression of HK2, while STAT3 could also inhibit the expression of HK2. Interestingly, we also identified a binding site for STAT3 on the promoter of miR-125b-5p-1 and demonstrated that STAT3 can repress miR-125b-5p-1 expression. These data suggest a possible feedback regulatory mechanism for STAT3/miR-125b-5p-1/HK2 to maintain intracellular glucose metabolism homeostasis. To further explore the effect on HK2 in the presence of STAT3 and miR-125b-5p-1 together, we cotransfected si-STAT3#2 and miR-125b-5p-1 mimic. The qRT-PCR and Western blot results showed that transfection of si-STAT3#2 or miR-125b-5p-1 mimic alone elevated or decreased HK2 expression, respectively, whereas the cotransfected group showed no significant change in HK2 mRNA expression or protein expression compared to the control group (Figures 4L, M). These data suggest that miR-125b-5p-1 plays a major regulatory role on HK2 under the combined effect of STAT3 and miR-125b-5p-1. In addition, it also confirms that SeMet can indeed suppress HK2 levels by reducing STAT3 and up-regulating miR-125b-5p-1 expression, thus exerting an anti-PDCoV effect.

Decreased STAT3 levels are utilized by SeMet to suppress PDCoV replication

We further explored whether STAT3 could act as an upstream of miR-125b-5p-1/HK2 signalling to influence PDCoV replication in LLC-PK1 cells. In conjunction with the previously mentioned ability of SeMet addition to show differential changes in STAT3 expression at different time points, we therefore investigated the effects on PDCoV replication at both overexpressed and knockdown STAT3 transcript and protein levels. The si-STAT3 interference or the STAT3 inhibitor Stattic reduced the mRNA expression of PDCoV M gene, whereas pcDNA-STAT3 increased the mRNA expression of M gene (Figure 5A). Next, we verified the link between STAT3 and SeMet or STAT3 and miR-125b-5p-1 in affecting PDCoV infection. The data showed that restoration of STAT3 expression attenuated the ability of SeMet to resist PDCoV replication (Figure 5B) and inhibition of miR-125b-5p-1 mRNA expression attenuated the role of si-STAT3 in inhibiting PDCoV replication (Figure 5C).

Discussion

Since 2012, when PDCoV was first identified in Hong Kong, China. There has been continued research into PDCoV vaccines, but no approved treatments or vaccines for PDCoV are currently on the market. Laboratory studies at this stage have focused on drugs to combat PDCoV infection *in vitro*. Melatonin (42), cholesterol 25 hydroxylase (CH25H) (43), goose deoxycholic acid (CDCA) and lithophanic acid (LCA) (44) have been found to have antiviral activity against a PDCoV-infected porcine kidney cell line (LLC-PK1). Our results showed that SeMet significantly inhibited the replication of PDCoV in LLC-PK1 cells, with the inhibitory effect enhanced in a concentration-dependent/time-dependent manner.

SeMet's low toxicity, high bioavailability and its use as an effective anti-PDCoV drug has raised expectations for its clinical

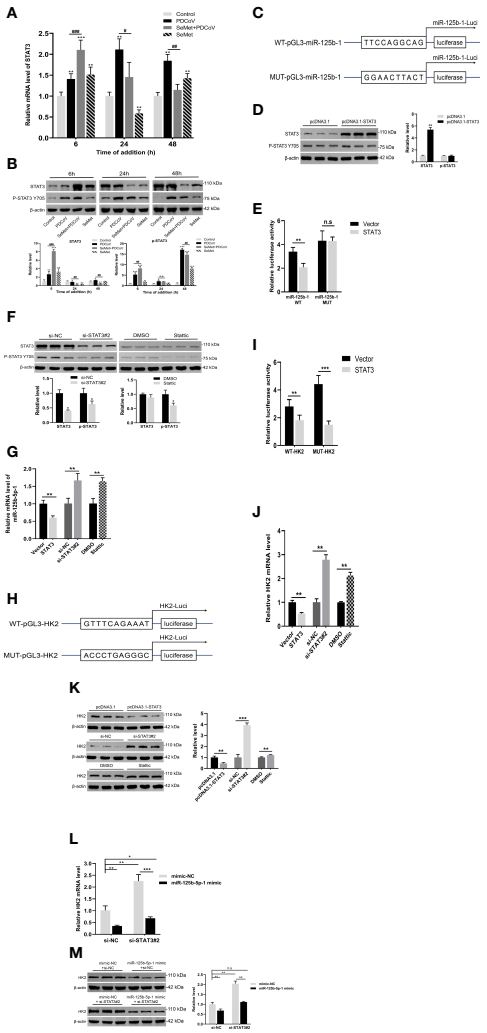

FIGURE 4
STAT3 directly regulates miR-125b-5p-1 expression. **(A, B)** LLC-PK1 cells were treated with PDCoV (100 $TCID_{50}$) and SeMet (150 μM) for 6, 24, and 48 h, and the level of STAT3 and phos-STAT3 (Tyr705) was determined by qRT-PCR or Western blot (n=3-6). **(C)** The base sequence and mutant sequence of miR-125b-5p-1 promoter. **(D)** The STAT3 protein expressions was determined by qRT-PCR and Western blot in LLC-PK1 cells when transfected with pcDNA3.1-vector or pcDNA3.1-STAT3 (n=3). **(E)** The pcDNA3.1-STAT3 or empty vector and WT-pGL3-miR-125b-1 or MUT- pGL3-miR-125b-1 were co-transfected into HEK293T cells. The luciferase reporter assay was used to detect whether STAT3 can target and bind on miR-125b-1 promoter (n=5). **(F)** The STAT3 protein expression was determined by qRT-PCR or Western blot in LLC-PK1 cells treated with siRNA-NC, siSTAT3, DMSO, and Stattic (STAT3 inhibitor, 0.75 μM) (n=3). **(G)** The miR-125b-5p-1 expression was measured by qRT-PCR when transfected with pcDNA3.1-STAT3, empty vector, siSTAT3, siRNA-NC, DMSO, Stattic (0.75 μM) (n=6). **(H)** The base sequence and mutant sequence of HK2 promoter. **(I)** The pcDNA3.1-STAT3 or empty vector and WT-pGL3-HK2 or MUT- pGL3-HK2 were co-transfected into HEK293T cells. The luciferase reporter assay was used to detect whether STAT3 can target and bind on HK2 promoter (n=5). **(J, K)** The HK2 mRNA and protein expressions were determined by qRT-PCR and Western blot in LLC-PK1 cells when transfected with pcDNA3.1-STAT3, empty vector, siSTAT3, siRNA-NC, DMSO, Stattic (0.75 μM) (n=3-6). **(L, M)** The siSTAT3 or siRNA-NC and miR-125b-5p-1 mimic or mimic-NC were co-transfected into LLC-PK1 cells. The HK2 mRNA and protein expressions were determined by qRT-PCR and Western blot (n=3-6). Means ± SD are shown. Statistical significance was determined by Student *t* test. ***, $P<0.001$; **, $P<0.01$; *, $P<0.05$; $^{###}$, $P < 0.001$; $^{##}$, $P<0.01$; $^{#}$, $P<0.05$; n.s: not significant. All experiments were repeated at least twice and representative results are shown.

application. Although increasing selenium intake in selenium-sufficient individuals is not advocated, some studies have shown that body selenium levels are positively correlated with cure rates and negatively correlated with morbidity and mortality in patients with viral infections, and that high selenium levels may attenuate the deleterious effects of viral infections (45–48). In addition, numerous studies have demonstrated the important role of selenium compounds in the fight against viral infections, such as the inhibition of human herpesvirus type 1/type 2, cerebral myocarditis virus, vesicular stomatitis

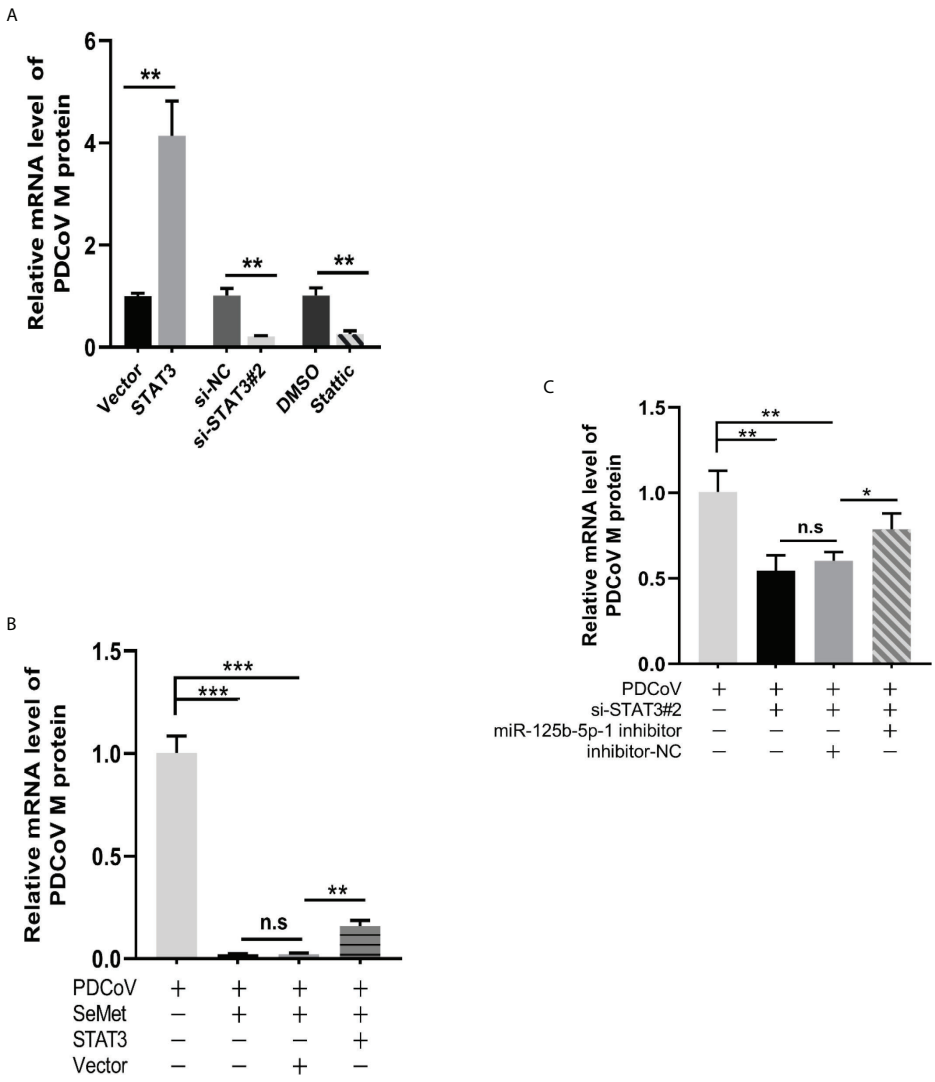

FIGURE 5
Decreased STAT3 levels are utilized by SeMet to suppress PDCoV replication. **(A)** Expression level of viral mRNAs was analyzed by qRT-PCR when transfected with pcDNA3.1-STAT3, empty vector, siSTAT3, siRNA-NC, DMSO, Stattic (0.75 μM) (n=6). **(B)** Cells were transfected with pcDNA3.1-vector or pcDNA3.1-STAT3, followed by treatment with SeMet and PDCoV. Viral mRNA expression was analyzed by qRT-PCR (n=6). **(C)** Expression level of viral mRNAs was analyzed by qRT-PCR when transfected with siSTAT3 and miR-125b-5p-1 inhibitor followed by infection with PDCoV (n=6). Means ± SD are shown. Statistical significance was determined by Student *t* test. ***, *P*<0.001; **, *P*<0.01; *, *P*<0.05; n.s, not significant. All experiments were repeated at least twice and representative results are shown.

virus, porcine circovirus type 2, EBV and hepatitis B/C virus replication (20, 49–53), so it is feasible to increase body selenium levels during the phase of viral infection in response to the acute phase.

Here, we found that early infection of LLC-PK1 cells by PDCoV significantly increased the expression of HK2 and LA in the cells and attenuated p-TBK1, a key protein in the RLRs signalling pathway, and the activation of the RLRs signalling pathway was inhibited; whereas when the expression of HK2 was reduced, the inhibitory effect of viral infection on the activation of the RLRs signalling pathway was attenuated and the expression of p-IRF3 and p-p65 proteins was further increased and viral replication was simultaneously reduced. The implication that HK2 can influence PDCoV replication in cells and its important role in the RLRs signalling pathway is supported by recent data (35, 36). Next, we explored the molecular mechanisms by which SeMet inhibits PDCoV. Indeed, selenium is able to play an immunomodulatory or metabolic regulatory role by participating in selenoprotein synthesis as a selenium-containing amino acid itself or as a selenium-derived donor (21, 23, 54, 55). HK2, the initial key rate-limiting enzyme that catalyzes the glycolytic reaction, was found to be significantly upregulated in

studies of multiple malignant diseases and was accompanied by high glucose uptake and increased rates of glycolysis (56). HK2 acts as a hub linking glycolysis and innate immunity, and we demonstrated that it plays a key role in the SeMet anti-PDCoV process.

MicroRNAs are involved in a variety of biological processes, including virus-mediated host innate immune responses, by repressing the expression of target genes. There have been few studies on miRNA and coronaviruses, but the relationship between SARS-CoV-2 infestation and miRNA regulation has been extensively studied in the last two years. Wang et al. (57) combined bioinformatics analysis and laboratory assays to screen for four inhibitory effects on spike-in glycoprotein (S protein) miRNAs (miR-223-3p, miR-24-3p, miR-145-5p, and miR-7-5p). Interestingly, the expression of CoV2-miR-7a.2 encoded by SARS-CoV-2 was comparable in infected cells to one of the most abundant human miRNAs, has-miR-let-7a, and the efficiency of CoV2-miR-7a.2 and Argonaute protein forming RNA silencing complex (degrading target mRNAs) was similar to that of miR-let-7a; in addition, CoV2-miR-7a.2 can target the human BATF2 gene (an interferon-stimulated gene) and inhibit ISG expression, thereby promoting SARS-CoV-2 replication (58). In our initial experiments, we have predicted miRNAs that can target binding to HK2 through bioinformatics databases and screened miR-125b-5p-1 for follow-up testing. The ability of miR-125b-5p to target the HK2 gene to affect cellular glycolysis has been reported to a lesser extent in recent years, but almost all studies have been related to cancer. Hui et al. (59) found that miR-125b-5p was significantly down-regulated in laryngeal carcinoma tissues and cell lines and that overexpression of miR-125b-5p inhibited LSCC cell proliferation and induced apoptosis. Further molecular studies showed that miR-125b-5p binds to the 3'UTR of HK2, and overexpression of miR-125b-5p downregulated the mRNA and protein level expression of HK2, significantly inhibiting glucose consumption and lactate production in LSCC cells. In a study to validate how miR-125b-5p is involved in bladder cancer (BCa) development, Liu et al. (60) found that miR-125b-5p exerts its inhibitory effect on BCA by targeting HK2 and inhibiting the PI3K/AKT pathway. In a study to address the resistance to cisplatin in some colon cancer patients, Shi et al. (61) found that overexpression of miR-125b-5p increased the sensitivity of colon cancer cells to cisplatin by directly targeting the 3'UTR of HK2 and inhibiting the glycolytic efficiency of the cells, while differentiation antagonist non-protein coding RNA (DANCR) can bind to the seed region of miR-125b-5p in the form of a competitive endogenous RNA (ceRNA) to reduce cisplatin sensitivity in colon cancer cells. All of these studies in cancer disease confirm that miR-125b-5p binds to the 3'UTR of HK2 and affects the efficiency of cellular glycolysis. Our experiments have also demonstrated that overexpression of miR-125b-5p-1 inhibits HK2 mRNA and protein expression by binding to the 3'UTR of the porcine HK2 gene, thus suppressing LA production in LLC-PK1 cells.

In addition, a few studies have shown that patients infected with viral hepatitis (HBV, HCV and HEV) are often accompanied by elevated serum miR-125b-5p levels and that miR-125b-5p levels correlate with viral load and severity of liver injury (62–65). Deng et al. (66) in exploring the regulation of miR-125b-5p on HBV replication at different stages of HBV transcription and assembly found that overexpression of miR-125b-5p increased HBV nucleocapsid protein formation but did not enhance HBV promoter activity or transcription, and further identified a mechanism by which miR-125b-5p stimulated HBV replication with the help of the LIN28B/miR-98 axis. Our experiments again validated that exogenous addition of porcine miR-125b-5p-1 mimic can reduce mRNA levels of PDCoV M gene, but there is no direct evidence that miR-125b-5p-1 can target the regulation of PDCoV transcription. However, whether it can play a role in regulating PDCoV replication by affecting PDCoV promoter activity needs further investigation.

Pathogen infection causes an acute phase response and is accompanied by activation of the STAT3 signalling pathway. For example, high expression of p-STAT3 was found in endothelial cells of small pulmonary veins and interstitial capillaries from COVID-19 patients (67); as well as increased expression of p-STAT3 in COVID-19-associated collapsed glomerulopathy biopsy samples (68). This is consistent with our observation that PDCoV infection, which is also a member of the coronaviridae family, is also capable of activating STAT3 phosphorylation. However, the relationship between PDCoV and the host molecule STAT3 is not well understood and whether PDCoV can specifically activate STAT3 similarly to other viruses such as HBV (29), HCV (69, 70) and HCMV (71, 72) that encode viral proteins needs further investigation. Our preliminary findings suggest that PDCoV infection persistently activates STAT3, while overexpression of STAT3 promotes PDCoV replication and inhibition of STAT3 expression attenuates PDCoV replication.

In this study, SeMet could inhibit PDCoV replication by regulating STAT3/miR-125b-5p-1/HK2, which seems to imply that SeMet could be a potential drug for the treatment of PDCoV infection. We also found that miR-125b-5p-1 could target HK2 to inhibit PDCoV replication; while STAT3 could target the miR-125b-5p-1 promoter while non-targeting the HK2 promoter, inducing a potential loop by reducing their expression. We hypothesize that there are also regulatory factors between STAT3 and HK2 that allow STAT3/miR-125b-5p-1/HK2 to form a regulatory loop that maintains intracellular glucose metabolism homeostasis. When cells are exposed to external stimuli, this dynamic balance is disrupted and STAT3 or miR-125b-5p-1 loses a mutual balance, leading to a disruption of intracellular HK2 and even glucose metabolism, making them more susceptible to invasion by viruses or other pathogenic microorganisms.

Data availability statement

The original contributions presented in the study are included in the article/Supplementary Material. Further inquiries can be directed to the corresponding author.

Author contributions

ZR, TD and HH contributed to conception and design of the study. TD and HH performed the statistical analysis. TD wrote the first draft of the manuscript. RS wrote sections of the manuscript. ZW and JD reviewed and revised the manuscript. All authors contributed to manuscript revision, read, and approved the submitted version.

Funding

The manuscript was supported by The National Science Foundation of China (32130106 and 31402269).

Conflict of interest

The authors declare that the research was conducted in the absence of any commercial or financial relationships that could be construed as a potential conflict of interest.

Publisher's note

Supplementary material

The Supplementary Material for this article can be found online at: https://www.frontiersin.org/articles/10.3389/fimmu.2022.952852/full#supplementary-material

References

1. Chen Q, Gauger P, Stafne M, Thomas J, Arruda P, Burrough E, et al. Pathogenicity and pathogenesis of a united states porcine deltacoronavirus cell culture isolate in 5-day-old neonatal piglets. *Virology* (2015) 482:51–9. doi: 10.1016/j.virol.2015.03.024

2. Jung K, Hu H, Eyerly B, Lu ZY, Chepngeno J, Saif LJ. Pathogenicity of 2 porcine deltacoronavirus strains in gnotobiotic pigs. *Emerg Infect Dis* (2015) 21:650–4. doi: 10.3201/eid2104.141859

3. Ma YM, Zhang Y, Liang XY, Lou FF, Oglesbee M, Krakowka S, et al. Origin, evolution, and virulence of porcine deltacoronaviruses in the United States. *mBio* (2015) 6:e00064. doi: 10.1128/mBio.00064-15

4. Woo PC, Lau SKP, Lam CSFL, Lau CCY, Tsang AKL, Lau JHN, et al. Discovery of seven novel mammalian and avian coronaviruses in the genus deltacoronavirus supports bat coronaviruses as the gene source of alphacoronavirus and betacoronavirus and avian coronaviruses as the gene source of gammacoronavirus and deltacoronavirus. *J Virol* (2012) 86:3995–4008. doi: 10.1128/JVI.06540-11

5. Lee S, Lee C. Complete genome characterization of Korean porcine deltacoronavirus strain KOR/KNU14-04/2014. *Genome Announc* (2014) 2: e01191–14. doi: 10.1128/genomeA.01191-14

6. Hu H, Jung K, Vlasova AN, Chepngeno J, Lu Z, Wang Q, et al. Isolation and characterization of porcine deltacoronavirus from pigs with diarrhea in the United States. *J Clin Microbiol* (2015) 53:1537–48. doi: 10.1128/JCM.00031-15

7. Song D, Zhou X, Peng Q, Chen Y, Zhang F, Huang T, et al. Newly emerged porcine deltacoronavirus associated with diarrhoea in swine in China: Identification, prevalence and full-length genome sequence analysis. *Transbound Emerg Dis* (2015) 62:575–80. doi: 10.1111/tbed.12399

8. Janetanakit T, Lumyai M, Bunpapong N, Boonyapisitsopa S, Chaiyawong S, Nonthabenjawan N, et al. Porcine deltacoronavirus, Thailand, 2015. *Emerg Infect Dis* (2016) 22:757–9. doi: 10.3201/eid2204.151852

9. Lorsirigool A, Saeng-Chuto K, Temeeyasen G, Madapong A, Tripipat T, Wegner M, et al. The first detection and full-length genome sequence of porcine deltacoronavirus isolated in lao PDR. *Arch Virol* (2016) 161:2909–11. doi: 10.1007/s00705-016-2983-8

10. Suzuki T, Hayakawa J, Ohashi S. Complete genome characterization of the porcine deltacoronavirus HKD/JPN/2016, isolated in Japan, 2016. *Genome Announc* (2017) 5:e00795–17. doi: 10.1128/genomeA.00795-17

11. Le VP, Song S, An BH, Park GN, Pham NT, Le DQ, et al. A novel strain of porcine deltacoronavirus in Vietnam. *Arch Virol* (2018) 163:203–7. doi: 10.1007/s00705-017-3594-8

12. Perez-Rivera C, Ramirez-Mendoza H, Mendoza-Elvira S, Segura-Velazquez R, Sanchez-Betancourt JI. First report and phylogenetic analysis of porcine deltacoronavirus in Mexico. *Transbound Emerg Dis* (2019) 66:1436–41. doi: 10.1111/tbed.13193

13. Jung K, Hu H, Saif LJ. Calves are susceptible to infection with the newly emerged porcine deltacoronavirus, but not with the swine enteric alphacoronavirus, porcine epidemic diarrhea virus. *Arch Virol* (2017) 162:2357–62. doi: 10.1007/s00705-017-3351-z

14. Liang QQ, Zhang HL, Li BX, Ding QW, Wang YB, Gao WM, et al. Susceptibility of chickens to porcine deltacoronavirus infection. *Viruses* (2019) 11:573. doi: 10.3390/v11060573

15. Li WT, Hulswit RJG, Kenney SP, Widjaja I, Jung K, Alhamo MA, et al. Broad receptor engagement of an emerging global coronavirus may potentiate its diverse cross-species transmissibility. *Proc Natl Acad Sci USA* (2018) 115:E5135–43. doi: 10.1073/pnas.1802879115

16. Roman M, Jitaru P, Barbante C. Selenium biochemistry and its role for human health. *Metallomics* (2014) 6:25–54. doi: 10.1039/c3mt00185g

17. Xie MH, Sun XY, Li P, Shen XC, Fang Y. Selenium in cereals: Insight into species of the element from total amount. *Compr Rev Food Sci Food Saf* (2021) 20:2914–40. doi: 10.1111/1541-4337.12748

18. Briviba K, Roussyn, Sharov VS, Sies H. Attenuation of oxidation and nitration reactions of peroxynitrite by selenomethionine, selenocystine and ebselen. *Biochem J* (1996) 319(Pt 1):13–5. doi: 10.1042/bj3190013

19. Suryo Rahmanto A, Davies MJ. Catalytic activity of selenomethionine in removing amino acid, peptide, and protein hydroperoxides. *Free Radic Biol Med* (2011) 51:2288–99. doi: 10.1016/j.freeradbiomed.2011.09.027

20. Chen X, Ren F, Hesketh J, Shi X, Li J, Gan F, et al. Selenium blocks porcine circovirus type 2 replication promotion induced by oxidative stress by improving GPx1 expression. *Free Radic Biol Med* (2012) 53:395–405. doi: 10.1016/j.freeradbiomed.2012.04.035

21. Zhang Y, Cartland SP, Henriquez R, Patel S, Gammelgaard B, Flouda K, et al. Selenomethionine supplementation reduces lesion burden, improves vessel

function and modulates the inflammatory response within the setting of atherosclerosis. *Redox Biol* (2020) 29:101409. doi: 10.1016/j.redox.2019.101409

22. Flouda K, Gammelgaard B, Davies MJ, Hawkins CL. Modulation of hypochlorous acid (HOCl) induced damage to vascular smooth muscle cells by thiocyanate and selenium analogues. *Redox Biol* (2021) 41:101873. doi: 10.1016/j.redox.2021.101873

23. Xu CX, Sun SG, Johnson T, Qi R, Zhang SY, Zhang J, et al. The glutathione peroxidase Gpx4 prevents lipid peroxidation and ferroptosis to sustain treg cell activation and suppression of antitumor immunity. *Cell Rep* (2021) 35:109235. doi: 10.1016/j.celrep.2021.109235

24. Labunskyy VM, Lee BC, Handy DE, Loscalzo J, Hatfield DL, Gladyshev VN. Both maximal expression of selenoproteins and selenoprotein deficiency can promote development of type 2 diabetes-like phenotype in mice. *Antioxid Redox Signal* (2011) 14:2327–36. doi: 10.1089/ars.2010.3526

25. Mita Y, Nakayama K, Inari S, Nishito Y, Yoshilka YY, Sakai N, et al. Selenoprotein p-neutralizing antibodies improve insulin secretion and glucose sensitivity in type 2 diabetes mouse models. *Nat Commun* (2017) 8:1658. doi: 10.1038/s41467-017-01863-z

26. Akira S, Nishio Y, Inoue M, Wang XJ, Shi We, Matsusaka T, et al. Molecular cloning of APRF, a novel IFN-stimulated gene factor 3 p91-related transcription factor involved in the gp130-mediated signaling pathway. *Cell* (1994) 77:63–71. doi: 10.1016/0092-8674(94)90235-6

27. Zhong Z, Wen Z, Darnell JEJr. Stat3: a STAT family member activated by tyrosine phosphorylation in response to epidermal growth factor and interleukin-6. *Science* (1994) 264:95–8. doi: 10.1126/science.8140422

28. Villarino AV, Kanno Y, O'Shea JJ. Mechanisms and consequences of jak-STAT signaling in the immune system. *Nat Immunol* (2017) 18:374–84. doi: 10.1038/ni.3691

29. Lee YH, Yun YD. HBx protein of hepatitis b virus activates Jak1-STAT signaling. *J Biol Chem* (1998) 273:25510–5. doi: 10.1074/jbc.273.39.25510

30. Waris G, Siddiqui A. Interaction between STAT-3 and HNF-3 leads to the activation of liver-specific hepatitis b virus enhancer 1 function. *J Virol* (2002) 76:2721–9. doi: 10.1128/jvi.76.6.2721-2729.2002

31. Wang Y, Lu YW, Toh ST, Sung WK, Tan P, Chow P, et al. Lethal-7 is down-regulated by the hepatitis b virus x protein and targets signal transducer and activator of transcription 3. *J Hepatol* (2010) 53:57–66. doi: 10.1016/j.jhep.2009.12.043

32. Gebert LFR, MacRae IJ. Regulation of microRNA function in animals. *Nat Rev Mol Cell Biol* (2019) 20:21–37. doi: 10.1038/s41580-018-0045-7

33. O'Brien J, Hayder H, Zayed Y, Peng C. Overview of MicroRNA biogenesis, mechanisms of actions, and circulation. *Front Endocrinol (Lausanne)* (2018) 9:402. doi: 10.3389/fendo.2018.00402

34. Rosenberger CM, Podyminogin RL, Diercks AH, Treuting PM, Peschon JJ, Rodriguez D, et al. miR-144 attenuates the host response to influenza virus by targeting the TRAF6-IRF7 signaling axis. *PLoS Pathog* (2017) 13:e1006305. doi: 10.1371/journal.ppat.1006305

35. Zhang W, Wang G, Xu ZG, Tu H, Lin HK. Lactate is a natural suppressor of RLR signaling by targeting MAVS. *Cell* (2019) 178:176–189.e115. doi: 10.1016/j.cell.2019.05.003

36. Zhou L, He R, Fang PN, Li MQ, Yu HS, Wang QM, et al. Hepatitis b virus rigs the cellular metabolome to avoid innate immune recognition. *Nat Commun* (2021) 12:98. doi: 10.1038/s41467-020-20316-8

37. Chen J, Fang PX, Wang MH, Peng Q, Ren J, Wang D, et al. Porcine deltacoronavirus nucleocapsid protein antagonizes IFN-beta production by impairing dsRNA and PACT binding to RIG-I. *Virus Genes* (2019) 55:520–31. doi: 10.1007/s11262-019-01673-z

38. Ji LK, Li SS, Zhu WX, Ma JJ, Yan YX. Porcine deltacoronavirus nucleocapsid protein suppressed IFN-beta production by interfering porcine RIG-I dsRNA-binding and K63-linked polyubiquitination. *Front Immunol* (2019) 10:1024. doi: 10.3389/fimmu.2019.01024

39. Liu X, Fang P, Fang L, Hong Y, Zhu X, Wang X, et al. Porcine deltacoronavirus nsp15 antagonizes interferon-beta production independently of its endoribonuclease activity. *Mol Immunol* (2019) 114:100–7. doi: 10.1016/j.molimm.2019.07.003

40. Fang PX, Fang LR, Xia SJ, Ren J, Zhang JS, Bai DC, et al. Porcine deltacoronavirus accessory protein NS7a antagonizes IFN-beta production by competing with TRAF3 and IRF3 for binding to IKKepsilon. *Front Cell Infect Microbiol* (2020) 10:257. doi: 10.3389/fcimb.2020.00257

41. Fang P, Hong Y, Xia S, Zhang J, Xiao S. Porcine deltacoronavirus nsp10 antagonizes interferon-beta production independently of its zinc finger domains. *Virology* (2021) 559:46–56. doi: 10.1016/j.virol.2021.03.015

42. Zhai X, Wang N, Jiao H, Zhang J, Li C, Ren W, et al. Melatonin and other indoles show antiviral activities against swine coronaviruses *in vitro* at pharmacological concentrations. *J Pineal Res* (2021) 71:e12754. doi: 10.1111/jpi.12754

43. Ke WT, Wu XL, Fang PX, Zhou YR, Xiao SB. Cholesterol 25-hydroxylase suppresses porcine deltacoronavirus infection by inhibiting viral entry. *Virus Res* (2021) 295:198306. doi: 10.1016/j.virusres.2021.198306

44. Kong F, Niu X, Liu M, Wang Q. Bile acids LCA and CDCA inhibited porcine deltacoronavirus replication *in vitro*. *Vet Microbiol* (2021) 257:109097. doi: 10.1016/j.vetmic.2021.109097

45. Zhang JS, Taylor EW, Bennett K, Saad R, Rayman MP. Association between regional selenium status and reported outcome of COVID-19 cases in China. *Am J Clin Nutr* (2020) 111:1297–9. doi: 10.1093/ajcn/nqaa095

46. Moghaddam A, Heller RA, Sun Q, Seelig JL, Schomburg L. Selenium deficiency is associated with mortality risk from COVID-19. *Nutrients* (2020) 12:2098. doi: 10.3390/nu12072098

47. Moya M, Bautista EG, Velazquez-Gonzalez A, Vazquez-Gutierrez F, Tzintzun G, Garcia-Arreola ME, et al. Potentially-toxic and essential elements profile of AH1N1 patients in Mexico city. *Sci Rep* (2013) 3:1284. doi: 10.1038/srep01284

48. Cirelli A, Ciardi M, Simone CD, Sorice F, Giordano R, Ciaralli L, et al. Serum selenium concentration and disease progress in patients with HIV infection. *Clin Biochem* (1991) 24:211–4. doi: 10.1016/0009-9120(91)90601-a

49. Sartori G, Jardim NS, Marcondes Sari MH, Dobrachinski F, Pesarico AP, Rodrigues LC, et al. Antiviral action of diphenyl diselenide on herpes simplex virus 2 infection in female BALB/c mice. *J Cell Biochem* (2016) 117:1638–48. doi: 10.1002/jcb.25457

50. Cheng Z, Zhi X, Sun G, Guo W, Huang Y, Sun W, et al. Sodium selenite suppresses hepatitis b virus transcription and replication in human hepatoma cell lines. *J Med Virol* (2016) 88:653–63. doi: 10.1002/jmv.24366

51. Mukherjee S, Weiner WS, Schroeder CE, Simpson DS, Hanson AM, Sweeney NL, et al. Ebselen inhibits hepatitis c virus NS3 helicase binding to nucleic acid and prevents viral replication. *ACS Chem Biol* (2014) 9:2393–403. doi: 10.1021/cb500512z

52. Pietka-Ottlik M, Potaczek P, Piasecki E, Mlochowski J. Crucial role of selenium in the virucidal activity of benzisoselenazol-3(2H)-ones and related diselenides. *Molecules* (2010) 15:8214–28. doi: 10.3390/molecules15118214

53. Jian SW, Mei CE, Liang YN, Li D, Cai TY. Influence of selenium-rich rice on transformation of umbilical blood b lymphocytes by Epstein-Barr virus and Epstein-Barr virus early antigen expression. *Ai Zheng* (2003) 22:26–9.

54. Misu H, Takamura T, Takayama H, Hayashi H, Matsuzawa-Nagata N, Seiichiro K, et al. A liver-derived secretory protein, selenoprotein p, causes insulin resistance. *Cell Metab* (2010) 12:483–95. doi: 10.1016/j.cmet.2010.09.015

55. Becker DJ, Reul B, Ozcelikay AT, Bucher JP, Henquin J-C, Brichard SM. Oral selenate improves glucose homeostasis and partly reverses abnormal expression of liver glycolytic and gluconeogenic enzymes in diabetic rats. *Diabetologia* (1996) 39:3–11. doi: 10.1007/BF00400407

56. Szablewski L. Expression of glucose transporters in cancers. *Biochim Biophys Acta* (2013) 1835:164–9. doi: 10.1016/j.bbcan.2012.12.004

57. Wang Y, Zhu X, Jiang XM, Guo J, Fu Z, Zhou Z, et al. Decreased inhibition of exosomal miRNAs on SARS-CoV-2 replication underlies poor outcomes in elderly people and diabetic patients. *Signal Transduct Target Ther* (2021) 6:300. doi: 10.1038/s41392-021-00716-y

58. Singh M, Chazal M, Quarato P, Bourdon L, Malabat C, Vallet T, et al. A virus-encoded microRNA contributes to evade innate immune response during SARS-CoV-2 infection. *bioRxiv* (2021) 9:459577. doi: 10.1101/2021.09.09.459577

59. Lian H, Zhang J, Guo X. MiR-125b-5p suppressed the glycolysis of laryngeal squamous cell carcinoma by down-regulating hexokinase-2. *BioMed Pharmacother* (2018) 103:1194–201. doi: 10.1016/j.biopha.2018.04.098

60. Liu S, Chen Q, Wang Y. MiR-125b-5p suppresses the bladder cancer progression *via* targeting HK2 and suppressing PI3K/AKT pathway. *Hum Cell* (2020) 33:185–94. doi: 10.1007/s13577-019-00285-x

61. Shi HJ, Li KJ, Feng JX, Liu GJ, Zhang XL. LncRNA-DANCR interferes with miR-125b-5p/HK2 axis to desensitize colon cancer cells to cisplatin vis activating anaerobic glycolysis. *Front Oncol* (2020) 10:1034. doi: 10.3389/fonc.2020.01034

62. Harms D, Choi M, Allers K, Wang B, Bock CT. Specific circulating microRNAs during hepatitis e infection can serve as indicator for chronic hepatitis e. *Sci Rep* (2020) 10:5337. doi: 10.1038/s41598-020-62159-9

63. Tao YC, Wang ML, Wang M, Ma YJ, Bai L, Feng P, et al. Quantification of circulating miR-125b-5p predicts survival in chronic hepatitis b patients with acute-on-chronic liver failure. *Dig Liver Dis* (2019) 51:412–8. doi: 10.1016/j.dld.2018.08.030

64. Shwetha S, Sharma G, Raheja H, Goel A, Aggarwal R, Das S. Interaction of miR-125b-5p with human antigen r mRNA: Mechanism of controlling HCV replication. *Virus Res* (2018) 258:1–8. doi: 10.1016/j.virusres.2018.09.006

65. Ninomiya M, Kondo Y, Kimura O, Funayama R, Nagashima T, Kogure T, et al. The expression of miR-125b-5p is increased in the serum of patients with chronic hepatitis b infection and inhibits the detection of hepatitis b virus surface antigen. *J Viral Hepat* (2016) 23:330–9. doi: 10.1111/jvh.12522

66. Deng WX, Zhang XY, Ma ZY, Lin Y, Lu MJ. MicroRNA-125b-5p mediates post-transcriptional regulation of hepatitis b virus replication *via* the LIN28B/let-7 axis. *RNA Biol* (2017) 14:1389–98. doi: 10.1080/15476286.2017.1293770

67. Doglioni C, Ravaglia C, Chilosi M, Rossi G. Covid-19 interstitial pneumonia: Histological and immunohistochemical features on cryobiopsies. *Respiration* (2021) 100:488–98. doi: 10.1159/000514822

68. Meliambro K, Li X, Salem F, Yi Z, Campbell KN. Molecular analysis of the kidney from a patient with COVID-19-Associated collapsing glomerulopathy. *Kidney Med* (2021) 3:653–8. doi: 10.1016/j.xkme.2021.02.012

69. Yoshida T, Hanada T, Tokuhisa T, Kosai KI, Sata M, Kohara M, et al. Activation of STAT3 by the hepatitis c virus core protein leads to cellular transformation. *J Exp Med* (2002) 196:641–53. doi: 10.1084/jem.20012127

70. Gong G, Waris G, Tanveer R, Siddiqui A. Human hepatitis c virus NS5A protein alters intracellular calcium levels, induces oxidative stress, and activates STAT-3 and NF-kappa b. *Proc Natl Acad Sci USA* (2001) 98:9599–604. doi: 10.1073/pnas.171311298

71. Lepiller Q, Abbas W, Kumar A, Tripathy MK, Herbein G. HCMV activates the IL-6-JAK-STAT3 axis in HepG2 cells and primary human hepatocytes. *PLoS One* (2013) 8:e59591. doi: 10.1371/journal.pone.0059591

72. Slinger E, Maussang D, Schreiber A, Siderius M, Rahbar A, Fraile-Ramos A, et al. HCMV-encoded chemokine receptor US28 mediates proliferative signaling through the IL-6-STAT3 axis. *Sci Signal* (2010) 3:ra58. doi: 10.1126/scisignal.2001180

frontiers | Frontiers in Immunology

TYPE Original Research
PUBLISHED 27 September 2022
DOI 10.3389/fimmu.2022.1007186

OPEN ACCESS

EDITED BY
Mengyao Guo,
Northeast Agricultural University, China

REVIEWED BY
Ranran Hou,
Qingdao Agricultural University, China
Xiaona Zhao,
Shandong Agricultural University, China

*CORRESPONDENCE
Yi Wu
wuyi2001cn@163.com;
wuyi2001cn@njau.edu.cn

†These authors have contributed equally to this work

SPECIALTY SECTION
This article was submitted to Nutritional Immunology, a section of the journal Frontiers in Immunology

RECEIVED 30 July 2022
ACCEPTED 29 August 2022
PUBLISHED 27 September 2022

CITATION
Wu Y, Zhou H, Wei K, Zhang T, Che Y, Nguyễn AD, Pandita S, Wan X, Cui X, Zhou B, Li C, Hao P, Lei H, Wang L, Yang X, Liang Y, Liu J and Wu Y (2022) Structure of a new glycyrrhiza polysaccharide and its immunomodulatory activity. *Front. Immunol.* 13:1007186. doi: 10.3389/fimmu.2022.1007186

Structure of a new glycyrrhiza polysaccharide and its immunomodulatory activity

Yu Wu[1,2†], Hui Zhou[1,2†], Kunhua Wei[3†], Tao Zhang[4], Yanyun Che[5], Audrey D. Nguyễn[6], Sakshi Pandita[6], Xin Wan[1,2], Xuejie Cui[1], Bingxue Zhou[1], Caiyue Li[1,2], Ping Hao[1,2], Hongjun Lei[1,2], Lin Wang[7], Xiaonan Yang[3], Ying Liang[3], Jiaguo Liu[1,2] and Yi Wu[1,2*]

[1]Ministry of Education (MOE) Joint International Research Laboratory of Animal Health and Food Safety, College of Veterinary Medicine, Nanjing Agricultural University, Nanjing, China, [2]Institute of Traditional Chinese Veterinary Medicine, College of Veterinary Medicine, Nanjing Agricultural University, Nanjing, China, [3]Guangxi Key Laboratory of Medicinal Resources Protection and Genetic Improvement/Guangxi Engineering Research Center of Traditional Chinese Medicine (TCM) Resource Intelligent Creation, Guangxi Botanical Garden of Medicinal Plant, Nan Ning, China, [4]Beijing Key Laboratory of Traditional Chinese Veterinary Medicine, Beijing University of Agriculture, Beijing, China, [5]Engineering Laboratory for National Healthcare Theories and Products of Yunnan Province, College of Pharmaceutical Science, Yunnan University of Chinese Medicine, Kunming, China, [6]Department of Biochemistry and Molecular Medicine, Davis Medical Center, University of California, Davis Medical, Sacramento, CA, United States, [7]Animal Science and Veterinary College, Jiangsu Vocational College of Agricultural and Forestry, Zhenjiang, China

A component of licorice polysaccharide (GPS-1) was extracted from licorice, its primary structure was identified and characterized for the first time, and its immunomodulatory activity was studied. Crude licorice polysaccharide was isolated and purified by DEAE sepharose FF ion-exchange column chromatography and Chromdex 200 PG gel filtration column chromatography to obtain a purified Glycyrrhiza polysaccharide named GPS-1. NMR and methylation analysis revealed that GPS-1 is composed of homogalacturonan (HG)-type pectin with 4)-D-GalpA-(1 as the backbone. This study of GPS-1 also examined its significant role in regulating immune activity *in vitro* and *in vivo*. As a result, GPS-1 promoted the secretion of IFN-γ and IL-4 in mice and increased the proportion of $CD3^+CD4^+$ and $CD3^+CD8^+$ T lymphocytes in their spleens. Dendritic cells (DCs) treated with GPS-1 showed promotion of DC maturation, antigen presentation, and phagocytic capacity. The results suggest that GPS-1 is a potential immunomodulator that stimulates the immune system by regulating multiple signaling pathways. Combined with our characterization of the primary structure of GPS-1, the present investigation provides the basis for future study of the form-function relationship of polysaccharides.

KEYWORDS

glycyrrhiza polysaccharide, structural characterization, immunomodulatory activity, dendritic cells, toll-like receptor

1 Introduction

Licorice is not only a widely used food but also traditional Chinese medicine (1). The use of licorice has been recorded in Europe as early as 2100 BC and is now a well-known natural food sweetener (2). Licorice's medicinal benefits are now recorded in the pharmacopeias of China, South Korea, and Japan (3). Studies of active ingredients in licorice have found that polysaccharides are important components (4, 5) and that one of the main functions of licorice polysaccharides is to improve immunity (4, 6, 7). Another investigation found that licorice polysaccharides could dose-dependently counteract cyclophosphamide-induced immunosuppression in mice (8). Researchers have also demonstrated a positive correlation between the immune activity of polysaccharides and their uronic acid content (9). Our previous study also confirmed that glycyrrhiza polysaccharides can prolong the efficacy and duration of the Newcastle disease virus (NDV) vaccine (10) and improve the intestinal immune function and microbial composition of roosters (4). In addition, the glycyrrhiza polysaccharide (GiP-B1) can cause significant phenotypic changes in dendritic cells (DCs) and the improvement of bioactive functions with a mechanism of action related to the TLRs/NF-B signaling pathway (11). In the present study, the purified glycan GPS-1 was isolated from licorice (*Glycyrrhiza uralensis*), then its structure was identified using methylation and NMR analysis. The immunomodulatory mechanisms and pathways of GPS-1 were also explored *in vivo* with mice and *in vitro* with dendritic cells.

2 Materials and methods

2.1 Separation and purification of glycyrrhiza polysaccharides

Using our previously reported methods (10), crude Glycyrrhiza polysaccharide (GPS) was extracted by boiling water from licorice (*Glycyrrhiza uralensis*) and then precipitated with 50% ethanol into GPS_{50} extract (12). Proteins were removed five times, sequentially, using the Sevag method. The final freeze-dried samples were stored at -20°C. Next, 30 g of decorin GPS_{50} was weighed, dissolved with 30 mL distilled water (dH_2O), and centrifuged at 8000 rpm for 10 min. Then, the precipitate was removed and filtered with a 0.45 μm microporous membrane. The filtrate was then run through a balanced ion-exchange chromatography column and eluted according to different salt concentrations (0.0 M NaCl, 0.2 M NaCl, 0.5 M NaCl, and 1.0 M NaCl) at a speed of 5.0 mL/min. At the same time, the eluents were collected (10 mL/tube) for 100 tubes, and then analyzed using the reported method (12). The eluents from the same peak (1-50 tubes and 51-100 tubes) were collected, combined, and concentrated, respectively, and then lyophilized to provide two samples (GPS-E1 and GPS-E2). The two samples were subjected to Chromdex 200 PG gel column and eluted with ultrapure water at a flow rate of 2mL/min. Each eluent was collected (10 mL/tube) and detected by the same method (12). The relevant eluents (170-190 min and 140-170 min) were gathered, combined, concentrated, and freeze-dried in a vacuum to give purified polysaccharide GPS-1 and GPS-2 (Refer to Figure 1D).

2.2 Characterization of the GPS-1 study

Due to the low sample yield of GPS-2 after purification, GPS-1 was studied in subsequent tests.

2.2.1 Molecular weight of GPS-1

Purified GPS-1 polysaccharide was mixed with 0.05 M NaCl to prepare a 5 mg/mL test solution, then filtered using a 0.22 μm membrane. Tests of the molecular weight of GPS-1 were performed using high-performance gel permeation chromatography (HPGPC, Agilent 1100 series HPLC, Agilent Technologies, Santa Clara, CA, USA). The fractions were isolated by OHpak SB-803 HQ column at a flow speed of 1 mL/min and detected by an Agilent G1362A Refractive Index Detector at room temperature. The purchased dextran standards with a series of molecular weights (1000, 5000, 12000, 25000, 50000, 80000, 150000, 270000, 410000, 670000 Da, Sigma-Aldrich, Merck, Germany) were used to plot the calibration curve. The molecular weight of GPS-1 was calculated according to the standard linear regression equation.

2.2.2 Monosaccharide composition of GPS-1

The monosaccharide composition of GPS-1 was analyzed by the reported method in the reference with a few modifications (13). The GPS-1 polysaccharide sample (5 ± 0.05 mg) was weighed, added into a reaction flask, and hydrolyzed with trifluoroacetic acid (TFA, 2mL of 1M) at 121 °C for 4h. After removing the remaining acid by flushing with N_2, the reaction products were evaporated to dryness under reduced pressure. The residue was dissolved by methanol (2 mL) and dried by flushing N_2 three times to remove the TFA completely, and then re-dissolved in fresh distilled water (1 mL). The solution (5 μL) was analyzed by high-performance anion-exchange chromatography (HPAEC) on a CarboPac PA-20 anion-exchange column (3 by 150 mm; Dionex) using a pulsed amperometric detector (PAD; Dionex ICS 5000 system). The isolation conditions are as follows: flow rate, 0.5 mL/min; injection volume, 5μL; solvent system, B: (0.1M NaOH, 0.2M NaAc); gradient program, 95:5 V/V at 0 min, 80:20 V/V at 30 min, 60:40 V/V at 30.1 min, 60:40 V/V at 45min, 95:5 V/V at 45.1 min, 95:5 V/V at 60 min. Data were acquired on the ICS5000 (Thermo Scientific) and processed using chameleon

10.3389/fimmu.2022.1007186

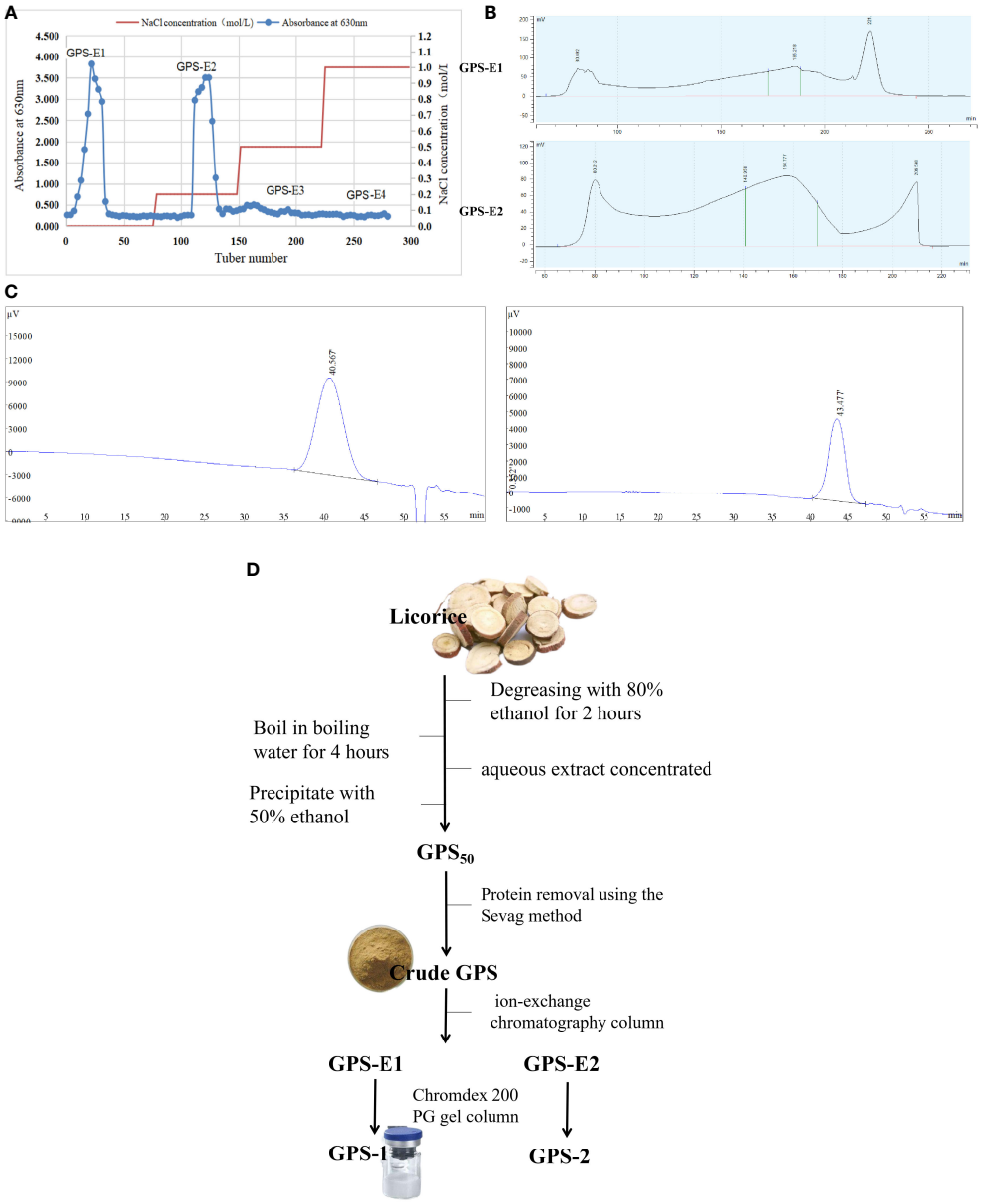

FIGURE 1
(A) Elution profile of GPS50 ion-exchange column chromatography. **(B)** Elution profiles of samples GPS-E1 and GPS-E2 gel filtration column chromatography **(C)** The HPGPC chromatogram of the GPS-1 (left) and GPS-2 (right). **(D)** The specific flow chart of GPS-1 extraction.

7.2 CDS (Thermo Scientific). Quantified data were output into excel format.

And the monosaccharide composition of GPS-1 was analyzed according to the literature-reported method (13). Chromatographic data were processed using Chromeleon™ chromatography data system software. In the standard sample ion chromatogram and the sample ion chromatogram, the abscissa is the detection retention time (Time, in minutes), and the ordinate is the response value of the ion detection (Response, in nC).

The content of each component in the sample (μg/mg) = C * V * F/M, where C is the instrument read concentration in μg/mL, V is the sample extract volume in mL, F is the dilution factor, and M is the total sample volume in mg.

2.2.3 Methylation analysis of GPS-1

Next, 10 mg of dried GPS-1 and 20 mg of dried NaOH were dissolved in 2000 μL DMSO to give a mixture. The mixture was kept at 25 °C for 10 h, and then reacted with an equal volume of methyl

iodide for 3 h. This methylation reaction was repeated for five times. After the reaction, the mixture was extracted with an equal volume of $CHCl_3$ five times, and the $CHCl_3$ extract solvent was combined and evaporated to dryness to provide a residue. The residue was hydrolyzed with 1 mL of TFA (2 M) at 120 °C for 2 h and then evaporated under vacuum to dryness. The sample was treated with $NaBH_4$ (60 mg) for 8h at room temperature and then neutralized with acetic acid (0.1 M). Afterward, the residue was dried at 101 °C and the product was dissolved in $CHCl_3$ and detected by an Agilent 7890A-5977B GC-MS instrument (Agilent Technologies Inc. CA, USA) equipped with an RXI-5 SIL MS column (30 m × 0.25 mm × 0.25 μm). The oven temperature was maintained at 140 °C for 2.0 min at first, and then increased from 140 °C to 230 °C at a speed of 3 °C/min, then maintained at 230 °C for 3 min. The carrier gas was Helium with a purity of 99.999%, and the flow rate was 1.0 mL/min.

2.2.4 Nuclear magnetic resonance (NMR) analysis of GPS-1

The lyophilized sample (30 mg) was dissolved in 0.5 mL of D_2O standard. A Bruker Ascend 600 spectrometer (Bruker, Stockholm, Sweden) at 600 MHz was used to determine the one-dimensional nuclear magnetic (^{1}H-NMR, ^{13}C-NMR, and ^{13}C-DEPT-135) and two-dimensional NMR [^{1}H-^{1}H COSY (correlated spectroscopy), TOCSY (total correlation spectroscopy), HSQC (heteronuclear single quantum coherence), HMBC (heteronuclear multiple bond correlation), and NOESY (nuclear Overhauser effect spectroscopy)] of GPS-1. Tetramethylsilane was used as an internal standard.

2.3 *In vivo* immunomodulatory activity study of GPS-1

2.3.1 Grouping and treatment of mice

A total of 20 male ICR mice were purchased from the Comparative Medicine Center of Yangzhou University (License Number: SCXK (Su) 2017-007) at 5 weeks of age. They were randomly divided into 4 groups, each with 5 mice. The control group was given only a regular diet, while the treatment groups received a regular diet plus oral GPS-1 at a low (GPS-L), medium (GPS-M), or high-dose (GPS-H). These groups received 300, 450, and 600 mg/kg/d, respectively, for 14 consecutive days. All mice were housed at the Animal Care Center of Nanjing Agricultural University under the guidelines of the Institutional Animal Care and Use Committee Institutional Animal Care and Use Committee (IACUC), as detailed in the IACUC-approved protocol (No.: 2020BAD25D34).

2.3.2 Determination of the cytokines in the serum

On day 14, all 5 mice in each group were sacrificed, and blood serum was sampled. The IFN-γ and IL-10 averages in each group were determined according to ELISA kit instructions (Wuhan Feen Biotechnology Co., LTD, product code: EM0093;EM0100).

2.3.3 Histological analysis

Each of these 5 mice per group also had their thymus, spleen, and small intestines collected on day 14 and preserved in 4% formaldehyde (Beijing Solarbio Biological Technology Co., LTD). These tissues were fixed, dewaxed, stained, mounted and mounted for H&E histological analysis.

2.3.4 Mouse spleen lymphocyte typing

After spleens were collected on day 14 (n = 5 per group), primary spleen lymphocytes were extracted according to literature reports (4, 10). The stained cells were incubated with lipopolysaccharides (LPS, from Sigma) and CD3-FITC, CD4-PC, and CD8-APC (eBioscience™, AB_2536505) for 24 h, then measured using a flow cytometer (BD Biosciences AccuriC6, USA).

2.4 *In vitro* modulation of DCs immune activity by GPS-1

2.4.1 Preparation of mouse bone marrow-derived dendritic cells

Male Balb/c mice were purchased from the Comparative Medicine Center of Yangzhou University (License No.: SCXK (Su) 2017-007) at 5 weeks of age. The tibia and femur of each hindlimb were removed and the bone marrow cavity was flushed using sterile PBS to obtain bone marrow multifunctional stem cell irrigation fluid. The precursor dendritic cells (DCs) were isolated according to the relevant methods reported in prior literature (14, 15). First, the irrigation fluid was centrifuged (1200rpm, 5min) to obtain cell pellets, and after re-suspension, bone marrow multifunctional stem cell were obtained by using mouse monocyte separation solution (Beijing Solarbio Biological Technology Co., LTD).These cells were then cultured in DMEM media (Gibco,USA) with 1% penicillin/streptomycin (Gibco, USA), 10% FBS (Gibco,USA), 1% Mouse-derived IL-4 stimulating factor (Gibco,USA,Cat#214-14),and 1% mouse-derived Colony-stimulating factor (acting on macrophages) GM-CSF stimulating factor (Gibco,USA, Cat#815-03) for 7 days at 37 °C and 5% CO_2 in a cell incubator. Immature DCs can be obtained after 7 days of induced differentiation and culture.

2.4.2 Determination of the safe concentration of GPS-1

Immature DCs were grown in 96-well plates to a confluence of 4.8 × 10^5 cells per mL and treated with GPS-1 at different concentrations (2000, 1000, 500, 250, 125, 62.5, 31.25, 15.625,

and 7.814 μg/mL), plus a blank control containing DCs in complete media. N = 6 wells per group, incubated at 37 °C and 5% CO_2 in a cell incubator for 36 hours. Absorption values were determined using the MTT method. Cell survival was calculated using the equation below, where OD is the optical density:

Cell viability (%) = OD in the drug group/OD of 100% in the blank group.

2.4.3 Determination of cytokines in dendritic cells

GPS-1 doses of 500, 250, and 125 μg/mL were added to 1 × 10^3 DCs per well in 96-well plates and incubated for 36 hours, along with a DC negative control group in complete media, and positive control of DCs treated with LPS. N = 4 for all groups. Cell culture supernatants were collected, and their IFN-γ, TNF-α, IL-1β, and IL-10 (Wuhan Feen Biotechnology Co., LTD, product code: EM0093; EM0183; EM0109; EM0100)contents were determined by ELISA.

2.4.4 Determination of the phagocytic capacity of dendritic cells

Dendritic cells were incubated in 96-well plates at 37°C and 5% CO_2 for 8 hours with either GPS-1 (500, 250, or 125 μg/mL), or complete media (Control), with n =4 for all groups. 20 μL of florescent-labeled ovalbumin antigen (OVA-FITC) was added to each well to mimic natural antigen phagocytosis by DCs. After 8 hours of incubation, cells were centrifuged at 1000 rpm/min for 10 min. Excess antigen was washed off with 1 ml PBS before cells were sorted by flow cytometry to determine the proportion of viable DCs. The optimal concentration of GPS-1 to stimulate DC antigen phagocytosis was determined to be 500 μg/mL.

Cells from the 500 μg/mL GPS-1 and blank (Control) groups were added to confocal dishes. The same OVA-FITC treatment described above was used to simulate antigen phagocytosis again. Nuclei were labeled with 5 μL of DAPI dye solution and incubated at 4°C for 10 min. Afterward, excess DAPI dye solution was rinsed twice with 1 ml PBS. Finally, a confocal laser microscope was used to compare the changes in antigen intake between the 500 μg/mL GPS-1 group and the control.

2.4.5 Determining the presentation ability of the dendritic cells

24-well plates were used to incubate 1 × 10^4 DCs/mL, 2 ml of cells in complete media per well (n = 4). Different concentrations of GPS-1 were added to achieve final concentrations of 500, 250, and 125 μg/mL, except for a blank (Control) group without GPS-1. All groups were incubated for 36 hours at 37 °C and 5% CO_2. 15 × 10^4 DCs per well were seeded in a 6-well plate and treated with 3 μl per well of 3 mouse antibodies (1 μl of each): anti-CD11c-PE-Cyanine5, anti-CD86-PE, and anti-CD80-FITC were incubated at 4°C for 30 min. The excess antibodies were subsequently washed off the DCs twice with 1 ml PBS. Then, flow cytometry was used to determine the expression levels of CD80 and CD86 costimulators on the surface of DCs from each group.

2.5 Dendritic cell active pathway mechanisms targeted by GPS-1

DCs were treated with 500 μg/mL of GPS-1 for 36 hours alongside a negative control group without GPS-1. DCs' total RNA was extracted by TRizol, followed by RNA quality detection using a NanoDrop spectrophotometer and an Agilent 2100 bioanalyzer. Fragments Count for each gene in each sample was counted by HTSeq (v 0.5.4 p3) software, and FPKM (Fragments Per Kilobase Per Million Mapped Fragments) was then calculated to estimate the expression level of genes in each sample. For analysis of DEGs, DESeq/DESeq2 was employed to detect the differential expression between the two groups using a model based on the negative binomial distribution. The P value was assigned to each gene and adjusted as q value by the Benjamini and Hochberg method for controlling the false discovery rate (FDR). Genes with q < 0.05 were defined as DEGs.The GO (Gene Ontology, http://geneontology.org) enrichment of DEGs was conducted by the hypergeometric test, in which P value was calculated and adjusted as q value. GO terms with q < 0.05 were considered to be significantly enriched. For pathway enrichment analysis, all DEGs were assigned to terms in KEGG (Kyoto Encyclopedia of Genes and Genomes, http://www.kegg.jp) database and searched for significantly enriched KEGG terms with the same analytic approach.

2.6 Statistical analysis

All results are expressed as the mean ± standard deviation, graphed using GraphPad Prism 6.0 software and SPSS 18.0 software for ANOVA multiple comparisons. P< 0.05 is considered statistically significant in this analysis.

3 Results

3.1 Separation and purification of licorice polysaccharide

The elution curves displayed in Figure 1 were obtained by gradient elution of GPS_{50} through an ion-exchange

chromatography column. The order of samples collected was: GPS-E1 (deionized water elution), GPS-E2 (0.2M NaCl elution), GPS-E3 (0.5M NaCl elution), and GPS-E4 (1.0M NaCl elution). The total sugar content of each was then determined by the anthrone-sulfuric acid method. As shown in Figure 1A, the peaks eluted with deionized water and 0.2M NaCl solution from the Ion-exchange column were selected for purification by Chromdex 200 PG gel column chromatography. As depicted in Figure 1B, the eluates of GPS-E1 between 210 and 230 min, and those of GPS-E2 between 140-170 min were collected and named GPS-2 and GPS-1, respectively. As the result, the total yield of GPS-1 and GPS-2 were 0.78% and 0.07%, and their sugar content was 98.95% and 97.03%, respectively.

Two single symmetrical and narrow peaks were exhibited in the HPGPC spectrum in Figure 1C, which indicated that GPS-1 and GPS-2 were homogeneous. The weight-average molecular weight (M_w) of GPS-1 and GPS-2 were 26.4 kDa and 8.9 kDa, and the number average molecular weight (M_n) of GPS-1 and GPS-2 were 18.0 kDa and 6.4 kDa, respectively. Additionally, the M_w/M_n value of GPS-1 and GPS-2 were 1.47 and 1.35, respectively. However, because of the poor weight of GPS-2 (less than 5 mg), further investigation was processed only on the structure and biological activities of GPS-1.

Comparison of peak heights and the presence or absence of peaks between the standard monosaccharide chromatogram and the monosaccharide chromatogram of the GPS-1 sample (Figure 1C led to the conclusion that GPS-1 is composed of 74.39% galacturonic acid, 10.12% arabinose, 6.36% rhamnose, 4.85% galactose, 1.52% mannuronic acid, 1.34% glucose, 0.92%, fucose, and 0.51% xylose. Roughly two-thirds of the monomers that make up GPS-1 are galacturonic acid. Arabinose, the second most prevalent, accounts for only 10.12%. See Table 1 for a complete summary of GPS-1 monosaccharides, including the concentrations calculated using peak areas.

3.2 Structure of GPS-1

3.2.1 GPS-1 methylation analysis

According to the results of complete acid hydrolysis methylation analysis, the sequence of sugar residues in GPS-1 is mainly 4-Gal(p)-UA, and the multiple ends are t-Rha(p), t-Ara(f), t -Fuc(p), t-Xyl(p), t-Gal(p), and t-Gal(p)-UA. The analysis indicates that GPS-1 is composed of multiple branched chains, with a complex secondary structure illustrated in Table 2.

3.2.2 GPS-1 one-dimensional NMR analysis

One-dimensional hydrogen nuclear magnetic resonance spectroscopy (^{1}H-NMR) (Figure 2A), and carbon spectroscopy (^{13}C-NMR) (Figure 2B), were used to further identify the glycosidic bond configuration of GPS-1 samples. In the ^{1}H-NMR spectrum (the peals at 5.18, 5.04, 4.96, 4.95, 4.80, and 4.47 ppm were assigned to H-1 of R_α, A_t, A, $A_{1,5}$, B and R_β residues. Peaks between 3.36 and 5.02 ppm belong to sugar ring protons. In the ^{13}C DEPT 135 spectrum (Figure 2C, negative peaks at 62.43 ppm were assigned to the A_t-C5. The main anomeric carbon peaks in the ^{13}C NMR spectrum observed at 108.90, 108.47, 101.55, 100.43, 97.65 and 93.69 ppm were corresponding to C-1 of $A_{1,5}$, A_t, B, A, R_β, and R_α sugar residues, signals at 176.94, 176.49 (× 2) and 172.20 ppm were attributed to the carbonyls of A, R_β/R_α and B galacturonic residues, peaks at 75.69 (× 2), 72.83, 72.12, 68.17 and 62.68 ppm belonged to the C-5 of R_β/R_α, A, B, $A_{1,5}$ and A_t, while other signals between 60 and 90 ppm were attributed to C-2, C-3 and C-4 of the sugar rings. These data confirmed the existence of Arabinosyl and galacturonic residues of GPS-1 (16).

3.2.3 GPS-1 2D NMR analysis

According to the monosaccharide composition and methylation analysis results of the polysaccharide samples, the

TABLE 1 Monosaccharide composition and ratio of GPS-1.

Monosaccharide	Mass conversion result (ug/mg)	The percentage of each component (%)
Fuc	2.84	0.92
Ara	31.20	10.12
Rha	19.59	6.36
Gal	14.94	4.85
Glc	4.12	1.34
Xyl	1.56	0.51
Man	None	None
Fru	None	None
Rib	None	None
Gal-UA	229.23	74.39
Gul-UA	None	None
Glc-UA	4.68	1.52
Man-UA	None	None

10.3389/fimmu.2022.1007186

TABLE 2 The sugar residue connection mode of GPS-1.

Connection method	Derivative name	molecular weight (MW)	relative molar ratio (%)
t-Rha(p)	1,5-di-O-acetyl-6-deoxy-2,3,4-tri-O-methyl rhamnitol	293	2.336
t-Ara(f)	1,4-di-O-acetyl-2,3,5-tri-O-methyl arabinitol	279	4.328
t-Fuc(p)	1,5-di-O-acetyl-6-deoxy-2,3,4-tri-O-methyl fucitol	293	1.174
t-Xyl(p)	1,5-di-O-acetyl-2,3,4-tri-O-methyl xylitol	279	0.944
2-Rha(p)	1,2,5-tri-O-acetyl-6-deoxy-3,4-di-O-methyl rhamnitol	321	1.246
3-Rha(p)	1,3,5-tri-O-acetyl-6-deoxy-2,4-di-O-methyl rhamnitol	321	1.123
t-Gal(p)	1,5-di-O-acetyl-2,3,4,6-tetra-O-methyl galactitol	323	4.051
t-Gal(p)-UA	1,5-di-O-acetyl-2,3,4,6-tetra-O-methyl galactitol	323	6.076
5-Ara(f)	1,4,5-tri-O-acetyl-2,3-di-O-methyl arabinitol	307	2.797
4-Ara(p)	1,4,5-tri-O-acetyl-2,3-di-O-methyl Araitol	307	1.352
4-Gal(p)-UA	1,4,5-tri-O-acetyl-2,3,6-tri-O-methyl galactitol	351	61.675
4-Glc(p)	1,4,5-tri-O-acetyl-2,3,6-tri-O-methyl glucitol	351	1.942
4-Glc(p)-UA	1,4,5-tri-O-acetyl-2,3,6-tri-O-methyl glucitol	351	1.942
6-Gal(p)-UA	1,5,6-tri-O-acetyl-2,3,4-tri-O-methyl galactitol	351	4.955
3,4-Glc(p)	1,3,4,5-tetra-O-acetyl-2,6-di-O-methyl glucitol	379	0.679
3,4-Glc(p)-UA	1,3,4,5-tetra-O-acetyl-2,6-di-O-methyl glucitol	379	0.679
2,4-Gal(p)-UA	1,2,4,5-tetra-O-acetyl-3,6-di-O-methyl galactitol	379	1.335
3,6-Gal(p)	1,3,5,6-tetra-O-acetyl-2,4-di-O-methyl galactitol	379	1.367

HSQC (Figure 2D and 1H-1H COSY (Figure 2E) NMR spectra showed that there were multiple signal peaks in the anomeric region, which were significant and could be used for structural analysis. The chemical shifts of the signals in the anomeric region were respectively δ 4.96/100.43 ppm, δ 4.80/101.55 ppm, δ 4.95/108.90 ppm, δ 5.04/108.47 ppm, δ 5.18/93.69 ppm, δ 4.47/97.65 ppm, named as sugar residues A, B, A1,5, At, and the reducing end groups Rα and Rβ. After the assignment of the anomeric signal was determined, through 1H-1H COSY, HSQC, HMBC (Figure 2F), and NOESY (Figure 2G), combined with the 1H-NMR and 13C-NMR spectra (Table 3), as well as the monosaccharide composition and methylation analysis results, the similar sugar residues substituted in the related literature were compared. Chemical shift data (13, 16, 17), the 1H and 13C chemical shift signals of the main types of sugar residues in the polysaccharide samples were assigned, and the results are shown in Table 4.

The connection sequence of each sugar residue can be further inferred by HMBC remote correlation spectrum and NOESY spectrum. As shown in the HMBC correlation spectrum (Figure 2F) and NOESY spectrum (Figure 2G) of the GPS-1, the following coupling signals can be found from the Figure : (1): There is a correlation signal peak (A H-1/A C-4) between H-1 (δ 4.96 ppm) of sugar residue A in HMBC spectrum and C-4 (δ 79.26 ppm) of sugar residue A itself. In the NOESY spectrum, there is a cross peak (A H-1/A H-4) between H-1 (δ 4.96 ppm) of sugar residue An and H-4 (δ 4.29 ppm) of sugar residue An itself. These results indicate that the connection mode of →4)-α-D-GalpA-(1→4)-α-D-GalpA-(1→ exists in GPS-1 (2). There is a cross peak (A H-1/B H-4) between H-1 (δ 4.96 ppm) of sugar residue A and H-4 (δ 4.44ppm) of sugar residue B in NOESY spectrum, which indicates that there is a connection mode of →4)-α-D-GalpA-(1→4)-α-D-GalpA-6-OMe-(1→ (3) There is a cross peak (B H-1/A H-4) between H-1 (δ 4.80ppm) of sugar residue B and H-4 (δ 4.29ppm) of sugar residue An in NOESY spectrum, which indicates that there is a →4)-α-D-GalpA-6-OMe-(1→4)-α-D-GalpA-(1→connection in GPS-1 (4). There is a cross peak (At H-1/A1,5 H-4) between the H-1 (δ 5.04ppm) of the sugar residue At and the H-5a (δ 3.67ppm) of the sugar residue A1,5 in the NOESY spectrum, indicating that there is a α-Lmurf-(1–5)-α-LmurAraf-(1 “) connection in GPS-1.

According to the results of monosaccharide composition, the polysaccharide sample is mainly GalA, and the proportion of GalA is 74.39%. Combined with the results of methylation and nuclear magnetic resonance (18, 19), there are a large number of 1,4-GalpA sugar residues and a small amount of methyl esterified galacturonic acid, which accords with the domain characteristics of homogalactan (HG) pectin (20–22). It is speculated that the main chain of HG pectin is composed of →4)-α-GalpA-(1→. The results of methylation analysis and NMR (23) showed that there were arabinose residues in the polysaccharide samples, indicating that there were a few branched chains in the main chain HG-type pectin, and there were →2,4)-α-D-GalpA-(1→ sugar residues in the methylation results. Due to the low content, the NMR signal was not clear, and the molar ratio of sugar residues →4)-α-GalpA-(1→and” →2,4)-α-D-GalpA-(1→ was 61.675:1.335.

Based on the analysis of monosaccharide composition, methylation results, and one-dimensional and two-dimensional NMR (24, 25), the preliminary structure of GPS-1 polysaccharides is a homogalacturonan (HG) – type with →4)-α-D-GalpA-(1→ as the main chain. Pectin, galacturonic acid has a small amount

10.3389/fimmu.2022.1007186

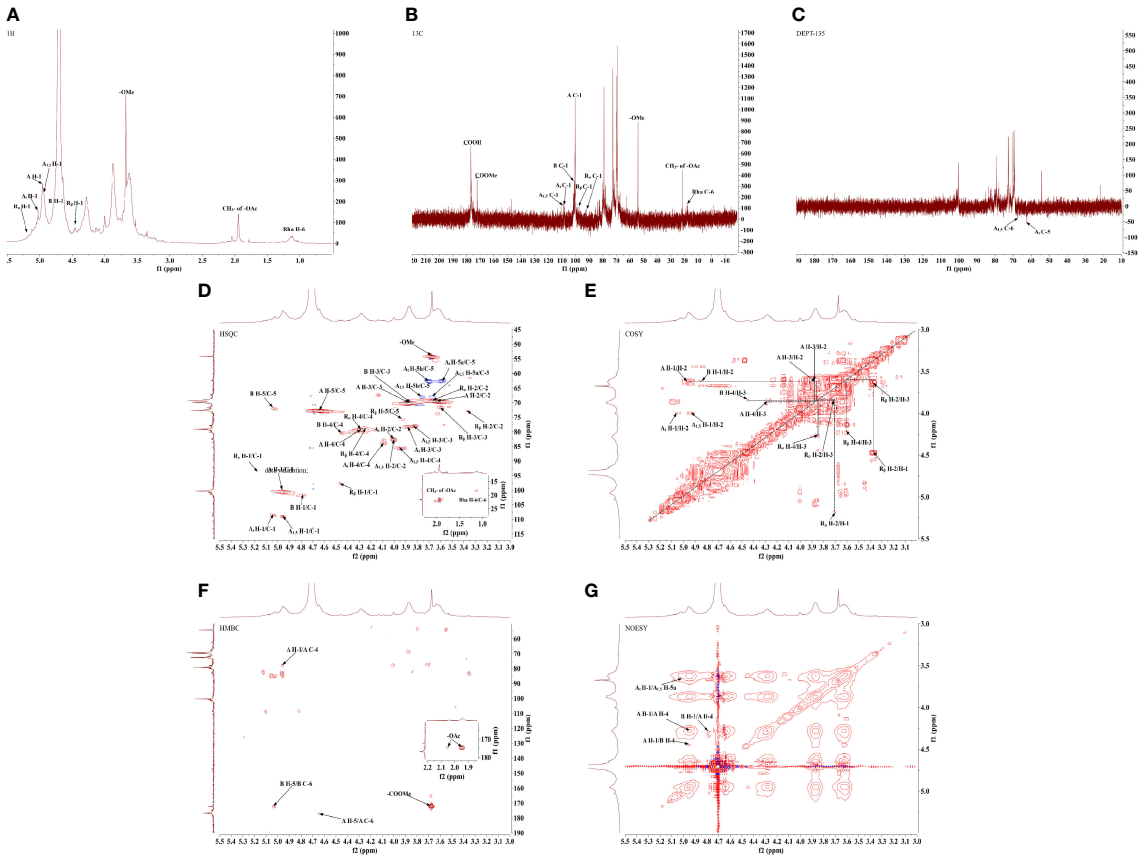

FIGURE 2
GPS-1 one-dimensional nuclear magnetic resonance spectrum **(A)** 1H-NMR. **(B)** 13C-NMR. **(C)**13C-DEPT.GPS-1 2D NMR spectrum **(D)** HSQC. **(E)** 1H-1H COSY. **(F)** HMBC. **(G)** NOESY.

TABLE 3 Assignment of chemical shifts of 1H and 13C of each sugar residue in GPS-1.

sugar residue			chemical shift(ppm)						
			1	2	3	4	5/5a	6/5b	CH_3- of OMe-
A	→4)-α-D-Gal*p*A-(1→	H	4.96	3.62	3.87	4.29	4.64		
		C	100.43	69.66	70.21	79.26	72.83	176.94	
B	→4)-α-D-Gal*p*A-6-OMe-(1→	H	4.80	3.62	3.85	4.44	5.02		3.67
		C	101.55	69.66	70.09	80.24	72.12	172.20	54.40
$\mathbf{A_{1,5}}$	→5)-α-L-Ara*f*-(1→	H	4.95	4.00	3.82	3.95	3.67	3.76	
		C	108.90	82.71	78.05	85.57	68.17		
$\mathbf{A_t}$	α-L-Ara*f*-(1→	H	5.04	4.00	3.88	4.09	3.59	3.71	
		C	108.47	82.71	78.32	83.93	62.68		
R_α	→4)-α-D-Gal*p*A	H	5.18	3.70	3.86	4.26	–		
		C	93.69	69.38	70.09	78.87	–	176.49	
R_β	→4)-β-D-Gal*p*A	H	4.47	3.36	3.60	4.23	3.93		
		C	97.65	72.83	71.73	78.99	75.69	176.49	

10.3389/fimmu.2022.1007186

TABLE 4 Molecular weight results for GPS-1.

RT(min)	lgM_p	lgM_w	lgM_n	M_p	M_w	M_n	M_w/M_n
40.567	4.371	4.422	4.255	23505	26440	17980	1.47

ofmethyl esterification, contains a small amount of O-2 and O-3 acetylated substitutions, linked by →2,4)-α-D-GalpA-(1→ at the O-2 position Side chain, the side chain contains α-L-Araf-(1→ and →5)-α-L-Araf-(1→, and contains →4)-α-D-GalpA and →4)-β-D Two reducing end groups of -GalpA, the possible structural models of which are shown in Figure 3.

3.3 *In vivo* immune-enhancing effect of GPS-1

3.3.1 GPS-1 increases serum cytokine secretion in mice

As shown in Figure 4A, after oral administration of GPS-1 for 14 days, compared with the control group, different concentrations of GPS-1 could significantly increase the levels of IFN-γ and IL-10 in the serum of mice in a dose-dependent manner.

3.3.2 GPS-1 improves the histological manifestations of small intestinal segments and immune organs in mice

As shown in Figure 4B, the intestines of mice in all groups were in a normal state, and the mouse intestinal villi were structurally intact and arranged in an orderly manner, without congestion or hemorrhage. Compared with the blank group (Control), the duodenal villi in each GPS-1 group were more abundant (indicated by red arrows), and the length was slightly increased; the jejunum showed an increase in the number of intestinal villi and a large increase in the number of crypts. (indicated by red arrows); histological analysis of the ileum also showed an increase in the number of crypts and intestinal villi (indicated by red arrows). Overall performance the high concentration of the GPS-1 (GPS-H) group can significantly improve the histological manifestations of the small intestine in mice.

As shown in Figure 4B, the HE sections of the spleen and thymus of the mice in each group were normal, without inflammatory cell infiltration, edema, congestion, and other phenomena. Spleen histology showed that compared with the blank group (Control), the germinal centers (indicated by red arrows) of the spleen in the GPS-M and GPS-H groups were more obvious, increased in number, and darker in color. The thymus results showed that the thymic cortex (indicated by the red arrow) was thickened and dark-stained in the GPS-M and GPS-H groups compared with the blank group (Control).

3.3.3 GPS-1 increased the proportion of CD3 + CD4 + and CD3 + CD8 + T lymphocytes in the mouse spleen

As shown in Figure 4C, three concentrations of GPS-1, low, medium, and high, were effective and significantly increased the ratio of CD3+CD4+ T cells and CD3+CD8+ T cells in the spleen of mice. The proportion of CD3+CD4+ T cells increased from4.09% in the blank control group to 5.13% in the GPS-H group, an increased rate of 25.43%; the proportion of CD3+CD8+ T cells increased from 2.76% in the blank control group to 3.92% in the GPS-H group, the increase rate is 42.03%.

3.4 The immune-enhancing effect of GPS-1 on DCs *in vitro*

3.4.1 The maximum safe concentration of GPS-1 on mouse DCs

The results of the determination of the maximum safe concentration of GPS-1 on mouse DCs are shown in Figure 5A. When the concentration of GPS-1 was in the range of 500 μg/mL~7.814 μg/mL, there was no significant difference between the cell viability of each group and the blank group ($P>0.05$). When the concentration of GPS-1 was greater than or equal to 1000 μg/mL, GPS-1 showed certain toxicity and

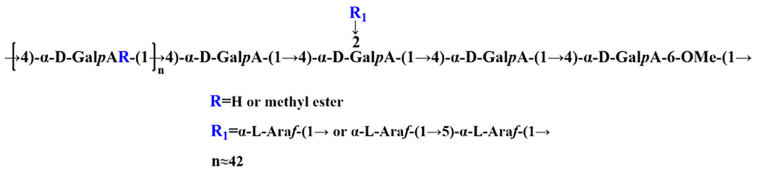

FIGURE 3
The structural model of GPS-1.

10.3389/fimmu.2022.1007186

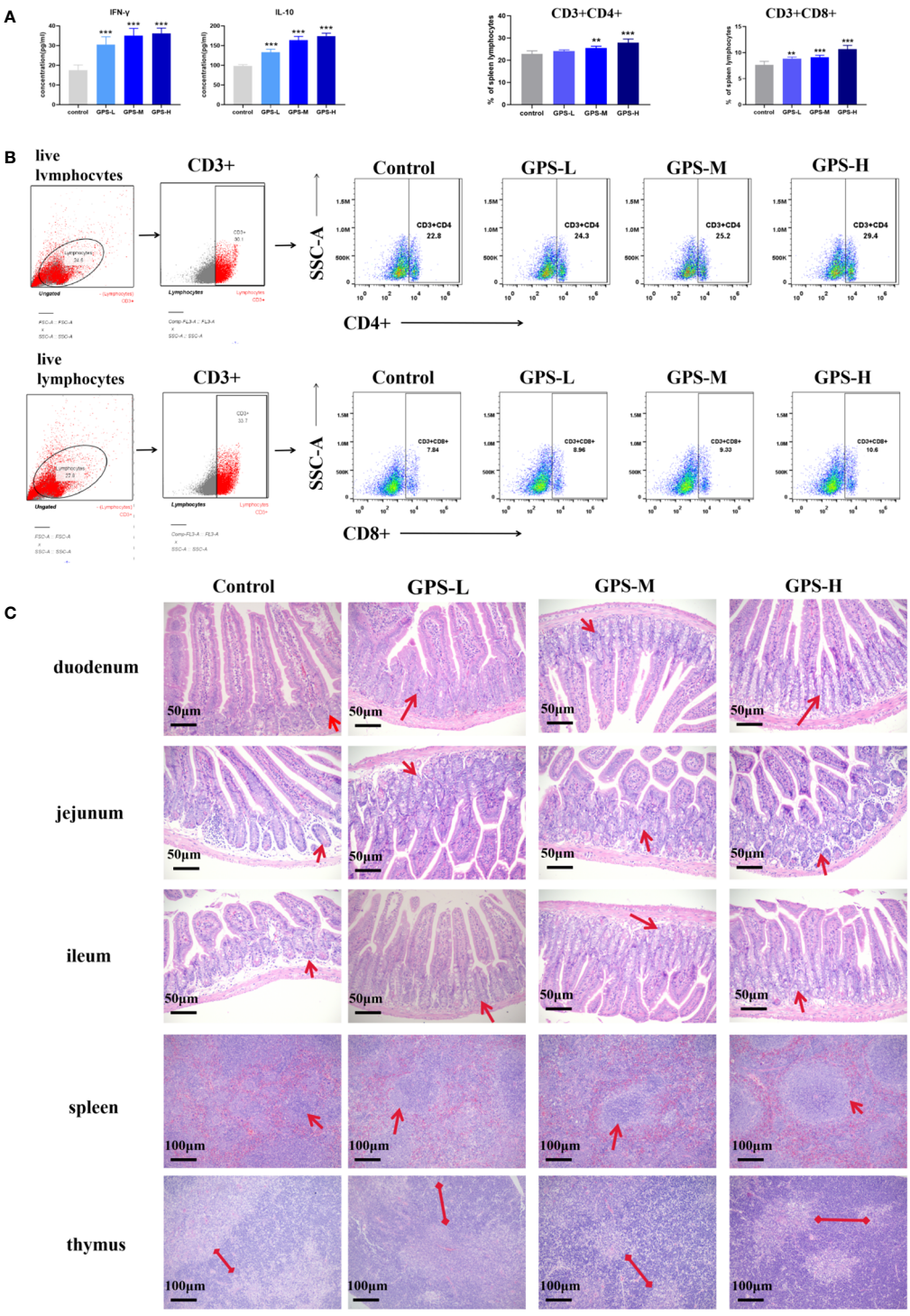

FIGURE 4
(A) Expression levels of IFN-γ and IL-10 in serum of mice in each group after 14 days of administration (n = 5). **(B)** Histological analysis diagram of each small intestinal segment (200×),. and thymus and spleen (100×) at 14 days after drug administration. **(C)** Expression of CD3+CD4+ and CD3+CD8+ T cells in mouse spleen lymphocytes 14 days after administration (n = 5) and representative flow scatter plots of CD3+CD4+ and CD3+CD8+ T lymphocytes.Compared with blank group (Control): **p<0.01, ***p<0.001

10.3389/fimmu.2022.1007186

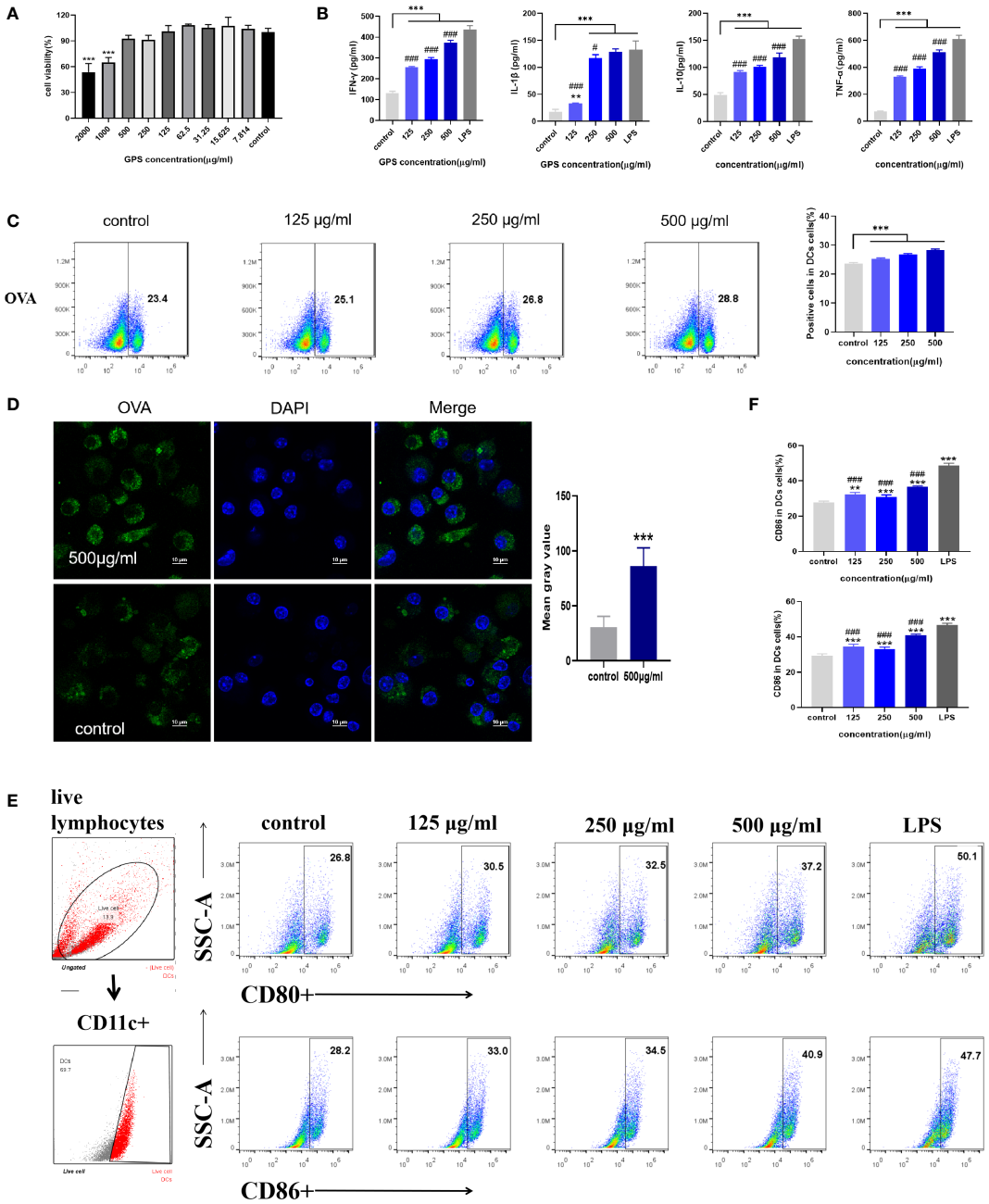

FIGURE 5
(A) The effect of GPS-1 on the activity of mouse DCs (n=6). **(B)** The effect of GPS-1 on cytokine secretion by DCs (n=4). **(C)** Flow cytometry and scatter diagram of GPS-1 enhancing the phagocytosis of DCs. **(D)** Confocal image of GPS-1 enhancing phagocytosis of DCs and statistics of fluorescence intensity. **(E)** GPS-1 increases the expression of CD80 and CD86 on the surface of DCs and the scatter plot. **(F)** GPS-1 increases the expression of CD80 and CD86 on DCs surface flow statistics Compared with blank group (Control): **p<0.01, ***p<0.001; compared with positive control group (LPS): $^{\#}$P<0.05, $^{\#\#\#}$P<0.001

significantly reduced the survival rate of DCs. This shows that GPS-1 has high safety, so we selected three concentrations under the highest safe concentration of 500μg/mL as the test concentration in the follow-up experiments.

3.4.2 GPS-1 increases the secretion levels of IFN-γ, TNF-α, IL-1β, and IL-10 in mouse DCs

The expression levels of IFN-γ, TNF-α, IL-1β, and IL-10 in the cell supernatant were measured by the ELISA kit (Figure 5B),

and the results showed that different concentrations of GPS-1 could dose-dependently increase the IFN-γ, TNF-α, IL-1β, and IL-10 in the cell supernatant, content. However, compared with the positive control group (LPS), there were also significant differences, indicating that GPS-1 could activate the activation of DCs to a certain extent.

3.4.3 The effect of GPS-1 on the phagocytosis of DCs

This experiment shows the effect of GPS-1 on the phagocytic ability of DCs within the same 8 hours of culture by flow cytometry (Figure 5C) and laser confocal image (Figure 5D). The FITC-OVA fluorescence intensity of cells in each GPS-1 treatment group (500 μg/mL, 250 μg/mL, and 125 μg/mL) and the blank group (Control) were counted, and the effect of GPS-1 on the phagocytosis of DCs was calculated by flow cytometry, the results showed that 500 μg/mL, 250 μg/mL and 125 μg/mL GPS-1 could significantly promote the phagocytosis of OVA antigens by DCs. 500 μg/mL GPS-1 was selected, and the phagocytosis of OVA was observed under a confocal microscope. Compared with the blank group (Control), the OVA fluorescence intensity (green) of the 500 μg/mL GPS-1 group was significantly higher than that of the blank group.

3.4.4 The effect of GPS-1 on the antigen-presenting ability of mouse DCs

As shown in Figures 5E, F, compared with the blank group (Control), the expression levels of co-stimulatory factors CD80 and CD86 on the surface of DCs were significantly increased after GPS-1 induction ($P < 0.01$). Therefore, the results indicate that GPS-1 can significantly promote the maturation and activation of DCs and the improvement of antigen presentation ability, and the positive control group (LPS) has a stronger stimulating effect than the GPS-1 group ($P<0.05$).

3.5 Study on the mechanism of GPS-1 regulating DCs activity pathway

3.5.1 Repetitive assessments

Triplicate repeatability assessments (n=3) were performed between samples in each group to eliminate within-group errors as much as possible. As shown in Figure 6A, the gene expression differences between the GPS-1-treated cells and the blank group were obvious, and the differences between the two groups were minimal and statistically significant.

3.6 Screening of differential genes

As shown in Figures 6B, C, differentially expressed genes (DEG) analysis was performed on the transcriptome samples of the GPS-1 group and the blank control group (Control), and it was found that after GPS-1 treatment, there were 574 differences between the two groups of samples genes, of which 316 were up-regulated (red), accounting for 55.05% of all differential genes. 258 down-regulated genes (green), accounting for 44.95% of all differential genes.

3.7 GO classification of differentially expressed genes

As shown in Figure 6D, the functions of differential genes after GPS-1 treatment were mainly enriched in cellular process, single-organism process biological regulation, response to stimulus, metabolic process, and immune system process-related biological processes such as metabolism and immune regulation. (red); cell part, membrane part, organelle, and cell junction-related molecular functions such as secretion and cell junction (green); binding, catalytic activity, molecular transducer function activity, and other related cellular components such as catalysis and transformation (blue) changes.

3.7.1 KEGG annotation of differentially expressed genes

KEGG annotation analysis was performed on the differential genes. The results shown in Figure 6E show that among immune-related pathways, the Toll-like receptors pathway, PI3K-Akt pathway, and Jak-STAT pathway are more highly enriched and more significant.

4 Discussion

Licorice is a traditional plant that is widely used for medicine and food. The analysis of glycyrrhiza components is also quite numerous. Among them, Licorice Polysaccharide, as a macromolecular carbohydrate, has been extensively studied in recent years due to its unique biological activity. Zhang et al. (26) extracted a new neutral polysaccharide AGP from glycyrrhiza residue with a molecular weight of 2.89 × 10 KDa, monosaccharide composition analysis indicated that AGP consisted of l-rhamnose: l-arabinose: d-xylose: d-mannose: d-glucose and d-galactose with a molar ratio of 1:2.33:2.85:0.69:3.05:1.54. AGP was composed of → 6)-β-d-Glcp-(→ backbone and the →4)-α-d-Xylp-(1→, →5)-α-l-Araf-(1→, →3) -α-l-Rhap-(1→, →6)-α-d-Galp-(1→, →3,6)-α-Manp-(1→ and →1)-β-d-Glcp as branche. Pan LC et al. (27) extracted a homogeneous polysaccharide GIBP from Glycyrrhiza Chinensis with a backbone composed of α-D-1,4-linked glucose and branch points composed of α-D-1,3,6 and α-D -1,2,3,6-linked glucose with side chains consisting of α-D-1,3

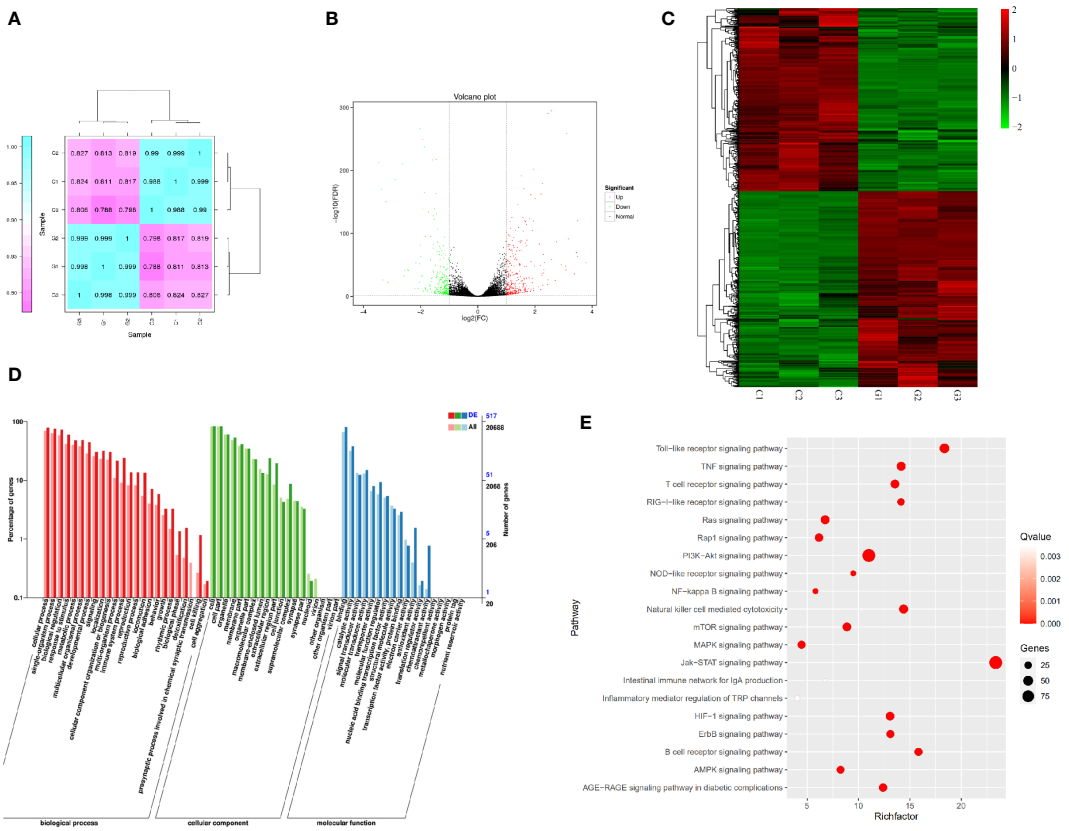

FIGURE 6
(A) Heat map of expression correlation of samples in different groups. **(B)** Differential gene expression volcano map. **(C)** Differential gene expression heat map. **(D)** Statistical chart of GO annotation classification of differentially expressed genes. **(E)** Bubble plot of differentially expressed genes KEGG enrichment.

and β-D-1,6-linked galactose, β-L-1,2-linked arabinose, α- It is composed of D-1,3 and β-D-1,3, and its activity is mainly manifested in antioxidant aspects such as the scavenging ability of DPPH radicals, OH radicals, O radicals and ABTS. Mutaillifu P et al. (28) reported a polysaccharide GPN extracted from Glycyrrhiza glabra with a molecular weight of 38.7 kDa. Monosaccharide composition analysis confirmed the presence of major glucose (98.03%) and trace amounts of mannose, arabinose, and galactose, the main glycosidic bonds in GPN comprised 1,4-linked Glcp, T-linked Glcp, 1,4,6-linked Glcp, and 1,6-linked Glcp. It can be seen from the above that the structure of Glycyrrhiza polysaccharide is complex and diverse, such as the degree of polymerization, the composition and connection sequence of sugar units, branched-chain structure and higher-order structure, etc., which directly affect its biological activity. A large number of studies have shown that Glycyrrhiza polysaccharides have strong pharmacological activities, such as antioxidant (29), immune regulation (30), anti-tumor (31), apoptosis (32), anti-microbial (33), anti-inflammatory (34), and intestinal flora regulation (35). This may be the different biological activities caused by different polysaccharide structures. In this study, the immunomodulatory activity of polyrhamnogalacturonic acid-type pectin-type polysaccharide GPS-1 was evaluated. First of all, in terms of immune regulation, GPS-1 showed an effective immune-enhancing function. And the results showed (Figure 3) that GPS-1 could effectively increase the secretion of mouse cytokines IFN-γ and IL-10 which are secreted by Th1-type cells and Th2-type cells, respectively. Correspondingly, the proportion of CD3+CD4+ (Th2) cells and CD3+CD8+ (Th2) cells in spleen lymphocytes also showed a dose-dependent increase. Intuitively, GPS-1 improve the histological manifestations of intestinal and immune organs. (Figures 4A, D). *In vitro* experiments, GPS-1 can effectively promote DCs to secrete IFN-γ, TNF-α, IL-1β, and IL-10, these cytokines can make quiescent lymphocytes differentiate into functional lymphocytes. At the same time, it promoted the increase of the expression levels of CD80 and CD86 on the surface of DCs.

The expression levels of CD80 and CD86 reflected the maturity of DCs, and mature DCs could play the function of antigen presentation more effectively. Antigen uptake assay showed that GPS-1 could help DCs phagocytose more antigens. To sum up, GPS-1 can help DCs to better exert their immune ability, promote lymphocyte differentiation, and help the body to obtain a higher immune level. Also in this experiment, polysaccharide GPS-1 also showed the immunomodulatory activity and the effect of improving intestinal immunity as reported in the above literature. But its structure is reported for the first time, GPS-1 is a polygalacturonic acid-type pectin, namely HG-type pectin. (Figure 3). Polygalacturonic acid HG is the most abundant pectin polysaccharide in plants. It is reported that some scholars have pointed out that the intake of pectin polysaccharide can be a therapeutic strategy for managing intestinal inflammation. Among them, anti-inflammatory cytokines and intestinal barrier function tend to be regulated by galactan-rich pectic polysaccharides (4). Since GPS-1 is a pectin polysaccharide rich in galacturonic acid, it has a positive effect on improving intestinal immunity, which is consistent with the previous study in our laboratory that GPS-1 can improve the intestinal immunity of laying hens. In laying hens, the addition of glycyrrhiza polysaccharide in the feed can regulate the abundance of intestinal flora and promote the increase of beneficial bacteria (4). It also suggested the effect of this type of polysaccharide on the intestinal barrier and immune function. Provide a scientific basis for the relationship between polysaccharide configuration and biological activity.

Preliminary studies have shown that Glycyrrhiza polysaccharides can affect signal transduction between cells, especially immune cells (6, 36). Glycyrrhiza polysaccharide can significantly promote the maturation and cytokine secretion of human monocyte-derived dendritic cells and mouse bone marrow-derived dendritic cells, which may be through toll-like receptor 4 (TLR4), downstream p38 signaling pathway, amino-terminal Kinase (JNK) and nuclear factor κb (NF-κB) signaling (8). Focusing on the pathways related to the regulation of immune cell function by polysaccharides, it can be found that polysaccharides such as Ganoderma lucidum polysaccharides and Lycium barbarum polysaccharides all further activate the intracellular MAPK and NF-κB signaling pathways by affecting the cellular TLR-2 and TLR-4 pathways (37, 38). In this study, we explored the pathway of GPS-1 affecting DCs through transcriptomics, analyzed the differences in the transcripts of DCs in GPS-1 intervention and DCs in the normal state (Figures 6A–C), and found the differential gene expression of cells in this state and the normal group to speculate on the pathways and mechanisms of the differences. Finally, the results we obtained through the analysis of transcriptome data GO (Figure 6D) and KEGG (Figure 6E) is consistent with the above literature reports and activate cellular immune function through the TLR pathway. At the same time, we also found that GPS-1 affects the downstream TLR-2 and TLR-4 pathways, ie PI3K-AKT signaling pathway. And with this pathway as the core, it also acts on various downstream pathways such as MAPK, NF-κB, NOD, mTOR, and AMPK to regulate the activation and maturation of DC cells in the nucleus, and various cytokines secreted in turn act on the cells. JAK-STAT signaling pathway on DCs cells. In this way, the multi-target effect of GPS-1 on DCs can be realized, and various cellular functions such as growth, differentiation, apoptosis, and immune regulation of DCs can be comprehensively adjusted.

5 Conclusion

A novel HG-type pectin glycopolysaccharide, glycyrrhiza polysaccharides GPS-1, is composed of fucose, rhamnose, arabinose, galactose, glucose, xylose, galacturonic acid, and mannuronic acid in the percentages 0.92%, 10.12%, 6.36%, 4.85%, 1.34%, 0.51%, 74.39%, and 1.52%. The main chain of GPS-1 The structure is composed of →4)-α-D-GalpA-(1→.

GPS-1 was able to show good immunomodulatory activity in both *in vitro* and *in vivo* experiments. In particular, it can effectively promote the phagocytosis and antigen-presenting ability of DCs in regulating the immune activity of dendritic cells *in vitro*. At the same time, the transcriptomic analysis revealed that GPS-1 influenced the TLR-2 and TLR-4 pathways, and further regulated the viability of DCs through the PI3K- AKT signaling pathway and various downstream signaling pathways.

Data availability statement

The datasets presented in this study can be found in online repositories. The names of the repository/repositories and accession number(s) can be found below: https://www.ncbi.nlm.nih.gov/, PRJNA864785.

Ethics statement

The animal study was reviewed and approved by Institutional Animal Care and Use Committee Institutional Animal Care and Use Committee.

Author contributions

YuW and HZ, data curation and writing-original draft preparation. KW, writing-original draft preparation, methodology, and visualization. TZ, methodology and editing. YC, writing-reviewing and methodology. AN, SP, BZ, XY, and YL, writing-reviewing. XW, PH, and LW, data validation. XC, data curation. CL and HL visualization. JL, methodology. YiW, conceptualization, funding acquisition, project administration,

and supervision. All authors contributed to the article and approved the submitted version.

Funding

This research was financially supported by the National Natural Science Foundation of China (NSFC, Grant No. 31872514 and 32172900), the Open Project Program of Beijing Key Laboratory of 490 Traditional Chinese Veterinary Medicine at Beijing University of Agriculture (No. kftcvm202101), Yunnan Provincial Science and Technology Department-Applied Basic Research Joint Special Funds of Yunnan University of Chinese Medicine [2018FF001 (-020), 2019FF002 (-012)], Guangxi Science and Technology Project (GuiKe ZY20198018, GuiKe AA18242040) and a project funded by the Priority Academic Program Development of Jiangsu Higher Education Institutions (PAPD). We appreciate the assistance from our distinguished colleagues in the Institute of Traditional Chinese Veterinary Medicine of Nanjing Agricultural University and the technological managers in Nanjing Super Biotech Co., Ltd.

Conflict of interest

The authors declare that the research was conducted in the absence of any commercial or financial relationships that could be construed as a potential conflict of interest.

Publisher's note

References

1. Lu Y, Yao G, Wang X, Zhang Y, Zhao J, Yu YJ, et al. Chemometric discrimination of the geographical origin of licorice in China by untargeted metabolomics. *Food Chem* (2022) 380:132235. doi: 10.1016/j.foodchem.2022.132235

2. Arbelaez P, Borrull F, Maria Marce R, Pocurull E. Trace-level determination of sweeteners in sewage sludge using selective pressurized liquid extraction and liquid chromatography-tandem mass spectrometry. *J Chromatogr A* (2015) 1408:15–21. doi: 10.1016/j.chroma.2015.07.001

3. Yang R, Li W, Yuan B, Ren G, Wang L, Cheng T, et al. The genetic and chemical diversity in three original plants of licorice, glycyrriza uralensis fisch., glycyrrhiza inflata bat. and glycyrrhiza glabra l. *Pak J Pharm Sci* (2018) 31(2):525–35.

4. Wu Y, Wu C, Che Y, Zhang T, Dai C, Nguyen AD, et al. Effects of glycyrrhiza polysaccharides on chickens' intestinal health and homeostasis. *Front Vet Sci* (2022) 9:891429. doi: 10.3389/fvets.2022.891429

5. Ain NU, Wu S, Li X, Li D, Zhang Z. Isolation, characterization, pharmacology and biopolymer applications of licorice polysaccharides: Review. *Mater (Basel)* (2022) 15(10). doi: 10.3390/ma15103654

6. Hong YK, Wu HT, Ma T, Liu WJ, He XJ. Effects of glycyrrhiza glabra polysaccharides on immune and antioxidant activities in high-fat mice. *Int J Biol Macromol* (2009) 45(1):61–4. doi: 10.1016/j.ijbiomac.2009.04.001

7. Li C, Zhao P, Shao Q, Chen W, Huang S, Wang X, et al. Effects of dietary glycyrrhiza polysaccharide on growth performance, blood parameters and immunity in weaned piglets. *J Anim Physiol Anim Nutr (Berl)* (2022). doi: 10.1111/jpn.13692

8. Aipire A, Mahabati M, Cai S, Wei X, Yuan P, Aimaier A, et al. The immunostimulatory activity of polysaccharides from glycyrrhiza uralensis. *PeerJ 8* (2020):e8294. doi: 10.7717/peerj.8294

9. Wu D, Zheng J, Mao G, Hu W, Ye X, Linhardt R, et al. Rethinking the impact of RG-I mainly from fruits and vegetables on dietary health. *Crit Rev Food Sci Nutr* (2020) 60(17):2938–60. doi: 10.1080/10408398.2019.1672037

10. Wu Y, Li N, Zhang T, Che Y, Duan K, Wang Y, et al. Glycyrrhiza polysaccharides can improve and prolong the response of chickens to the Newcastle disease vaccine. *Poult Sci* (2022) 101(1):101549. doi: 10.1016/j.psj.2021.101549

11. Cong Y, RemilaMijiti, Palida A, MirenshaYakufu C, Chen XM. Effects of polysaccharide from glycyrrhiza inflata on immune function of RAW264.7 macrophage cell line In: Chinese Archives of traditional Chinese medicine. *Chin J Tradit Chin Med Pharm* (2018) 36(5):1044–7. doi: 10.13193/j.issn.1673-7717.2018.05.004

12. Wu Y, Yi L, Li E, Li Y, Lu Y, Wang P, et al. Optimization of glycyrrhiza polysaccharide liposome by response surface methodology and its immune activities. *Int J Biol Macromolecules* (2017) 102:68–75. doi: 10.1016/j.ijbiomac.2017.04.006

13. Sheng Z, Wen L, Yang B. Structure identification of a polysaccharide in mushroom lingzhi spore and its immunomodulatory activity. *Carbohydr Polymers* (2021) 278:118939. doi: 10.1016/j.carbpol.2021.118939

14. Chasan AI, Beyer M, Kurts C, Burgdorf S. Isolation of a specialized, antigen-loaded early endosomal subpopulation by flow cytometry. *Methods Mol Biol* (2013) 960:379–88. doi: 10.1007/978-1-62703-218-6_28

15. Shen H, Ackerman AL, Cody V, Giodini A, Hinson ER, Cresswell P, et al. Enhanced and prolonged cross-presentation following endosomal escape of exogenous antigens encapsulated in biodegradable nanoparticles. *Immunology* (2006) 117(1):78–88. doi: 10.1111/j.1365-2567.2005.02268.x

16. Petersen BO, Meier S, Duus JO, Clausen MH. Structural characterization of homogalacturonan by NMR spectroscopy-assignment of reference compounds. *Carbohydr Res* (2008) 343(16):2830–3. doi: 10.1016/j.carres.2008.08.016

17. Perrone P, Hewage CM, Thomson AR, Bailey K, Sadler IH, Fry SC. Patterns of methyl and O-acetyl esterification in spinach pectins: new complexity. *Phytochemistry* (2002) 60(1):67–77. doi: 10.1016/s0031-9422(02)00039-0

18. Yang J, Wen L, Zhao Y, Jiang Y, Tian M, Liu H, et al. Structure identification of an arabinogalacturonan in citrus reticulata blanco 'Chachiensis' peel. *Food Hydrocolloids* (2018) 84:481–8. doi: 10.1016/j.foodhyd.2018.06.022

19. Makarova EN, Shakhmatov EG. Structural characteristics of oxalate-soluble polysaccharides from Norway spruce (Picea abies) foliage. *Carbohydr Polym* (2020) 246:116544. doi: 10.1016/j.carbpol.2020.116544

20. Shakhmatov EG, Toukach PV, Makarova EN. Structural studies of the pectic polysaccharide from fruits of punica granatum. *Carbohydr Polym* (2020) 235:115978. doi: 10.1016/j.carbpol.2020.115978

21. Prado S, Santos GRC, Mourao PAS, Fabi JP. Chelate-soluble pectin fraction from papaya pulp interacts with galectin-3 and inhibits colon cancer cell proliferation. *Int J Biol Macromol* (2019) 126:170–8. doi: 10.1016/j.ijbiomac.2018.12.191

22. Panda BC, Mondal S, Devi KS, Maiti TK, Khatua S, Acharya K, et al. Pectic polysaccharide from the green fruits of momordica charantia (Karela): structural characterization and study of immunoenhancing and antioxidant properties. *Carbohydr Res* (2015) 401:24–31. doi: 10.1016/j.carres.2014.10.015

23. Roman L, Guo M, Terekhov A, Grossutti M, Vidal NP, Reuhs BL, et al. Extraction and isolation of pectin rich in homogalacturonan domains from two

cultivars of hawthorn berry (Crataegus pinnatifida). *Food Hydrocolloids* (2021) 113. doi: 10.1016/j.foodhyd.2020.106476

24. Zhang H, Zhong J, Zhang Q, Qing D, Yan C. Structural elucidation and bioactivities of a novel arabinogalactan from coreopsis tinctoria. *Carbohydr Polym* (2019) 219:219–28. doi: 10.1016/j.carbpol.2019.05.019

25. Freitas CMP, Coimbra JSR, Souza VGL, Sousa RCS. Structure and applications of pectin in food, biomedical, and pharmaceutical industry: A review. *Coatings* (2021) 11(8). doi: 10.3390/coatings11080922

26. Zhang X, Kong X, Hao Y, Zhang X, Zhu Z. Chemical structure and inhibition on α-glucosidase of polysaccharide with alkaline-extracted from glycyrrhiza inflata residue. *Int J Biol Macromolecules* (2020) 147:1125–35. doi: 10.1016/j.ijbiomac.2019.10.081

27. Pan LC, Zhu YM, Zhu ZY, Xue W, Liu CY, Sun HQ, et al. Chemical structure and effects of antioxidation and against alpha-glucosidase of natural polysaccharide from glycyrrhiza inflata batalin. *Int J Biol Macromol* (2020) 155:560–71. doi: 10.1016/j.ijbiomac.2020.03.192

28. Mutaillifu P, Bobakulov K, Abuduwaili A, Huojiaaihemaiti H, Nuerxiati R, Aisa HA, et al. Structural characterization and antioxidant activities of a water soluble polysaccharide isolated from glycyrrhiza glabra. *Int J Biol Macromol.* (2020) 144:751–9. doi: 10.1016/j.ijbiomac.2019.11.245

29. Zeng F, Weng Z, Zheng H, Xu M, Liang X, Duan J. Preparation and characterization of active oxidized starch films containing licorice residue extracts and its potential against methicillin-resistant s. *aureus. Int J Biol Macromol* (2021) 187:858–66. doi: 10.1016/j.ijbiomac.2021.07.179

30. Ota M, Makino T. History and the immunostimulatory effects of heat-processed licorice root products with or without honey. *J Ethnopharmacol* (2022) 292:115108. doi: 10.1016/j.jep.2022.115108

31. Zeng G, Shen H, Tang G, Cai X, Bi L, Sun B, et al. A polysaccharide from the alkaline extract of glycyrrhiza inflata induces apoptosis of human oral cancer SCC-25 cells *via* mitochondrial pathway. *Tumour Biol* (2015) 36(9):6781–8. doi: 10.1007/s13277-015-3359-5

32. Pandiella-Alonso A, E. Diaz-Rodriguez, . Sanz E. Antitumoral properties of the nutritional supplement ocoxin oral solution: A comprehensive review. *Nutrients* (2020) 12(9). doi: 10.3390/nu12092661

33. Nakamura T, Nishibu A, Yoshida N, Yasoshima M, Anzawa K, Watanabe Y, et al. Glycyrrhetinic acid inhibits contact hypersensitivity induced by trichophytin *via* dectin-1. *Exp Dermatol* (2016) 25(4):299–304. doi: 10.1111/exd.12931

34. Cho BO, Shin JY, Kang HJ, Park JH, Hao S, Wang F, et al. Antiinflammatory effect of chrysanthemum zawadskii, peppermint, glycyrrhiza glabra herbal mixture in lipopolysaccharidestimulated RAW264.7 macrophages. *Mol Med Rep* (2021) 24 (1). doi: 10.3892/mmr.2021.12171

35. Simayi Z, Rozi P, Yang X, Ababaikeri G, Maimaitituoheti W, Bao X, et al. Isolation, structural characterization, biological activity, and application of glycyrrhiza polysaccharides: Systematic review. *Int J Biol Macromol* (2021) 183:387–98. doi: 10.1016/j.ijbiomac.2021.04.099

36. Wang XR, Hao HG, Chu L. Glycyrrhizin inhibits LPS-induced inflammatory mediator production in endometrial epithelial cells. *Microb Pathog* (2017) 109:110–3. doi: 10.1016/j.micpath.2017.05.032

37. Kubota A, Kobayashi M, Sarashina S, Takeno R, Okamoto K, Narumi K, et al. Reishi mushroom ganoderma lucidum modulates IgA production and alpha-defensin expression in the rat small intestine. *J Ethnopharmacol* (2018) 214:240–3. doi: 10.1016/j.jep.2017.12.010

38. Liu Q, Han Q, Lu M, Wang H, Tang F. Lycium barbarum polysaccharide attenuates cardiac hypertrophy, inhibits calpain-1 expression and inhibits NF-kappaB activation in streptozotocin-induced diabetic rats. *Exp Ther Med* (2019) 18 (1):509–16. doi: 10.3892/etm.2019.7612

frontiers | Frontiers in Immunology

TYPE Original Research
PUBLISHED 04 January 2023
DOI 10.3389/fimmu.2022.1017178

OPEN ACCESS

EDITED BY
Ziwei Zhang,
Northeast Agricultural University, China

REVIEWED BY
Nicole Ursula Stoffel,
ETH Zürich, Switzerland
Sebastian Dolff,
University Duisburg-Essen, Germany

*CORRESPONDENCE
Martin H. De Borst
m.h.de.borst@umcg.nl

SPECIALTY SECTION
This article was submitted to Nutritional Immunology, a section of the journal Frontiers in Immunology

RECEIVED 11 August 2022
ACCEPTED 05 December 2022
PUBLISHED 04 January 2023

CITATION
Vinke JSJ, Altulea DHA, Eisenga MF, Jagersma RL, Niekolaas TM, van Baarle D, Heiden MvD, Steenhuis M, Rispens T, Abdulahad WH, Sanders J-SF and De Borst MH (2023) Ferric carboxymaltose and SARS-CoV-2 vaccination-induced immunogenicity in kidney transplant recipients with iron deficiency: The COVAC-EFFECT randomized controlled trial. *Front. Immunol.* 13:1017178. doi: 10.3389/fimmu.2022.1017178

Ferric carboxymaltose and SARS-CoV-2 vaccination-induced immunogenicity in kidney transplant recipients with iron deficiency: The COVAC-EFFECT randomized controlled trial

Joanna Sophia J. Vinke[1], Dania H. A. Altulea[1], Michele F. Eisenga[1], Renate L. Jagersma[1], Tessa M. Niekolaas[1], Debbie van Baarle[2], Marieke van Der Heiden[2], Maurice Steenhuis[3], Theo Rispens[3], Wayel H. Abdulahad[2], Jan-Stephan F. Sanders[1] and Martin H. De Borst[1]*

[1]Department of Nephrology, University Medical Center Groningen, Groningen, Netherlands, [2]Department of Immunology, University Medical Center Groningen, Groningen, Netherlands, [3]Department of Immunopathology, Sanquin Research, Amsterdam, Netherlands

Background: Kidney transplant recipients (KTRs) have an impaired immune response after vaccination against severe acute respiratory syndrome coronavirus-2 (SARS-CoV-2). Iron deficiency (ID) may adversely affect immunity and vaccine efficacy. We aimed to investigate whether ferric carboxymaltose (FCM) treatment improves humoral and cellular responses after SARS-CoV-2 vaccination in iron-deficient KTRs.

Methods: We randomly assigned 48 iron-deficient KTRs to intravenous FCM (1-4 doses of 500mg with six-week intervals) or placebo. Co-primary endpoints were SARS-CoV-2-specific anti-Receptor Binding Domain (RBD) Immunoglobulin G (IgG) titers and T-lymphocyte reactivity against SARS-CoV-2 at four weeks after the second vaccination with mRNA-1273 or mRNA-BNT162b2.

Results: At four weeks after the second vaccination, patients receiving FCM had higher plasma ferritin and transferrin saturation (P<0.001 vs. placebo) and iron (P=0.02). However, SARS-CoV-2-specific anti-RBD IgG titers (FCM: 66.51 [12.02-517.59] BAU/mL; placebo: 115.97 [68.86-974.67] BAU/mL, P=0.07) and SARS-CoV-2-specific T-lymphocyte activation (FCM: 93.3 [0.85-342.5] IFN-ɣ spots per 10^6 peripheral blood mononuclear cells (PBMCs), placebo: 138.3 [0.0-391.7] IFN-ɣ spots per 10^6 PBMCs, P=0.83) were not significantly different among both arms. After the third vaccination, SARS-CoV-2-specific anti-RBD IgG titers remained similar between treatment groups (P=0.99).

10.3389/fimmu.2022.1017178

Conclusions: Intravenous iron supplementation efficiently restored iron status but did not improve the humoral or cellular immune response against SARS-CoV-2 after three vaccinations.

KEYWORDS

iron deficiency, SARS-CoV-2, kidney transplantation, vaccination, randomized controlled (clinical) trial

Introduction

Coronavirus Disease 2019 (COVID-19) has affected more than 500 million people worldwide since the beginning of the pandemic early 2020, leading to more than six million deaths (1). Kidney transplant recipients (KTRs) who are infected with severe acute respiratory syndrome coronavirus-2 (SARS-CoV-2) have an increased risk of adverse outcome, with a 17-23% mortality rate (2–5). Immunosuppressive medication in KTRs impedes powerful humoral (6–11) and cellular (10, 12) immune responses against SARS-CoV-2 after vaccination. Previous studies identified higher age, pre-transplantation dialysis, deceased donor type, worse graft function, recent use of high-dose corticosteroids and use of mycophenolic acid as risk factors for a poor antibody response after SARS-CoV-2 vaccination in KTRs (8, 10, 13). Still, identification of new modifiable risk factors for an impaired immune response in KTRs is urgently needed (6, 8, 10).

Iron deficiency (ID) is highly prevalent after kidney transplantation (14), and has recently been proposed as potential treatment target to improve vaccine efficacy (15). Iron is involved in nucleotide synthesis for replication of deoxyribonucleic acid and in mitochondrial energy metabolism (16). Therefore, rapidly proliferating cells such as lymphocytes are prone to be affected by ID. Recent studies demonstrated impaired B-cell proliferation, plasma cell differentiation and immunoglobulin production in iron-deficient mice (17). In humans, ID is associated with reduced antibody production in response to various vaccinations (17), while pre-vaccination iron supplements improved vaccination-induced immune responses (18). Given these observations, the European Hematology Association recently published an expert opinion advising to correct ID before vaccination against SARS-CoV-2 (19). Whether correcting ID improves SARS-CoV-2 vaccine efficacy in KTRs is unknown. Therefore, we aimed to address the hypothesis that in iron-deficient KTRs, ferric carboxymaltose (FCM) improves the humoral and cellular response after vaccination against SARS-CoV-2.

Abbreviations: BAU, international Binding Antibody Units; BMI, body mass index; CKD-EPI, Chronic Kidney Disease Epidemiology Collaboration; COVID-19, coronavirus disease 2019; DMSO, dimethyl sulfoxide; eGFR, estimated glomerular filtration rate; ELISA, enzyme-linked immunosorbent assay; FCM, ferric carboxymaltose; ID, iron deficiency; IFN-γ, interferon-gamma; IgG, immunoglobulin G; IQR, interquartile range; KTR, kidney transplant recipient; METc, medical ethical committee; nOD, normalized optical density unit; PBMC, peripheral blood mononuclear cell; RBD, receptor binding domain; SARS-CoV-2, severe acute respiratory virus 2; SD, standard deviation; SFC, spot forming cells; TSAT, transferrin saturation.

Materials and methods

Patient population and study design

COVAC-EFFECT is a secondary analysis performed in a subpopulation of the ongoing EFFECT-KTx study (NCT03769441, also covering COVAC-EFFECT), a randomized, placebo-controlled, parallel-arm clinical trial aiming to address the effects of FCM versus placebo on exercise tolerance, cardiac function and other clinical outcomes in iron-deficient KTRs. In the mother trial, 158 subjects receive up to four doses of FCM (containing 500 mg Fe3+ per dose) or placebo (0.9% sodium chloride solution) intravenously, with six-week intervals. In case of severe hypophosphatemia (plasma phosphate ≤1.55 mg/dL) or active systemic infection on the day of the study visit, one treatment is withheld. In case of imminent iron overload, defined as a plasma ferritin level of ≥800 ug/L or 500-799 ug/L in combination with a transferrin saturation (TSAT) of ≥45% on the day of the study visit, patients in the FCM arm receive a dose of placebo instead of FCM. The study protocol of the EFFECT-KTx study and COVAC-EFFECT was approved by the medical ethical committee of the University Medical Center Groningen (METc 2018/482), conducted in accordance with the principles of the Declaration of Helsinki and consistent with the Good Clinical Practice guidelines provided by the International Council for Harmonization of Technical Requirements for Pharmaceuticals for Human Use. All participants had given their informed consent prior to enrollment in the EFFECT-KTx study as well as to enrollment in COVAC.

The current study could be performed since the ongoing EFFECT-KTx trial coincided with the Dutch national SARS-CoV2 vaccination program. Given this setting, a formal *a priori* sample size calculation was not performed; instead, all patients enrolled in the mother trial (EFFECT-KTx) who met the inclusion criteria for the current substudy were invited to participate. Participants who had received at least one treatment with study medication were eligible. The unblinded researchers who analyzed the data for the current study worked completely independent of the study team working on the mother trial, to ensure that these investigators remained blinded. An overview of the study design is provided in Figure 1. For the current study, we enrolled 48 iron-deficient EFFECT-KTx participants with a functional graft for more than six months post-transplantation who had not reported COVID-19 and who agreed to vaccination against SARS-CoV-2. Two patients who tested positive for SARS-CoV-2 within four weeks after the first or the second vaccination were excluded.

Vaccination

Participants were vaccinated against SARS-Cov-2 as part of the Dutch national vaccination campaign. Patients who were eligible for early vaccination, because of high age or occupation in healthcare, received two mRNA-BNT162b2 vaccinations (COMIRNATY, ®Pfizer-BioNTech) with an interval of 35 days. All other participants received two mRNA-1273 vaccinations (®Moderna Biotech Spain, S.L.) with an interval of 28 days according to the manufacturer's instructions. Six months after the second vaccination dose, participants received a third vaccination dose.

Data collection and definitions

Co-primary outcomes of this study were the humoral and cellular immune responses at four weeks after the second vaccination. At this timepoint, SARS-CoV-2-specific anti-Receptor Binding Domain (RBD) immunoglobulin G (IgG) levels, expressed in international Binding Antibody Units (BAU)/mL, were measured in venous blood. Furthermore, capillary blood was collected with a self-collection finger prick set prior to the first and the second vaccination and four weeks after the third vaccination for additional SARS-CoV-2-specific anti-RBD IgG titer measurements. To assess cellular immunogenicity, peripheral blood mononuclear cells (PBMCs) were isolated from the blood sample that was taken four weeks after the second vaccination.

Baseline characteristics were registered and measurements were performed before treatment with FCM or placebo. Body Mass Index (BMI) was calculated as weight in kilograms divided by height in meters squared. Plasma creatinine was measured in venous blood with an enzymatic photometry assay (Roche Diagnostics, Mannheim, Germany). The estimated glomerular filtration rate (eGFR) was calculated using the Chronic Kidney Disease Epidemiology Collaboration (CKD-EPI) equation, omitting the black race coefficient (20). Plasma iron was measured with a colorimetric assay, ferritin with an immunoassay and transferrin with a turbidimetric assay (Roche Diagnostics), all in venous blood samples. TSAT was calculated as 100 x (plasma iron (µg/dL) ÷ (total iron binding capacity (µg/dL)). Hemoglobin was measured in venous blood with spectrophotometry. ID was defined as a plasma ferritin concentration below 100 µg/L or a ferritin concentration between 100 and 299 µg/L in combination with a TSAT below

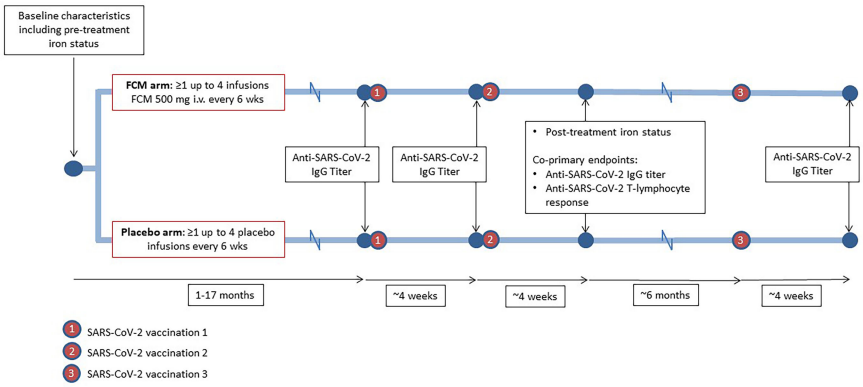

FIGURE 1
Study design. During participation in the EFFECT-KTx study, iron-deficient kidney transplant recipients are being randomized to receive four doses of ferric carboxymaltose (FCM) or placebo with six-week intervals after baseline measurements, including iron status assessment, have been performed. During or after participation in the EFFECT-KTx study, patients received three vaccinations against SARS-CoV-2. Before the first vaccination and four weeks after the successive vaccinations, anti-SARS-CoV-2 IgG titer was measured. Four weeks after the second vaccination, anti-SARS-CoV-2 T-lymphocyte response was assessed.

20% (21). Severe ID was defined as a ferritin concentration below 30 µg/L (22). IgG deficiency was defined as a total IgG concentration below 7.0 g/L (23).

Anti-SARS-CoV-2 antibody response

Serum was isolated from capillary blood samples (fingerpick sampled at home) taken before the first and the second vaccination and four weeks after the third vaccination, or from venous blood sample drawn four weeks after the second vaccination. SARS-CoV-2-specific anti-RBD IgG antibodies were measured using an in-house (Sanquin, Amsterdam, the Netherlands) enzyme-linked immunosorbent assay (ELISA) assay, as described by Steenhuis et al. (24) IgG titers were compared with the World Health Organization reference sample (NIBSC code: 20/136) and expressed as BAU/ml. Cut-off for seroconversion was defined based on the 98th percentile of signals of 240 pre-outbreak plasma samples, corresponding to an anti-RBD IgG titer of ≥50 BAU/mL (24, 25). In addition, to detect previous exposure to SARS-CoV-2, a highly sensitive and specific total antibody SARS-CoV-2 RBD bridging assessment was performed on all samples, using a double antigen sandwich ELISA based assay developed by Sanquin, as described previously (24, 26). Outcome of this assay was compared to a Sanquin in-house calibrator of pooled convalescent plasma and expressed as normalized optical density units (nOD). An nOD >0.1 was considered as seropositive for total SARS-CoV-2-specific anti-RBD antibodies (24, 26). Furthermore, SARS-CoV-2-specific anti-nucleocapsid protein IgG antibodies were measured in samples from patients with a nOD >0.1 or an anti-RBD IgG titer of ≥50 BAU/mL at baseline, using an ELISA assay (26). Since these antibodies do not react to vaccination and are highly specific for previous exposure to the virus itself, they can be used to assess whether antibodies are induced by SARS-CoV-2 vaccination or infection.

T-lymphocyte reactivity against Spike protein

In all participants, the SARS-CoV-2-specific T-lymphocyte response was measured after stimulation of PBMCs isolated from heparinized venous blood obtained four weeks after the second vaccination, using SepMate tubes (STEMCELL). The number of Interferon-gamma (IFN-ɣ)-producing T-lymphocytes after stimulation with SARS-CoV-2 Spike overlapping peptide pools was assessed using an IFN-ɣ enzyme-linked immune adsorbent spot (ELISpot) assay. SARS-CoV-2 S1 and S2 peptide pools (JPT Peptide Technologies), consisting of 15-mer peptides overlapping 11 amino acids that cover the entire sequence of the viral proteins were used for overnight stimulation of the PBMCs in a concentration of 0.5 µg/mL. 0.4% dimethyl sulfoxide (DMSO, Sigma) was used as negative control and Phytohaemagglutinin (Remel Europe Ltd; 4 µg/mL) as a positive control. Spot forming cells (SFC) were quantified with the AID ELISpot/Fluorospot reader and calculated to SFCs/10^6 PBMCs. The average of the DMSO negative control was subtracted per stimulation. To define the total Spike-specific SFC, the SFC of the separate S1 and S2 peptide pools were summed. Results are expressed in number of IFN-ɣ spots per 10^6 PBMCs. KTRs who had more than 50 IFN-ɣ spots per 10^6 PBMCs were considered to be responders (27).

Statistical analyses

We used IBM SPSS Statistics version 23.0 (SPSS Inc., Chicago, USA) and Prism 8.0 (GraphPad Software Inc., San Diego, USA) to analyze the data. Normally distributed data are presented as mean ± standard deviation (SD). Data with a skewed distribution are presented as median (interquartile range [IQR]). Categorical data are expressed as number (percentage).

To assess changes between baseline and post-vaccination measurements, we used the paired T-test for normally distributed data or the Wilcoxon-signed rank test for data with a skewed distribution. To assess differences between the two study arms at four weeks after the successive vaccinations, the independent samples T-test and Mann-Whitney Test were used. To adjust for differences in baseline lymphocyte count or eGFR, analysis of covariance was performed. Correlations were analyzed using the Spearman's rank test.

The primary analyses were performed according to the intention-to-treat principle. We additionally performed ten sensitivity analyses. First, a per-protocol analysis was performed, excluding KTRs who were still iron-deficient after treatment with FCM, as well as KTRs who were not iron-deficient despite placebo treatment. In a second sensitivity analysis, we excluded four patients who were seropositive for total SARS-CoV-2-specific anti-RBD antibodies (n=3) or anti-SARS-CoV-2 IgG antibodies (n=1) at baseline. As a third sensitivity analysis, we excluded KTRs who were IgG-deficient at baseline. Fourth, we repeated the analyses in a subpopulation restricted to patients who had received the mRNA-1273 vaccine. In a fifth sensitivity analysis, only patients with severe ID (ferritin <30 µg/L) were included. Sixth, we analyzed patients on dual or triple immunosuppressive therapy separately. Seventh, patients who had received treatment with alemtuzumab, methylprednisolone or anti-thymocyte globulin <2 years prior to vaccination were excluded. In an eighth sensitivity analysis, the subgroup of patients who used mycophenolic acid was studied. Moreover, the subgroup of patients using mycophenolic acid with a dosage of 500mg twice daily was analyzed separately. Finally, we analyzed men and women separately. In all analyses, a P value of ≤0.05 was considered significant.

10.3389/fimmu.2022.1017178

Results

Baseline characteristics and vaccines

Forty-six KTRs (age 53 [43-65] years, 61% male) were included. Baseline characteristics are shown in Table 1. Patient characteristics in both treatment arms were generally well balanced, except for small but significant differences in lymphocyte count, eGFR and prevalence of hypertension. Forty-one patients received the mRNA-1273 vaccine, and five KTRs received the mRNA-BNT162b2 vaccine. Four patients had a nOD of >0.1 or an anti-RBD IgG titer of ≥50 BAU/mL at baseline; three of them also had anti-nucleocapsid protein IgG antibodies at baseline. Time between enrollment in the EFFECT-KTx study and first vaccination was 33 ± 24 weeks.

Iron status

Iron status was assessed at baseline before treatment with FCM or placebo and four weeks after the second vaccination, which was on average 42 ± 24 weeks after baseline (Table 2). Patients in the FCM arm showed an increase in plasma ferritin levels from 49 [26–79] µg/L to 464 [272–621] µg/L (P<0.001 vs baseline), while in the placebo group, ferritin did not significantly change (34 [24–62] µg/L to 42 [23–69] µg/L, P=0.39, Figure 2A). Ferritin levels at four weeks after the second vaccination were significantly higher in the FCM arm than in the placebo arm (P<0.001). TSAT also increased significantly in the FCM arm (from 21 ± 8% to 34 ± 12%, P<0.001), but not in the placebo arm (21 ± 8% vs 21 ± 10%, P=0.84 vs placebo baseline, P<0.001 vs FCM, Figure 2B). Plasma iron levels increased significantly in the FCM arm (from 75.4 ± 25.7 µg/dL to 98.8 ± 29.0 µg/dL, P=0.004), but not in the placebo arm (78.2 ± 22.9 µg/dL to 79.3 ± 34.1 µg/dL, P=0.89 vs placebo baseline, P=0.02 vs FCM, Figure 2C). Two months after the second vaccination, only two patients in the FCM arm were still iron-deficient. One patient was not iron-deficient anymore despite placebo treatment. Finally, there was a small but significant effect of FCM on hemoglobin levels (from 13.2 ± 1.1 g/dL to 14.0 ± 1.1 g/dL, P<0.001) which was not observed in the placebo arm (13.5 ± 1.0 g/dL vs 13.5 ± 1.1 g/dL, P=0.95).

Anti-SARS-CoV-2 antibody response

There was no significant difference between the treatment groups in SARS-CoV-2-specific anti-RBD IgG concentration at four weeks after the second vaccination dose (P=0.07), which was one of the two co-primary outcomes of this study. Also after the first (P=0.12), or the third vaccination (P=0.99) there was no difference in SARS-CoV-2-specific anti-RBD IgG concentration between the study groups (Figure 3A). During the four weeks after the first vaccination, there was no significant increase in SARS-CoV-2-specific anti-RBD IgG concentration in patients in the FCM arm (2.31 [1.18–9.53] BAU/mL to 1.18 [1.18-20.63] BAU/mL, P=0.14). At four weeks after the second vaccination, SARS-CoV-2-specific anti-RBD IgG concentration significantly increased to 66.51 [12.02–517.59] BAU/mL in the FCM group (P<0.001 vs before first vaccination). Finally, four weeks after the third vaccination, SARS-CoV-2-specific anti-RBD IgG concentration further increased to 464.71 [52.13 – 1255.30] in the FCM group (P<0.001 vs before first vaccination). In the placebo arm, SARS-CoV-2-specific anti-RBD IgG concentration increased from 1.18 [1.18–10.33] BAU/mL before the first vaccination to 13.75 [1.18–46.18] BAU/mL four weeks later (P=0.03), to 115.97 [68.86–974.67] BAU/mL at four weeks after the second vaccination (P<0.001 vs before the first vaccination) and to 476.46 [45.00 – 1286.60] after the third vaccination (P=0.004 vs before first vaccination). An *a posteriori* power calculation indicated that, based on measured antibody levels, this study had 80% power to detect a 30% increase in (natural log-transformed) SARS-CoV-2-specific anti-RBD IgG concentrations at four weeks after the third vaccination.

After adjusting for total lymphocyte count (P=0.61) or eGFR (P=0.19) at baseline, there was still no significant difference in SARS-CoV-2-specific anti-RBD IgG concentration between the treatment groups at four weeks after the second vaccination. We found no correlation between TSAT (Spearman's rho -0.05, P=0.72) or plasma ferritin (Spearman's rho -0.15, P=0.33) or plasma iron (Spearman's rho -0.01, P=0.94) and SARS-CoV-2-specific anti-RBD IgG concentration at four weeks after the second vaccination (Figures 3B, C). There was also no significant correlation between SARS-CoV-2-specific anti-RBD IgG concentration measured at four weeks after the second vaccination, and the total lymphocyte count at baseline (Spearman's rho 0.26, P=0.09).

Seroconversion increased from 19% in the FCM group and 17% in the placebo group (P=0.85 between groups) at four weeks after the first vaccination to 56% in the FCM group and 80% in the placebo group (P=0.09 between groups) after the second vaccination and to 84% in the FCM group and 79% in the placebo group (P= 0.68 between groups) after the third vaccination. In all sensitivity analyses, results were highly comparable to those of the main analysis (Supplementary Tables 1–24).

SARS-CoV-2-specific T-lymphocyte response

We subsequently evaluated the effect of FCM on the SARS-CoV2-specific cellular vaccination response, expressed in number of IFN-ɣ-producing T-lymphocytes after stimulation with SARS-CoV-2 Spike, at four weeks after the second

10.3389/fimmu.2022.1017178

TABLE 1 Baseline characteristics.

Characteristics	Total (N=46)	FCM (N=25)	Placebo (N=21)
Age, yr	53 (43–65)	55 (46–64)	51 (39-69)
Male sex, n (%)	28 (61)	12 (48)	16 (76)
Body mass index, kg/m^2	26 ± 4	26 ± 4	27 ± 5
Diabetes, n (%)	13 (28)	6 (24)	7 (33)
Hypertension, n (%)	40 (87)	19 (76)	21 (100)
Alcohol consumption, units per week	0 (0-3)	0 (0-3)	1 (0–4)
Current tobacco use, n (%)	3 (7)	0 (0)	3 (14)
Time since transplantation, yr	3 (1-4)	2 (1–4)	3 (1–5)
History of dialysis, n (%)	27 (59)	16 (64)	11 (52)
Living donor, n (%)	34 (74)	17 (68)	17 (81)
Medication use			
Dual immunosuppressive therapy, n (%)	8 (17)	4 (16)	4 (19)
Triple immunosuppressive therapy, n (%)	40 (83)	21 (84)	17 (81)
Prednisone use, n (%)	46 (100)	25 (100)	21 (100)
Calcineurin inhibitor use, n (%)	42 (91)	23 (92)	19 (91)
Antiproliferative agent use, n (%)	40 (87)	21 (84)	19 (91)
Mycophenolic acid use, n (%)	38 (83)	20 (80)	18 (86)
Azathioprine use, n (%)	2 (4)	1 (4)	1 (5)
mTOR inhibitor use, n (%)	2 (4)	2 (8)	0 (100)
Anti-thymocyte globulin treatment ≤2 years, n (%)	1 (2)	1 (4)	0 (0)
Alemtuzumab treatment ≤2 years, n (%)	0 (0)	0 (0)	0 (0)
Methylprednisolone treatment ≤2 years, n (%)	0 (0)	0 (0)	0 (0)
Vaccination against SARS-CoV-2			
mRNA-1273 (Moderna), n (%)	41 (89)	23 (92)	18 (86)
mRNA-BNT162b2 (COMIRNATY), n (%)	5 (11)	2 (8)	3 (14)
Time since last study treatment at time of first vaccination, weeks	10 (2 – 39)	11 (2 – 42)	10 (2 – 38)
Laboratory parameters			
Hemoglobin, g/dL	13.4 ± 1.1	13.2 ± 1.1	13.5 ± 1.0
MCV, fL	90 ± 5	90 ± 7	89 ± 3
Leucocyte count - 10^9/L	7.2 ± 1.8	7.0 ± 2.0	7.3 ± 1.6
CRP, mg/L	1.3 (0.7 – 3.0)	1.6 (0.9 – 2.9)	1.2 (0.6 – 3.6)
Lymphocyte count - 10^9/L	1.5 ± 0.7	1.2 ± 0.5	1.7 ± 0.8
eGFR, mL/min/1.73 m^2	63 ± 18	59 ± 16	68 ± 18
Iron, µg/dL	76.5 ± 24.0	75.4 ± 25.7	78.2 ± 22.9
Ferritin, µg/L	37 (26–70)	57 (29–79)	32 (24–62)
TSAT, %	21 ± 8	21 ± 8	21 ± 8

(Continued)

TABLE 1 Continued

Characteristics	Total (N=46)	FCM (N=25)	Placebo (N=21)
TIBC, µg/dL	373 ± 63	369 ± 70	378 ± 55
Total IgG, g/L	8.4 ± 2.0	8.3 ± 1.9	8.5 ± 2.2

Baseline characteristics, assessed on the morning before the first treatment with FCM or placebo, and vaccination characteristics. Data are presented as mean ± standard deviation (SD), median with interquartile range (IQR) or number (n) with percentage (%). CRP, C-reactive protein; eGFR, estimated glomerular filtration rate; FCM, ferric carboxymaltose; IgG, Immunoglobulin G; MCV; mean corpuscular volume; mTOR, mammalian target of rapamycin; SARS-CoV-2, severe acute respiratory syndrome coronavirus; TIBC, total iron binding capacity; TSAT, transferrin saturation.

vaccination. This was the second co-primary outcome of this study. KTRs in the FCM arm had a median of 93.3 [0.85–342.5] IFN-ɣ spots per 10^6 PBMCs, compared to 138.3 [0.0–391.7] IFN-ɣ spots per 10^6 PBMCs in the KTRs in the placebo arm (P=0.83, Figure 3D). Also after adjusting for total lymphocyte count (*P*=0.93) or eGFR (*P*=0.96) at baseline, there was no difference in SARS-CoV2-specific cellular response between the treatment groups after the second vaccination. The number of IFN-ɣ spots significantly correlated with the SARS-CoV-2-specific anti-RBD IgG concentration (Spearman's rho 0.44, *P*=0.002), but not with TSAT (Spearman's rho 0.16, *P*=0.30, [Figure 3E]), plasma ferritin (Spearman's rho 0.00, *P*=0.98), plasma iron (Spearman's rho 0.11, *P*=0.45, Figure 3F) or total lymphocyte count at baseline (Spearman's rho 0.10, *P*=0.50). 60% of KTRs in the FCM group and 62% of KTRs in the placebo group were T-lymphocyte responders (P=0.90). The between-group differences were non-significant in all sensitivity analyses (Supplementary Tables 25–36). An example of the results of an ELISPOT assay is depicted in Figure 3G.

Discussion

The main finding of this study is that correction of ID with FCM does not improve the humoral or cellular post-vaccination immune response against SARS-CoV-2 in KTRs. Although iron-

TABLE 2 Inflammation and iron status parameters at baseline and four weeks after the second vaccination.

	FCM (N=25)	Placebo (N=21)	P-value
Leucocyte count - 10^9/L			
Baseline	7.0 ± 2.0	7.3 ± 1.6	0.28
4 weeks after vaccination 2	7.3 ± 1.9	7.1 ± 1.6	0.36
CRP, mg/L			
Baseline	1.6 (0.9 – 2.9)	1.2 (0.6 – 3.6)	0.50
4 weeks after vaccination 2	1.8 (0.8 – 5.4)	1.2 (0.7 – 2.3)	0.24
Iron, µg/dL			
Baseline	75.4 ± 25.7	78.2 ± 22.9	0.36
4 weeks after vaccination 2	98.8 ± 29.0	79.3 ± 34.1	0.02
Ferritin, µg/L			
Baseline	57 (29–79)	32 (24–62)	0.18
4 weeks after vaccination 2	457 (269 – 627)	41 (23 – 71)	<0.001
TSAT, %			
Baseline	21 ± 8	21 ± 8	0.49
4 weeks after vaccination 2	34 ± 12	21 ± 10	<0.001
TIBC, µg/dL			
Baseline	369 ± 70	378 ± 55	0.34
4 weeks after vaccination 2	303 ± 56	381 ± 52	<0.001

Inflammation and iron status parameters at baseline and four weeks after the second vaccination. Data are presented as mean ± standard deviation (SD), median with interquartile range (IQR) or number (n) with percentage (%). CRP, C-reactive protein; TIBC, total iron binding capacity; TSAT, transferrin saturation.

10.3389/fimmu.2022.1017178

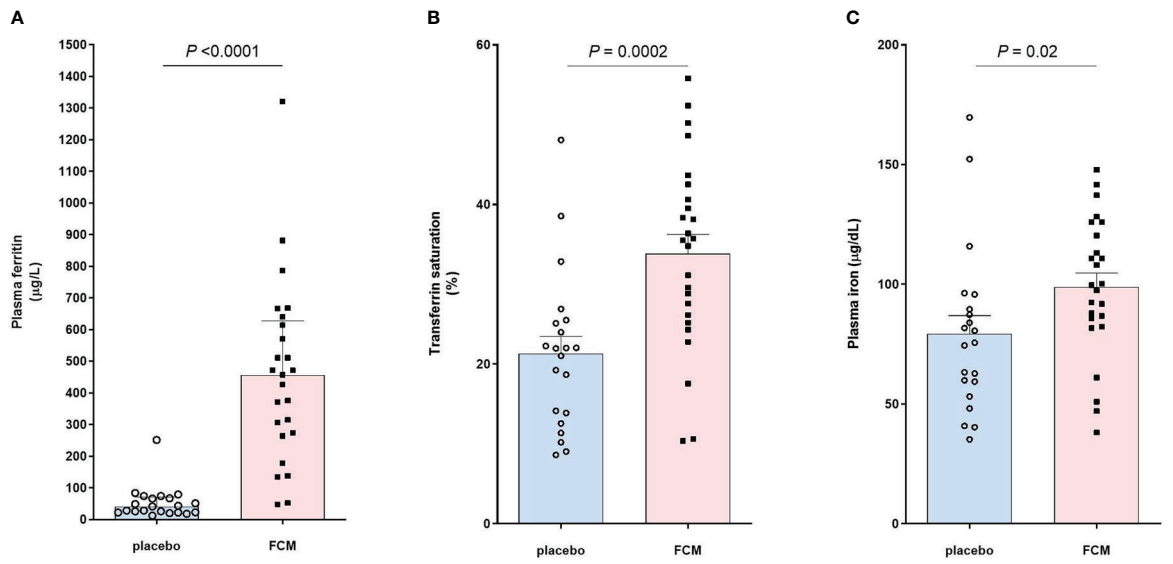

FIGURE 2
Effect of FCM or placebo on **(A)** plasma ferritin levels, **(B)** transferrin saturation and **(C)** plasma iron levels in iron-deficient KTRs.

deficient KTRs who were treated with FCM showed a significant increase in plasma ferritin and TSAT compared to placebo, there was no difference in SARS-CoV-2-specific anti-RBD IgG concentration, seroconversion rate or number of IFN-ɣ-producing T-lymphocytes after vaccination. These results are in contrast with studies in other populations, reporting improved vaccination efficacy after iron supplementation (15). A prior study showed that the antibody response after vaccination against measles virus was significantly stronger in iron-sufficient, compared to iron-deficient Chinese individuals (17). In Kenyan infants, higher TSAT predicted a stronger antibody response after vaccination against *Corynebacterium diphtheriae* and *Streptococcus pneumonia* while a lower transferrin receptor level was associated with a stronger antibody response after vaccination against poliovirus (18). In a randomized trial among the same population, oral iron supplementation before vaccination improved antibody response against measles virus (18). Iron is essential for activation, proliferation and function of T- and B-lymphocytes (17, 28), which might explain impaired vaccine efficacy associated with ID. Based on these findings we hypothesized that correction of ID would improve the immune response against SARS-CoV-2 after vaccination in KTRs. There are several potential explanations for the negative outcome of our study. First, other transplantation-related factors affecting the immune system, most importantly the use of immunosuppressive medication, may have overruled the potential effect of iron supplementation. The majority (83%) of participants was on triple immunosuppressive therapy and used mycophenolic acid; both are factors strongly associated with impaired vaccine response (10). The detrimental effect of mycophenolic acid on vaccine efficacy in KTRs was highlighted by a german study (29) reporting a beneficial effect of temporarily withholding antimetabolite treatment around the time of vaccination, although a recently published trial could not confirm these results (30). Second, we cannot exclude the possibility that iron supplementation has unfavorable effects on the immune system that might have counterbalanced potential beneficial effects. In a recently published meta-analysis, intravenous iron supplementation was associated with a higher infection risk (31), although this was not found in the PIVOTAL trial (32). While specific strains of pathogens need iron to thrive, intravenous iron supplementation may also indirectly increase the risk of infection by inducing oxidative stress, which is toxic to macrophages, neutrophils (33, 34), and lymphocytes (33, 35, 36). Third, the pathophysiological basis of ID in Dutch KTRs likely differs from ID in the previously reported populations, in which nutritional deficits and parasite infections may have played a major role (37). In our KTR population, ID is more likely induced by pro-inflammatory cytokines through upregulation of hepcidin, which prevents iron absorption from the gut and promotes iron entrapment in monocytes (38). In the context of inflammation, systemic ID may result from disordered iron distribution rather than an absolute deficit (39). It could be that only absolute ID affects vaccination response. However, in animal studies, it has been shown that not only absolute ID but also inflammation-associated ID affects T-lymphocyte response to vaccination against adenovirus (40). Furthermore, in humans with genetic hepcidin overexpression, antibody titers against various pathogens after vaccination are decreased (40). Finally, the definition of ID used in the current study may be too liberal. Since ferritin is an acute-phase protein, it can be increased by pro-inflammatory

10.3389/fimmu.2022.1017178

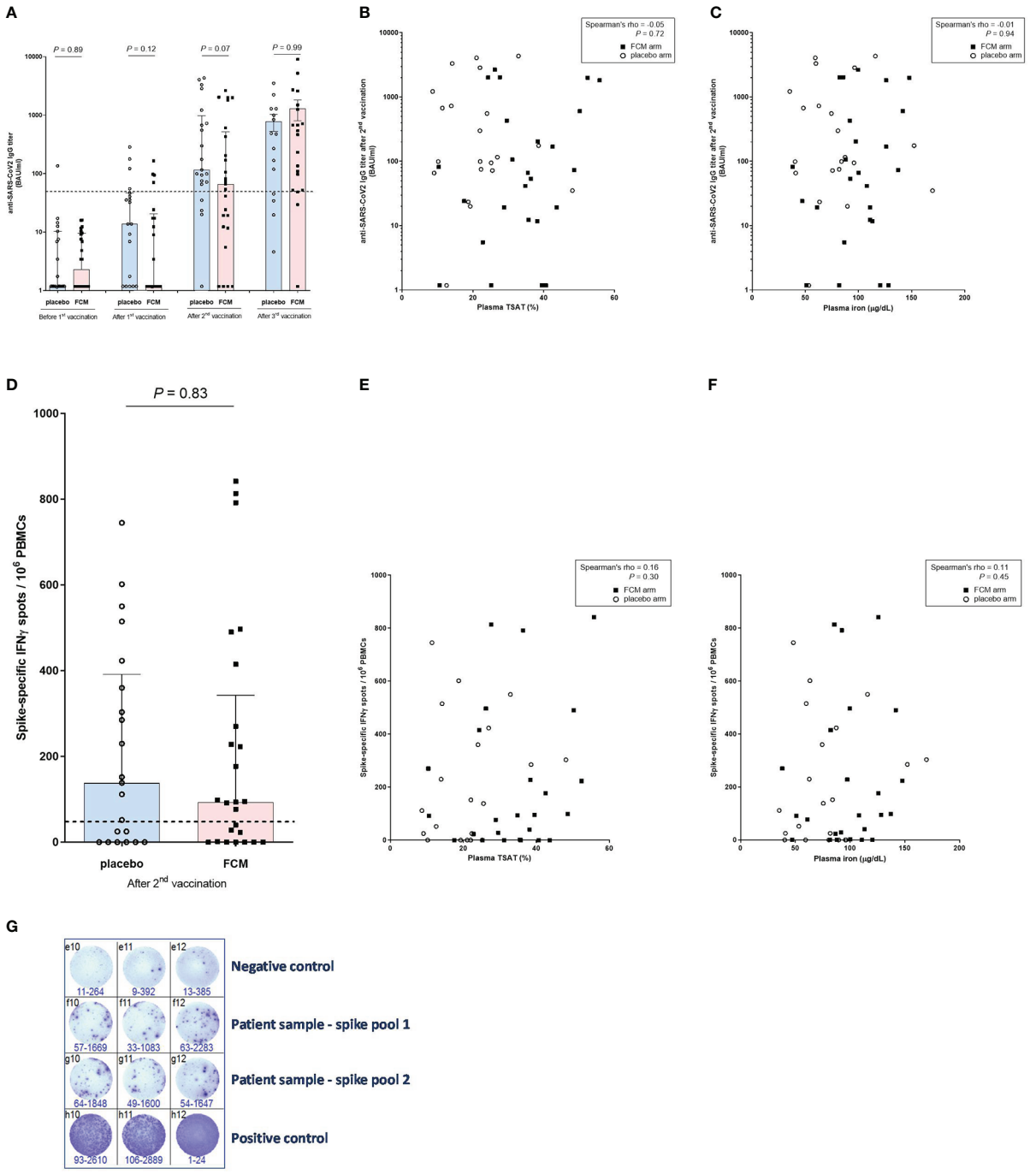

FIGURE 3
Anti-SARS-CoV-2 antibody and T-lymphocyte response. **(A)** Anti-SARS-CoV-2 IgG titers before vaccination and after the successive vaccinations in iron-deficient KTRs who had been treated with ferric carboxymaltose or placebo. The dashed horizontal line represents the threshold for IgG seropositivity. **(B)** Anti-SARS-CoV-2 IgG titers and transferrin saturation (in all participants). **(C)** Anti-SARS-CoV-2 IgG titers and plasma iron (in all participants). **(D)** SARS-CoV-specific T-lymphocyte response in iron-deficient KTRs who had been treated with ferric carboxymaltose or placebo. The dashed horizontal line represents the threshold for a positive T-lymphocyte response. **(E)** SARS-CoV-specific T-lymphocyte response and transferrin saturation (in all participants). **(F)** SARS-CoV-specific T-lymphocyte response and plasma iron (in all participants). **(G)** Example of representative results of an ELISpot assay, with which the SARS-CoV-2-specific T-lymphocyte response was measured in a patient (Spike pool 1 and 2). Interferon-gamma-producing T-lymphcytes after stimulation with SARS-CoV-2 Spike overlapping peptide pools are colored purple. All stimulations are performed in triplicate per peptide pool and the average of the six measurements is calculated. To correct for background activation, the average signal of the negative control is subtracted from the spike response.

cytokines despite a depletion of iron (38). Therefore, we used a much higher cut-off value for plasma ferritin levels than what would be appropriate as a reference in the general population, although it is commonly used in chronic heart failure patients (41). In a sensitivity analysis including only KTRs with severe ID, although with limited statistical power, there was also no difference in SARS-CoV-2-specific vaccine efficacy between the two treatment arms (Supplementary Tables 5, S16, S27).

Notably, although there were no significant differences in antibody response between the treatment groups after any of the three vaccination doses, a small advance of the placebo-treated group seemed to decrease after each vaccination dose, until after the third dose, the median SARS-CoV-2-specific anti-RBD IgG concentration was slightly higher in the FCM-treated group. Another study (13), focusing on the lower antibody response to vaccination in individuals of higher age, showed that the difference between age groups decreased with each dose, thereby highlighting the efficacy of booster vaccination doses, which has also been observed in kidney transplant recipients (30).

In the current study, only 68% of patients had a positive SARS-CoV-2-specific anti-RBD IgG response and 61% had SARS-CoV-2-specific T-lymphocyte activation after the second vaccination. These numbers are similar to results of other studies among KTRs (6–10, 12). In accordance with prior studies (10, 12), there was a significant correlation between SARS-CoV-2-specific anti-RBD IgG titer and the number of IFN-ɣ spots per 10^6 PBMCs. However, it should be emphasized that in some KTRs who remain seronegative after vaccination against SARS-CoV-2, a cellular antibody response can be detected (42). One patient in our study had a SARS-CoV-2-specific anti-RBD IgG concentration above the threshold for a positive response before the first vaccination. This patient was seronegative for total SARS-CoV-2-specific anti-RBD antibodies, but positive for antinucleocapsid antibodies. Therefore, it is unclear whether this patient had previous exposure to SARS-CoV-2 before or the positive IgG titer was based on cross-reactivity with antibodies against other coronaviruses or antigens. Previous studies among KTRs show an incidence of a positive pre-vaccination SARS-CoV-2-specific anti-RBD IgG response of 10% (12). Three patients had a total SARS-CoV-2- specific anti-RBD antibody OD above the threshold at baseline. Two of them also had anti-nucleocapsid antibodies, suggesting previous exposure to SARS-CoV-2. In a sensitivity analysis, all four patients were excluded, and this did not affect the results (Supplementary Table 2, S13, S24).

Our study has several strengths as well as limitations. We had the unique chance to assess vaccine efficacy within the scope of a running clinical trial assessing the impact of treatment with FCM versus placebo in iron-deficient KTRs. Another strength is the simultaneous availability of SARS-CoV-2-specific anti-RBD IgG concentration and data on SARS-CoV-2-specific T-lymphocyte activation. Limitations include the relatively small number of participants; nevertheless, since we did not find any trend towards a positive effect, a larger sample size would be unlikely to lead to a different outcome. The current study involved patients participating in an ongoing clinical trial who had not received all study treatments at the time of the Dutch national COVID-19 vaccination campaign, as well as patients who had finished their participation in the trial up to a year before vaccination. Therefore, there was considerable heterogenicity in the number of treatments received at the time of vaccination and the time between the last treatment and vaccination. Nevertheless, there was a clear difference in iron status between the two arms at the time of measurements four weeks after the second vaccination. At the time of the first vaccination, only a small amount of serum was collected from a finger capillary blood sample (collected with a fingerpick sampled at home). Unfortunately, these samples did not allow us to measure iron status parameters at that time. Furthermore, most patients received the mRNA-1273 vaccine whereas some received the mRNA-BNT162b2 vaccine. However, the results were robust in a sensitivity analysis excluding patients who were vaccinated with mRNA-BNT162b2 (Supplementary Tables 4, S15, S26). We did not perform a pre-vaccination measurement of the SARS-CoV-2-specific T-lymphocyte activation. It can therefore not be excluded that some participants had baseline cellular reactivity, for example resulting from cross-reactivity against antigens of other coronaviruses, which is found in 11% of KTRs (12). Moreover, the results may be biased by other differences between the treatment arms. Patients in both groups were generally well balanced at baseline except for a slightly but significantly lower lymphocyte count and eGFR in the FCM arm. Although lymphocytopenia might restrain an adequate immune response after vaccination (10), thereby masking an effect of FCM, we did not observe an effect of FCM on vaccine efficacy after adjusting for these potential confounders. Of note, there was no correlation between lymphocyte count and number of IFN-ɣ-producing T-lymphocytes or antibody titer. Furthermore, we have not measured neutralizing antibody responses, which would have been an interesting secondary outcome. Finally, the results of our study may be specific for KTRs and cannot be extrapolated to other immunocompromised populations.

In conclusion, in KTRs with ID, intravenous iron supplementation efficiently restored iron status but did not improve the humoral or cellular immune response against SARS-CoV-2 after three vaccinations.

Data availability statement

The raw data supporting the conclusions of this article will be made available by the authors, without undue reservation.

Ethics statement

The studies involving human participants were reviewed and approved by Medical ethical committee of the University Medical Center Groningen (METc 2018/482). The patients/participants provided their written informed consent to participate in this study.

Author contributions

MD and JV developed the study design. JV coordinated the trial. MHdB supervised the trial. DB, MS, TR and J-SS contributed to the study design. DA, RJ, TN, MvdH.and MS performed analyses. All authors contributed to the article and approved the submitted version.

Funding

This study was financially supported by the Dutch Kidney Foundation (grant 17OKG18), Vifor Pharma, and the Tekke Huizenga Foundation (grant STHF-2021.01.02).

Acknowledgments

We thank R. Karsten for organisational support, and W. Dam for technical support.

Conflict of interest

JV received consulting fees from Vifor Pharma (to employer). MHdB has consultancy agreements with Amgen, Astellas, Astra Zeneca, Bayer, Kyowa Kirin, Vifor Pharma, and Sanofi Genzyme, and received grant support from Sanofi Genzyme and Vifor Pharma (all to employer). ME received consultant fees and speakers bureaus from Vifor Pharma and serves on the Advisory Board for Cablon Medical. The results presented in this paper have not been published previously in whole or part, except in abstract format.

The remaining authors declare that the research was conducted in the absence of any commercial or financial relationships that could be construed as a potential conflict of interest.

Publisher's note

Supplementary material

The Supplementary Material for this article can be found online at: https://www.frontiersin.org/articles/10.3389/fimmu.2022.1017178/full#supplementary-material

References

1. Available at: https://covid19.who.int/.

2. Hilbrands LB, Duivenvoorden R, Vart P, Franssen CFM, Hemmelder MH, Jager KJ, et al. COVID-19-related mortality in kidney transplant and dialysis patients: results of the ERACODA collaboration. *Nephrol Dial Transplant* (2020) 35(11):1973–83. doi: 10.1093/ndt/gfaa261

3. Kremer D, Pieters TT, Verhaar MC, Berger SP, Bakker SJL, van Zuilen AD, et al. A systematic review and meta-analysis of COVID-19 in kidney transplant recipients: Lessons to be learned. *Am J Transplant* (2021) 21(12):3936–45. doi: 10.1111/ajt.16742

4. Caillard S, Chavarot N, Francois H, Matignon M, Greze C, Kamar N, et al. Is COVID-19 infection more severe in kidney transplant recipients? *Am J Transplant* (2021) 21(3):1295–303. doi: 10.1111/ajt.16424

5. Goffin E, Candellier A, Vart P, Noordzij M, Arnol M, Covic A, et al. COVID-19-related mortality in kidney transplant and haemodialysis patients: A comparative, prospective registry-based study. *Nephrol Dial Transplant* (2021) 36(11):2094–105. doi: 10.1093/ndt/gfab200

6. Grupper A, Rabinowich L, Schwartz D, Schwartz IF, Ben-Yehoyada M, Shashar M, et al. Reduced humoral response to mRNA SARS-CoV-2 BNT162b2 vaccine in kidney transplant recipients without prior exposure to the virus. *Am J Transplant* (2021) 21(8):2719–26. doi: 10.1111/ajt.16615

7. Husain SA, Tsapepas D, Paget KF, Chang JH, Crew RJ, Dube GK, et al. Postvaccine anti-SARS-CoV-2 spike protein antibody development in kidney transplant recipients. *Kidney Int Rep* (2021) 6(6):1699–700. doi: 10.1016/j.ekir.2021.04.017

8. Rozen-Zvi B, Yahav D, Agur T, Zingerman B, Ben-Zvi H, Atamna A, et al. Antibody response to SARS-CoV-2 mRNA vaccine among kidney transplant recipients: A prospective cohort study. *Clin Microbiol Infect* (2021) 27(8):1173. doi: 10.1016/j.cmi.2021.04.028

9. Danthu C, Hantz S, Dahlem A, Duval M, Ba B, Guibbert M, et al. Humoral response after SARS-CoV-2 mRNA vaccination in a cohort of hemodialysis patients and kidney transplant recipients. *J Am Soc Nephrol* (2021) 32(9):2153–8. doi: 10.1681/ASN.2021040490

10. Sanders JF, Bemelman FJ, Messchendorp AL, Baan CC, van Baarle D, van Binnendijk R, et al. The RECOVAC immune-response study: The immunogenicity, tolerability, and safety of COVID-19 vaccination in patients with chronic kidney disease, on dialysis, or living with a kidney transplant. *Transplantation* (2022) 106 (4):821–34. doi: 10.1097/TP.0000000000003983

11. Korth J, Jahn M, Dorsch O, Anastasiou OE, Sorge-Hädicke B, Eisenberger U, et al. Impaired humoral response in renal transplant recipients to SARS-CoV-2 vaccination with BNT162b2 (Pfizer-BioNTech). *Viruses* (2021) 13(5):756. doi: 10.3390/v13050756

12. Cucchiari D, Egri N, Bodro M, Herrera S, Del Risco-Zevallos J, Casals-Urquiza J, et al. Cellular and humoral response after MRNA-1273 SARS-CoV-2 vaccine in kidney transplant recipients. *Am J Transplant* (2021) 21(8):2727–39. doi: 10.1111/ajt.16701

13. van den Hoogen LL, Boer M, Postema A, de Rond L, de Zeeuw-Brouwer ML, Pronk I. Reduced antibody acquisition with increasing age following

vaccination with BNT162b2: Results from two longitudinal cohort studies in the Netherlands. *Vaccines (Basel)* (2022) 10(9):1480. doi: 10.3390/vaccines10091480

14. Eisenga MF, Minović I, Berger SP, Kootstra-Ros JE, van den Berg E, Riphagen IJ. Iron deficiency, anemia, and mortality in renal transplant recipients. *Transpl Int* (2016) 29(11):1176–83. doi: 10.1111/tri.12821

15. Drakesmith H, Pasricha SR, Cabantchik I, Hershko C, Weiss G, Girelli D. Vaccine efficacy and iron deficiency: an intertwined pair? *Lancet Haematol* (2021) 8(9):e666–9. doi: 10.1016/S2352-3026(21)00201-5

16. Camaschella C. Iron deficiency. *Blood* (2019) 133(1):30–9. doi: 10.1182/blood-2018-05-815944

17. Jiang Y, Li C, Wu Q, An P, Huang L, Wang J, et al. Iron-dependent histone 3 lysine 9 demethylation controls b cell proliferation and humoral immune responses. *Nat Commun* (2019) 10(1):2935. doi: 10.1038/s41467-019-11002-5

18. Stoffel NU, Uyoga MA, Mutuku FM, Frost JN, Mwasi E, Paganini D, et al. Iron deficiency anemia at time of vaccination predicts decreased vaccine response and iron supplementation at time of vaccination increases humoral vaccine response: A birth cohort study and a randomized trial follow-up study in Kenyan infants. *Front Immunol* (2020) 11:1313. doi: 10.3389/fimmu.2020.01313

19. Dufour C, Papadaki H, Warren A. Available at: https://ehaweb.org/covid-19/eha-statement-on-covid-19-vaccines/recommendations-for-covid-19-vaccination-in-patients-with-non-malignant-hematologic-diseases/.

20. Levey AS, Stevens LA, Schmid CH, Zhang Y, Castro AF, Feldman HI, et al. A new equation to estimate glomerular filtration rate. *Ann Intern Med* (2009) 150 (9):604–12. doi: 10.7326/0003-4819-150-9-200905050-00006

21. Okonko DO, Grzeslo A, Witkowski T, Mandal AKJ, Slater RM, Roughton M, et al. Effect of intravenous iron sucrose on exercise tolerance in anemic and nonanemic patients with symptomatic chronic heart failure and iron deficiency FERRIC-HF: a randomized, controlled, observer-blinded trial. *J Am Coll Cardiol* (2008) 51(2):103–12. doi: 10.1016/j.jacc.2007.09.036

22. Camaschella C. Iron-deficiency anemia. *N Engl J Med* (2015) 372(19):1832–43. doi: 10.1056/NEJMra1401038

23. Jolliff CR, Cost KM, Stivrins PC, Grossman PP, Nolte CR, Franco SM, et al. Reference intervals for serum IgG, IgA, IgM, C3, and C4 as determined by rate nephelometry. *Clin Chem* (1982) 28(1):126–8. doi: 10.1093/clinchem/28.1.126

24. Steenhuis M, van Mierlo G, Derksen NI, Ooijevaar-de Heer P, Kruithof S, Loeff FL, et al. Dynamics of antibodies to SARS-CoV-2 in convalescent plasma donors. *Clin Transl Immunol* (2021) 16(10)(5):e1285. doi: 10.1002/cti2.1285

25. Ducloux D, Colladant M, Chabannes M, Bamoulid J, Courivaud C. Factors associated with humoral response after BNT162b2 mRNA COVID-19 vaccination in kidney transplant patients. *Clin Kidney J* (2021) 14(10):2270–2. doi: 10.1093/ckj/sfab125

26. Vogelzang EH, Loeff FC, Derksen NIL, Kruithof S, Ooijevaar-de Heer P, van Mierlo G, et al. Development of a SARS-CoV-2 total antibody assay and the dynamics of antibody response over time in hospitalized and nonhospitalized patients with COVID-19. *J Immunol* (2020) 205(12):3491–9. doi: 10.4049/jimmunol.2000767

27. van der Veldt AAM, Oosting SF, Dingemans AC, Fehrmann RSN, GeurtsvanKessel C, Jalving M, et al. COVID-19 vaccination: the VOICE for patients with cancer. *Nat Med* (2021) 27(4):568–9. doi: 10.1038/s41591-021-01240-w

28. Schaefer B, Effenberger M, Zoller H. Iron metabolism in transplantation. *Transpl Int* (2014) 27(11):1109–17. doi: 10.1111/tri.12374

29. Schrezenmeier E, Rincon-Arevalo H, Jens A, Jens A, Stefanski AL, Hammett C, Osmanodja B, et al. Temporary antimetabolite treatment hold boosts SARS-CoV-2 vaccination-specific humoral and cellular immunity in kidney transplant recipients. *JCI Insight* (2022) 7(9):e157836. doi: 10.1172/jci.insight.157836

30. Kho MML, Lianne Messchendorp A, Frölke SC, Imhof C, Koomen VJCH, Malahe SRK, et al. Alternative strategies to increase the immunogenicity of COVID-19 vaccines in kidney transplant recipients not responding to two or three doses of an mRNA vaccine (RECOVAC): A randomised clinical trial. *Lancet Infect Dis* (2022). doi: 10.2139/ssrn.4176376

31. Shah AA, Donovan K, Seeley C, Dickson EA, Palmer AJR, Doree C, et al. Risk of infection associated with administration of intravenous iron: A systematic review and meta-analysis. *JAMA Netw Open* (2021) 4(11):e2133935. doi: 10.1001/jamanetworkopen.2021.33935

32. Macdougall IC, Bhandari S, White C, Anker SD, Farrington K, Kalra PA, et al. Intravenous iron dosing and infection risk in patients on hemodialysis: A prespecified secondary analysis of the PIVOTAL trial. *J Am Soc Nephrol* (2020) 31 (5):1118–27. doi: 10.1681/ASN.2019090972

33. Ichii H, Masuda Y, Hassanzadeh T, Saffarian M, Gollapudi S, Vaziri ND. Iron sucrose impairs phagocytic function and promotes apoptosis in polymorphonuclear leukocytes. *Am J Nephrol* (2012) 36(1):50–7. doi: 10.1159/000339285

34. Rosen GM, Pou S, Ramos CL, Cohen MS, Britigan BE. Free radicals and phagocytic cells. *FASEB J* (1995) 9(2):200–9. doi: 10.1096/fasebj.9.2.7540156

35. Weiss G. Iron and immunity: a double-edged sword. *Eur J Clin Invest* (2002) 32 Suppl 1:70–8. doi: 10.1046/j.1365-2362.2002.0320s1070.x

36. de Sousa M, Reimão R, Porto G, Grady RW, Hilgartner MW, Giardina P. Iron and lymphocytes: reciprocal regulatory interactions. *Curr Stud Hematol Blood Transfus* (1991) 58):171–7. doi: 10.1159/000419357

37. Pasricha SR, Atkinson SH, Armitage AE, Khandwala S, Veenemans J, Cox SE, et al. Expression of the iron hormone hepcidin distinguishes different types of anemia in African children. *Sci Transl Med* (2014) 6(235):235re3. doi: 10.1126/scitranslmed.3008249

38. Camaschella C, Girelli D. The changing landscape of iron deficiency. *Mol Aspects Med* (2020) 75:100861. doi: 10.1016/j.mam.2020.100861

39. Malyszko J, Malyszko JS, Mysliwiec M. A possible role of hepcidin in the pathogenesis of anemia among kidney allograft recipients. *Transplant Proc* (2009) 41(8):3056–9. doi: 10.1016/j.transproceed.2009.08.003

40. Frost JN, Tan TK, Abbas M, Wideman SK, Bonadonna M, Stoffel NU, et al. Hepcidin-mediated hypoferremia disrupts immune responses to vaccination and infection. *Med (N Y)* (2021) 12 (2)(2):164–79. doi: 10.1016/j.medj.2020.10.004

41. Anker SD, Comin Colet J, Filippatos G, Willenheimer R, Dickstein K, Drexler H, et al. Ferric carboxymaltose in patients with heart failure and iron deficiency. *N Engl J Med* (2009) 361(25):2436–48. doi: 10.1056/NEJMoa0908355

42. Dolff S, Zhou B, Korth J, Luo D, Dai Y, Jahn M, et al. Evidence of cell-mediated immune response in kidney transplants with a negative mRNA vaccine antibody response. *Kidney Int* (2021) 100(2):479–80. doi: 10.1016/j.kint.2021.05.013

frontiers | Frontiers in Immunology

TYPE Original Research
PUBLISHED 12 January 2023
DOI 10.3389/fimmu.2022.985538

OPEN ACCESS

EDITED BY
Mengyao Guo,
Northeast Agricultural University,
China

REVIEWED BY
Shiwen Xu,
Northeast Agricultural University,
China
Eileen Fung,
InnoSense, United States

*CORRESPONDENCE
Ranjan Kumar Nanda
ranjan@icgeb.res.in
Anjan Das
dranjan_gb@yahoo.in

SPECIALTY SECTION
This article was submitted to Nutritional Immunology, a section of the journal Frontiers in Immunology

RECEIVED 04 July 2022
ACCEPTED 28 November 2022
PUBLISHED 12 January 2023

CITATION
Kaushik SR, Sahu S, Guha H, Saha S, Das R, Kupa R-u, Kapfo W, Deka T, Basumatary R, Thong A, Dasgupta A, Goswami B, Pandey AK, Saikia L, Khamo V, Das A and Nanda RK (2023) Low circulatory Fe and Se levels with a higher IL-6/IL-10 ratio provide nutritional immunity in tuberculosis. *Front. Immunol.* 13:985538. doi: 10.3389/fimmu.2022.985538

Low circulatory Fe and Se levels with a higher IL-6/IL-10 ratio provide nutritional immunity in tuberculosis

Sandeep R. Kaushik[1], Sukanya Sahu[1], Hritusree Guha[2], Sourav Saha[2], Ranjit Das[2], Rukuwe-u Kupa[3], Wetetsho Kapfo[3], Trinayan Deka[4], Rumi Basumatary[4], Asunu Thong[5], Arunabha Dasgupta[6], Bidhan Goswami[7], Amit Kumar Pandey[8], Lahari Saikia[4,9], Vinotsole Khamo[3], Anjan Das[2*] and Ranjan Kumar Nanda[1*]

[1]Translational Health Group, International Centre for Genetic Engineering and Biotechnology, New Delhi, India, [2]Department of Respiratory Medicine, Agartala Government Medical College, Agartala, Tripura, India, [3]Healthcare Laboratory and Research Centre, Naga Hospital Authority, Kohima, Nagaland, India, [4]Department of Microbiology, Assam Medical College, Dibrugarh, Assam, India, [5]District Tuberculosis Centre, Kohima, Nagaland, India, [6]Department of Medicine, Agartala Government Medical College, Agartala, Tripura, India, [7]Department of Microbiology, Agartala Government Medical College, Agartala, Tripura, India, [8]Mycobacterial Pathogenesis Laboratory, Translational Health Science and Technology Institute (THSTI), Faridabad, Haryana, India, [9]Department of Microbiology, Gauhati Medical College, Guwahati, Assam, India

Tuberculosis (TB) patients show dysregulated immunity, iron metabolism, and anemia. In this study, circulatory cytokines, trace metals, and iron-related proteins (hepcidin, ferroportin, transferrin, Dmt1, Nramp1, ferritin, ceruloplasmin, hemojuvelin, aconitase, and transferrin receptor) were monitored in case (active tuberculosis patients: ATB) and control (non-tuberculosis: NTB and healthy) study populations (n = 72, male: 100%, mean age, 42.94 years; range, 17–83 years). Using serum elemental and cytokine levels, a partial least square discriminate analysis model (PLS-DA) was built, which clustered ATB patients away from NTB and healthy controls. Based on the PLS-DA variable importance in projection (VIP) score and analysis of variance (ANOVA), 13 variables were selected as important biosignatures [IL-18, IL-10, IL-13, IFN-γ, TNF-α, IL-5, IL-12 (p70), IL-1β, copper, zinc, selenium, iron, and aluminum]. Interestingly, low iron and selenium levels and high copper and aluminum levels were observed in ATB subjects. Low circulatory levels of transferrin, ferroportin, and hemojuvelin with higher ferritin and ceruloplasmin levels observed in ATB subjects demonstrate an altered iron metabolism, which partially resolved upon 6 months of anti-TB therapy. The identified biosignature in TB patients demonstrated perturbed iron homeostasis with anemia of inflammation, which could be useful targets for the development of host-directed adjunct therapeutics.

KEYWORDS

iron metabolism, tuberculosis, anemia of inflammatiom, cytokines, selenium

Introduction

Tuberculosis (TB) is caused by *Mycobacterium tuberculosis* (*Mtb*) infection and is still a major killer worldwide (1). TB patients present with a dysregulated immune system and release pro-inflammatory cytokines inducing a cascade of activities hampering iron homeostasis (2). Hepcidin from hepatocytes is released into the circulation, which subsequently binds to ferroportin, the only known iron exporter, and induces its degradation through ubiquitylation (3). Increased ferroportin degradation leads to reduced circulatory iron and causes anemia of inflammation (AI) (2, 4). Furthermore, during AI, even though the host may have enough stored iron, it becomes unavailable for use and the dietary iron absorption is lowered as well. Although the AI is described as a hallmark of TB, it is only present in a subset of TB patients as shown by a Korean study (5). Moreover, as the metabolic crossroads of iron are also linked to copper, zinc, and selenium levels, and due to their heightened reactivity, intracellular levels of these trace metals are regulated critically by the host (6, 7). However, the host system exploits the indispensability and toxicity of these metals to safeguard itself from bacterial invaders (8). Nutritional immunity is involved in the mechanism that withholds trace metals like iron to limit the pathogen's growth (9, 10). The iron carrier protein transferrin also plays a major role in nutritional immunity by binding and removing labile iron from circulation. In addition, iron transporters Nramp1 and Nramp2/Dmt1 play an essential part in maintaining intracellular iron levels. Nramp2/Dmt1 also helps the host in the dietary uptake of iron from the duodenum. Interlinking host immuno-profile with levels of circulatory trace metals and iron-related proteins may help to better understand the pathophysiology of TB and design newer approaches to develop adjunct therapeutics for TB. In this study, these important molecules were monitored in newly diagnosed TB patients, controls, and followed up TB patients.

Methodology

Ethics statement and subject recruitment

This study was part of a project activity approved by the institutional review board and ethics committees of Agartala Government Medical College-Agartala (protocolF.4[6-9]/AGMC/Academic/IEC Committee/2015/8965, dated 25 April 2018), Nagaland Hospital Authority-Kohima (NHAK/HLRC/RES3/2013/64), Assam Medical College-Dibrugarh (AMC/EC/PG/3530), and International Centre for Genetic Engineering and Biotechnology (ICGEB) New Delhi (ICGEB/IEC/2014/07). After receiving signed informed consent, subjects presenting with 2 weeks of cough, fever, and weight loss at the outpatient departments of the partnering hospitals were recruited (Figure 1A).

Sample collection and subject classification

The sputum and whole blood samples (for serum preparation) were collected from the study subjects. Collected sputum samples were subjected to microscopy and GeneXpert tests, and subjects with positive test results for both tests were grouped as active tuberculosis patients (ATB) while those with negative results were grouped as non-TB (NTB) (Figure 1B) (11). NTB subjects were clinically diagnosed as suffering from asthma, chronic obstructive pulmonary diseases (COPD), lung cancer, and pneumonia. Only male subjects with negative HIV test results were selected. Healthy subjects from a similar background of patients who did not receive any medication for at least 1 week before sampling were recruited as controls. Whole blood samples (4 ml) were collected in vacutainer tubes for serum isolation by centrifuging at 1,500 *g* for 10 min at 4°C. Aliquots of serum were stored at −80°C till further analysis and a maximum of two freeze–thaw cycles were allowed. For the longitudinal study, TB patients were followed up until completion of 6 months of anti-TB treatment [recommended by Revised National TB Control and Programme (RNTCP), Government of India]. TB patients were given a fixed dose of four drugs (isoniazid, rifampicin, ethambutol, and pyrazinamide) during 2 months of intensive phase followed by two drugs (isoniazid and rifampicin) during the continuation phase (Figure 1B).

Micronutrient profiling in serum samples using inductive coupled plasma mass spectrometry (ICP-MS)

Serum samples (50 µl) were subjected to microwave digestion using HNO_3 (225711, Sigma, USA) and H_2O_2 (Supelco, 107298, Hydrogen peroxide 30% Suprapur®) in a Multiwave-Pro digestor (Anton Paar, USA) for 30 min at 140°C. The digested serum samples were diluted using ultrapure water (Honeywell) to bring the acid concentration below permissible limit for ICP-MS data acquisition. The diluted digested samples were fed to ICP-MS (Thermo Scientific iCAP-TQ) in kinetic energy discrimination (KED) mode using helium for data acquisition (12, 13). Serum trace metal levels in the test samples were quantified using the total dilution factor.

Serum cytokine profiling

Serum pro-inflammatory [interleukin (IL)-1β, IL-18, IL-2, IL-6, IL-12, interferon (IFN)-γ, and tumor necrosis factor (TNF)-α] and anti-inflammatory cytokine (IL-4, IL-5, IL-10, and IL-13) levels were quantified using a Bioplex Microplate

array reader (Bio-Rad Bio-Plex 200 Systems, USA) by using a 11-plex custom kit from Bio-Rad. Briefly, to the diluted serum samples, conjugated beads (Bio-Rad, USA) were added followed by biotinylated detection antibodies. After adding streptavidin to the test samples, standards, and blanks, the fluorescence intensity for all the bead regions was measured using a Bioplex Microplate array reader (Bio-Rad Bio-Plex 200 Systems, USA). All the washing steps were performed using the MAGPIX wash station.

Western blot experiment

Equal amounts of serum proteins related to iron metabolism (transferrin, transferrin receptor, ferroportin, hepcidin, Dmt1, Nramp1, aconitase, hemojuvelin, ferritin, and ceruloplasmin) from study subjects were probed by Western blot analyses. Briefly, denatured serum proteins were loaded on sodium dodecyl sulfate-polyacrylamide gel electrophoresis (SDS-PAGE) gel for separation and transferred to PVDF membrane using a Semi-dry transfer apparatus (TE77, semi dry apparatus, Amersham). The blots were incubated with primary antibody (transferrin; ab82411, dilution: 1/10,000), transferrin receptor; ab1086 (1/500), ferroportin; ab78066 (1/500), hepcidin; ab30760 (1/250), Dmt1; ab55735 (1/500), Nramp1; ab59696 (1/500), aconitase; ab126595 (1/1,500), and hemojuvelin; ab54431 (1/1,000) from Abcam, USA and ferritin; D1D4 (1/1,000) and ceruloplasmin; D7Q5W (1/1,000) from Cell Signaling Technology, USA) overnight at 4°C using a shaker. After washing, the blots were incubated with secondary antibody (Anti-Rabbit, Sigma A-6154) for 2 h and developed using Pico-Plus enhanced chemiluminescence (ECL) (Pierce, Thermo Fisher) on x-ray films or imaging system (ChemiDoc MP Bio-Rad, USA). ImageJ (version 1.53e) was used for densitometric calculations. Parallel gels were run using an equal serum protein amount (5 µg) from the study samples and silver stained for every blot.

Statistical analysis

MetaboAnalyst 5.0 tool was used for Partial Least Square-Discriminate Analysis (PLS-DA) model building (14). Variables with a variable importance in projection (VIP) score >0.6 and analysis of variance (ANOVA) were selected as important markers. OriginPro 2020b (64-bit) 9.7.5.184 (Student Version) was used for box plots, line plots, scatter plots, and correlation analysis. Univariate statistical tools like Student's *t*-test (paired or unpaired) were performed to calculate the significance level of variation between groups and a *p*-value <0.05 was considered as statistically significant at the 95% confidence interval.

Results

Study subjects

A total of 72 male subjects from northeastern parts of India were included in this study (Figure 1A and Table 1). Circulatory iron levels are significantly altered during the reproductive cycle of female subjects and thus excluded from the present study (4, 15). All study subjects were age-matched including ATB (n = 29, mean age in years 41.62), NTB (n = 20, 46.30), and healthy (n = 23, 41.43) groups and show statistically insignificant variation in their age between study groups (Figure 1C). Approximately 40% of these patients were smokers or ex-smokers in ATB and NTB groups (Table 1).

Tuberculosis patients show reduced circulatory iron and selenium levels

Lower levels of circulatory iron were observed in the ATB study group compared to healthy controls (Figure 2A). Although the serum iron levels were quite low in all ATB subjects, it was not statistically significant compared to healthy subjects. In ATB subjects, lower selenium levels were observed compared to healthy subjects (Figure 2B). Additionally, lower selenium levels were observed in NTB subjects as well compared to healthy individuals (Figure 2B). Interestingly, both TB patients and disease control groups showed similar selenium levels, and it was found to be significantly lower only in the ATB group compared to healthy controls group ($p < 0.05$).

Higher aluminum abundance can be a risk factor for TB

Higher aluminum levels were noticed in ATB patients consistently compared to both control groups (Figure 2C). Aluminum levels were found to be elevated (>2-fold) in the ATB group ($p < 0.05$) compared to the healthy group. Interestingly, both ATB and NTB patient groups showed higher serum aluminum levels compared to healthy controls (Figure 2C).

Pro-inflammatory cytokines were comparable except IL-18

High circulatory interleukin-18 (IL-18) levels were observed in ATB compared to both NTB and healthy controls ($p < 0.01$) (Figure 3A). The IL-18 levels were roughly threefold higher in the ATB group compared to the NTB group (fold change: FC = 2.46) and healthy group (FC = 2.74). IL-1β, IL-2, IL-6, and TNF-α levels were comparable among all three groups (Figures 3D–G). Interestingly, we observed lower IL-12 and IFN-γ levels in the ATB group (Figures 3B, C).

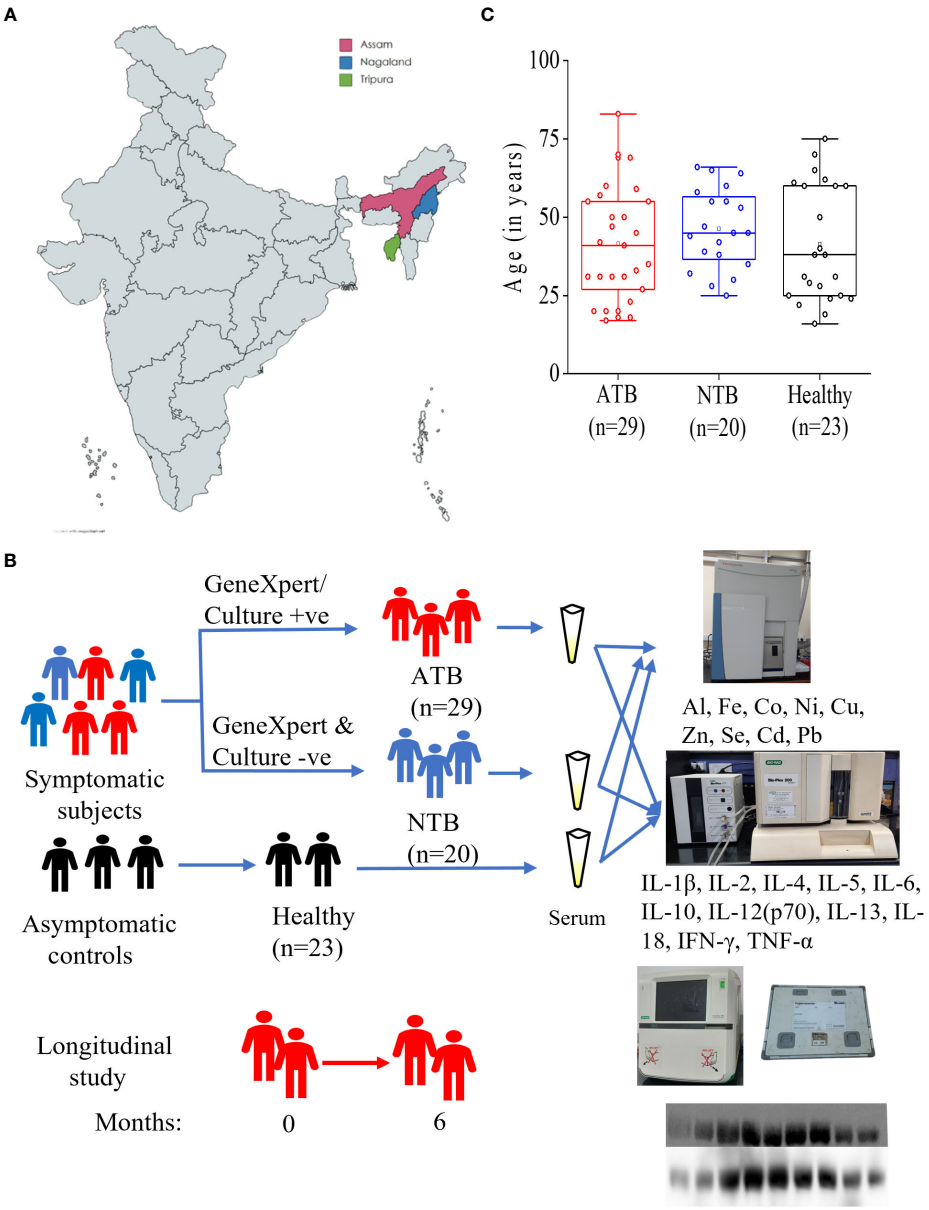

FIGURE 1
Schematic representation of study cites **(A)**, subject classification for serum elemental, cytokine and iron metabolism related protein analyses **(B)**. Box plot representing the age of active tuberculosis (ATB), non-tuberculosis (NTB) and healthy control subjects **(C)**.

Cytokine profiling revealed downregulated Th2 cytokines' expression

A lower level of anti-inflammatory cytokines (IL-4, IL-5, IL-10, and IL-13) was observed in the ATB group compared to healthy controls (Figures 3H–K). The anti-inflammatory interleukins were found to be comparable in both control groups and the lowest in the ATB group. It shows an overall low Th2 cytokines' profile in the ATB group.

IL-6/IL-10 and TNF-α/IL-10 ratios characterized the ATB profile

Although the IL-6 levels were comparable between three groups, a significantly higher IL-6/IL-10 were observed in the ATB study group (threefold) compared to the healthy group (4.88, 1.58; $p < 0.05$) (Figure 4A). Similarly, we observed a more than fivefold higher TNF-α/IL-10 in the ATB group (18.4, $p < 0.001$) compared to the healthy group (3.4) (Figure 4B). This indicated

10.3389/fimmu.2022.985538

TABLE 1 Epidemiological details of the study subjects used in this study.

Study groups	Total	ATB	NTB	Healthy
Subject (*n*)	72	29	20	23
Clinical sites (AGMC/AMC/NHAK)	46/14/12	15/8/6	14/3/3	17/3/3
Mean age (range) in years	42.94 (16–83)	41.62 (17–83)	46.30 (25–66)	41.43 (16–75)
Male (%)	100%	100%	100%	100%
AFB or GeneXpert (+ve/−ve/na)	29/20/23	29/-/-	-/20/-	-/-/23
Alcoholic (yes/no/Ex/na)	12/38/1/21	1/16/-/12	4/12/1/3	7/10/-/6
Smoker (yes/no/Ex/na)	20/28/3/21	4/11/2/12	7/9/1/3	9/8/-/6
Expectoration (yes/no/na)	41/14/17	23/5/1	15/2/3	3/7/13
Cough (yes/no/na)	49/6/17	25/3/1	17/-/3	7/3/13
Fever (yes/no/na)	19/33/18	13/15/2	6/8/3	-/10/13
Hemoptysis (yes/no/na)	10/46/16	7/22/-	3/14/3	-/10/13
Chest Pain (yes/no/na)	24/31/17	15/13/1	6/11/3	3/7/13
Breathlessness (yes/no/na)	21/33/17	13/14/1	6/11/3	2/8/13
Wheeze (yes/no/na)	15/38/19	9/18/2	4/12/4	2/8/13

AGMC, Agartala Government Medical College Agartala; AMC, Assam Medical College-Dibrugarh; NHAK, Nagaland Hospital Authority-Kohima; +ve, positive; −ve, negative; na, Not available; n, sample size (available data).

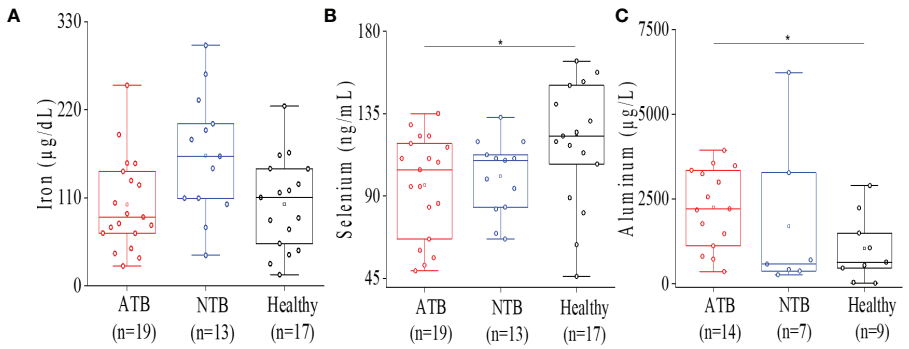

FIGURE 2
Serum ICP-MS analysis showed altered micro elemental profile in ATB patients. Box plot representation for iron levels in ATB, NTB, and healthy groups **(A)**. Box plot representation for selenium levels in ATB, NTB, and healthy groups **(B)**. Box plot representation for aluminum levels in ATB, NTB, and healthy groups **(C)** (*$p < 0.05$).

Th1 cytokine predominance and pronounced Th1 expression in the ATB group. Interestingly, we noticed a strong inverse correlation between IL-6 and iron levels in the ATB group, which was absent in the NTB group (Figures 4C, S1).

A potential biosignature of essential elements and cytokines could differentiate ATB patients from controls

We combined the cytokine and trace metal data to build a predictive partial least square discriminate analysis (PLS-DA) model that could cluster the ATB study subjects away from both control groups (Figure 2, S2, 3, 5A). Based on the VIP score and analysis of variance (ANOVA), a total of 13 variables [IL-18, IL-10, IL-13, IFN-γ, TNF-α, IL-5, IL-12 (p70), IL-1β, Cu, Zn, Al, Fe, and Se] were selected for pairwise correlation (Pearson *r*) analysis (Figures 5B, C). The IL-1β, IFN-γ, TNF-α, and IL-18 cytokines were found to be highly correlated with each other in the ATB group. In addition, a highly negative correlation ($r = -0.87$) was observed between selenium and aluminum in ATB patients (Figures 5C, S3). Furthermore, we observed a fairly negative correlation between IFN-γ and aluminum in ATB ($r = -0.5$) and NTB ($r = -0.52$), while a moderately positive correlation was observed in the healthy control group ($r = 0.53$) (Figures 5C, S3). Also, we noticed a strong correlation ($r = 0.87$) between aluminum and IL-10 in the NTB group (Figures 5C, S3). In addition, iron, zinc, and selenium were also found to be fairly correlated among themselves, while a weak to moderate correlation was observed with certain cytokines (Figures 5C, S3).

10.3389/fimmu.2022.985538

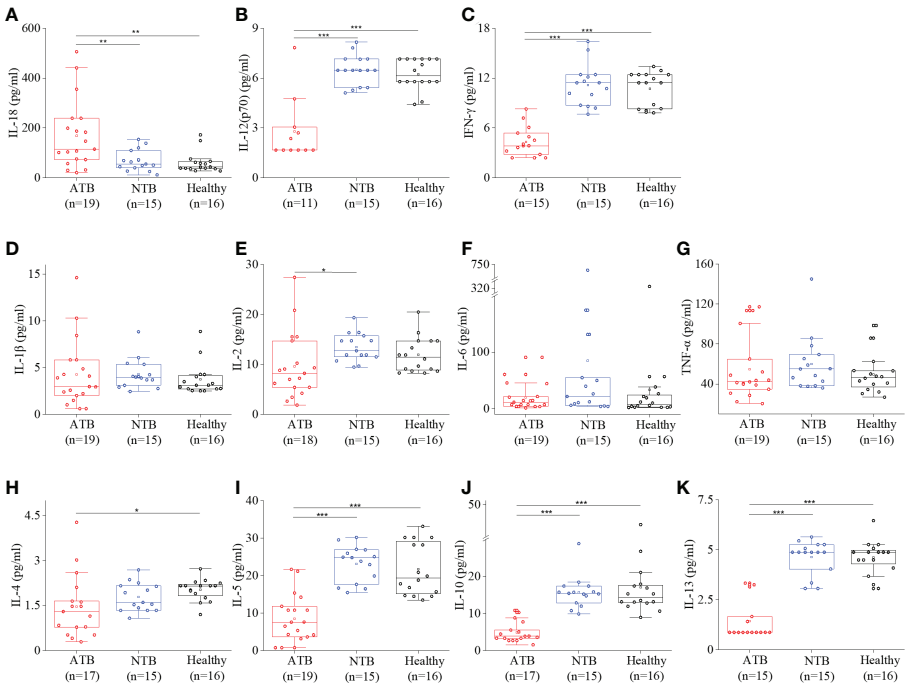

FIGURE 3
Cytokine profiling showed a robust Th1 response in ATB patients. Box plots for individual serum cytokine levels using Bioplex-200 for **(A)** IL-18, **(B)** IL-12, **(C)** IFN-γ, **(D)** IL-1β, **(E)** IL-2, **(F)** IL-6, **(G)** TNF-α, **(H)** IL-4, **(I)** IL-5, **(J)** IL-10, and **(K)** IL-13 in ATB, NTB, and healthy groups (*$p < 0.05$, **$p < 0.01$, ***$p < 0.001$).

Higher expression of inflammatory marker proteins observed in ATB and NTB subjects

In chronic diseases, like TB, higher levels of inflammatory marker proteins (ceruloplasmin and ferritin) were expected, and we also observed higher abundance in ATB patients and NTB controls compared to healthy subjects (Figure 6A). In addition, we also monitored the hepcidin levels, and the lowest levels were observed in the ATB group. In longitudinally followed up ATB patients, we observed a treatment-induced reduction in the abundance of these proteins (Figure 6A).

Iron carrier proteins were found to be reduced in TB patients

The iron carrier protein (i.e., transferrin) levels were monitored in serum samples of study subjects to get a better understanding of iron homeostasis. Interestingly, the serum transferrin levels in ATB patients were lower compared to both control groups (Figure 6B). Interestingly, the circulatory sTfR (serum transferrin receptor) levels were higher in TB patients compared to healthy controls (Figure 6B). Both these proteins showed a reverse longitudinal trend in followed up patients, and we noticed increased transferrin levels with reduced TfR levels in ATB patients completing 6 months of TB treatment compared to their drug-naïve status (Figure 6B).

Iron-sensing protein hemojuvelin and aconitase 1 (IRP1) were found altered in TB patients

Furthermore, we monitored the expression of hemojuvelin (HJV), an important iron-sensing protein, and observed a significantly lower circulatory level in ATB patients compared to controls (Figure 6C). We also monitored the circulatory level of the iron regulatory protein (IRP1) and observed lower levels of it in ATB subjects compared to controls (Figure 6C). In the longitudinally followed samples, the trend of HJV and IRP1 showed significant improvement in patients completing TB treatment (Figure 6C).

Iron transporters and their expression in TB patients

Iron transporters play a critical role in iron metabolism, and we monitored the circulatory levels of iron transporters (ferroportin, Nramp1, and Dmt1) to assess the altered iron

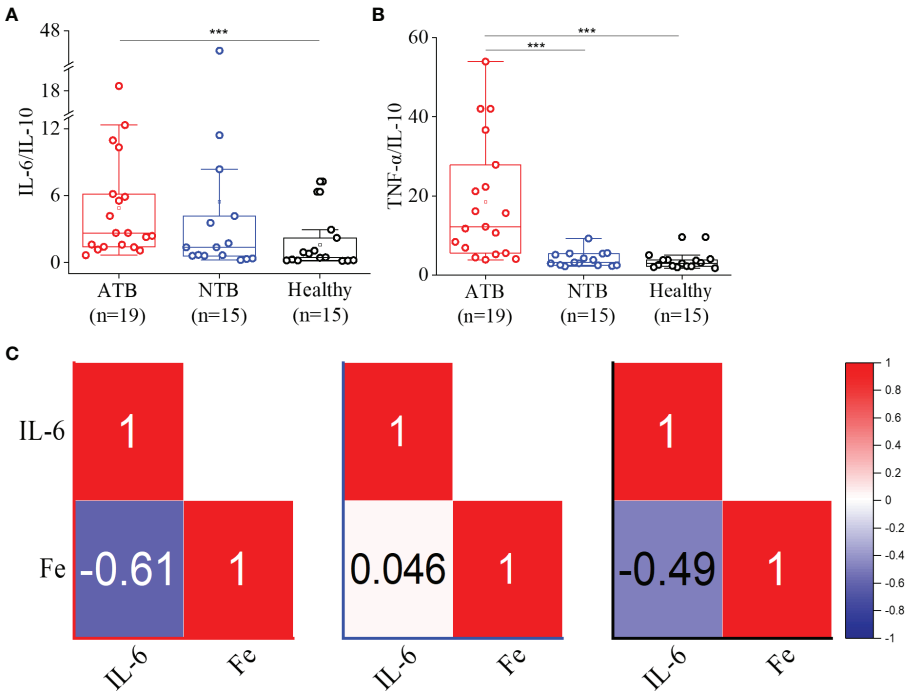

FIGURE 4
Higher IL-6/IL-10 and TNF-α/IL-10 ratios observed in ATB patients. Box plots for IL-6/IL-10 **(A)** and TNFα/IL-10 **(B)** ratios in the ATB, NTB, and healthy study groups. Correlation (Pearson *r*) values between the serum IL-6 and iron (Fe) levels in active tuberculosis (ATB), non-tuberculosis (NTB), and healthy control groups **(C)** (***$p < 0.001$).

metabolism in TB patients. The lowest ferroportin levels were observed in ATB patients, with intermediate levels in NTB patients and the highest levels in healthy subjects (Figure 6D). We also monitored circulatory Nramp1 levels and interestingly observed significantly lower levels in ATB patients compared to both control groups, which slightly improves after completion of treatment (Figure 6D). A similar trend was also noticed for Nramp2/Dmt1 (Figure 6D).

Discussion

Iron is an important metal for all life forms as it is involved in several key processes like DNA synthesis, energy production, and respiration; thus, iron homeostasis is extremely vital. Iron homeostasis is regulated by several key hormones and transporters, which modulate the cellular and circulatory iron levels in response to various stimuli such as erythropoiesis requirement, and inflammation and change in labile iron pool constitute an integral part of this modulation (Figure 7A) (4). Free iron is known to cause Fenton reaction and is thus involved in free radical generation, which can aggravate the inflammation. Therefore, iron levels are maintained in a narrow range to avoid excess or deficiency, both of which are detrimental to the host.

Iron is equally important to the *Mtb* as to the host, and thus, there is a constant fight for this crucial element between host and pathogen. Humans and *Mtb* have evolved constantly to develop various strategies to control this essential element, and it is evident that the host developed intrinsic tools to keep the available iron in check and limits its access to *Mtb*. From our results and literature, it is proven that the host takes imminent steps to lock the iron in cellular stores even at the cost of self-damage (anemia); thus, there is significantly low iron present in circulation (16). As iron is one of the important redox elements, we have looked into other redox elements as well and noticed that copper levels were marginally increased during infection (Figure S2). We noticed a severe drop in selenium levels, which is extremely important for free radical neutralization being part of selenoproteins including glutathione peroxidase (17). Through nutritional immunity, the host sequesters circulatory trace metals, including iron, to limit pathogenicity during infection and the observed changes in trace metal levels might be benefiting the host (9, 10, 15–17).

We have also estimated the serum aluminum levels of study subjects. Interestingly, serum aluminum levels were found to be significantly higher in ATB patients and were inversely correlated to selenium levels (Figures 2, 5C). As we know, aluminum is a trivalent ion, and it can replace ferric iron. Higher circulatory aluminum may saturate transferrin binding

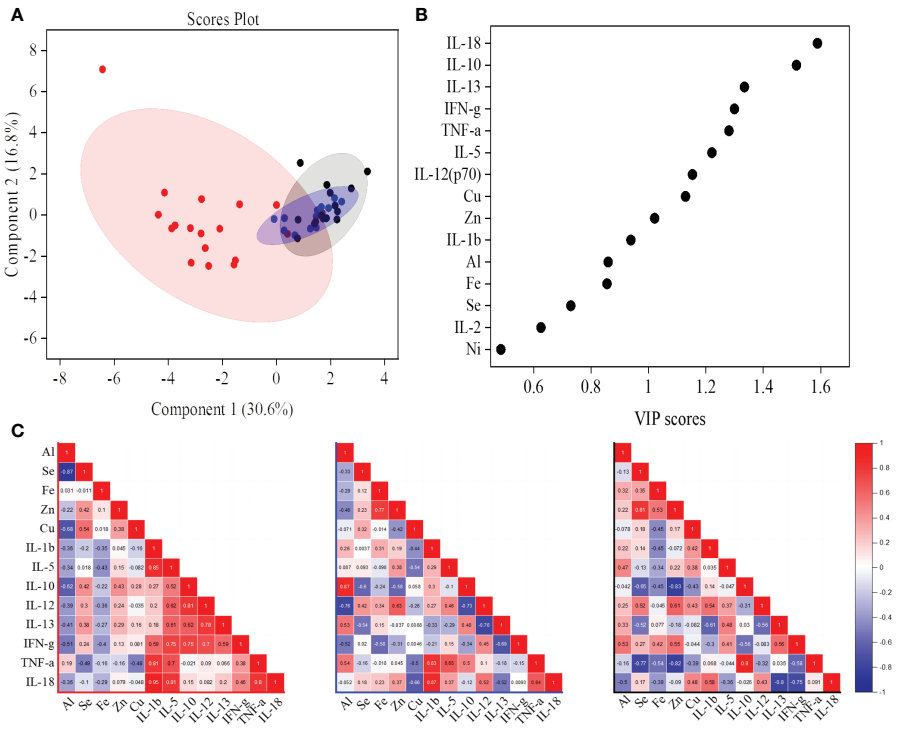

FIGURE 5
A partial least squares discriminant analysis (PLS-DA) model of identified serum cytokines and trace metals showed the active tuberculosis (ATB) study group cluster away from non-tuberculosis (NTB) and healthy control subjects **(A)**. Important cytokines and trace metals identified based on the variable importance in projection (VIP) score from the PLS-DA model **(B)**. Correlation (Pearson *r*) values between important markers [common molecules from VIP score and analysis of variance (ANOVA)] in ATB, NTB, and healthy study groups **(C)**.

sites and aluminum toxicity may impact hematopoiesis under hypoferric conditions (18, 19). Our findings indicate that low iron and high aluminum circulatory levels in TB patients have a negative impact on the immunity. Interestingly, we noticed a negative correlation between aluminum levels and IFN-γ, which could be responsible for lower IFN-γ levels observed in ATB patients. The role of aluminum in TB disease establishment and pathology needs further validation in a larger cohort. In the study population, circulatory levels of other microelements (zinc, nickel, and cobalt) did not show significant variation between the groups (Figure S2). In addition, heavy metals like lead and cadmium were monitored, and a marginally higher cadmium level in ATB patients that was below the toxic level (<5 μg/L) (Figure S2) was observed (20).

It is well known that in chronic inflammatory conditions, the pro-inflammatory as well as anti-inflammatory cytokine profiles are altered. Inflammation is an integral part of infectious diseases like TB and similar observations were observed in our study subjects (21). IL-18 is a pro-inflammatory cytokine and belongs to the IL-1 superfamily like IL-1β, and we observed a strong correlation between these two (r = 0.95). A higher level of circulatory IL-18 was observed in ATB patients corroborating earlier reports (22). It initiates the cascade of signaling to induce Th1 response especially IFN-γ in the presence of IL-12 and enhances the cell-mediated cytotoxicity (23, 24). As expected, IL-18 levels were significantly high in TB patients, but to our surprise, we did not witness a high IL-12 level, which further shows why we did not observe a mounted IFN-γ response in contrast to earlier reports (22, 25). Another reason for low serum IFN-γ levels could be because IFN-producing cells localize near the site of infection in TB, resulting in low circulatory IFN-γ levels. Interestingly, other important pro-inflammatory cytokines like IL-1β, IL-2, IL-6, and TNF-α did not show any significant changes among study groups but were found to be correlated with each other in the ATB group (Figures 3D–G). At the same time, we did notice that the anti-inflammatory cytokine IL-4 was significantly low in ATB patients compared to controls. IL-4 determines the Th2 response through STAT6 and GATA3. As IL-4 is low, it is anticipated that Th2 cytokines will be low, and similar findings were observed in this study. Importantly, high IL-6/IL-10 and TNF-α/IL-10 ratios were observed in ATB patients. Lower levels of IFN-γ and IL-10 have been reported to be directly linked to TB cure, and we have observed a positive correlation between these two (26). From the individual cytokine levels, it seems that ATB patients do not show a strong Th1 response, but the cytokine ratios prove it otherwise (Figures 4A, B).

10.3389/fimmu.2022.985538

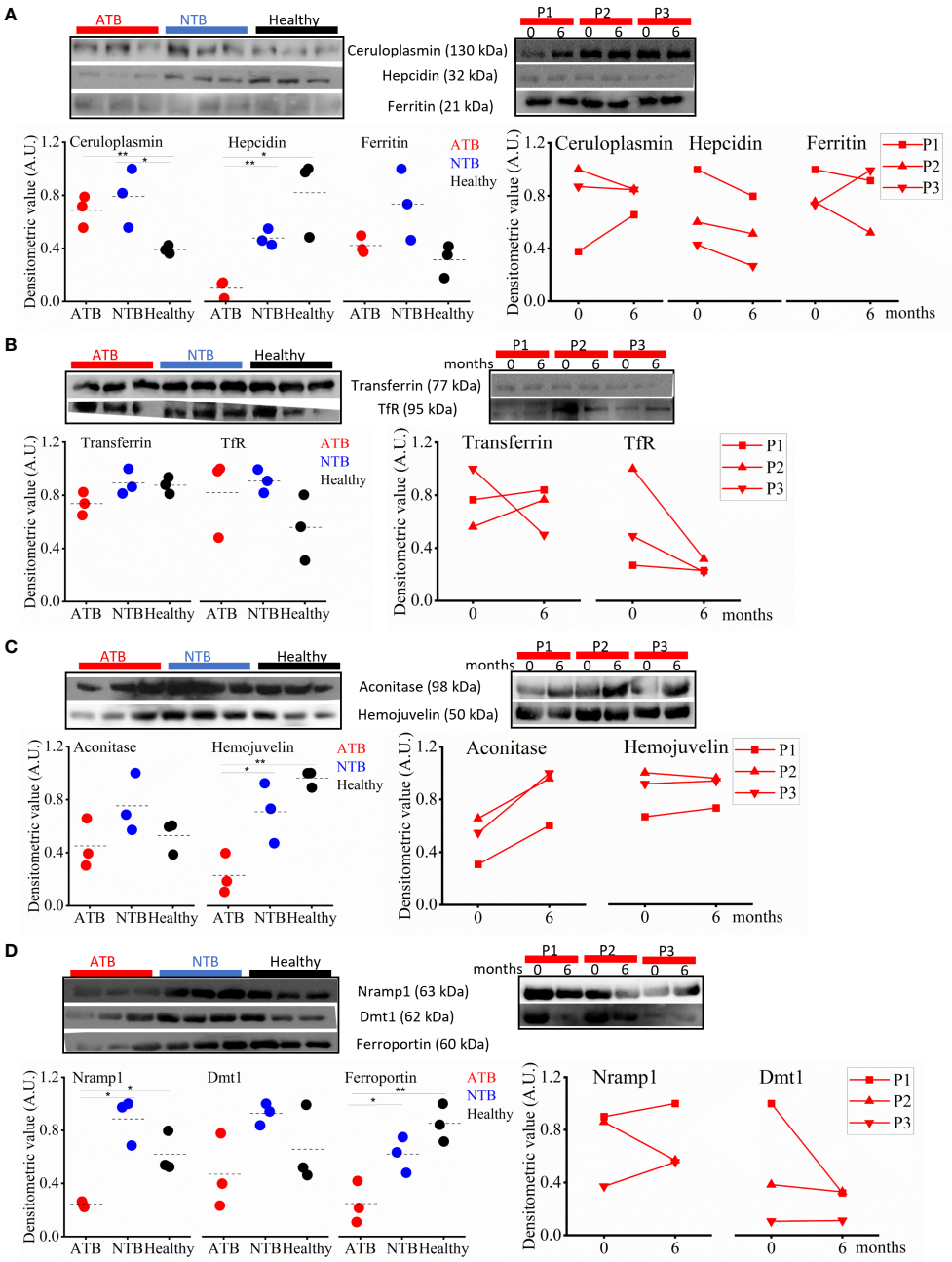

FIGURE 6
Perturbed iron homeostasis indicating iron sequestration observed in active tuberculosis (ATB) patients. Western blot images and densitometric value expression in ATB, non-tuberculosis (NTB), and healthy controls and in longitudinally followed up tuberculosis patients at case presentation (0 months) and upon completion of treatment (6 months) in inflammatory marker proteins (ceruloplasmin, ferritin, and hepcidin) **(A)**, iron carrier proteins (transferrin and TfR) **(B)**, iron-sensing proteins (hemojuvelin and IRP1) **(C)**, and iron transporter proteins (ferroportin1, Nramp1, and Dmt1) **(D)** (P, patient; TfR, Transferrin receptor; IRP1, Iron regulatory protein 1; Nramp1, Natural resistance-associated macrophage protein 1; Dmt1, Divalent metal ion transporter 1; A.U., arbitrary unit; $*p < 0.05$; $**p < 0.01$).

The inflammatory response in infectious diseases like TB lowers labile iron pool and alters erythropoiesis requirements, which may be contributed by differential expression of iron carrier, transporters, and storage proteins. First, we looked into the inflammatory marker proteins' expression and found significantly higher circulatory ceruloplasmin and ferritin levels, and as expected, reduced abundance of these molecules was observed in ATB patients completing anti-TB therapy

(Figures 6A, 7B) (16, 27, 28). Ferritin stores iron; hence, under infection-associated inflammation conditions, its level should increase to sequester the iron in cellular stores. Next, we looked at the hepcidin–ferroportin axis; although we did not notice a surge in hepcidin, we interestingly observed significantly low levels of ferroportin in TB patients, which further point towards iron sequestration in cellular stores (29–33). The reduced circulatory levels of iron carrier proteins like transferrin in ATB patients (Figure 6B) might be because of reduced circulatory iron levels (16). Higher transferrin receptor and low transferrin levels observed in ATB subjects (Figure 6B and Figures S4–S8) might enhance holotransferrin–transferrin receptor complex formation to deplete the circulatory iron and transferrin. Iron-sensing proteins like hemojuvelin and aconitase (IRP1) were found to be

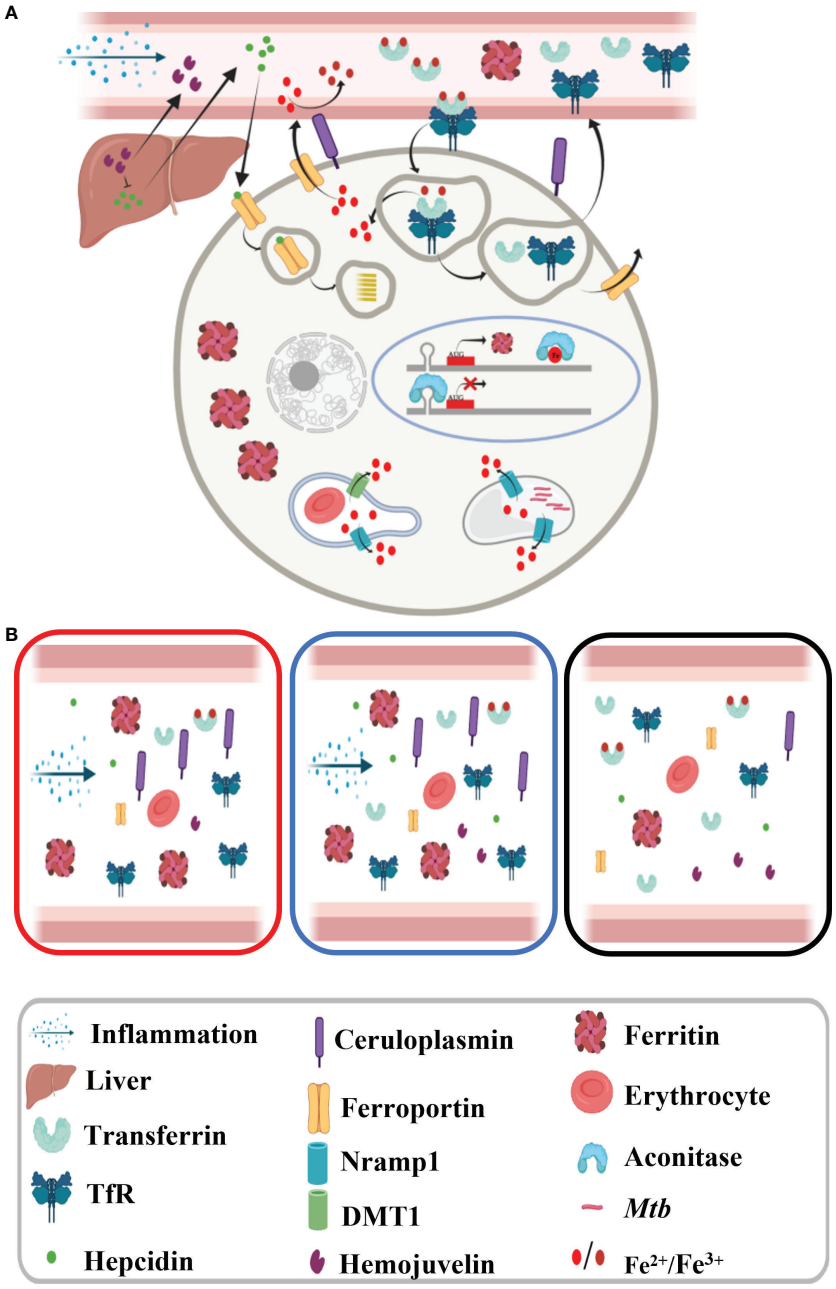

FIGURE 7
Schematic diagram showing iron metabolism in healthy subjects. **(A)** Macrophage showing iron metabolism homeostasis and **(B)** dysregulated iron metabolism in tuberculosis patients and non-tuberculosis subjects compared to healthy controls.

lower in ATB subjects (Figures 6C, S4–S8) (33, 34). Inflammation reduces hepatic hemojuvelin production and impacts iron sensing, which might be happening in these TB patients (Figure 7B) (35, 36). In addition, the iron transporters Nramp1 and Nramp2 (Dmt1) involved in cellular influx of iron were found to be reduced in TB patients' serum samples compared to NTB and healthy controls. Nramp1 is involved in an evolutionary role to deplete the phagosomal iron by transporting phagosomal iron (Fe^{2+}) to the cytosol; it may be an important host factor to starve the pathogen for iron. Decreased Nramp1 levels indicate that *Mtb* interferes with the host system to retain the iron in the phagosome to survive and thrive. Keeping in view the Nramp1 polymorphism, this can be an interesting aspect to explore nutritional immunity. Most of these iron-metabolizing proteins show a trend returning towards baseline after completion of a 6-month-long anti-TB treatment (Figures 6A–D and S7) and none of these TB drugs targeting on the host iron metabolism. It seems that although altered iron metabolism in TB patients is well known, its therapeutic potential is less explored. Although this study has a small population size, it provides detailed profiling of trace metals, cytokines, and abundance of iron-metabolizing proteins in an important study population. These findings, after careful validation in a larger population size in diverse clinical settings, will be useful to understand nutritional immunity and develop additional therapeutic strategies.

In conclusion, our study demonstrated a dysregulated iron homeostasis and suppressed Th2 profile. This research provides evidence for paradigms in nutrient metal homeostasis at the host–pathogen interface. The clinical benefits of selenium supplementation in TB patients need further validation. Additionally, the observed AI and dysregulated iron homeostasis in TB patients may provide a useful target for adjunct therapeutics development.

Data availability statement

The raw data supporting the conclusions of this article will be made available by the authors, without undue reservation.

Ethics statement

The studies involving human participants were reviewed and approved by Institutional Ethics Committee, AGMC, NHAK, AMC and ICGEB. Written informed consent to participate in this study was provided by the participants' legal guardian/next of kin.

Author contributions

SK and SuS carried out all the laboratory profiling experiments. Study subject recruitment for classification was conducted by HG, RD, SoS, RD, RK, WK, TD, and RB under the guidance of AT, ArD, BG, LS, VK, and AnD. Funds for this work were generated by RN, LS, VK, and AnD. AP shared resources and was involved in experimental planning. SK and RN wrote the first draft of the manuscript and revised it, incorporating the comments of all authors. All authors contributed to the article and approved the submitted version.

Funding

Department of Biotechnology (DBT), Government of India: BT/510/NE/TBP/2013 Department of Biotechnology (DBT), Government of India: MDR-TB/2017/39.

Acknowledgments

We acknowledge the Department of Biotechnology (DBT), Government of India for supporting activities through research grants (BT/510/NE/TBP/2013 dated 11-08-2014 and MDR-TB/2017/39) and ICGEB New Delhi for providing access to ICP-MS facility and core support. SK received Senior Research Fellowship from the DBT and SuS received support from the Council of Scientific and Industrial Research (CSIR) New Delhi. All hospital staff involved in subject recruitment, testing, and classification are highly acknowledged. We thank Subia Akram for assisting in diagram preparation using BioRender.

Conflict of interest

The authors declare that the research was conducted in the absence of any commercial or financial relationships that could be construed as a potential conflict of interest.

Publisher's note

Supplementary material

The Supplementary Material for this article can be found online at: https://www.frontiersin.org/articles/10.3389/fimmu.2022.985538/full#supplementary-material

References

1. *GLOBAL TUBERCULOSIS REPORT* (2020). Available at: https://apps.who.int/iris/bitstream/handle/10665/336069/9789240013131-eng.pdf (Accessed 12/Aug/2021).

2. Gil-Santana L, Cruz LAB, Arriaga MB, Miranda PFC, Fukutani KF, Silveira-Mattos PS, et al. Tuberculosis-associated anemia is linked to a distinct inflammatory profile that persists after initiation of antitubercular therapy. *Sci Rep* (2019) 9(1381):1–8. doi: 10.1038/s41598-018-37860-5

3. Domenicoa ID, Lo E, Ward DM, Kaplan J. Hepcidin-induced internalization of ferroportin requires binding and cooperative interaction with Jak2. *PNAS* (2009) 106(10):3800 –3805. doi: 10.1073/pnas.0900453106

4. Drakesmith H, Nemeth E, Ganz T. Ironing out ferroportin. *Cell* (2015) 22 (5):777–87. doi: 10.1016/j.cmet.2015.09.006

5. Lee SW, Kang AY, Yoon YS, Um SW, Lee SM, Yoo CG, et al. The prevalence and evolution of anemia associated with tuberculosis. *J Korean Med Sci* (2006) 21 (6):1028–32. doi: 10.3346/jkms.2006.21.6.1028

6. Choi JW, Kim SK. Relationships of lead, copper, zinc, and cadmium levels versus hematopoiesis and iron parameters in healthy adolescents. *Ann Clin Lab Sci* (2005) 35(4):428–34.

7. Nhien NV, Khan NC, Yabutani T, Ninh NX, Chung LTK, Motonaka J, et al. Relationship of low serum selenium to anemia among primary school children living in rural Vietnam. *J Nutr Sci Vitaminol* (2008) 54(6):454–9. doi: 10.3177/jnsv.54.454

8. Paradkar PN, Domenico ID, Durchfort N, Durchfort N, Zohn I, Kaplan J, et al. Iron depletion limits intracellular bacterial growth in macrophages. *Blood* (2008) 112(3):866–74. doi: 10.1182/blood-2007-12-126854

9. Iatsenkoa I, Marraa A, Boquetea JP, Peña J, Lemaitre B. Iron sequestration by transferrin 1 mediates nutritional immunity in drosophila melanogaster. *PNAS* (2020) 117(13):7317–25. doi: 10.1073/pnas.1914830117

10. Hood MI, Skaar EP. Nutritional immunity: transition metals at the pathogen-host interface. *Nat Rev Microbiol* (2012) 10:525–37. doi: 10.1038/nrmicro2836

11. Bishwal SC, Das MK, Badireddy VK, Dabral D, Das A, Mahapatra AR, et al. Sputum proteomics reveals a shift in vitamin d-binding protein and antimicrobial protein axis in tuberculosis patients. *Sci Rep* (2019) 9(1036):(1–9). doi: 10.1038/s41598-018-37662-9

12. Nawia AM, China SF, Jamal R. Simultaneous analysis of 25 trace elements in micro volume of human serum by inductively coupled plasma mass spectrometry (ICP-MS). *Pract Lab Med* (2020) 18:e00142 (1–10). doi: 10.1016/j.plabm.2019.e00142

13. Davcheva DM, Kirova GK, Tsvetkova TZ, Terzieva DD, Kiryakova MT, Kmetov VJ. Sample preparation and calibration optimization for ICP-MS analysis of copper, zinc, selenium, rubidium, strontium, magnesium, iron, molybdenum and barium in human serum. *Bulg. Chem Commun* (2019) 51(D):52–7.

14. Pang Z, Chong J, Zhou G, de Lima Morais DA, Chang L, Barrette M, et al. MetaboAnalyst 5.0: narrowing the gap between raw spectra and functional insights. *Nucl Acids Res* (2021) 49(W1):W388–96. doi: 10.1093/nar/gkab382

15. Kim I, Yetley EA, Calvo MS. Variations in iron-status measures during the menstrual cycle. *Am J Clin Nutr* (1993) 58(5):705–9. doi: 10.1093/ajcn/58.5.705

16. Dai Y, Shan W, Yang Q, Guo J, Zhai R, Tang X, et al. Biomarkers of iron metabolism facilitate clinical diagnosis in mycobacterium tuberculosis infection. *Thorax* (2019) 74:1161–7. doi: 10.1136/thoraxjnl-2018-212557

17. Qi C, Wang H, Liu Z, Yang H. Oxidative stress and trace elements in pulmonary tuberculosis patients during 6 months anti-tuberculosis treatment. *Biol Trace Elem Res* (2021) 199:1259–67. doi: 10.1007/s12011-020-02254-0

18. Chmielnickaa J, Nasiadeka M, Lewandowska-Żyndula EL, Pińkowski R. Effect of aluminum on hematopoiesis after intraperitoneal exposure in rats. *Ecotoxicol. Environ Saf* (1996) 33(3):201–6. doi: 10.1006/eesa.1996.0026

19. Kałkowska KG, Kanoniuk D, Szubartowska E, Winiarczyk AU. Influence of drinking water-administered aluminium on morphology and respiratory function of blood in rats *Pol. J Environ Stud* (2004) 13(5):515–9.

20. Available at: https://www.euro.who.int/:data/assets/pdf_file/0016/123073/AQG2ndEd_6_3Cadmium.PDF.

21. Djoba Siawaya JF, Beyers N, van Helden P, Walzl G.. Differential cytokine secretion and early treatment response in patients with pulmonary tuberculosis. *Clin Exp Immunol* (2009) 156(1):69–77. doi: 10.1111/j.1365-2249.2009.03875.x

22. Yamada G, Shijubo N, Shigehara K, Okamura H, Kurimoto M, Abe S. Increased levels of circulating interleukin-18 in patients with advanced tuberculosis. *Am J Respir Crit Care Med* (2000) 161:1786–9. doi: 10.1164/ajrccm.161.6.9911054

23. Kaplanski G. Interleukin- 18: Biological properties and role in disease pathogenesis. *Immunol Rev* (2018) 281:138–53. doi: 10.1111/imr.12616

24. Biet F, Locht C, Kremer L. Immunoregulatory functions of interleukin 18 and its role in defense against bacterial pathogens. *J Mol Med* (2002) 80:147–62. doi: 10.1007/s00109-001-0307-1

25. Vankayalapati R, Wizel B, Weis SE, Klucar P, Shams H, Samten B, et al. Serum cytokine concentrations do not parallel mycobacterium tuberculosis–induced cytokine production in patients with tuberculosis. *Clin Infect Dis* (2003) 36:24–8. doi: 10.1086/344903

26. Redford PS, Murray PJ, O'Garra A. The role of IL-10 in immune regulation during M. tuberculosis infection. *Mucosal Immunol* (2011) 4(3):261–70. doi: 10.1038/mi.2011.7

27. Batra HS, Singh P, Somani BL, Gupta A, Sampath S, Ambade V. Serum ferroxidase albumin ratio as a marken in pulmonary tuberculosis. *Indian J Clin Biochem* (2007) 22(2):106–8. doi: 10.1007/BF02913325

28. Cernat RI, Mihaescu T, Vornicu M, Vione D, Olariu RI, Arsene C. Serum trace metal and ceruloplasmin variability in individuals treated for pulmonary tuberculosis. *Int J Tuberc. Lung Dis* (2011) 15(9):1239–45. doi: 10.5588/ijtld.10.0445

29. Nemeth E, Rivera S, Gabayan V, Keller C, Taudorf S, Pedersen BK, et al. IL-6 mediates hypoferremia of inflammation by inducing the synthesis of the iron regulatory hormone hepcidin. *J Clin Invest* (2004) 113(9):1271–6. doi: 10.1172/JCI200420945

30. Lee P, Peng H, Gelbart T, Wang L, Beutler E. Regulation of hepcidin transcription by interleukin-1 and interleukin-6. *PNAS* (2005) 102(6):1906–10. doi: 10.1073/pnas.0409808102

31. Ganz T. Hepcidin, a key regulator of iron metabolism and mediator of anemia of inflammation. *Blood* (2003) 102(3):783–8. doi: 10.1182/blood-2003-03-0672

32. Cercamondi CI, Stoffel N, Moretti D, Zoller T, Swinkels DW, Zeder C, et al. Iron homeostasis during anemia of inflammation: a prospective study in patients with tuberculosis. *Blood* (2021) 138(15):1293–303. doi: 10.1182/blood.2020010562

33. Nairz M, Ferrinmg-Appel D, Casarrubea D, Sonnweber T, Viatte L, Schroll A, et al. Iron regulatory proteins mediate host resistance to salmonella infection. *Cell Host Microbe* (2015) 18(2):254–61. doi: 10.1016/j.chom.2015.06.017

34. Canonne-Hergaux F, Gruenheid S, Ponka P, Gros P. Cellular and subcellular localization of the Nramp2 iron transporter in the intestinal brush border and regulation by dietary iron. *Blood* (1999) 93(12):4406–17. doi: 10.1182/blood.V93.12.4406

35. Babitt JL, Huang FW, Wrighting DM, Xia Y, Sidis Y, Samad TA, et al. Bone morphogenetic protein signaling by hemojuvelin regulates hepcidin expression. *Nat Genet* (2006) 38(5):531–9. doi: 10.1038/ng1777

36. Niederkofler V, Salie R, Arber S. Hemojuvelin is essential for dietary iron sensing, and its mutation leads to severe iron overload. *J Clin Invest* (2005) 115 (8):2180–6. doi: 10.1172/JCI25683

Frontiers in Immunology

Explores novel approaches and diagnoses to treat immune disorders.

The official journal of the International Union of Immunological Societies (IUIS) and the most cited in its field, leading the way for research across basic, translational and clinical immunology.

Discover the latest Research Topics

See more →

Frontiers

Avenue du Tribunal-Fédéral 34
1005 Lausanne, Switzerland
frontiersin.org

Contact us

+41 (0)21 510 17 00
frontiersin.org/about/contact